



**UNIVERSITY OF
CAMBRIDGE**

Chemical Engineering and
Biotechnology

Mitigating fouling of heat exchangers with fluoropolymer coatings

by

Ole Mathis Magens

Churchill College

This dissertation is submitted for the degree of

Doctor of Philosophy

December 20, 2018

Abstract

Fouling is a chronic problem in many heat transfer systems and results in the need for frequent heat exchanger (HEX) cleaning. In the dairy industry, the associated operating cost and environmental impact are substantial. Antifouling coatings are one mitigation option. In this work, the fouling behaviour of fluoropolymer, polypropylene and stainless steel heat transfer surfaces in processing raw milk and whey protein solution are studied. Methodologies to assess the economics of antifouling coatings are developed and applied.

Two experimental apparatuses were designed and constructed to study fouling at surface temperatures around 90°C. A microfluidic system with a 650 × 2000 μm flow channel enables fouling studies to be carried out by recirculating 2l of raw milk. The apparatus operates in the laminar flow regime and the capability to probe the local composition of delicate fouling deposit *in-situ* with histological techniques employing confocal laser scanning microscopy. A larger bench-scale apparatus with a 10 × 42 mm flow channel was built to recirculate 17l of solution in the turbulent flow regime which is more representative of conditions in an industrial plate HEX.

Experimental results demonstrate that fluoropolymer coatings can reduce fouling masses from raw milk and whey protein solution by up to 50%. Surface properties affect the structure and composition of the deposit. At the interface with apolar surfaces raw milk fouling layers are high in protein, whereas a strongly attached mineral-rich layer is present at the interface with steel. Whey protein deposits generated on apolar surfaces are more spongy and have a lower thermal conductivity and/or density than deposits on steel. The attraction of denatured protein towards apolar surfaces and the formation of a calcium phosphate layer on steel at later stages of fouling are explained with arguments based on the interfacial free energy of these materials in water.

The financial attractiveness of coatings is considered for HEXs subject to linearly and asymptotically increasing fouling resistance and using a spatially resolved fouling model. An explicit solution to the cleaning-scheduling problem is presented for the case of equal heat capacity flow rates in a counter-current HEX. Scenarios where the use of coatings may be attractive or where there is no financial benefit in cleaning a fouled exchanger are identified. Finally, experimental data are used to estimate the economic potential of fluoropolymer coated HEXs in the ultra-high-temperature treatment of milk. In the considered case, the value of a fluoropolymer coating inferred from the reduction in fouling is estimated to be around 2000 US\$ m⁻².

Acknowledgements

I would like to thank the following people for their contributions towards the completion of my PhD project: Firstly, I would like to thank Prof. Ian Wilson for supervising my work and for offering helpful advice and patience. I would also like to thank Drs Jurgen Hofmans, Joke Nelissen and Yves Adriaenssens from The Chemours Company, LLC for providing helpful discussions and advice. The sponsorship of this project by Chemours is appreciated.

I am appreciative of the commitment and support from MPhil students Yingda Liu and Hyungsik Shim. Petar Besevic has been a great help in using ICP-MS. Thanks also go to the mechanical and electronics section staff at the Department of Chemical Engineering, in particular Andy Hubbard, for discussing the design of the bench-scale heat exchanger. It has been a delight to work with Sebastien Cosnefroy on wiring up the apparatuses. Dairy Supervisor Bernadette Molloy from the Cambridge University Park Farm kindly supplied raw milk for my research.

Finally, I would like to thank my family and my wife Miriam, who have been constantly supporting me and who ultimately made this work possible.

Publications

Some of the material presented in this dissertation has been published in the following papers:

1. Magens, O. M., Hofmans, J., Pabon, M., & Wilson, D. I. (2015). Value pricing of antifouling coatings in heat exchangers. In *Heat Exchanger Fouling and Cleaning Conference* (pp. 350–357). Enfield, Ireland.
2. Magens, O. M., Ishiyama, E. M., & Wilson, D. I. (2016). Quantifying the ‘implementation gap’ for antifouling coatings. *Appl. Therm. Eng.*, *99*, 683–689.
3. Magens, O. M., Hofmans, J., & Wilson, D. I. (2017). A fouling micro-system for investigating fluoropolymer antifouling coatings in bovine milk pasteurisation, In *Heat Exchanger Fouling and Cleaning Conference* (pp. 140–147). Aranjuez, Spain.
4. Magens, O. M., Liu, Y., Hofmans, J. F. A., Nelissen, J. A., & Ian Wilson, D. I. (2017). Adhesion and cleaning of foods with complex structure: Effect of oil content and fluoropolymer coating characteristics on the detachment of cake from baking surfaces. *Journal of Food Engineering*, *197*, 48–59.
5. Magens, O. M., Hofmans, J. F. A., Adriaenssens, Y., & Ian Wilson, D. I. (2018). Comparison of fouling of raw milk and whey protein solution on stainless steel and fluorocarbon coated surfaces: Effects on fouling performance, deposit structure and composition. *Chemical Engineering Science*, *in press*.

The following additional paper was published during the project period:

1. Hallmark, B., Bryan, M., Bosson, E., Butler, S., Hoier, T., Magens, O. M., ... Wilson, D. I. (2016). A portable and affordable extensional rheometer for field testing. *Measurement Science and Technology*, *27*(12).

Table of contents

Abstract	iii
Acknowledgements	v
Publications	vii
Table of contents	ix
List of figures	xiii
List of tables	xvii
Nomenclature	xix
1 Introduction	1
1.1 Context	1
1.2 Project objectives	1
1.3 Structure of this dissertation	2
2 Literature review	5
2.1 Fouling in heat exchangers	5
2.2 Milk fouling	6
2.2.1 Fouling in milk heat treatment	6
2.2.2 Surface-foulant interactions	9
2.3 Antifouling coatings in heat exchangers	10
2.3.1 Fluoropolymer coatings	10
2.3.2 Other types of coatings	13
2.3.3 Economics of antifouling coatings in heat exchangers	16
2.4 Research techniques	18
2.4.1 Surface characterisation	18
2.4.2 Test rigs to study fouling	22
2.4.3 Fouling deposit analysis	24
2.4.4 Summary of the state of the art	25
3 Techno-economics of antifouling coatings in heat exchangers	27
3.1 Introduction	27
3.2 Lumped model	27
3.2.1 Phenomenological fouling models	27
3.2.2 Objective functions for preheater operations subject to fouling	29
3.2.3 Impact of asymptotic fouling in a simple heat exchanger	30

3.2.4	Explicit solutions for cases of counter-current flow and equal heat capacity flow rates	33
3.2.5	Illustrative case study: evaluating the water scaling performance of a PFPE coating	39
3.2.6	Results and discussion	41
3.3	Dynamic model	46
3.3.1	Modelling of a fouling heat exchanger in space and time	46
3.3.2	Temperature and velocity dependent surface integration crystallisation fouling model	47
3.3.3	Solution method	48
3.3.4	Illustrative case study: evaluating crystallisation fouling performances of polymer coatings	49
3.3.5	Results and Discussion	52
3.3.6	Effect of antifouling performance on coating value	54
3.4	Summary	57
4	Surface characterisation	59
4.1	Coating and substrate materials	59
4.2	Coating thickness, thermal resistance and surface topography	59
4.3	Surface energy	62
5	Milk fouling studies	67
5.1	Introduction	67
5.2	Materials	68
5.2.1	Raw milk	68
5.2.2	Whey protein solution	69
5.3	Fouling layer analysis methods	71
5.3.1	Confocal laser scanning microscopy (CLSM)	71
5.3.2	Confocal thickness scanning (CTS)	72
5.3.3	Inductively coupled plasma mass spectrometry (ICP-MS)	72
5.4	The microfluidic heat exchanger apparatus	73
5.4.1	Design & construction	73
5.4.2	Thermo-hydraulic characterisation	75
5.4.3	Raw milk fouling studies on steel and fluoropolymers	79
5.5	The bench-scale heat exchanger rig	94
5.5.1	Design & construction	94
5.5.2	Control hard- & software	96
5.5.3	Thermo-hydraulic characterisation	97

5.5.4	Whey protein solution and raw milk fouling studies on steel and fluoropolymer surfaces	100
5.6	Summary	118
6	Economic potential of FP antifouling coatings in UHT plate HEXs	121
6.1	Setting up the case	121
6.2	Results and discussion	125
6.3	Summary	129
7	Conclusions and future work	131
7.1	Conclusions	131
7.1.1	Experimental studies	131
7.1.2	Techno-economics of antifouling coatings	132
7.2	Future work	133
7.2.1	Experimental studies	133
7.2.2	Techno-economics of antifouling coatings	134
7.2.3	Millimanipulation	135
	Appendices	136
	Appendix A Thermogravimetric analysis	136
	Appendix B Raw milk CLSM micrographs	137
	Appendix C Microfluidic HEX fouling resistance evolution	138
	Appendix D Bench-scale HEX rig graphical user interface	139
	Appendix E Appended publication on Millimanipulation	140
	References	154

List of figures

2.1	Simplified schematic of a plate HEX used for milk heat treatment based on Bylund (2015).	6
2.2	Schematic denaturation mechanism of β -LG, adopted from Tolkach and Kulozik (2007).	8
2.3	Chemical structures of (a) PTFE (a homopolymer), (b) FEP, and (c) PFA (both copolymers) (McKeen, 2007).	12
2.4	Schematic of a fouling-cleaning cycle in an uncoated (a) and coated (b) single HEX over time t'	17
2.5	Schematic of a particle (here, a polymer strand) (a) adsorbing to a surface and (b) aggregating with a second particle of identical nature.	21
3.1	Idealised evolutions of fouling resistance over time as summarised by Bott (1995, 2001).	28
3.2	Non-dimensionalised objective functions of a HEX which is never cleaned (<i>i.e.</i> $t \rightarrow \infty$) assuming asymptotic fouling, counter-current flow, and equal heat capacity flow rates.	33
3.3	Lambert-W function for real valued arguments showing the principal and lower branch, $W_0 \geq -1$ and $W_{-1} \leq -1$, respectively (after Valluri, Jeffrey, & Corless, 2000).	34
3.4	Fouling resistance-time data for uncoated (SS) and coated (PFPE) HEX reported by Oldani <i>et al.</i> (2013).	39
3.5	Effect of processing period length on (a) time averaged heat duty, (b) time averaged operating cost, and (c) operating cost per heat transferred in lumped model case study.	42
3.6	Impact of fouling model parameters t_f and R_f^∞ on the optimal operating cost for the uncoated SS unit in Table 3.2.	45
3.7	Elements of the enthalpy balance on either side of an increment of length for a counter-current heat exchanger (Fryer & Slater, 1985).	47
3.8	Hot stream (red lines) and cold stream (blue lines) bulk temperature distribution along the uncoated HEX at selected times, t'	52
3.9	Fouling Biot number distribution in uncoated HEX at selected times, t'	52
3.10	Evolution of the overall fouling resistance, R_f , of the uncoated unit over the processing time, t'	53

3.11	Effect of processing period length on (a) time averaged heat duty, (b) time averaged operating cost, and (c) operating cost per heat transferred in dynamic model case study.	54
3.12	Effect of non-dimensional antifouling coating performance on the ratio of optimal operating cost to that of the uncoated exchanger.	56
3.13	Value prices of coatings for different ratios of deposition rates, three asset lifetimes, and four dimensionless cleaning period lengths.	56
4.1	Filtered and interpolated surface topographies. Height scales are in micrometres and differ between figures.	61
4.2	CLSM images of PTFE-2 surface infused with dodecane containing 0.1 % g g^{-1} oil red O.	62
4.3	Apolar, γ^{LW} , and electron donor, γ^- , contributions to surface energy.	65
5.1	Microfluidic HEX cell assembly.	73
5.2	Photograph of the microfluidic HEX cell	74
5.3	Microfluidic HEX process schematic. Labels explained in text.	75
5.4	(a) electrical resistance and (b) heat loss in the microfluidic HEX.	76
5.5	Estimated bulk and surface temperature distribution in the microfluidic fouling cell for standard operating conditions.	78
5.6	Example of microfluidic HEX monitoring record for a fouling test on stainless steel.	80
5.7	Pressure drop profiles for fouling tests with raw milk using the microfluidic HEX.	81
5.8	Estimated thickness evolution of uniform raw milk deposit layers in the microfluidic HEX calculated with Equation 5.8.	81
5.9	Fouling resistance profiles for raw milk fouling tests with microfluidic HEX on (a) SS and (b) FEP-2.	83
5.10	Deposit coverage (dry mass per unit area) from raw milk after a test duration of 120 min (except for PFA-2: 65 min, see Figure 5.7a).	84
5.11	Representative pictures of dried raw milk deposits from the microfluidic HEX after 120 min (or otherwise indicated) of processing.	85
5.12	CLSM sections through a raw milk fouling layer on SS.	86
5.13	CLSM images showing the composition of raw milk deposit generated with the microfluidic HEX on apolar surfaces.	87
5.14	Contours of interfacial free energy of interaction, $\Delta G_{123}^{\text{IF}}$ (mJ m^{-2}), of (subscript 1) denatured BLG and (2) monopolar surfaces, in (3) (a) water and (b) air.	89

5.15	Contours of the change in interfacial free energy of interaction of denatured BLG and surfaces on drying, ΔG^{drying} .	90
5.16	Contours of interfacial free energy of interaction, $\Delta G_{123}^{\text{IF}}$ (mJ m^{-2}), (subscript 1) of (a) DCPD (b) OCP (c) HAP and (2) monopolar surfaces in (3) water.	91
5.17	Contours of the change in interfacial free energy, $\Delta G^{\text{CP integration}}$ (mJ m^{-2}), of a calcium phosphate layer forming between adsorbed BLG and the surface.	92
5.18	Bench-scale HEX process schematic with labelled sub-systems.	94
5.19	The bench-scale HEX assembly. Labels are explained in the text.	96
5.20	Bench-scale HEX heater characterisation: (a) steady state heat loss to the environment over temperature driving force at $T_{\text{env}} = 21\text{ }^{\circ}\text{C}$ and (b) heating rate as a function of electrical heater power at $T_h \approx 100\text{ }^{\circ}\text{C}$.	97
5.21	Thermochromic liquid crystal coated SS sample in bench-scale HEX observed through window.	99
5.22	Bench-scale HEX mean film heat transfer coefficient, h_m , over volumetric flow rate, \dot{V} , and Reynolds number, Re .	99
5.23	Overall heat transfer coefficient, U_{cl} , of unpressurised bench-scale HEX loaded with sample FEP-2 for different water flow rates, \dot{V} , and heater temperatures, T_h .	99
5.24	Example of bench-scale HEX monitoring record for a WP fouling test on SS.	101
5.25	Evolution of fouling resistance, R_f , and pH (solid circles) for a bench-scale HEX fouling test with WP solution on SS.	101
5.26	pH evolution of (a) WP solutions and (b) raw milk during bench-scale HEX fouling experiments.	102
5.27	Fouling resistance profiles for fouling tests with bench-scale HEX using WP solution.	103
5.28	Fouling resistance profiles for fouling tests in bench-scale HEX with (a) WP solution with 10 g l^{-1} milk fat added at $T_s = 89\text{ }^{\circ}\text{C}$ and (b) raw milk at $T_s = 92.5\text{ }^{\circ}\text{C}$.	104
5.29	Deposit coverage (dry mass per area) for different surfaces tested in the bench-scale HEX for a duration of 150 min.	105
5.30	Relationship between final fouling resistance and whey protein dry deposit mass coverage for different surfaces tested with the bench-scale HEX.	106
5.31	CLSM top views and orthogonal sections of WP fouling layers from the bench-scale HEX on (a) SS and (b) PFA-4.	108
5.32	CLSM micrographs of fat at the deposit-sample interface from bench-scale HEX tests using WP solution with added cream on (a) SS, (b) FEP-3, and (c) PP.	109

5.33	Representative photographs of dried deposits from bench-scale HEX after 150 min of processing WP solution at $\dot{V} = 81 \text{ min}^{-1}$, $T_{s,m} = 89^\circ\text{C}$, $T_{b,t1} = 61^\circ\text{C}$ on (a) SS, (b) PP, and (c) FPs.....	110
5.34	Dry thickness of deposit from WP solution generated in the bench-scale HEX on (a,c) SS and (b) FEP-3 determined by CTS.....	111
5.35	Deposit coverage (dry mass per area), m_f , from WP solution in the bench-scale HEX after a test duration of 150 min at $T_s = 89^\circ\text{C}$ for (a) different flow rates, \dot{V} , and (b) corresponding average wall shear stresses, τ_m	112
5.36	Fouling resistance profiles for fouling tests in bench-scale HEX with WP solution at $T_s = 89^\circ\text{C}$ for different flow rates.	113
5.37	Representative pictures of dried deposits from bench-scale HEX after 150 min of processing WP solution at $\dot{V} = 51 \text{ min}^{-1}$ to 71 min^{-1} , $T_{s,m} = 89^\circ\text{C}$, $T_{b,t1} = 61^\circ\text{C}$ on SS (a-c) and and PFA-4 (d-e)	114
5.38	Interaction potentials over separation distance, l , of a MFG ($D = 2 \mu\text{m}$) and flat surfaces of (a) SS, (b) FEP-3, and (c) PP at $T = 362 \text{ K}$	117
6.1	Simplified schematic of a plate HEX used for UHT treatment of pre-pasteurised milk based on Bylund (2015) and Lalande, Tissier, and Corrieu (1984).	122
6.2	Fouling resistance evolution of SS HEX in UHT case study.	123
6.3	Effect of processing period length on (a) time averaged heat duty, (b) time averaged operating cost, and (c) operating cost per heat transferred in UHT case study.....	126
6.4	Effect of cleaning enhancement on value prices of coatings for different ratios of cleaning costs, $C_{cl,coat}/C_{cl}$ and five dimensionless cleaning period lengths, τ_{coat}/τ . The grey solid circle marks the case study unit ‘coated HEX B’.....	129
A.1	Thermogravimetric analysis (TA instruments Q500) results of (a) β -LG, (b) Hiprotal WP 35 concentrate and bench-scale HEX deposits from WP solution on (c) SS, and (d) PP.	136
B.1	CLSM images of raw milk as received (a) and treated (b,c).	137
C.1	Fouling resistance profiles for raw milk fouling tests with microfluidic HEX on (a) PFA-2, (b) PFA-3, (c) PTFE-1, (d) PFA-2 precoated with rapeseed oil and (e) FEP-2 precoated with butter fat.	138
D.1	Graphical user interface of the bench-scale HEX rig.....	139

List of tables

2.1	Summary of studies on antifouling coatings for milk-related products based on a table by Gomes da Cruz <i>et al.</i> (2015).....	15
3.1	Explicit solutions to the cleaning scheduling problem of a single counter-current HEX with equal heat capacity flow rates for different fouling behaviours and objective functions.	38
3.2	Lumped model case study parameters.....	40
3.3	Comparison of optimal performance indices in lumped model case study (parameters in Table 3.2).	43
3.4	Capital costs and maximum coating costs per area of the HEXs considered in the lumped model case study with parameters given in Table 3.2.	44
3.5	Crystallisation fouling kinetic parameters, experimental conditions, and fouling layer properties (Pääkkönen <i>et al.</i> , 2015)	50
3.6	Design, operating and cost parameters of the coated and uncoated HEXs. .	51
4.1	Characteristics of the surfaces studied.	60
4.2	Advancing contact angles, β , measured at 20 °C and surface energy components calculated with the van Oss, Good, and Chaudhury (1987) approach.	64
5.1	Composition of raw milk sample (Aug. 2017) and typical raw milk composition reported in the literature.	68
5.2	Composition of rapeseed oil (Sainsbury’s SO organic rapeseed oil), clarified butter (East End pure butter ghee) and single cream (Sainbury’s fresh single cream) according to packaging information.....	70
5.3	Composition of Hiprotal whey protein 35 and final 18.2 g l ⁻¹ solution according to the supplied data sheet.	70
5.4	Average and local Nusselt numbers, Nu_m and Nu , for thermally developing laminar flow in rectangular channels with aspect ratio 1/3 heated from four sides for various dimensionless positions.	77
5.5	Calcium fraction of solution dry solids (reproduced from Table 5.1 and 5.3) and fouling deposits determined by ICP-MS.	107
6.1	UHT steriliser case study parameters.	124
6.2	Comparison of optimal performance indices in UHT case study (parameters in Table 3.2).	127

6.3 Capital costs and maximum coating costs per area of the HEXs considered
in the UHT case study with parameters given in Table 6.1. 128

Nomenclature

Symbols - Latin

A	Heat transfer area	m^2
a	Channel width	m
a_1	Reciprocal asymptotic fouling resistance in Eq. 3.6	$\text{W m}^{-2} \text{K}^{-1}$
a_2	Reciprocal asymptotic fouling Biot number in Eq. 3.6	1
a_3	HEX model constant in Eq. 3.11	kW
a_4	Dimensionless HEX model constant in Eq. 3.12	1
a_5	Model constant in Eq. 3.21	s
b	Channel height	m
Bi_f	Fouling Biot number, $Bi_f = U_{cl}R_f$	1
C	Cost per HEX unit	$\text{US\$}$
c_{coat}	Coating cost per area	$\text{US\$ m}^{-2}$
c_E	Cost per unit heat not transferred	$\text{US\$ J}^{-1}$
C_{IF}	CaCO_3 concentration at the deposit-solution interface	kg m^{-3}
c_p	Specific heat capacity	$\text{J kg}^{-1} \text{K}^{-1}$
C_{sat}	CaCO_3 saturation concentration	kg m^{-3}
D	Diameter	m
D_h	Hydraulic diameter	m
E_a	Activation energy	J mol^{-1}
f_D	Darcy friction factor	1
G	Free energy, absolute or per area	J, mJ m^{-2}
h	Film heat transfer coefficient	$\text{W m}^{-2} \text{K}^{-1}$
j	Order of reaction	1
k	Thermal conductivity	$\text{W m}^{-1} \text{K}^{-1}$
k_B	Boltzmann constant, $k_B = 1.381 \times 10^{-23} \text{J K}^{-1}$	J K^{-1}
k_d	Deposition rate factor	$\text{m}^4 \text{kg}^{-1} \text{s}^{-2}$
k'_d	Deposition rate factor $k'_d = k_d \mu / (\rho v_*^2)$	$\text{m}^4 \text{kg}^{-1} \text{s}^{-1}$
L	Length of the HEX	m
l_0	Minimum equilibrium distance of two condensed-phase surfaces	m
m	Mass	kg
\dot{m}	Mass flow rate	kg s^{-1}
N	Total number of nodes	1
n	A natural number	1
NTU	Number of heat transfer units	1
Nu	Nusselt number	1

P	Pressure	Pa
Pe	Péclet number	1
Pr	Prandtl number	1
q	Heat duty of a HEX	W
q_e	Electric heater power	W
q_{env}	Heat loss to the environment	W
R	Gas constant, $R = 8.314 \text{ J mol}^{-1} \text{ K}^{-1}$	$\text{J mol}^{-1} \text{ K}^{-1}$
r	Radius	m
R_f	Fouling resistance	$\text{m}^2 \text{ K W}^{-1}$
r_f	Rate const. in linear fouling model	$\text{m}^2 \text{ K J}^{-1}$
R_h	Electrical heater resistance	Ω
Re	Reynolds number	1
S_a	Arithmetic mean roughness	nm
S_q	Root mean square roughness	nm
T	Temperature	K
t	Operating period	d
t'	Time, used as variable in integrand $0 \leq t' \leq t$	d
t^*	$t^* = t' - t_{ind}$	d
t_f	Characteristic fouling time scale	d
t_{lf}	Asset lifetime or depreciation period	year
t_{cycle}	Fouling-cleaning period	d
t_{ind}	Induction period	d
U	Overall heat transfer coefficient	$\text{W m}^{-2} \text{ K}^{-1}$
v	Velocity	m s^{-1}
\dot{V}	Volumetric flow rate	l min^{-1}
v_*	Friction velocity	m s^{-1}
W	Heat capacity flow rate	W K^{-1}
x	Position in the HEX	m
x^*	Dimensionless position, $x^* = x/D_h Pe$	1

Symbols - Greek

β	Contact angle	$^\circ$
γ	Surface free energy or surface tension	mJ m^{-2}
Δ	Difference operator	–
δ	Thickness	m
ε	Effectiveness	1
η	Relative approximation error	1
λ	Characteristic decay length of water	m
μ	Viscosity	Pa s

τ	Time taken for cleaning, shear stress	d, Pa
ϕ	Average cost per time or per unit heat transferred	US\$ d ⁻¹ , US\$ J ⁻¹
χ_1	Model constant, see Equation 3.21	s
$\chi_{2,3,4}$	Dimensionless model constants, see Table 3.1	1

Subscripts and superscripts

∞	Asymptotic value
t'	Temporal
x	Spatial
+	Electron acceptor
-	Electron donor
1,2,3	Medium 1,2,3
AB	Lewis acid-base interactions
approx	Approximately
b	Bulk
base	Per HEX unit without coating
c	Cold side
cl	Clean
coat	Coating, coated heat exchanger
crit	Critical
CS	Carbon steel
f	Fouling
h	Heater, Hot side
IF	Interfacial
in	Inlet
LW	Lifshitz-van der Waals interactions
m	Mean
max	Maximum
min	Minimum
new	New
op	Operating
opt	Optimum
out	Outlet
Q	Per heat transferred
rev	Revamped
s	Surface
SS	Stainless steel
t1, t2, t3	Tank 1, 2, 3
w	Wall

Abbreviations

β -LG	β -lactoglobulin protein
BEM	Bonnet, one pass shell, fixed tubesheet bonnet
CA	Cellulose acetate
CG	Calcium green A1
CLSM	Confocal laser scanning microscopy/microscope
CNT	Carbon nanotube
CP	Calcium phosphate
CS	Carbon steel
CTS	Confocal thickness scanning
CVD	Chemical vapour deposition
DCPD	Dicalcium phosphate dihydrate
DLC	Diamond like carbon
ELISA	Enzyme-linked immunosorbent assay
FEP	Fluorinated ethylene propylene
FP	Fluoropolymer
HAP	Hydroxyapatite
HEX	Heat exchanger
HTST	High temperature short time
ICP-MS	Inductively coupled plasma mass spectroscopy
ICP-OES	Inductively coupled plasma optical emission spectroscopy
MFG	Milk fat globule
Ni-P-PTFE	Nickel-phosphorus-polytetrafluoroethylene
NMR	Nuclear magnetic resonance
OCP	Octacalcium phosphate
PE	Polyethylene
PECVD	Plasma enhanced chemical vapour deposition
PEEK	polyether-ether-ketone
PFA	Perfluoroalkoxy
PFPE	Perfluoropolyether
PMMA	Polymethyl methacrylate
PP	Polypropylene
PS	Polystyrene
PTFE	Polytetrafluoroethylene
PVD	Physical vapour deposition
SMUF	Simulated milk ultrafiltrate
SS	Stainless steel
TG	Triglyceride
TR-SC	Texas red sulfonyl chloride
UHT	Ultra-high temperature

WP Whey protein
XDLVO Extended Derjaguin, Landau, Verwey and Overbeek
 (theory)

Chapter 1

Introduction

1.1 Context

Fouling, the accumulation of unwanted deposit on heat transfer surfaces, reduces the performance of heat exchangers (HEXs) and incurs substantial operating expenses. These are costs due to oversized HEX units, increased thermal inefficiency and pressure drop, loss of production, maintenance and cleaning (Epstein, 1983). Cleaning introduces further, non-energetic, environmental impacts associated with consumption and disposal of cleaning chemicals and wasted product. The thermal load of HEXs in the food industry is commonly in the order of megawatts. A reduction of the regenerative heating duty thus also leads to a sizeable increase in greenhouse gas emissions.

Fouling is determined by the nature and source of the foulant, additives, bulk temperature, flow velocity, flow regime and residence time (Geddert, Bialuch, Augustin, & Scholl, 2009). At the heat transfer surface, the local temperature and its surface energy, topography and amount of nucleation sites are important. In most industrial heat exchangers the processing conditions are confined to a narrow range. An option to stop or slow down the accumulation of unwanted deposits is to apply surface antifouling materials to reduce deposit attachment and promote cleaning. This work focuses on fluoropolymer (FP) based coatings which show potential to slow down fouling in equipment for milk heat treatment.

1.2 Project objectives

The aim of this project was to apply and extend the knowledge of FP coatings to mitigate fouling in HEX applications. The focus lay on fouling from raw milk and milk model systems. It is important to note that this project did not involve development of new FP materials or coatings. The two main questions to be answered were:

- A. How well do FP materials need to work to be economically attractive?

- B. How well and by what mechanism(s) do they mitigate fouling? Can this then be predicted?

Four objectives were identified to answer questions A and B, with modelling and experimental components.

Addressed question	Objective
A	Development of techno-economic models to determine the economical feasibility of FP HEX units versus conventional units over multiple fouling and cleaning cycles.
A, B	Measuring the characteristic properties including surface energy, roughness, topology and thermal resistance of FP materials provided by the project sponsors.
A, B	Development and application of laboratory HEX(s), safe for use with microbiologically active raw milk, to analyse the fouling and cleaning behaviour of FP coatings over several fouling and cleaning cycles under conditions simulating industrial operations.
A	Utilisation of the data from coating characterisation and fouling experiments in the techno-economic analysis to refine the economical assessment of FP coatings in milk pasteurisers.

1.3 Structure of this dissertation

This dissertation begins by giving an introduction to fouling and reviewing literature concerned with milk fouling in particular. The reader is introduced to the manufacture, the unique properties and application of FP coatings. Recent studies on antifouling coatings in HEXs for milk heat treatment are summarised. The methods developed by researchers to assess the value of antifouling coatings by coupling economic objective functions with physical HEX models are discussed. The physical models require experimental data from coating characterisation and fouling test rigs: these research techniques and methods to analyse fouling deposits are described at the end of Chapter 2.

Chapter 3 is concerned with improving techno-economic models to value antifouling coatings in HEXs. Two approaches are considered: A lumped model based on the ‘number of

transfer units' method gives valuable fundamental insight into the economics of antifouling strategies and cleaning-scheduling of HEXs. A spatially resolved model demonstrates how a mechanistic fouling model can be employed in the 'value-pricing' framework. These approaches are illustrated with case studies based on data from the literature.

Chapter 4 reports the properties of the coatings and substrate materials studied: coating material, thickness, thermal resistance, surface topography and surface energy.

A major fraction of this work is dedicated to experimental fouling studies with laboratory apparatuses using raw milk and whey protein (WP) solution. Chapter 5 describes the design and operation of a microfluidic fouling system and bench-scale HEX rig. The apparatuses are used to measure the fouling performance of coating systems against the performance of a stainless steel (SS) reference material. Emphasis is laid on studying how the surface material affects the structure and composition of fouling deposit. The experimental results are interpreted by considering the free energy of interaction of fouling particles with heat transfer surfaces in an aqueous environment.

In Chapter 6 the information from coating characterisation and fouling experiments are utilised to estimate the economic potential of FP coated plate HEXs in the ultra-high temperature (UHT) treatment of milk. The incremental financial return of coating improvements is determined to provide guidance for future coating research and development projects.

This dissertation concludes with Chapter 7 by summarising the key scientific advances and proposing avenues for further research.

Chapter 2

Literature review

2.1 Fouling in heat exchangers

Fouling is defined as the accumulation of unwanted deposits on surfaces. It can take place in isothermal conditions, but it is often most severe in the presence of a temperature gradient (Epstein, 1983). Fouling of heat transfer surfaces arises because heating or cooling of the processed stream promotes a complex and often not fully understood set of effects, namely crystallisation, particulate, chemical reaction, corrosion and biological fouling (Bohnet, 1985; Epstein, 1983). Within this classical framework milk fouling is characterised by a combination of chemical reactions of polymerising protein and crystallising milk salts (Bansal & Chen, 2006).

Epstein breaks the possible events of fouling down to:

- ① Initiation, ② Transport, ③ Attachment, ④ Removal and ⑤ Ageing.

After starting HEX operation, early ① initiation steps occur on the heat transfer surface which are specific for the type of fouling: *e.g.* nucleation of crystals or the adsorption of conditioning films. During this time, often referred to as the ‘induction period’, the consequences of fouling are small on a macro-scale level, *e.g.* determined by the overall heat transfer performance (Albert *et al.*, 2011; Bott, 1997; Geddert *et al.*, 2009). Further fouling species are brought to the surface by relatively well understood mechanisms of ② mass transport and ③ adsorb to the wall or already deposited material with a certain probability (Belmar-Beiny *et al.*, 1993; Bott, 1997). This probability is a function of the attachment mechanisms and the operating conditions (Bott, 1997). Subsequently, chemical bonds may be formed which increase the adhesion strength of the particle, molecule or ion. Depending on the fluid shear exerted and the cohesive and adhesive strength of the deposit, small parts or entire layers may be ④ released at any of the preceding steps. After extended periods of operation the remaining deposit may undergo ⑤ ageing, *i.e.* reactions or consolidation effects which almost always yield a stronger, more cohesive deposit which is harder to clean (Wilson, 2005).

Unsolved problems with heat transfer equipment have led to fouling being treated as a ‘chronic disease’ in the processing sector. Several researchers have estimated the total

cost of HEX fouling in different countries, reporting values in the range of 0.1 to 0.35 % of the gross domestic product (Garrett-Price, 1985; Pritchard, 1988; Steinhagen *et al.*, 1993; Xu *et al.*, 2005).

2.2 Milk fouling

2.2.1 Fouling in milk heat treatment

All dairy products are heated prior to consumption to reduce the amount of viable pathogens to a level where they do not constitute a significant health hazard (Holsinger, Rajkowski, & Stabel, 1997). In high temperature short time (HTST) pasteurisation milk is heated to 72–75 °C and held there for 15–25 s, depending on particle content (Bylund, 2015; Holsinger *et al.*, 1997). Another common method is UHT treatment where milk is heated to 135–150 °C for a few seconds (Bylund, 2015). The UHT method sterilises the product and gives it a longer shelf-life. Typically, plate HEXs, using stacked metal plates as heat transfer surfaces, are used in these applications. A schematic of a milk heating process employing a plate HEX is depicted in Figure 2.1.

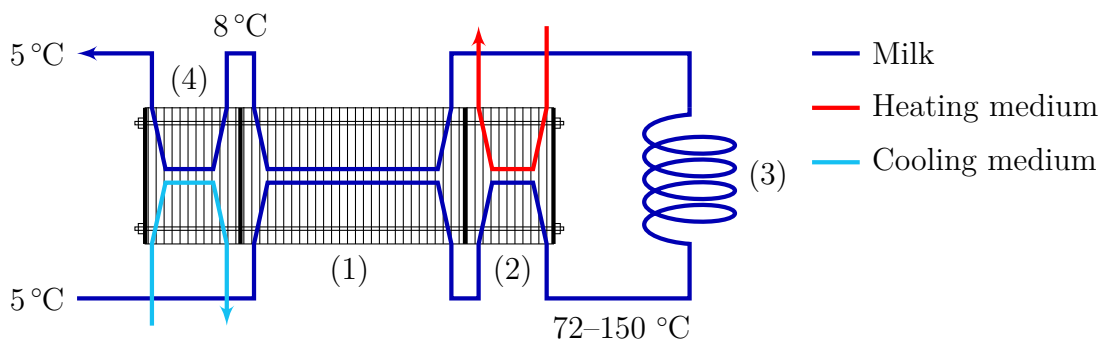


Figure 2.1: Simplified schematic of a plate HEX used for milk heat treatment based on Bylund (2015). The (1) regenerative, (2) heating, (3) holding and (4) cooling sections are indicated.

In a dairy, cold milk is pumped from receiving tanks to the regenerative heating section (labelled 1 on the Figure) of a HEX where it is heated to 68–120 °C. Often there is a homogeniser placed after the regenerative heating section which reduces the size of milk fat globules by mechanical shear forces to increase colloidal stability (not shown). Subsequently, additional heat is transferred from a heating medium (typically water or steam) to increase temperature to 72–75 °C for HTST or 135–150 °C for UHT treatment

(2). The milk passes an insulated holding tube (3) which ensures sufficient residence time for pathogen inactivation and enters the regenerative section a second time, on the hot side. A large amount of heat is transferred back to the incoming stream, lowering the temperature of the milk to 8 °C and substantially reducing the heat load in the cooling section (4). Up to 95 % of the overall heating and cooling duty can be achieved in the regenerative section (Bylund, 2015).

Unfortunately, milk fouling is a common phenomenon in the regenerative and heating sections and reduces their efficiency (Bansal & Chen, 2006; Sadeghinezhad *et al.*, 2013). Fouling accounts for a major fraction of operating costs in dairy processing (Steinhagen *et al.*, 1993). It increases resistance to heat transfer, pressure loss, cleaning costs and compromises product quality and safety (Sadeghinezhad *et al.*, 2013). Direct costs for cleaning and indirect costs in terms of lost production can be much greater than energy losses.

The two main constituents of fouling deposits – and key species involved in deposition – are calcium phosphate and whey proteins (Bansal & Chen, 2006; Sadeghinezhad *et al.*, 2013). Tolkach and Kulozik (2007) described the aggregation and polymerisation pathway of β -lactoglobulin (β -LG), a heat sensitive globular whey protein, as involving the steps shown in Figure 2.2: at bovine physiological conditions β -LG is present as a dimer (labelled N_2), dissociating reversibly at temperatures above around 40 °C into two native monomers ($2N$). At temperatures from 40 to 55 °C some side chains undergo minor reversible conformational changes, improving accessibility of its free thiol group. In this, so-called R-state (N_R), β -LG can polymerise, albeit at very low rates. Above 60 °C β -LG partially unfolds and exposes the free thiol group. This stage is called the molten globule state (U_{MG}) in which intramolecular disulphide exchanges become possible, rendering this transition irreversible. Exposed apolar patches facilitate the association of β -LG to and from aggregates (U_n), simultaneously taking part in thiol exchange reactions to form a polymer (U_m). Above 130 °C native β -LG unfolds completely and loses its secondary structure. Calcium ions mediate the aggregation by screening electrostatic repulsion (Simons *et al.*, 2002). The presence of a solid surface may lead to adsorption and deposition at all of these stages, most notably via hydrophobic attraction and covalent bonds. The ability of surfaces to participate in hydrophobic attraction is determined by their surface energy (van Oss, 2003).

Concomitantly, the solubility of calcium phosphate decreases with temperature (Bansal & Chen, 2006). This leads to nucleation and crystal growth of calcium phosphate on the heat transfer surface and in the bulk liquid. Nucleation is favoured on existing particles (Mullin, 2001). Hagsten *et al.* (2016) showed that particles formed in the bulk can also

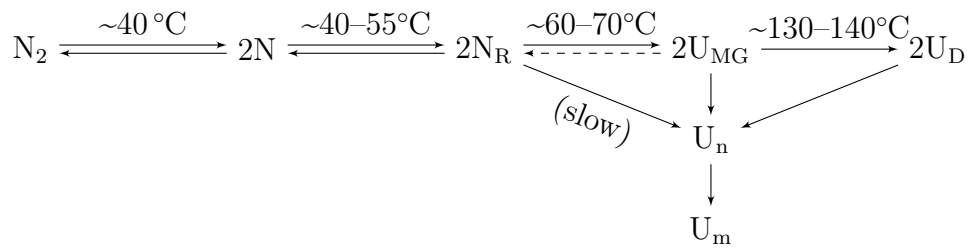


Figure 2.2: Schematic denaturation mechanism of β -LG, adopted from Tolkach and Kulozik (2007).

adhere to the surface, which creates a complex composite matrix on many length-scales. They used confocal laser scanning microscopy and fluorescent dyes exhibiting an increase in fluorescence upon binding to investigate the structure and composition of deposits formed in high temperature (milk stone) fouling.

Milk fouling deposits can be roughly categorised into type A and type B, grouped by material composition and rheological properties (Foster, Britten, & Green, 1989; Lalande *et al.*, 1984). Burton (1968) described type A deposit as a soft, voluminous, curd-like proteinaceous material, white or cream in colour, which may overlay a harder base layer. It is formed at temperatures up to 100 °C. Type B fouling is found at higher temperatures; Burton described it as brittle, gritty, and grey in colour. This deposit has higher mineral and lower protein contents than type A.

Although the mechanisms in dairy fouling are qualitatively understood (Sadeghinezhad *et al.*, 2013), few effective strategies have been identified to reduce deposit formation or its consequences in practice. One approach is the use of antifouling coatings, minimising the adhesion or mediating the build-up of deposit which is subsequently easier to clean. Some studies have demonstrated the effect of the surface on deposit composition (Boxler *et al.*, 2013c) but to the authors' knowledge few studies have considered the spatial distribution of the species on non-metallic surfaces. The sequence of events involved in milk fouling has been debated at length. With stainless steel, some studies have reported a high concentration of minerals close to the heat transfer surface at 100 and 140 °C (Foster *et al.*, 1989; Foster & Green, 1990) whereas others, using calcium phosphate-rich WP solution as a model material, stated that they found a dense sub-layer but could not measure a difference in composition (Boxler *et al.*, 2013c). The experimental time-scales in these studies differed from 15 min to 2 h and may have had an influence on the micro-structures observed. In particular, mineral and ion diffusion through the deposit, dissolution, and recrystallisation events at later stages of the fouling process cannot be excluded (Belmar-Beiny *et al.*, 1993). In general, deposit with a high mineral mass fraction is found to adhere more strongly (Foster *et al.*, 1989; Foster & Green, 1990; Lalande *et al.*, 1984).

Extended periods of high temperature exposure lead to the above mentioned recrystallisation processes and to further cross-linking of proteins, yielding a material which is harder and more difficult to clean (Fickak *et al.*, 2012). Because the operating periods in the food industry are bound by hygienic considerations, ageing to the extent seen in other industrial sectors, *e.g.* oil refineries (Ishiyama *et al.*, 2014), is generally not observed.

2.2.2 Surface–foulant interactions

The interactions between the heat transfer surface and the fouling species can have an effect on four out of the five basic events of fouling.

Initially, when milk comes into contact with the heated surface, proteins adsorb to the interface to form a thin layer (Visser & Jeurnink, 1997). The composition of this layer is not necessarily constant over extended periods of operation (Foster *et al.*, 1989; Foster & Green, 1990). Hydrophobic materials have been reported to induce extensive conformational changes of β -LG on adsorption, which has been shown experimentally (Karlsson *et al.*, 1996; Kim *et al.*, 2002) and computationally with molecular dynamics simulations (Zare *et al.*, 2015). Zare *et al.*, who studied β -LG at the decane–water interface, showed that hydrophobic amino acid residues, some of which are normally buried within the protein at physiological conditions, are exposed to the hydrocarbons on adsorption. β -LG is able to bind small hydrophobic molecules, such as fatty acids, in a central hydrophobic cavity. Bound conjugated linoleic acid stabilises the protein against heat and pressure induced unfolding and aggregation (Considine *et al.*, 2007).

The nucleation of calcium phosphates is affected by surface roughness and surface energy. Rough surfaces provide energetically favourable sites for crystal nucleation (Mullin, 2001). Rosmaninho and Melo (2006) investigated nucleation of calcium phosphate on surfaces which varied in surface energy but were similar in roughness. They found that surfaces with many Lewis base (electron donor) sites generated more numerous crystal nuclei with a higher total mass, albeit with a smaller individual size. The mineral deposit on surfaces rich in electron donor sites was also more compact and harder to clean. The medical sciences are interested in calcium phosphate nucleation and growth because it is the major constituent of bones. SS 316 is used for medical implants and binds successfully with calcium phosphate bone material (Javidi *et al.*, 2008).

Intermolecular forces and chemical reactions between the foulant particles, the solution and the HEX surface ultimately determine attachment and removal of fouling deposit. Since many soiling layers are many microns thick (they are visible to the naked eye) cohesive interactions also determine how the layer responds to an imposed force.

Mass transport of small particles, molecules and ions is classically treated as a diffusion process taking place from the fluid core through the mass transfer boundary layer to the heat transfer surface (Epstein, 1983). Although mass transfer (and heat transfer, as they are linked) can be affected by the roughness of the heat transfer surface by means of a higher friction factor (Pääkkönen *et al.*, 2015), the local interactions at the solid–liquid interface are generally not considered in classical transport models.

In some cases, the surface can act as a catalyst in ageing reactions, *e.g.* different metals are reported to affect oxidation rates of fats and oils (Ziels & Schmidt, 1945).

2.3 Antifouling coatings in heat exchangers

2.3.1 Fluoropolymer coatings

Antifouling materials and coatings are typically employed in HEXs to stop or slow down the accumulation of unwanted deposits and to promote cleaning. A distinction can be drawn between coating a heat transfer surface made from conventional materials (*e.g.* stainless steel (SS)) and exchanging the conventional base material for an antifouling one. While the focus of this work is on coatings, it is acknowledged that mono-material FP solutions can be more suitable in highly corrosive environments (Cevallos *et al.*, 2012). Coatings may be permanent or sacrificial (see Yang *et al.*, 2015) and can be applied by a number of techniques.

There are several requirements for a permanent antifouling material in a HEX application. It should, *e.g.*

- extend the operating period before cleaning is required, and/or improve cleaning rates or effectiveness.
- retain its effectiveness and be mechanically and chemically stable over many fouling and cleaning cycles. The alternative, of disposable units, is not usually practicable in industrial processes.
- not impair heat transfer to a large extent, since this will require a larger heat transfer area to achieve the same heat duty.
- satisfy application specific criteria, *e.g.* high temperature resistance, compliance with food-grade standards, or corrosion performance.

In this work, the focus lies on FP based coating systems, which possess potentially desirable attributes for fouling mitigation. These coating systems may consist of different layers, matrices and particles and can be best understood as composite materials designed to meet the above mentioned requirements. McKeen (2007) outlines the main constituents of FP coating systems as:

- *Primer*: This first coating layer acts as a bonding agent between the substrate and the rest of the coating system.
- *Binder*: Includes all polymers in the coating and acts as an adhesive to join elements of the coating system.
- *Pigment, Filler, Extender*: Insoluble fine particles added to the coating to
 - alter the appearance of the coating or hide the substrate;
 - increase the roughness of the coating;
 - alter rheological properties in the production process;
 - reduce the cost by adding inexpensive ingredients;
 - reduce permeability;
 - improve physical properties such as strength and abrasion resistance;
 - act as a carrier for active materials, which may (i) protect the substrate from corrosion, (ii) prevent bacterial growth on the surface, (iii) provide fire resistance, (iv) be electrically conducting and (v) protect against ultraviolet light.

The layer primarily responsible for the antifouling performance of the coating system is the ‘topcoat’, which is in direct contact with the process stream. A distinction exists between per-fluoropolymers and partially fluorinated polymers. In the latter, other atoms, such as hydrogen or chlorine, replace the fluorine. The polymers are further classified as homopolymers, copolymers or terpolymers *etc.* (see Figure 2.3), being polymerised from a single, two or three *etc.* monomer(s), respectively.

The most prominent and simplest example of a FP is polytetrafluoroethylene (PTFE), discovered by Roy Plunkett in 1938 (McKeen, 2007). Fig. 2.3a shows the linear structure of PTFE, which is in fact twisted along its longitudinal axis (not shown). The fundamental properties of FPs arise from the molecular structure and high bond enthalpies between fluorine and carbon (single bonds: C—C, 348 kJ mol⁻¹, C—F, 484 kJ mol⁻¹, Atkins

(1986)). The fluorine atoms provide a uniform sheath around the carbon-carbon bonds and protect them from attack. PTFE is rated for use up to 260 °C, does not dissolve in any common solvent, has a very low surface energy, is apolar and hard to polarise. There are many related polymers, such as fluorinated ethylene propylene (FEP) and perfluoroalkoxy (PFA). They can differ in molecular weights, grades of crystallinity and endgroups but share, however, the common attributes of FPs to a large extent.

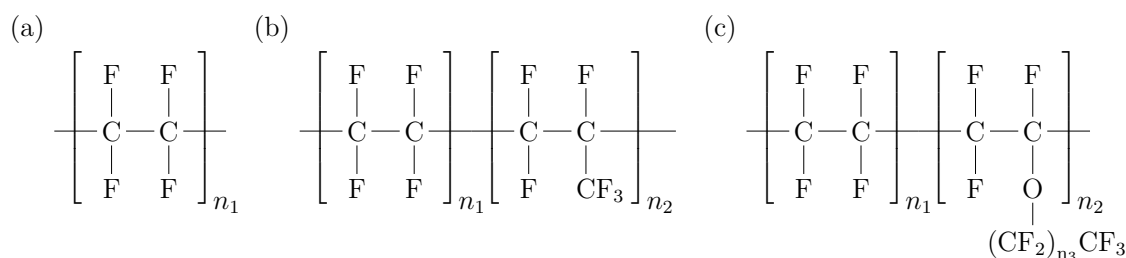


Figure 2.3: Chemical structures of (a) PTFE (a homopolymer), (b) FEP, and (c) PFA (both copolymers) (McKeen, 2007).

Although FPs have mostly been employed to date in the processing industry for their good corrosion resistance, they have been recognised by some researchers for their antifouling properties. Zhao *et al.* (2002) conducted a fouling experiment with a 2 g l⁻¹ CaSO₄ solution in water flowing with a mean velocity of 0.8 m s⁻¹ and did not observe any noticeable deposition on a heated rod coated with nickel-phosphorus-polytetrafluoroethylene (Ni-P-PTFE). According to Rosmaninho and Melo (2006), modified PTFE coatings like Ni-P-PTFE show better antifouling behaviour, especially when a certain shear stress (explicit values of shear stress were not reported) is exerted on the fouling layer during operation. Interestingly, they also reported that lower surface energies lead to less dense and presumably weaker fouling layers. Barish and Goddard (2013) demonstrated a 97% reduction in fouling mass coverage from raw milk at 85 °C on electroless nickel plated SS with co-deposited PTFE particles. Kananeh *et al.* (2010) reported a 90% reduction in cleaning in place (CIP) time to remove deposits generated from a whey protein solution on a PTFE coated SS (type not specified) laboratory HEX. Therefore, it might be expected that the lower adhesive strength of fouling layers on PTFE-based coatings would give better cleanability.

Low total surface energies do not necessarily result in less fouling. According to Förster and Bohnet (2000), PTFE has negligible influence on aqueous crystallisation fouling and several workers, as summarised by Gomes da Cruz *et al.* (2015), have reported a negative impact of FPs on milk fouling in HEXs. The ‘Baier-curve’ demystifies these contrary findings somewhat as it gives a relation between the surface energy and relative bacterial adhesion (Baier, 2006). The curve shows a minimum in bacterial adhesion at a surface

energy of around 25 mN m^{-1} , which was reported by Zhao *et al.* (2005) to apply to the adhesion of calcium sulphate deposit as well. This minimum is considered to coincide with the dispersive force contribution to the surface free energy of water (Baier, 2006). While it may be possible to tailor the surface energy (and its components) to reach a desired value, Förster and Bohnet (2000) noted that relatively rough polymer surfaces may provide favourable heterogeneous nucleation sites for crystallisation fouling.

Due to mechanical, chemical and thermal stress, a FP coating may experience ageing and change in performance, composition, coherence and appearance. This can occur because of chemical and thermal attack of polymer endgroups, delamination of coating layers, process material sticking in pores, or mechanically induced failure. The ‘history’ of the coating has a strong impact on its durability. Several defects can originate from production: air entrapment, bubbles, blisters, pinholing, popping, mud cracking, stress cracking, cratering, fisheyes and structuring due to Bernard cells (McKeen, 2007).

From the heat transfer perspective, coatings can be classified as those which impose significant extra thermal resistance and those with negligible impact on heat transfer. To ensure an even distribution and durability, FP coatings are often a few to a hundred micrometres thick and thus add an additional heat transfer resistance.

At this level of knowledge it is not straightforward to select a coating for a specific application. Initial screening tests have to be undertaken to identify which coating or coating properties are suitable for a given foulant. In the long term this might yield a matrix to select coating properties as a function of operating conditions and foulant.

Considerable effort has been spent on improving the abrasion resistance and adhesion of FPs to the substrate (*e.g.* Siperko & Thomas, 1989; Thomas *et al.*, 2001). Their non-stick properties have set the benchmark in household applications and are effective even after years of harsh thermal conditions and cleaning procedures. Ultimately however, only a significant improvement in fouling and cleaning performance, and therefore lower operating costs, will justify the application of a low surface energy coating on a HEX.

2.3.2 Other types of coatings

Gomes da Cruz *et al.* (2015) presented an overview of experimental studies on the effect of surface coatings on fouling and cleaning of milk related deposits. Table 2.1 gives an overview based on the table by Gomes da Cruz *et al.* (2015) extended with more recent studies marked with asterisks. Researchers used a variety of coating types, including FP coatings as discussed earlier and other polymers, such as polyethylene (PE), poly-

methyl methacrylate (PMMA), polystyrene (PS), cellulose acetate (CA) and polyether-ether-ketone (PEEK), applied as a resin or solution. Other popular groups of techniques are chemical vapour deposition (CVD), physical vapour deposition (PVD) and plasma enhanced chemical vapour deposition (PECVD) which generate thin coatings with negligible thermal resistance. Deposited materials include diamond like carbon (DLC), SiO_x and TiN.

Less than half of the studies employed unprocessed raw milk or ‘near-natural’ products such as pasteurised milk or whey. A majority of tests were conducted with WP solutions, simulated milk ultrafiltrate (SMUF) and combinations thereof. SMUF is a salt solution which resembles the composition of milk serum (Morison & Tie, 2002).

Only a fraction of the coatings would be practical for industrial use: some coatings could release potentially harmful materials like carbon nanotubes (CNTs) (Rungraeng *et al.*, 2012). Others are not resistant against chemical attack from cleaning solutions (Barish & Goddard, 2014). Polyethylene glycol grafted polymer brushes repel protein by hydrophilic repulsion and could be effective candidates against WP fouling (Mérian & Goddard, 2012; van Oss, 2003). Unfortunately, the material degrades by oxidation in water and air at a moderate temperature of 70 °C (Glastrup, 1996).

Table 2.1: Summary of studies on antifouling coatings for milk-related products based on a table by Gomes da Cruz *et al.* (2015).

	Material	Foulant	Fouling	Cleaning	Sources
PTFE-based	PTFE	Raw milk	+	-	Gordon <i>et al.</i> (1968)
		Whey	+		Dupeyrat <i>et al.</i> (1987)
		Milk	+		McGuire and Swartzel (1989)
		Raw whole milk	+	0	Yoon and Lund (1994)
		WP concentrate	+	-	Kananeh <i>et al.</i> (2010)
	Ni-P-PTFE	Pasteurised milk	+		Rungraeng <i>et al.</i> (2012)
		Dairy model fluid	-	-	Beuf <i>et al.</i> (2004)
		Skim milk	-		Balasubramanian and Puri (2008, 2009)
		WP isolate in SMUF	-		Rosmaninho and Melo (2008)
		Raw milk	-		Barish and Goddard (2013)
CNT-PTFE Excalibur [®] , Xylan [®]	Raw milk, chocolate milk	-	-	Huang and Goddard (2015)*	
	Pasteurised milk	-		Rungraeng <i>et al.</i> (2012)	
	Dairy model fluid	- Xylan [®]	-	Beuf <i>et al.</i> (2004)	
Other polymers	PE; silicone and fluorine resins	Whey	0		Dupeyrat <i>et al.</i> (1987)
	Nylon, PMMA, PS, CA, agarose	Raw whole milk	- PMMA, CA	- PMMA	Britten <i>et al.</i> (1988)
	Silicone	Raw whole milk	+		Yoon and Lund (1994)
	Silica sol-gel	WP isolate	+		Santos <i>et al.</i> (2006)
	Lectroflour [™] , AMC148-18	Skim milk	+		Balasubramanian and Puri (2008, 2009)
	FEP, PEEK+FP, nanocomposites	WP isolate	-, + PEEK+FP	-	Mauermann <i>et al.</i> (2009)
	Epoxy & polyurethane coatings FEP, PFA, epoxy-PTFE	WP concentrate Raw milk	- - FEP	- - FEP, PFA	Kananeh <i>et al.</i> (2010) Magens <i>et al.</i> (2015)*
CVD	DLC (prepared by PECVD)	Dairy model fluid	+		Beuf <i>et al.</i> (2004)
	DLC and Si-O-DLC	WP isolate	- at pH 6.7, + at pH 7.8	0	Santos <i>et al.</i> (2006)
	DLC	WP isolate	-	-	Premathilaka <i>et al.</i> (2007)
	Si-O-DLC (prepared by PECVD)	WP isolate in SMUF	- 85 °C	-	Rosmaninho and Melo (2008)
	Si-O-DLC (prepared by PECVD)	WP isolate	+	-	Mauermann <i>et al.</i> (2009)
	Doped DLC (prepared by PECVD)	Milk, whey	0	0	Patel <i>et al.</i> (2013)
	DLC, Si-DLC, Si-O-DLC (prepared by PECVD)	WP isolate, SMUF, WP isolate in SMUF	-, 0 for batchwise deposition at 120 °C	-	Boxler <i>et al.</i> (2013a, 2013b, 2013c)
	SiO _x	Dairy model fluid WP isolate in SMUF	- -	+	Beuf <i>et al.</i> (2004) Rosmaninho and Melo (2008)
	PVD	DLC	WP isolate	- at pH 6.7, + at pH 7.8	0
TiN		WP isolate	+	-	Premathilaka <i>et al.</i> (2007)
Ti-DLC		WP isolate in SMUF	+		Rosmaninho and Melo (2007)
		WP isolate	-	-	Mauermann <i>et al.</i> (2009)
Other	Ion impl.: silica, SiF ⁺ , MoS ₂	Dairy model fluid	-	+	Beuf <i>et al.</i> (2004)
	Ion impl.: silica, SiF ₃ , MoS ₂ , TiC	WP isolate	- at pH 6.7, + MoS ₂	0, - SiF ₃	Santos <i>et al.</i> (2006)
	Ion impl.: Silica, MoS ₂	WP isolate in SMUF	+ at 85 °C		Rosmaninho and Melo (2008)
	Ceramic alumio-silicate	Whole milk	-		McGuire and Swartzel (1989)
	Chromium oxide, methylated silica Perfluorodecyltriethoxysilane	β -LG WP concentrate and CaCl ₂	+	0 or + -	Karlsson <i>et al.</i> (1996) Zouaghi <i>et al.</i> (2018)*

Symbols: + more fouling or more cleaning effort; 0 no change in fouling or cleaning behaviour; - less fouling or less cleaning effort

2.3.3 Economics of antifouling coatings in heat exchangers

A key question to be answered when considering antifouling coatings in HEX applications is how well a coating must perform to be financially attractive. This question is likely to be asked during the development of a coating business plan. A coating is attractive in a specific application when this barrier to implementation is bridged. The inverse problem is to quantify the financial attractiveness of a coating with a given performance. The answer to this problem is sought when assessing the antifouling performance of existing coatings. Likewise, a business considering investment in a coated HEX is interested in the long term benefits compared to a reference case, such as an existing unit.

Antifouling coatings should extend the operating period before cleaning is required, and/or improve cleaning rates or effectiveness: the financial benefit of this needs to be balanced against the cost of installing a new or revamped unit. This is the core of the ‘value pricing’ concept introduced by Gomes da Cruz *et al.* (2015) and involves a series of modelling and optimisation calculations.

The decision when and how to clean a fouling HEX is an optimisation problem, first considered by Ma and Epstein (1981). Fig. 2.4a illustrates the underlying problem for a single uncoated HEX. Operation for a period of length t incurs an amount of energy loss. Cleaning restores the heat duty, q , to the clean state, q_{cl} . However, cleaning requires the unit to be taken offline for time τ , and induces further costs for the cleaning operation, C_{cl} . A practical example of this problem was presented by Casado (1990) and a dimensional analysis, including the effects of deposit ageing, was given by Ishiyama *et al.* (2014). Pogiatzis *et al.* (2015) developed methods for identifying the optimal fouling-cleaning cycle period, *i.e.*, $t + \tau$, for cases where there is a choice of cleaning methods.

Possible effects of antifouling coatings, namely delaying the onset of fouling (larger t_{ind}), hindering fouling (maintain q near q_{cl}), as well as enhancing cleaning (reduce τ and/or C_{cl}), are illustrated in Fig. 2.4b. ‘Non-stick’ coatings often incur additional capital spending related to the cost and manufacturing of coated surfaces. There can also be a reduction in the overall heat transfer coefficient when the layer has a relatively low thermal conductivity. This reduction has to be offset by increasing the heat transfer area of the coated HEX. The financial attractiveness (*i.e.* the economic sustainability) of installing a coated HEX then depends on the trade-off between capital and operating costs over the lifetime of the unit. In practice the lifetime of the unit is likely to be determined by the effectiveness of the layer, as the layer is likely to degrade or otherwise suffer reduced performance over time. The balance between these costs will differ between a new system and a revamped or retrofitted one. In the latter case, an existing exchanger is replaced

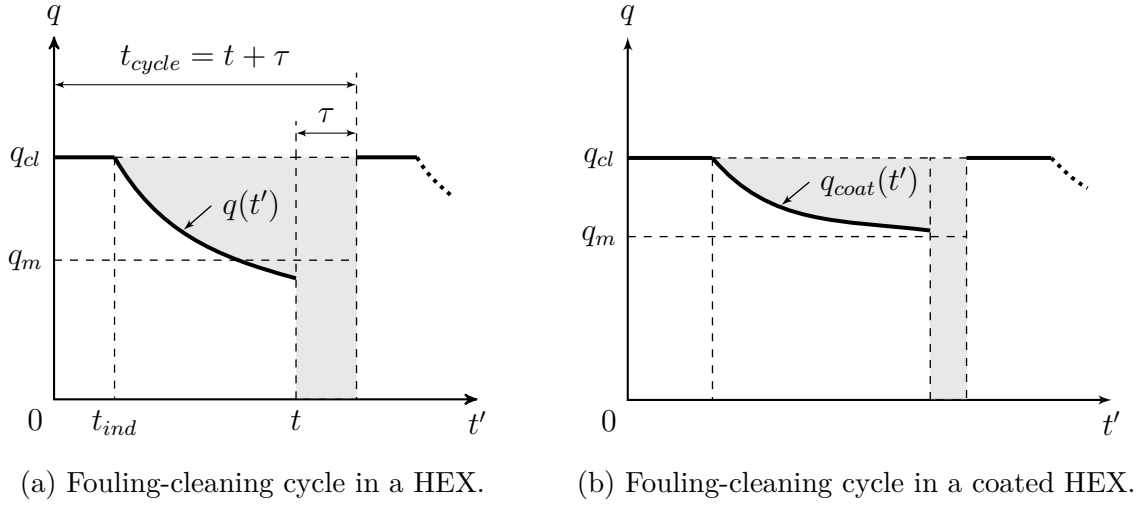


Figure 2.4: Schematic of a fouling-cleaning cycle in an uncoated (a) and coated (b) single HEX over time, t' . Following an induction period with negligible deposition of length t_{ind} , the heat duty, q , falls from the clean value, q_{cl} . After operating for time t the unit is cleaned, taking time τ , and performance is restored to q_{cl} . q_m represents the time-averaged heat duty and the grey shaded area represents energy lost.

and the extra capital outlay needs to be recovered from improved operation.

These financial considerations – which can include CO₂ taxes associated with extra energy consumption – effectively set bounds on the price of antifouling coatings, determined by comparing manufacturing costs and the maximum saving that can be achieved from fouling mitigation, in a ‘value pricing’ calculation. Order of magnitude estimates for different applications can establish the potential attractiveness of antifouling coatings for a given scenario.

Computation of the operating cost requires knowledge of the fouling behaviour over time, $q(t')$. If this is available, it allows the operator or designer to determine the optimal operating strategy and configuration of a HEX. Gomes da Cruz *et al.* (2015) considered the linear fouling case, where the overall fouling resistance, R_f , increases at a constant rate. They used the lumped *NTU*-effectiveness method (see Bergman & Incropera, 2011) to predict the HEX performance over time. They quantified the attractiveness of antifouling coatings to mitigate fouling using a techno-economic analysis of the optimal operating performance of an individual HEX and compared this with the cost of installation of a coated unit. The upper price that can be charged for a coating is set by its ability to reduce deposition and enhance cleaning, while the lower limit is set by manufacturing costs. Identifying this price range, wherein value is created for the vendor and purchaser, should ideally be performed early in the decision process as it helps to set targets for the

coating performance as well as manufacturing cost.

Changes in processing conditions and the conditions at the heat transfer interface influence the local fouling rate and cause predictions from lumped models to be inaccurate. These deviations occur due to the nature of ‘phenomenological fouling models’ which resemble fouling kinetics for specific conditions. While Gomes da Cruz *et al.* (2015) used a lumped model to calculate the heat duty over time, others like Fryer and Slater (1985) modelled HEXs subject to fouling with distributed models. This has practical implications since the local fouling rates may then be predicted by a ‘mechanistic or pseudo-mechanistic fouling model’, sensitive to processing and interface conditions. Parameters of models describing the fouling kinetics have to be set. This requires fouling experiments employing operating conditions likely to be expected in industrial HEXs.

2.4 Research techniques

2.4.1 Surface characterisation

Surface topography and roughness

It is well-known that surface roughness increases heat transfer by (i) enlarging the surface area relative to the smooth wall and by (ii) increasing turbulence in the thermal boundary layer (Albert *et al.*, 2011). In fouling, the surface topography and roughness play a role, by (i) determining the area available for interaction; (ii) controlling the interaction such as by the lotus leaf effect, where small, regular features modify the effective contact angle (Barthlott & Ehler, 1977); and (iii) affecting the nature of the soiling layer, *via* the potential to promote nucleation (*e.g.* for crystallisation, see Junghahn (1964); or condensation, see Zamuruyev *et al.* (2014)), and mechanical interlocking.

In the initial stages of fouling, the length-scales of depositing particles (*e.g.* proteins, calcium phosphate crystals) determine the relevant length-scales of surface features. Particles can be trapped in crevices and cracks or move to matching surface features which provide larger intimate contact area than the equivalent flat surface (Oliveira, 1997; Zouaghi *et al.*, 2018). Conversely, when the length-scale of roughness features becomes smaller than the particle diameter, a smaller number of contact points can potentially reduce the strength of adhesion (Visser, 1988). At later stages of fouling, when individual particles developed a network by physical and chemical interactions, it may be expected that roughness

length-scales comparable to the overall fouling layer thickness also become important for adhesion.

Methods of measuring surface topography are summarised in the ISO 25178 (2016) standard. Generally it is distinguished between tactile measurements (*e.g.* profilometer, atomic force microscopy) and optical measurements (*e.g.* coherence scanning interferometry, confocal microscopy).

Industrial norms, such as the ISO 25178, define equations which convert two- or three-dimensional topography data into single valued roughness parameters. Most notably the arithmetic mean roughness, S_a , is defined as the arithmetic mean of the absolute surface height deviations from the mean plane. Similarly, the root mean square roughness, S_q , is defined as the quadratic mean of the absolute surface height deviations from the mean plane. The length or area over which this parameter is calculated acts as a short-pass filter (Howell & Behrends, 2006).

Surface free energy and its significance

The scientific principles underpinning adhesion and cohesive interactions are well established. In an aqueous environment the forces between a substrate and an adhering species are determined by contributions from electrostatic, Van der Waals, and solvation forces (Israelachvili, 2011). One approach which has been applied successfully in many situations is the extended Derjaguin, Landau, Verwey and Overbeek (XDLVO) theory (van Oss, 2003). This theory superimposes energies of interaction from Van der Waals, Lewis acid-base, and electric double layer forces.

The electric double layer repulsion of particles arises from the osmotic pressure of counterions attracted by surface charges (Israelachvili, 2011). It decays spatially with the characteristic Debye length, which is solely a property of the solution and decreases with increasing ionic strength. The ionic strength of milk is 80 mM (Walstra, Wouters, & Geurts, 2005), which gives a Debye length of 1 nm, *i.e.* the electric potential reduces to $1/e \approx 37\%$ within the first nanometre (van Oss, 2003). This renders effects from osmotic pressure negligible compared to the other two forces within the XDLVO framework. Auspiciously, Van der Waals and Lewis acid-base interactions can be considered collectively in some theories describing surface energy.

The surface tension of a liquid or the surface free energy of a solid (termed surface energy, γ , hereafter) is classically treated as the sum of apolar and polar forces, *i.e.* $\gamma = \gamma^{LW} + \gamma^{AB}$ (van Oss, Chaudhury, & Good, 1987). Here, γ^{LW} is the Lifshitz-van der Waals forces,

i.e. the sum of the electrodynamic London, Keesom, and Debye forces which decay with distance at the same rate and generally obey the same combining rules. The polar hydrogen bonding forces are either lumped in a single parameter as in the pioneering work of Fowkes (1962) and Owens and Wendt (1969), or are split into acidic, γ^+ (electron acceptor), and basic, γ^- (electron donor), contributions according to van Oss *et al.* (1987) to yield

$$\gamma = \gamma^{\text{LW}} + 2\sqrt{\gamma^+\gamma^-} . \quad (2.1)$$

Interfacial energies obey the geometric mean ‘combination rules’ described by Fowkes (1963). For cases where both apolar and polar interactions operate across an interface between material 1 and 2 van Oss *et al.* (1987) showed that the interfacial energy at molecular contact is given by

$$\gamma_{12} = \underbrace{\left(\sqrt{\gamma_1^{\text{LW}}} - \sqrt{\gamma_2^{\text{LW}}}\right)^2}_{\gamma_{12}^{\text{LW}}} + 2 \underbrace{\left(\sqrt{\gamma_1^+\gamma_1^-} + \sqrt{\gamma_2^+\gamma_2^-} - \sqrt{\gamma_1^+\gamma_2^-} - \sqrt{\gamma_2^+\gamma_1^-}\right)}_{\gamma_{12}^{\text{AB}}} . \quad (2.2)$$

Here, γ_i is the surface energy between substance *i* and vacuum: the subscript for vacuum is omitted here for convenience, as in many texts. Moreover, $\gamma_{i,\text{air}} \approx \gamma_i$. The interfacial free energy of interaction in an immersed system is estimated from the difference in total interfacial energy when adsorbing species 1 contacts a substrate 2 in medium 3. Note that in the literature, subscript 2 sometimes refers to the surrounding medium. As outlined by van Oss *et al.* (1987), following arguments of Dupré (1869), the interfacial free energy of interaction is given by

$$\Delta G_{123}^{\text{IF}} = \gamma_{12} - \gamma_{13} - \gamma_{23} , \quad (2.3)$$

where γ_{12} , γ_{13} and γ_{23} are the interfacial energies between respective materials at contact, *i.e.* minimum equilibrium distance. Figure 2.5a illustrates the process for a polymer strand adsorbing to a surface in water. The adsorbing strand displaces the interstitial medium, *i.e.* it replaces the particle-water and surface-water interfaces with a particle-surface interface. Aggregation and dissolution of like particles, as shown in Figure 2.5b, can be understood as a similar process (van Oss & Good, 1992). Type A milk fouling deposit generated below 100 °C is mainly a product of aggregated protein which forms a porous matrix with a large water content (Bansal & Chen, 2006; Hagsten *et al.*, 2016). Besides chemical bonds, the physical interactions within the wet protein matrix contribute to the cohesion of the material. Therefore, the interfacial free energy of interaction of protein chains within this matrix provides an important contribution to cohesion.

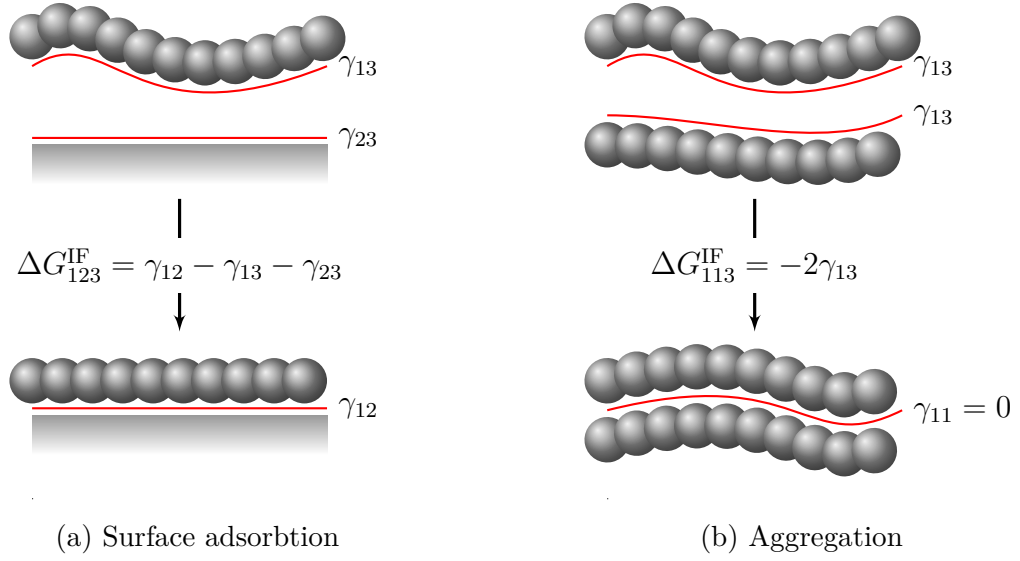


Figure 2.5: Schematic of a particle (here, a polymer strand) (a) adsorbing to a surface and (b) aggregating with a second particle of identical nature. The interfacial free energies of interaction associated with these processes are presented in the centres of the schematics. The relevant interfaces are highlighted with red lines. The subscripts denote: 1 – particle; 2 – surface; 3 – water.

By combining Equations 2.2 and 2.3 it can be shown that

$$\Delta G_{123} = \Delta G_{123}^{LW} + \Delta G_{123}^{AB} \quad (2.4)$$

$$= \left(\sqrt{\gamma_1^{LW}} - \sqrt{\gamma_3^{LW}} \right) \left(\sqrt{\gamma_3^{LW}} - \sqrt{\gamma_2^{LW}} \right) + 2 \left[\sqrt{\gamma_3^+} \left(\sqrt{\gamma_1^-} + \sqrt{\gamma_2^-} - \sqrt{\gamma_3^-} \right) \right. \\ \left. + \sqrt{\gamma_3^-} \left(\sqrt{\gamma_1^+} + \sqrt{\gamma_2^+} - \sqrt{\gamma_3^+} \right) - \sqrt{\gamma_1^+ \gamma_2^-} - \sqrt{\gamma_1^- \gamma_2^+} \right]. \quad (2.5)$$

ΔG_{123}^{IF} can be positive or negative depending on the materials involved. If medium 3 is aqueous and $\Delta G_{123}^{IF} < 0$, species 1 and substrate 2 exhibit a hydrophobic attraction and, conversely, hydrophilic repulsion if $\Delta G_{123}^{IF} > 0$. $\Delta G_{123}^{IF} = 0$ represents the special case of no net interaction. Note that even in a system of apolar materials net repulsion between species 1 and substrate 2 is possible if $\gamma_1^{LW} > \gamma_3^{LW} > \gamma_2^{LW}$ or $\gamma_1^{LW} < \gamma_3^{LW} < \gamma_2^{LW}$.

The Lifshitz-van der Waals contribution to the interfacial free energy of interaction of a sphere (*e.g.* a milk fat globule (MFG)) with diameter D and a flat plate (*e.g.* a heat transfer surface) decays with their separation distance, l , as

$$\Delta G_{123}^{LW}(l) = \frac{\pi l_0^2 D \Delta G_{123}^{LW}(l_0)}{l}, \quad (2.6)$$

where l_0 is the minimum equilibrium distance of two condensed-phase surfaces ($l_0 =$

0.157 ± 0.001 nm at 20 °C, van Oss, 2003). In water, Lewis acid-base forces decay as

$$\Delta G_{123}^{AB}(l) = \pi D \lambda \Delta G_{123}^{AB}(l_0) \exp((l_0 - l)/\lambda) , \quad (2.7)$$

where λ is the characteristic decay length of water ($\lambda = 1.0$ nm at 20 °C, van Oss, 2003). Since Lifshitz-van der Waals forces decay more gradually with distance than Lewis acid-base forces, there can be an energy barrier and a secondary minimum in the free energies of interaction over distance (van Oss, 2003). Given knowledge of surface energy parameters and assuming a simple ternary system, the above model gives an estimate of the tendency of a particle in milk to adhere to the pasteuriser heat transfer surface.

The surface energy of solids is commonly determined by measuring the contact angles of liquid drops with known surface tension. Equations 2.1 and 2.3 are substituted into the force equilibrium of Young (1805),

$$\gamma_1 \cos \beta = \gamma_2 - \gamma_{12} , \quad (2.8)$$

where β is the contact angle between a liquid 1 on a surface 2, giving

$$(1 + \cos \beta) \gamma_1 = 2 \left(\sqrt{\gamma_1^{LW} \gamma_2^{LW}} + \sqrt{\gamma_1^- \gamma_2^+} + \sqrt{\gamma_1^+ \gamma_2^-} \right) . \quad (2.9)$$

As stated by van Oss (2003), the three unknown components of the solid's surface energy are found by measuring contact angles of three test liquids with known parameters (γ^{LW}, γ^+ and γ^-), *e.g.* one apolar and two polar liquids, of which one must be water. Note that the condition $\gamma_1 > \gamma_2$ must be satisfied to obtain a finite, measurable contact angle. Because γ^+ and γ^- always appear as products in all model equations, their absolute values are beyond direct experimental accessibility by the contact angle method. By convention, the electron donor and acceptor contributions of water are taken to be of equal magnitude.

2.4.2 Test rigs to study fouling

This section provides a brief overview of typical designs and characteristics of experimental apparatuses used to study fouling. Chenoweth (1988) gave a comprehensive review on liquid fouling research units and operating schemes.

The simplest configuration for studying the fouling performance of different surfaces is the 'hot or cold finger', where a heated or cooled rod is immersed in a temperature controlled, stirred tank containing liquid prone to fouling. Fouling fingers have been used to simulate deposit formation from crude oil on cold pipeline walls (*e.g.* dos Santos *et al.*, 2004) and

hot heat transfer surfaces (Eaton, 1983). This technique was used by Boxler *et al.* (2013b), to study the deposition behaviour of whey protein, calcium phosphate and a combination of the two on common SS and enhanced diamond-like carbon surfaces.

However, the flow conditions and temperatures near the heat transfer surface can only be estimated, limiting the technique's applicability to parameterise fouling models. Hence, an apparatus with more readily controllable flow conditions is favourable in these cases. This can be achieved by moving the hot or cold heat transfer-surface at a controlled speed rather than moving the liquid. The 'spinning disc apparatus', developed by Nigo *et al.* (2009) within the P⁴G research group, uses this principle and features a liquid cooled, rotating vertical cylinder, which is immersed in a warm test solution. The circular test surface is at the bottom of the cylinder and the adjacent solution features a uniform heat transfer coefficient. The shear stress acting on the deposit and its surface temperature were estimated with computational fluid dynamics and the calculated heat transfer coefficients laid within the margins of experimental error. Since all heating and cooling is supplied by liquid media, the supplies could be exchanged to obtain a heated spinning disk.

The axisymmetric laminar flow fields employed in the above devices are not comparable with those used in many industrial HEXs, where the flow is turbulent. Bench-scale HEXs, which effectively simulate the conditions in a part of a full-scale unit, are more suitable. These are typically designed to provide easy access to surfaces and generated fouling deposits, for inspection and material analysis. Down-scaled plate HEXs often feature a simplified externally heated rectangular flow channel (*e.g.* Förster & Bohnet, 2000; Pääkkönen *et al.*, 2015). Fouling in tubes and annuli is often studied with sections of electrically heated pipe (*e.g.* Macchietto *et al.*, 2011). To enhance heat transfer, full-scale exchangers may have geometries generating turbulence (*e.g.* corrugated plates, fins, fluted pipes, inclined baffles). To study mechanisms of fouling and cleaning, bench-scale HEXs are simplified as a compromise between a realistic representation and predictable, uniform flow. They do allow studies with well defined shear stress and temperature, which are typically not well defined in industrial units.

Studying fouling at turbulent flow conditions necessitates high flow rates and large liquid volumes. Laboratory equipment is therefore often designed to recirculate the fouling stream (Boxler *et al.*, 2013c; Kananeh *et al.*, 2010; Rungraeng *et al.*, 2012), with the disadvantage that its properties and composition change with proceeding thermal treatment and deposition.

Experimental apparatuses typically operate with either constant temperature driving force (*e.g.* Barish & Goddard, 2013; Britten *et al.*, 1988) or constant heat flux (*e.g.* Boxler

et al., 2013b; Kananeh *et al.*, 2010; Rungraeng *et al.*, 2012). Apparatuses operating at constant temperature driving force experience a decrease in heat flux over time because fouling adds a thermal resistance. The temperature at the deposit-solution interface then reduces concomitantly. Operation at constant heat flux allows to keep this temperature constant if the thermal boundary layer is unaffected by the presence of the deposit and the properties and distribution of the deposit are uniform. As fouling proceeds, the temperature within the deposit rises, which accelerates ageing.

2.4.3 Fouling deposit analysis

Besides interpretation of the on-line data from the fouling experimental apparatus, various techniques qualify for subsequent analysis of deposit amount, composition or structure. This introduction gives an overview but is not intended to be exhaustive.

The simplest way to determine the mass of collected deposit is by weighing the clean and fouled heat exchanger surface or sample in the wet or consistently dried state. This is non-destructive and common practice in research. Depending on the amount of deposit, its thickness can be determined by simple traditional methods or by more advanced techniques *e.g.* confocal thickness scanning (CTS). Some of the the surface metrology techniques discussed in Section 2.4.1 are applicable to dry deposits. Soft and wet layers are suitable for analysis with fluid dynamic gauging, which can also give information about deposit elasticity, cohesion and cleanability (Tuladhar *et al.*, 2002a).

The average elemental composition of a fouling layer may be obtained with spectroscopy techniques such as inductively coupled plasma optical emission spectroscopy (ICP-OES) (Boxler *et al.*, 2013c; Hagsten *et al.*, 2016). The protein fraction can be measured with the Kjeldahl method (Foster *et al.*, 1989) or by protein assays, such as the one developed by Bradford (Belmar-Beiny *et al.*, 1993). A simple way of determining the mineral fraction is by ashing in an oven or by thermogravimetric analysis at temperatures above 450 °C (Boxler *et al.*, 2013c; Lalande *et al.*, 1984).

The micro- and nano-structure of fouling deposits is often imaged with scanning electron microscopy (*e.g.* by Foster & Green, 1990; Hagsten *et al.*, 2016; Rosmaninho & Melo, 2008). Electron backscatter diffraction can further provide information about local properties of crystalline deposits (Besevic *et al.*, 2017). Elemental and chemical information can be obtained by X-ray photoelectron spectroscopy (Premathilaka *et al.*, 2007). Confocal laser scanning microscopy (CLSM) in conjunction with histology techniques originally developed to image biological samples has been successfully applied to study the structure and local composition of foodstuffs and fouling layers (Auty *et al.*, 2001; Hagsten *et al.*,

2016). The transparency of thin wet milk fouling deposits would potentially allow *in situ* imaging with CLSM.

2.4.4 Summary of the state of the art

Antifouling coatings for mitigating fouling of milk-related products have been studied since the first paper on this topic in 1968 by Gordon *et al.* Interest in this approach has grown substantially over the last decade. 41 sets of fouling experiments using coated heat transfer surfaces were identified in the literature, of which 26 used simple milk model formulations which do not necessarily represent the complexity of real milk. The reported data on antifouling performance gives a mixed picture and does not allow simple conclusions. The key mechanisms of milk fouling on steels were identified, but it remains largely unknown how events of milk fouling are affected by varying types of surfaces – which may in turn have resulted in the broad spectrum of reported performances. It is therefore necessary to develop tools to study the effect of surfaces on structure and composition of fouling layers generated in conditions relevant to industrial practice. The main challenge in understanding milk fouling is the complexity of the problem, which necessitates fusing insights from a broad spectrum of physics, chemistry, biology and engineering.

Although some coatings have proven to be successful over several fouling-cleaning-cycles on the laboratory scale, to the author's knowledge there are currently no coated HEXs for milk heat treatment in industrial use. There is thus an implementation gap due to the risks associated with the scale-up from laboratory to plant-scale. In order to bridge this gap, further work is needed to demonstrate efficacy of coatings on the pilot-scale.

The economics of antifouling coatings is a topic which recently received attention from researchers following the pioneering paper by Gomes da Cruz *et al.* in 2015. In their work they assumed a linearly increasing fouling resistance over time, which is rarely found in practice due to autoretardation effects at later stages of fouling. Their approach was based on the analysis of falling rate processes by Ma and Epstein (1981), but lacks a graphical or analytical solution and relies on numerical analysis to solve the underlying optimisation problem. An analytical analysis would provide further insight by revealing the sensitivity of the solution to key performance and operating variables. This project aims to combine experimental fouling data with techno-economic models to study the applicability of FP coatings in an industrial setting.

Chapter 3

Techno-economics of antifouling coatings in heat exchangers

3.1 Introduction

Two approaches have been developed to enable researchers and practitioners to evaluate the benefits arising from the use of antifouling coatings. To quantify the margin available for coating solutions, energy, cleaning and investment costs as well as sector-specific criteria are incorporated. Related sustainability considerations, such as thermal losses due to fouling resistances and cleaning operations, can be studied with these methods as well. Individual HEXs are considered, rather than units in a network.

The first approach, referred to as the ‘lumped model’, combines the *NTU*-Method (see Bergman & Incropera, 2011) and an asymptotic fouling model with a finite induction period in a novel way to find an explicit expression for the optimal operating strategy in a fouling-cleaning cycle.

The second model, named the ‘dynamic model’, is more advanced and solves the enthalpy balances of the cold and hot stream along the exchanger and over time. Together with a fouling model sensitive to operating and surface conditions, it predicts the heat duty and local fouling dynamics.

3.2 Lumped model

3.2.1 Phenomenological fouling models

Fouling can be quantified by the reduction of the overall heat transfer coefficient, U , of a HEX over time, t' , due to an additional overall fouling resistance, R_f , *viz.*

$$\frac{1}{U(t')} = \frac{1}{U_{cl}} + R_f(t') , \quad (3.1)$$

where U_{cl} is the value after cleaning (where all the fouling deposit has been removed). Differences in dynamics of mass deposition and removal can result in the evolutions of R_f which are depicted in Figure 3.1 (Bott, 1995, 2001). There may be an induction period with negligible deposition, t_{ind} , in which initiation mechanisms of fouling take place. These are type-specific, *e.g.* crystal nucleation in crystallisation fouling or adsorption of organic molecules in biofouling (Epstein, 1983; Jain & Bhosle, 2009). During this early period, heat transfer can be slightly enhanced due to increases in surface roughness giving a larger film heat transfer coefficient and surface area.

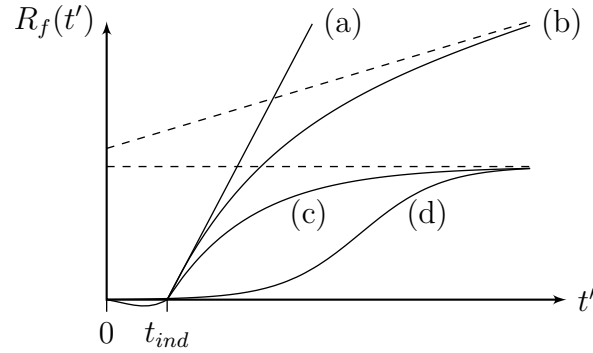


Figure 3.1: Idealised evolutions of fouling resistance over time as summarised by Bott (1995, 2001). (a) linear, (b) falling rate, (c) asymptotic, and (d) sigmoidal fouling, approaching asymptote in (c). Dashed lines indicate asymptotes.

A steady increase in fouling resistance ((a) in Figure 3.1) is frequently reported for crystallisation fouling (Bansal, Chen, & Müller-Steinhagen, 2008). Gomes da Cruz *et al.* (2015) assumed this simple fouling behaviour for their economic analysis, *i.e.* where the overall fouling resistance, R_f , increased linearly with time at constant fouling rate, r_f , *viz.*

$$R_f = r_f t' . \quad (3.2)$$

In practice, linear $R_f - t'$ behaviour, as described by Eq. 3.2, is often not observed as (i) there may be an induction period and (ii) autoretardation effects can reduce the rate of fouling at later stages owing to changes in surface temperature and deposit strength *etc.* This leads to falling rate or even asymptotic fouling ((b) and (c) in Figure 3.1). It is possible that, given constant operating conditions and sufficient processing time, a trend formerly identified as falling rate fouling finally develops to be similar to asymptotic fouling, wherein R_f approaches a limit at long times (Bott, 1995). This is often described by the Kern-Seaton model (Kern & Seaton, 1959),

$$R_f = \begin{cases} 0, & t' < t_{ind} \\ R_f^\infty \left(1 - \exp\left(-\frac{t_{ind}-t'}{t_f}\right)\right), & t' \geq t_{ind} \end{cases} . \quad (3.3)$$

Here, t_f is the characteristic timescale (the kinetic parameter), and R_f^∞ is the asymptotic fouling resistance. The latter parameter is frequently employed in overdesigning HEXs subject to fouling, even though this approach tends to promote fouling in a ‘self-fulfilling prophecy’ (Hays, 1989). Curve (d) in Figure 3.1 illustrates a case typical for biofouling where three stages of result in a sigmoidal evolution of fouling resistance (Dürr & Thomason, 2010).

This list of behaviours is not exhaustive and there may be effects that lead to more complex dynamics such as ageing or sloughing of deposit (Epstein, 1983). In real measurements of R_f a considerable amount of fluctuation is to be expected from the fouling dynamics, process variables, and measuring chain.

The following sections develop the ‘value pricing’ concept for HEXs subject to asymptotic fouling, extending the numerical analysis of Gomes da Cruz *et al.* (2015) to one type of fouling behaviour which is of direct relevance to industrial practice. Criteria determining when an exchanger should be cleaned are identified. One case of equal heat capacity flow rates is identified, where an explicit result can be obtained which does not require tedious calculation. The ‘value pricing’ concept is illustrated with a case study based on data reported by Oldani *et al.* (2013), comparing water crystallisation fouling on stainless steel tubes and ones with a perfluoropolyether (PFPE) coating.

3.2.2 Objective functions for preheater operations subject to fouling

To assess the attractiveness of an antifouling coating, the benefit of its application has to be found in comparison against a reference material – typically SS in food applications – by evaluation of an objective function. The objective function quantifies the HEX performance during a fouling-cleaning cycle. The optimal operating period (*i.e.* the time until the unit should be cleaned) is unknown but can be found by maximising or minimising the objective function as long as no other operational constraints apply (*e.g.* hygiene constraints, working shifts, or mechanical integrity checks).

Depending on whether the motivation for optimising the fouling-cleaning cycle is aimed at (a) maximising the time-averaged heat duty, q_m , (see Ma & Epstein, 1981), (b) minimising the time-averaged operating cost, ϕ_{op} , (see Casado, 1990; Gomes da Cruz *et al.*, 2015; Ishiyama *et al.*, 2014), or (c) minimising the operating cost per unit of heat transferred,

ϕ_Q , (see Ma & Epstein, 1981), the objective function to be optimised is calculated thus:

$$\text{Time averaged heat duty: } q_m(t) = \frac{\int_0^t q(t') dt'}{t + \tau} \quad (3.4a)$$

$$\text{Time averaged operating cost: } \phi_{op}(t) = \frac{c_E[\int_0^t q_{cl} - q(t') dt' + q_{cl}\tau] + C_{cl}}{t + \tau} \quad (3.4b)$$

$$\text{Operating cost per unit of heat transferred: } \phi_Q(t) = \frac{\phi_{op}(t)}{q_m(t)} = \frac{c_E q_{cl}(t + \tau) + C_{cl}}{\int_0^t q(t') dt'} - c_E \quad (3.4c)$$

Here, c_E is the cost per unit of heat not transferred due to fouling. Inspection of Eq. 3.4a,b and c shows there will be an optimal processing period, t_{opt} , if $dq_m/dt = 0$, $d\phi_{op}/dt = 0$, or $d\phi_Q/dt = 0$, which requires

$$q_m(t_{opt}) = q(t_{opt}) \quad (3.5a)$$

$$\phi_{op}(t_{opt}) = c_E(q_{cl} - q(t_{opt})) \quad (3.5b)$$

$$\phi_Q(t_{opt}) = c_E \left(\frac{q_{cl}}{q(t_{opt})} - 1 \right) . \quad (3.5c)$$

Furthermore, the condition for a minimum in q_m , ϕ_{op} , and ϕ_Q to exist requires the heat duty to decline continuously: $dq/dt < 0$. If an optimal processing period exists, it will therefore always exceed the induction period. For asymptotic fouling there are two other results of practical interest:

- (i) Where t_{opt} is large (*i.e.* long operating periods), such that $t_{opt} \gg t_f$, asymptotic fouling behaviour results in $dq/dt \approx 0$ and there is little benefit in cleaning the exchanger: it should be left to operate in its fouled state, or until another criterion applies.
- (ii) If fouling is very fast, such that R_f^∞ is reached quickly, the unit is best left to operate in its fouled state. Fouling mitigation should be given stronger consideration.

Only under these conditions should the unit be designed with a U_{cl} value including R_f^∞ , which is the basis of the TEMA (1999) approach.

3.2.3 Impact of asymptotic fouling in a simple heat exchanger

The instantaneous heat duty of a HEX, $q(t')$, is calculated using the *NTU*-effectiveness method (Bergman & Incropera, 2011). Ishiyama *et al.* (2014) analysed the problem for

linear fouling. For asymptotic fouling, Equations 3.1 and 3.3 are combined to give the overall heat transfer coefficient, U , *viz.*

$$U = \frac{1/R_f^\infty}{1/(U_{cl}R_f^\infty) + 1 - \exp\left(\frac{t_{ind}-t'}{t_f}\right)} = \frac{a_1}{a_2 + 1 - \exp\left(-\frac{t^*}{t_f}\right)}. \quad (3.6)$$

Here, $a_1 = 1/R_f^\infty$, $a_2 = 1/(U_{cl}R_f^\infty)$ and $t^* = t' - t_{ind}$, for brevity. a_2 is the reciprocal of an asymptotic fouling Biot number $Bi_f^\infty = U_{cl}R_f^\infty$. The number of heat transfer units of the HEX, NTU , is given by

$$NTU = \frac{UA}{W_{\min}} = \frac{a_1A}{W_{\min}\left(a_2 + 1 - \exp\left(-\frac{t^*}{t_f}\right)\right)}, \quad (3.7)$$

where A is the heat transfer area, and $W = \dot{m}c_p$ is a stream heat capacity flow rate. W_{\min} is the smaller heat capacity flow rate of the two streams entering the exchanger. Solutions of the objective functions Eq. 3.4a,b, or c subject to U given by Equation 3.6 and HEX performance relationships such as the NTU -effectiveness approach usually require numerical calculation. This is illustrated here by considering one of the simplest practical cases, that of the counter-current HEX with equal heat capacity flow rates ($W_{\min} = W_{\max} = W$). Examples where $W_{\min} = W_{\max}$ arise include preheaters (where an outlet stream is used to preheat or precool itself as an inlet stream) *e.g.* the regenerative section of dairy plate HEXs. The effectiveness, ε , is given by the simple relationship

$$\varepsilon = \frac{NTU}{1 + NTU} = \frac{a_1A}{a_1A + W\left(a_2 + 1 - \exp\left(-\frac{t^*}{t_f}\right)\right)}. \quad (3.8)$$

ε is the ratio of the actual rate of heat transfer, q , to the thermodynamically maximum possible duty, $q_{\max} = W\Delta T_{\max}$, where ΔT_{\max} is the maximum heat transfer driving force. With this, the heat duty is

$$q = \varepsilon q_{\max} = \frac{a_1A}{a_1A + W\left(a_2 + 1 - \exp\left(-\frac{t^*}{t_f}\right)\right)} W\Delta T_{\max}. \quad (3.9)$$

This can be rewritten as

$$q = \frac{a_3}{a_4 - \exp\left(-\frac{t^*}{t_f}\right)}. \quad (3.10)$$

It follows from combining Eq. 3.7 – 3.10 that

$$a_3 = a_1A\Delta T_{\max} = \frac{A\Delta T_{\max}}{R_f^\infty} = q_{cl} \frac{1 + NTU_{cl}}{U_{cl}R_f^\infty} = q_{cl} \frac{1 + NTU_{cl}}{Bi_f^\infty}, \quad (3.11)$$

$$a_4 = a_2 + \frac{a_1A}{W} + 1 = \frac{1}{U_{cl}R_f^\infty} + \frac{A}{WR_f^\infty} + 1 = \frac{1 + NTU_{cl} + Bi_f^\infty}{Bi_f^\infty}, \quad (3.12)$$

where NTU_{cl} is the number of transfer units of the clean unit. The clean heat duty at $t^* = 0$, *i.e.* $t' = t_{ind}$, is equal to $q_{cl} = a_3/(a_4 - 1)$, whereas the heat duty after a long period of operation, *i.e.* $t' \rightarrow \infty$, is $q = a_3/a_4$. Integrating Eq. 3.10 yields

$$\int_0^t q(t') dt' = \int_0^{t_{ind}} q_{cl} dt' + \int_{t_{ind}}^t q(t') dt' \quad (3.13)$$

$$= q_{cl}t_{ind} + \frac{a_3}{a_4}t_f \ln \left(\frac{1 - a_4 \exp((t - t_{ind})/t_f)}{1 - a_4} \right) . \quad (3.14)$$

This is substituted into the objective functions, Eq. 3.4a,b, and c. Substituting Eq. 3.10 into the objective functions, Eq. 3.4a,b, and c, and integrating yields

$$q_m(t) = \frac{q_{cl}t_{ind} + \frac{a_3}{a_4}t_f \ln \left(\frac{1 - a_4 \exp((t - t_{ind})/t_f)}{1 - a_4} \right)}{t + \tau} , \quad (3.15a)$$

$$\phi_{op}(t) = \frac{c_E \left[q_{cl}(t - t_{ind} + \tau) - \frac{a_3}{a_4}t_f \ln \left(\frac{1 - a_4 \exp((t - t_{ind})/t_f)}{1 - a_4} \right) \right] + C_{cl}}{t + \tau} , \quad (3.15b)$$

$$\phi_Q(t) = \frac{c_E q_{cl}(t + \tau) + C_{cl}}{q_{cl}t_{ind} + \frac{a_3}{a_4}t_f \ln \left(\frac{1 - a_4 \exp((t - t_{ind})/t_f)}{1 - a_4} \right)} - c_E . \quad (3.15c)$$

If the unit is never cleaned (*i.e.* $t \rightarrow \infty$), the time-averaged heat duty will approach the instantaneous heat duty asymptotically

$$\lim_{t \rightarrow \infty} q_m(t) = \lim_{t \rightarrow \infty} q(t) = q_{cl} \frac{1 + NTU_{cl}}{1 + NTU_{cl} + Bi_f^\infty} , \quad (3.16)$$

the operating cost per time will approach the thermal cost penalty asymptotically

$$\lim_{t \rightarrow \infty} \phi_{op} = \lim_{t \rightarrow \infty} c_E (q_{cl} - q(t)) = c_E q_{cl} \frac{Bi_f^\infty}{1 + NTU_{cl} + Bi_f^\infty} , \quad (3.17)$$

and the operating cost per heat transferred will approach the thermal cost penalty per heat transferred asymptotically

$$\lim_{t \rightarrow \infty} \phi_Q(t) = \lim_{t \rightarrow \infty} c_E \left(\frac{q_{cl}}{q(t)} - 1 \right) = c_E \frac{Bi_f^\infty}{1 + NTU_{cl}} . \quad (3.18)$$

These equations show that a large exchanger (NTU_{cl} large) is generally less sensitive to fouling if $1 + NTU_{cl} \gg Bi_f^\infty$. This is illustrated in Figure 3.2 where the above equations are plotted in a non-dimensionalised fashion. With increasing HEX size (*i.e.* larger NTU_{cl}) the time averaged heat duty monotonically increases for all asymptotic fouling Biot numbers in Figure 3.2a. Conversely, the cost functions in Figure 3.2a and c decrease. Unfortunately, a larger HEX is often a poor solution to a fouling problem because there are more sites for deposition and a larger pressure drop associated with the additional area. If the fouling is more extensive, the pressure drop penalty might require operation being interrupted to restore the hydraulic performance.

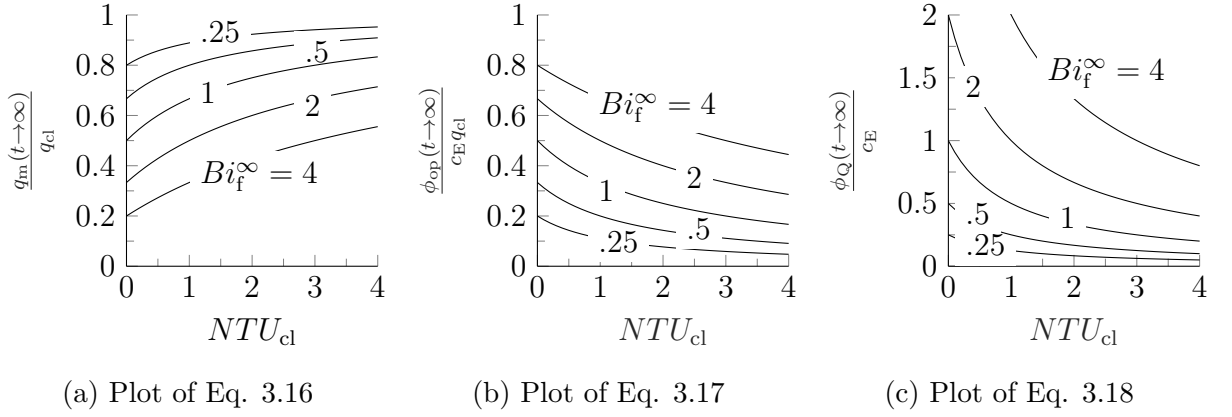


Figure 3.2: Non-dimensionalised objective functions if a HEX is never cleaned (*i.e.* $t \rightarrow \infty$) assuming asymptotic fouling, counter-current flow, and equal heat capacity flow rates. Loci plotted for $0.25 \leq Bi_f^\infty \leq 4$.

For an optimal processing period to exist, *i.e.* $q_{m,\max}$, $\phi_{op,\min}$ or $\phi_{Q,\min}$, Eq. 3.5a,b or c has to hold. This can be solved numerically for t_{opt} . In engineering applications, however, such as scheduling cleaning or as an instrument to quantify the financial attractiveness of HEX coatings, a simplified approach is desirable. This is considered in the next section where a tractable explicit solution is presented.

3.2.4 Explicit solutions for cases of counter-current flow and equal heat capacity flow rates

Linear fouling

Ishiyama *et al.* (2014) obtained an implicit solution for the minimum time averaged operating cost (Equation 3.4b) for the case of linear fouling (Equation 3.2) in a counter-current HEX with equal heat capacity flow rates. The following demonstrates the explicit solution to maximise the time averaged heat duty, q_m . This procedure also serves as an illustration to solve fouling-scheduling problems for the case of asymptotic fouling with an induction period. As in Section 3.2.3, the heat duty of a counter-current HEX with $W_{\min} = W_{\max}$ subject to linear fouling is found:

$$q(t') = q_{cl} \frac{1 + NTU_{cl}}{1 + NTU_{cl} + U_{cl} r_f t'} \quad (3.19)$$

Note the similarity to the terminal heat duty in asymptotic fouling given by Equation

3.16. Integrating yields

$$\int_0^t q(t') dt' = q_{cl} \frac{1 + NTU_{cl}}{U_{cl} r_f} \ln \left(\frac{q_{cl}}{q(t)} \right) . \quad (3.20)$$

Substituting Equation 3.19, 3.20 and 3.4a into the optimality criterion (Equation 3.5a) yields

$$\frac{t_{opt} + \tau}{t_{opt} + \chi_1} = \ln \left(\frac{t_{opt}}{\chi_1} + 1 \right) \quad (3.21)$$

$$\chi_1 = \frac{1 + NTU_{cl}}{U_{cl} r_f} . \quad (3.22)$$

Writing Equation 3.21 in the form $Y = Xe^X$ allows one to solve explicitly for X using the Lambert-W function discussed by Euler (1783): $X = W(Y)$. $W(Y)$ is multivalued and it has a principal and lower branch shown in Figure 3.3. After some manipulation the principal branch W_0 yields the physically relevant solution to the problem, *viz.*

$$\frac{\tau - \chi_1}{t_{opt} + \chi_1} = \ln \left(\frac{t_{opt}}{\chi_1} + 1 \right) - 1 \quad (3.23)$$

$$\Leftrightarrow \frac{\tau - \chi_1}{\chi_1} = \left(\ln \left(\frac{t_{opt}}{\chi_1} + 1 \right) - 1 \right) \left(\frac{t_{opt}}{\chi_1} + 1 \right) \quad (3.24)$$

$$\Leftrightarrow \frac{\tau - \chi_1}{\chi_1 e} = \left(\ln \left(\frac{t_{opt}}{\chi_1} + 1 \right) - 1 \right) e^{\ln \left(\frac{t_{opt}}{\chi_1} + 1 \right) - 1} \quad (3.25)$$

$$\Leftrightarrow t_{opt} = \chi_1 \left(e^{W_0 \left(\frac{\tau - \chi_1}{\chi_1 e} \right) + 1} - 1 \right) . \quad (3.26)$$

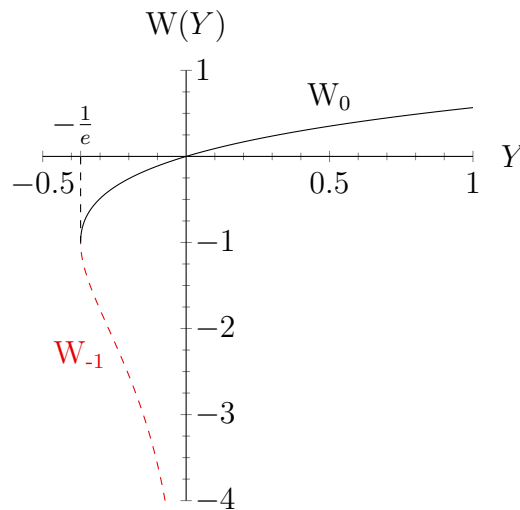


Figure 3.3: Lambert-W function for real valued arguments showing the principal and lower branch, $W_0 \geq -1$ and $W_{-1} \leq -1$, respectively (after Valluri *et al.*, 2000).

Optimising a preheating HEX or milk pasteurisation operation according to this paradigm will result in optimal energy recovery from the hot stream. It should be noted that energy consumption during cleaning is not captured here, but could be included if desired. Explicit solutions to minimise the time averaged operating cost, ϕ_{op} , and the cost per heat transferred, ϕ_{Q} , in case of linear fouling could not be obtained, but can be found graphically (Ma & Epstein, 1981) or iteratively.

Asymptotic fouling with induction period

Employing the asymptotic fouling model in the *NTU*-effectiveness method (Equation 3.10) does not, to the author's knowledge, yield explicit solutions for t_{opt} with any of the optimality conditions (Equations 3.5a,b and c). This section describes an explicit approximation, which can be computed without iteration. The heat duty from Equation 3.10 can be rewritten as

$$q = \frac{a_3}{a_4 - \exp(-t^*/t_f)} + \frac{a_3}{a_4} - \frac{a_3}{a_4} = \frac{a_3}{a_4} \left(\frac{\exp(-t^*/t_f)}{a_4 - \exp(-t^*/t_f)} + 1 \right). \quad (3.27)$$

If $a_4 \gg \exp(-t^*/t_f) \forall t^* \geq t_{\text{ind}}$, Equation 3.27 becomes

$$q \approx q_{\text{approx}} = \frac{a_3}{a_4} \left(\frac{\exp(-t^*/t_f)}{a_4 - 1} + 1 \right). \quad (3.28)$$

The approximate heat duty gives the exact result for $t^* = 0$ and $t^* \rightarrow \infty$. The relative approximation error at other instances of t^* is calculated from

$$\eta = \frac{q - q_{\text{approx}}}{q} = 1 - \left(\frac{\exp(-t^*/t_f)}{a_4 - 1} + 1 \right) \left(1 - \frac{\exp(-t^*/t_f)}{a_4} \right). \quad (3.29)$$

To find the maximum error, $d\eta/dt^*$ is set to zero. The maximum relative error for a physically feasible time occurs at $t_{\eta, \text{max}}^* = t_f \ln(2)$. This corresponds to a maximum relative error of

$$\eta_{\text{max}} = \eta(t_{\eta, \text{max}}^*) = -\frac{1}{4a_4(a_4 - 1)}. \quad (3.30)$$

It should be noted that the relative error is negative, since $a_4 > 1$. If the relative error is constrained to lie with $\eta_{\text{max}} > \eta_{\text{crit}} = -5\%$, the minimum value of a_4 is (ignoring the physically infeasible negative solution for a_4) given by

$$a_4 = \frac{1}{Bi_f^\infty} (1 + NTU_{\text{cl}} + Bi_f^\infty) > \frac{1}{2} + \sqrt{\frac{1}{4} - \frac{1}{4\eta_{\text{crit}}}} \approx 2.8. \quad (3.31)$$

This condition holds for many HEXs in practice, where the flow is counter-current, since the number of heat transfer units of a thermally well-designed HEX is greater than 3 (Bergman & Incropera, 2011). Integrating the approximate heat duty yields

$$\int_0^t q_{\text{approx}}(t') dt' = \int_0^{t_{\text{ind}}} q_{\text{cl}} dt' + \int_{t_{\text{ind}}}^t q_{\text{approx}}(t') dt' \quad (3.32)$$

$$= q_{\text{cl}} t_{\text{ind}} + \frac{a_3}{a_4} \left[\frac{t_f}{a_4 - 1} \left(1 - \exp\left(-\frac{t - t_{\text{ind}}}{t_f}\right) \right) + t - t_{\text{ind}} \right]. \quad (3.33)$$

Note that this approximation does not have a nested exponential function in a logarithm whereas the exact result, Equation 3.14, does. Combining Equations 3.28 and 3.33, the objective functions (Equations 3.4a,b and c) and respective optimality conditions (Equations 3.5a,b and c), yields the optimal processing periods of the three objective functions. Some algebraic transformations, analogous to the ones illustrated for linear fouling and utilising the negative branch of the Lambert-W function, give the approximate optimal processing periods presented on the right half of Table 3.1. The positive branch of the Lambert-W function would give negative processing periods – which are physically infeasible.

Criteria can be found by inspection of the three solutions indicating under which conditions there is no optimum, *i.e.* it is not attractive to clean the unit. Depending on whether the unit is optimised for maximum heat duty, minimum time averaged operating cost or minimum operating cost per heat transferred, parameter χ_2 , χ_3 , or χ_4 is calculated (see Table 3.1). If no other constraints apply, *e.g.* hygiene considerations in food processing or scheduled mechanical integrity checks, it is attractive to leave the exchanger in its fouled state if one applicable of the following conditions holds:

$$\chi_2, \chi_3 \text{ or } \chi_4 < 0. \quad (3.34)$$

By comparing the solutions and acknowledging that all parameters in the objective functions are positive valued it is also apparent that

$$t_{\text{opt}}(q_m) < t_{\text{opt}}(\phi_Q) < t_{\text{opt}}(\phi_{\text{op}}). \quad (3.35)$$

If the cost to clean a fouled HEX is greater than zero (which is generally the case) it is always financially more attractive to clean a unit later than optimal in terms of a consideration based purely on thermal arguments. Note that in this simplified methodology (which *e.g.* does not account for environmental damage due to cleaning chemicals) there is an inherent conflict between environmental and financial motivations, although the disparity depends on how costly cleaning is compared to the cost of energy.

Given a counter-current HEX with identical, constant heat capacity flow rates, static inlet temperatures, fouling data being available, and $a_4 > 2.8$, application of the approximate

method is straightforward. If χ_2 , χ_3 , or $\chi_4 < 0$, there is no resultant energy or cost benefit of cleaning and the exchanger should be allowed to operate in the fouled state. In this case, the terminal value of the objective function can be calculated with Equation 3.16, 3.17 or 3.18. Otherwise, the respective Equation in Table 3.1 is used to schedule cleaning. The approximate optimal time averaged heat duty, operating cost, or operating cost per heat transferred is then calculated by inserting the approximate solution for the optimal processing period, $t_{\text{opt,approx}}$, in Equation 3.15a,b or c. This methodology enables researchers and practitioners to estimate the economic value of antifouling coatings in HEXs without employing involved numerical techniques such as those described in Gomes da Cruz *et al.* (2015).

Table 3.1: Explicit solutions to the cleaning scheduling problem of a single counter-current HEX with equal heat capacity flow rates for different fouling behaviours and objective functions. ‘-’ indicates no explicit solution found.

Objective function	Condition for t_{opt}	Linear	Asymptotic
		$R_f = \eta_f t'$	$R_f = \begin{cases} 0 & t' < t_{\text{ind}} \\ R_f^\infty \left(1 - \exp\left(\frac{t_{\text{ind}} - t'}{t_f}\right)\right) & t' \geq t_{\text{ind}} \end{cases}$
Heat duty, Eq. 3.4a	$q_m = q$	$t_{\text{opt}} = \chi_1 \left[\exp\left(W_0\left(\frac{\tau - \chi_1}{e\chi_1}\right) + 1\right) - 1 \right]$ $\chi_1 = \frac{1 + NTU_{\text{cl}}}{U_{\text{cl}}\eta_f}$	$t_{\text{opt}} \approx -\tau - t_f [1 + W_{-1}(-\chi_2 \exp(-(t_{\text{ind}} + \tau)/t_f - 1))]^*$ $\chi_2 = 1 + \frac{t_{\text{ind}}}{t_f} - \frac{1 + NTU_{\text{cl}} \tau}{Bi_f^\infty t_f}$
Operating cost, Eq. 3.4b	$\phi_{\text{op}} = c_E(q_{\text{cl}} - q)$	-	$t_{\text{opt}} \approx -\tau - t_f [1 + W_{-1}(-\chi_3 \exp(-(t_{\text{ind}} + \tau)/t_f - 1))]^*$ $\chi_3 = 1 + \frac{t_{\text{ind}}}{t_f} - \frac{1 + NTU_{\text{cl}} \tau}{Bi_f^\infty t_f} - \frac{C_{\text{cl}}}{c_E q_{\text{cl}} t_f} \left(1 + \frac{1 + NTU_{\text{cl}}}{Bi_f^\infty}\right)$
Cost per heat transferred, Eq. 3.4c	$\phi_Q = c_E \left(\frac{q_{\text{cl}}}{q} - 1\right)$	-	$t_{\text{opt}} \approx -\tau - \frac{C_{\text{cl}}}{c_E Q_{\text{cl}}} - t_f \left[1 + W_{-1}\left(-\chi_4 \exp\left(-\frac{t_{\text{ind}} + \tau + \frac{C_{\text{cl}}}{c_E Q_{\text{cl}}}}{t_f} - 1\right)\right)\right]^*$ $\chi_4 = 1 + \frac{t_{\text{ind}}}{t_f} - \frac{1 + NTU_{\text{cl}}}{Bi_f^\infty t_f} \left(\tau + \frac{C_{\text{cl}}}{c_E q_{\text{cl}}}\right)$

*Error of heat duty approximation lies within 5% if $\frac{1}{Bi_f^\infty}(1 + NTU + Bi_f^\infty) > 2.8$. If no other constraints apply, *e.g.* hygiene considerations in food processing or scheduled mechanical integrity checks, it is not attractive to clean the exchanger (*i.e.* the objective functions have no optimum) if χ_2, χ_3 or $\chi_4 < 0$.

3.2.5 Illustrative case study: evaluating the water scaling performance of a PFPE coating

A case study, based on data taken from the literature, is used to illustrate the quantifying of the financial benefit of antifouling coatings. Oldani *et al.* (2013) reported the performances of a SS and a PFPE coated SS single-pass counter-current shell-and-tube unit with constant flow rates and approach temperatures. The process and utility streams were both aqueous, and the unit was subject to crystallisation fouling. The $R_f - t'$ data sets in Figure 3.4 were interpreted to exhibit asymptotic fouling behaviour and were fitted by the least-squares method to Equation 3.3. Data were only collected from the 60th day onward. The model parameters are reported in Table 3.2.

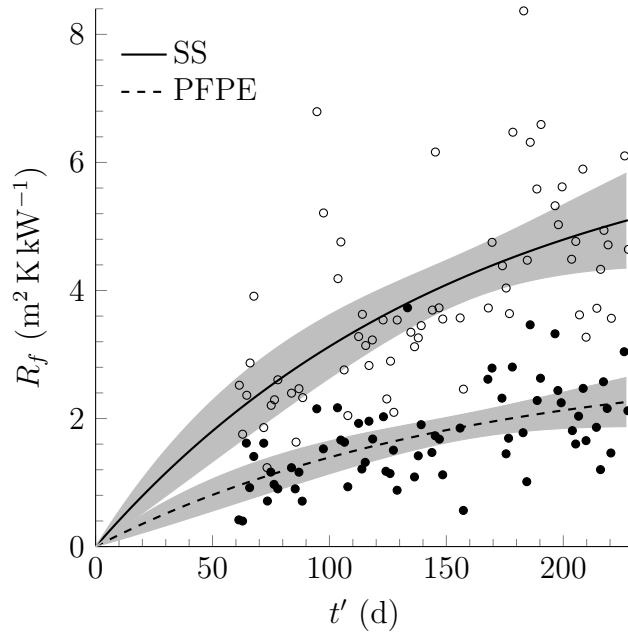


Figure 3.4: Fouling resistance-time data for uncoated (SS) and coated (PFPE) HEX reported by Oldani *et al.* (2013). Loci show the fit of the Kern–Seaton model (Equation (3)) to the data, with parameters given in Table 3.2. Grey areas show simultaneous 95% confidence bounds. R^2 for the coated and uncoated fits were 0.319 and 0.378, respectively.

In this case the PFPE coating reduced the rate of fouling and magnitude of the asymptotic fouling resistance. The characteristic fouling time scale remained similar. No induction period was observed for either surface.

The design and operating parameters of the exchangers considered in this study are summarised in Table 3.2.

Table 3.2: Lumped model case study parameters.

Design		
A	Heat transfer surface area ¹	500 m ²
r_h	Tube internal radius ¹	3 mm
r_c	Tube external radius ¹	5 mm
Thermal properties		
c_p	Cold and hot stream heat capacity	4180 J kg ⁻¹ K ⁻¹
h_h	Tube side heat transfer coefficient ²	800 W m ⁻² K ⁻¹
h_c	Shell side heat transfer coefficient ²	500 W m ⁻² K ⁻¹
k_{ss}	SS thermal conductivity ²	16 W m ⁻¹ K ⁻¹
k_{cs}	CS thermal conductivity ²	54 W m ⁻¹ K ⁻¹
Q_{cl}	Clean heat duty	2.29 MW
Fouling performance		
t_{ind}	Induction period ¹	0 d
$t_{ind,coat}$	Induction period, coated unit ¹	0 d
R_f^∞	Asymptotic fouling resistance ¹	6.70 m ² K kW ⁻¹
$R_{f,coat}^\infty$	Asymptotic fouling resistance, coated unit ¹	2.94 m ² K kW ⁻¹
t_f	Characteristic fouling timescale ¹	159.4 d
$t_{f,coat}$	Characteristic fouling timescale, coated unit ¹	156.4 d
τ	Cleaning period, uncoated and coated unit ²	4 d
Coating properties		
δ_{coat}	Coating thickness ²	10 μ m
k_{coat}	Coating thermal conductivity ²	0.1 W m ⁻¹ K ⁻¹
Operation		
\dot{m}_c, \dot{m}_h	Cold and hot stream mass flow	30 kg s ⁻¹
$T_{c,in}$	Cold stream inlet temperature ¹	20 °C
$T_{h,in}$	Hot stream inlet temperature ¹	50 °C
Costs		
c_E	Cost per unit heat ²	5.7 US\$ GJ ⁻¹
C_{cl}	Cleaning cost ²	4200 US\$
t_{lf}	Asset lifetime (depreciation) ²	10 year

¹data taken from Oldani *et al.* (2013)²data taken from Gomes da Cruz *et al.* (2015)

The parameters resemble the conditions in the model HEXs of Oldani *et al.* (2013). Some parameters were not reported, and these values were taken from the case study by Gomes da Cruz *et al.* (2015), where the fouling behaviour was modelled as linear. The two major differences between this work and the work of Gomes da Cruz *et al.* are: (i) the use of an asymptotic fouling model, and (ii) identical heat capacity flow rates. The clean heat duties are comparable. It should be noted that Oldani *et al.*'s experiments employed bench scale units, and their results are assumed to apply at a larger scale. This is expected to be valid if the processing conditions and conditions at the heat transfer interface are comparable (Geddert *et al.*, 2009). Processing conditions include the nature and source of the foulant, additives, bulk temperature, flow velocity, and flow regime. The time to clean, τ , is assumed to be independent of processing history. This assumption is expected to be valid if the exchanger has to be disassembled for cleaning.

An uncoated SS unit and a coated unit are compared. In addition, because FPs coating systems can provide good corrosion resistance, a coated carbon steel (CS) unit will be considered. CS is generally cheaper and conducts heat better than SS: this could compensate for the additional thermal conductivity associated with the coating (Gomes da Cruz *et al.*, 2015). The different conductivities of the wall material and the coating are included in the evaluation of U_{cl} via (Bergman & Incropera, 2011):

$$U_{cl} = (1/h_h + \delta_{coat}/k_{coat} + r_h/k_w \log(r_c/r_h) + r_h/(r_c h_c))^{-1} . \quad (3.36)$$

Here h_h is the internal and h_c the external film heat transfer coefficient, δ_{coat} the coating thickness, and k_{coat} and k_w are the coating and tube wall thermal conductivities, respectively. The internal and external radii of the tube are r_h and r_c . For the uncoated unit, δ_{coat} is zero. To achieve the specified clean heat duty, the coated unit will require a different heat transfer area, which is calculated from the definition of NTU_{cl} , *i.e.*

$$A_{coat} = AU_{cl}/U_{cl,coat} . \quad (3.37)$$

3.2.6 Results and discussion

The effect of the operating period on the objective functions for the uncoated and coated SS units are presented in Figure 3.5. The crosses mark the optimal operating periods where Equations 3.5a-c apply. The optimal processing period of the uncoated unit, t_{opt} , is reached after 40 d, 63 d or 59 d of processing, depending on whether cleaning scheduling is optimised for maximum average heat duty, time averaged operating cost, or operating cost per unit heat transferred. The approximate explicit solutions (see Table 3.1) are shown as solid dots and are in good agreement with the exact solutions, despite the small

$a_4 = 1.97$ for the uncoated unit. It can be seen that the maximum in q_m and minima in ϕ_{op} and ϕ_Q are not symmetrical, so that the penalty for cleaning early is slightly larger than that for cleaning later.

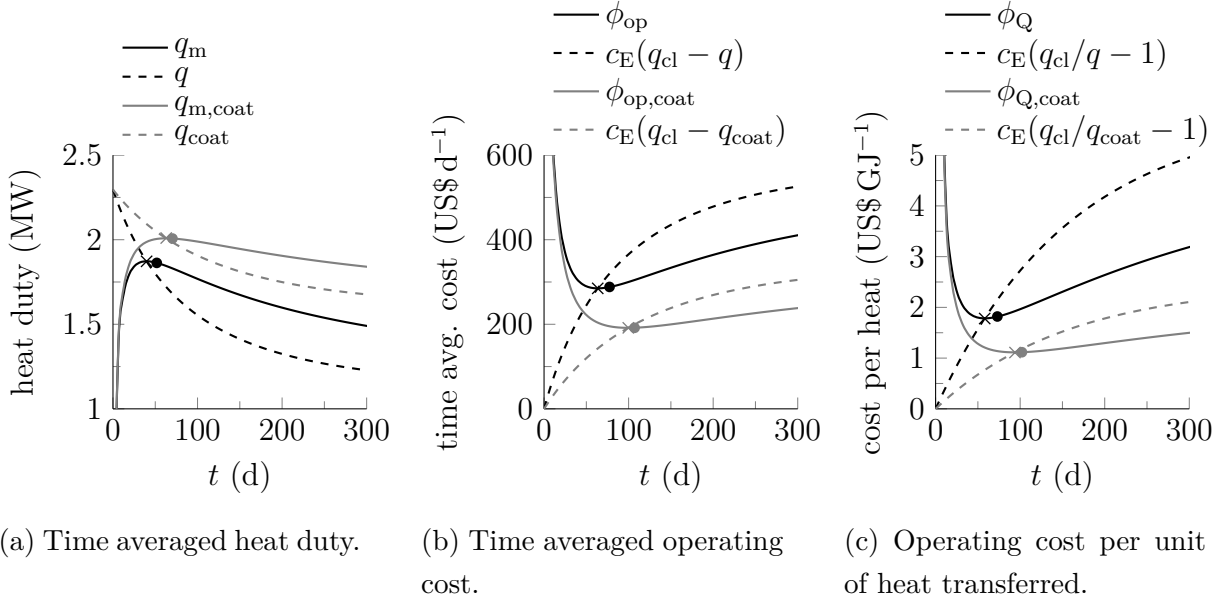


Figure 3.5: Effect of processing period length on (a) time averaged heat duty, (b) time averaged operating cost, and (c) operating cost per heat transferred for uncoated (black) and coated (grey) stainless steel HEXs in lumped model case study. Crosses – optimal processing periods; solid dots – approximate optimal processing periods.

The optimised schedules and optimal performance indices for the uncoated SS unit and the coated SS and CS units are summarised in Table 3.3. Both of the coated exchangers have a smaller clean heat transfer coefficient and require a larger heat transfer area. The higher thermal conductivity of CS almost compensates for the heat transfer resistance introduced by the coating. Regardless of the objective function used, the optimal operating periods of the coated units are 53 % to 62 % longer than for the uncoated unit, which means cleaning has to be done much less frequently. This is desirable, because cleaning of the HEX leads to a reduction in product throughput, consumption, and disposal of chemicals and waste product. Applying the coating improves the optimal time averaged heat duty by a mere 7%, but the gap widens when the units are operated for longer. When optimising for cost (*i.e.* ϕ_{op} and ϕ_Q), the cost objective functions reduce in a range from 32 % to 38 %, indicating that the antifouling coating can give an appreciable financial benefit.

A holistic approach means that the capital cost has also to be considered. Excluding the capital cost of the coating, the capital cost of the base unit, C_{base} , is calculated and expressed as an amortised cost, ϕ_{base} , by assuming straight line depreciation over

the unit (or coating) lifetime. The HEXs differ in base material, heat transfer area and coating. According to Hewitt and Pugh (2007), a 500 m² CS bonnet, one pass shell, fixed tubesheet bonnet (BEM) type HEX (TEMA, 1999) cost approximately 80 £ m⁻² in 1994. Conversion into US\$ and updating it with the chemical engineering plant index of 2017 yields an installed cost of 182 US\$ m⁻². A SS HEX with this area is roughly twice as expensive.

Table 3.3: Comparison of optimal performance indices in lumped model case study (parameters in Table 3.2). t_{opt} and $t_{\text{opt,approx}}$ are calculated with Equation 3.4a-c using the exact and approximate heat duty, respectively.

	Uncoated SS HEX	Coated SS HEX	Coated CS HEX	Unit
Design				
A	500.0	520.6	507.4	m ²
U_{cl}	392.8	377.2	387.1	W m ⁻² K ⁻¹
a_4	1.97	3.32	3.27	1
Optimised schedule for maximum q_{m}				
$t_{\text{opt}} + \tau$	40 + 4	63 + 4	62 + 4	d
$t_{\text{opt,approx}} + \tau$	52 + 4	70 + 4	70 + 4	d
$t_{\text{opt,coat}}/t_{\text{opt}}$	–	1.57	1.55	1
$q_{\text{m,opt}}$	1.87	2.0	2.0	MW
$q_{\text{m,coat,opt}}/q_{\text{m,opt}}$	–	1.07	1.07	1
Optimised schedule for minimum ϕ_{op}				
$t_{\text{opt}} + \tau$	64 + 4	100 + 4	98 + 4	d
$t_{\text{opt,approx}} + \tau$	77 + 4	107 + 4	106 + 4	d
$t_{\text{opt,coat}}/t_{\text{opt}}$	–	1.56	1.53	1
$\phi_{\text{op,opt}}$	285.1	191.3	193.8	US\$ d ⁻¹
$\phi_{\text{op,coat,opt}}/\phi_{\text{op,opt}}$	–	0.67	0.68	1
Optimised schedule for minimum ϕ_{Q}				
$t_{\text{opt}} + \tau$	58 + 4	94 + 4	92 + 4	d
$t_{\text{opt,approx}} + \tau$	73 + 4	102 + 4	101 + 4	d
$t_{\text{opt,coat}}/t_{\text{opt}}$	–	1.62	1.59	1
$\phi_{\text{Q,opt}}$	1.78	1.11	1.13	US\$ GW ⁻¹
$\phi_{\text{Q,coat,opt}}/\phi_{\text{Q,opt}}$	–	0.62	0.63	1

In the following steps we focus on scheduling by minimising the operating cost, ϕ_{op} .

The capital costs of the base units and total time averaged costs are presented in Table 3.4. The total time averaged costs of the coated SS and coated CS HEXs are 28% and 35% lower than the reference (uncoated) case, respectively. Assuming a straight line depreciation period of ten years, the maximum price of the coating per unit area ranges from (i) 644 US\$ m⁻² to 834 US\$ m⁻², for a greenfield application, where the unit is new, and (ii) 294 US\$ m⁻² to 475 US\$ m⁻² for a revamp. This sum is the ‘value price’ and represents the maximum benefit which needs to be shared between the operator and the coating vendor.

Table 3.4: Capital costs and maximum coating costs per area of the HEXs considered in the lumped model case study with parameters given in Table 3.2.

	Uncoated SS HEX	Coated SS HEX	Coated CS HEX	Unit
Capital cost of the base unit				
C_{base}	182 000	189 500	92 400	US\$
Time averaged cost				
$\phi_{\text{base}} = C_{\text{base}}/t_{\text{lf}}$	49.9	51.9	25.3	US\$ d ⁻¹
$\phi_{\text{opt}} = \phi_{\text{op,opt}} + \phi_{\text{base}}$	335.0	243.2	219.1	US\$ d ⁻¹
$\phi_{\text{opt,coat}}/\phi_{\text{opt}}$	–	0.73	0.65	1
Maximum coating cost per area: new, greenfield unit				
$c_{\text{coat,max,new}} =$ $(\phi_{\text{opt}} - \phi_{\text{opt,coat}})t_{\text{lf}}/A_{\text{coat}}$	–	644	834	US\$ m ⁻²
Maximum coating cost per area: revamped unit				
$c_{\text{coat,max,rev}} =$ $(\phi_{\text{op,opt}} - \phi_{\text{opt,coat}})t_{\text{lf}}/A_{\text{coat}}$	–	294	475	US\$ m ⁻²

It is important to note that ϕ_{base} is inversely proportional to the unit (or coating) lifetime, t_{lf} . In practice, the coating lifetime is likely to set t_{lf} , as the layer is likely to degrade or otherwise suffer reduced performance over time. It can be seen that this parameter affects the techno-economic calculation strongly. A simple finding is that $t_{\text{lf}} \geq t_{\text{opt}}$, the coating should last at least as long as the operating period. When $t_{\text{lf}} \approx t_{\text{opt}}$, one can consider renewable coatings, *i.e.* ones which are applied regularly, such as at the completion of a cleaning operation before the unit is put back on-line.

The NTU_{cl} value for this case study unit is about 1: it is close to the NTU_{cl} of the exchangers used to generate the fouling data, but it is not well designed. With this low NTU_{cl} , the a_4 parameter for the uncoated unit is < 2.8 , which was the criterion for

accurate estimation using the approximate scheduling approach. However, Figure 3.5 reports that scheduling the exchanger with the simplified method results in a difference in operating costs of only 1%. Considering the potential error in the parameters involved, particularly in predicting the fouling rate, this is not a significant difference. The approximate analysis is more readily calculable and suitable for initial estimates.

Sensitivity of heat exchanger operating cost to antifouling performance

This techno-economic model allows one to determine whether the cost of the performance improvement provided by surface coating is justified by satisfactory financial returns via the reduction in operating cost. The main source of uncertainty in these calculations lies in the fouling kinetics. A sensitivity analysis was conducted on the two Kern-Seaton parameters, t_f and R_f^∞ , based on the uncoated unit in Table 3.2. Fig. 3.6 shows the impact of t_f and R_f^∞ on the optimal operating cost. Increasing R_f^∞ (more severe fouling) and reducing t_f (faster fouling) both increase ϕ_{op} .

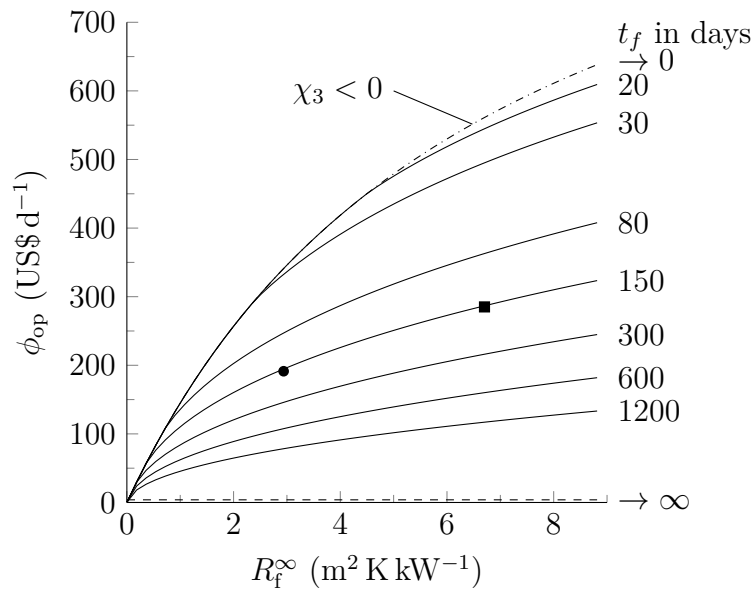


Figure 3.6: Impact of fouling model parameters t_f and R_f^∞ on the optimal operating cost for the uncoated SS unit in Table 3.2. Dash-dot line shows where the criterion $\chi < 0$ applies. Dash-dash line indicates the no-fouling case. Case study units: solid square, uncoated SS unit; solid circle, coated SS unit.

The dash-dot and dash-dash lines indicate the special cases when the characteristic fouling time constant approaches zero and infinity, respectively. If t_f is small, fouling occurs very quickly and cleaning is not attractive. The dash-dot line shows where the criterion $\chi_3 < 0$ holds. In this region, the corresponding minimum in Figure 3.5b is shallow or practically

non-existent. Figure 3.6 shows that the operating cost is then only dependent on four variables, given by Eq. 3.17.

In contrast, if fouling is slow, *i.e.* t_f tends towards infinity, cleaning is not attractive either. The figure confirms what might be an obvious result, that cleaning is therefore only economically sensible if fouling is neither too fast nor too slow. The value of this analysis is that it allows the terms ‘too fast’ and ‘too slow’ to be quantified.

A favourable effect of a coating, compared to an uncoated surface, might be that the corresponding locus in Figure 3.6 is moved down and to the left, close to the upper constraint ($\chi_3 < 0$). If the antifouling performance is sustainable and there are no other restrictions (for instance, hygienic considerations in the food and biotechnology sectors; product changeover in the fast moving consumer goods sector), cleaning facilities would not be needed for this HEX. This in turn would release capital.

3.3 Dynamic model

3.3.1 Modelling of a fouling heat exchanger in space and time

The lumped approach presented above is simple and easy to compute but is not sensitive to changes in local operating conditions. In the following sections, spatially and temporally dynamic fouling behaviour are considered.

The one-dimensional temperature distribution within a single pass counter-current HEX is calculated over time. A local crystallisation fouling model sensitive to processing and interface conditions is incorporated using the approach presented by Fryer and Slater (1985). More complex simulations such as the one reported by Coletti *et al.* (2010) could be used, if desired. Similarly, other types of fouling could be implemented (Fryer and Slater studied chemical reaction fouling by milk).

Fig. 3.7 shows a differential element of area of the HEX: $dA = A\delta x/L$. Enthalpy balances on the hot and cold streams yield the following constitutive partial differential equations for the (well-mixed) bulk fluid temperatures at axial position, x , and time, t' :

Hot side fluid $T_h(t', z)$:

$$\frac{\partial T_h}{\partial t'} = -\frac{UA v_h}{LW_h}(T_h - T_c) + v_h \frac{\partial T_h}{\partial x} \quad (3.38)$$

Cold side fluid $T_c(t', x)$:

$$\frac{\partial T_c}{\partial t'} = \frac{UA v_c}{LW_c}(T_h - T_c) - v_c \frac{\partial T_c}{\partial x} \quad (3.39)$$

Here, v_c and v_h are the local bulk fluid velocities. The local heat transfer coefficient, U , includes the film heat transfer coefficients, the wall and any fouling resistances. U varies with time and position.

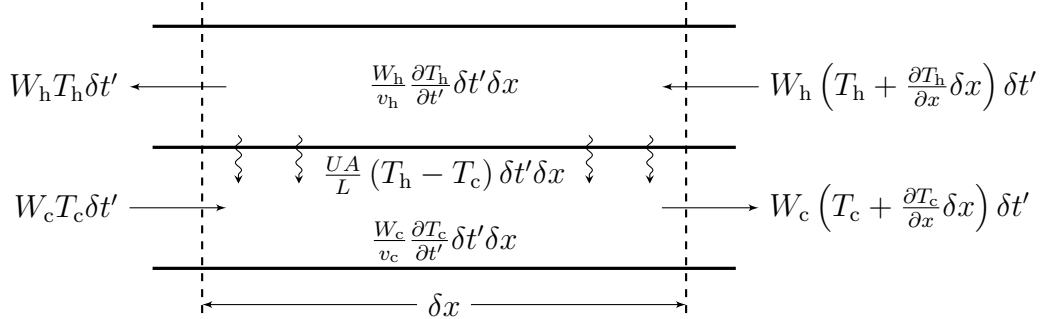


Figure 3.7: Elements of the enthalpy balance on either side of an increment of length for a counter-current heat exchanger (Fryer & Slater, 1985).

Both streams are aqueous. Water property variation with temperature is calculated from the VDI database (VDI, 2010). This approach allows the local deposit interface temperature and transport coefficients to be evaluated and changes with time accounted for.

3.3.2 Temperature and velocity dependent surface integration crystallisation fouling model

The cold stream is assumed to contain dissolved calcium carbonate which causes crystallization fouling. Solubility is a function of the conditions at the location of crystal formation, in particular the temperature (Bott, 1997). The effect of pH, pressure, and the presence of other chemical species is not considered here but could be included if desired. Assuming the solid phase to be calcite, the saturation concentration, C_{sat} (in kg m^{-3}), at the deposit-solution interface temperature, T_{IF} , is calculated using the correlation reported by Pääkkönen *et al.* (2015) (where T_{IF} is in $^{\circ}\text{C}$):

$$C_{\text{sat}} = -379.33 \cdot 10^{-10} T_{\text{IF}}^3 + 128.11 \cdot 10^{-7} T_{\text{IF}}^2 - 167.15 \cdot 10^{-5} T_{\text{IF}} + 122.11 \cdot 10^{-3} \quad (3.40)$$

Aragonite and vaterite have higher solubilities and are not expected to participate (Helal-zadeh *et al.*, 2000). The temperature distribution and flow conditions are assumed to favour surface integration controlled deposition (Bansal *et al.*, 2008; Bott, 1997). The integration step is a complex process, involving the physics of heterogeneous nucleation, chemistry of the solid-liquid interface and local thermo- and hydrodynamics (Pääkkönen

et al., 2015). Rather than modelling all these processes in detail, the rate of deposition into the foulant crystal lattice is calculated using

$$\frac{dm_f}{dt'} = k'_d \exp\left(\frac{-E_a}{RT_{IF}}\right) (C_{IF} - C_{sat})^j, \quad (3.41)$$

where k'_d is the deposition rate factor, E_a is the activation energy, R is the gas constant, C_{IF} is the concentration at the interface, and the reaction order is set to $j = 2$ (Bansal *et al.*, 2008; Helalizadeh *et al.*, 2000; Mwaba *et al.*, 2006; Pääkkönen *et al.*, 2015). If the integration step controls fouling, the concentration of species at the integration front, C_{IF} , is practically equal to the bulk concentration. The interface temperature is calculated using the cold stream film heat transfer coefficient, h_c , *via*

$$T_{IF} = \frac{U}{h_c}(T_h - T_c) + T_c. \quad (3.42)$$

The deposition rate factor, k'_d , is expected to be a function of local flow velocity or residence time. The sticking factor formulation suggested by Epstein (1994) is used: $k'_d = k_d \mu / (\rho v_*^2)$, where μ denotes the viscosity of the liquid and ρ is the liquid density evaluated at interface temperature. The friction velocity, v_* , is estimated using the Blasius correlation for simplicity (Bergman & Incropera, 2011):

$$v_* = \sqrt{\frac{\tau_{IF}}{\rho}} = v_c \sqrt{\frac{f_D}{8}} = v_c \sqrt{\frac{0.316}{8Re^{0.25}}}. \quad (3.43)$$

Here, τ_{IF} is the shear stress imposed on the fouling layer, f_D is the Darcy friction factor, and Re is the Reynolds number of the cold stream evaluated at the interface temperature. Incorporation of additional material into the deposit becomes more difficult as the crystal layer grows and long crystals are likely to be less robust against removal forces (Bott, 1997). A suppression term could be included to address this, but is neglected here.

The fouling layer is assumed to be homogeneous and fouling slowly, so that the bulk concentration of fouling precursors does not change with x . The local fouling resistance is calculated from

$$R_f = \frac{m_f}{\rho_f k_f}. \quad (3.44)$$

The local duct diameter changes as a result of layer growth (thickness $\delta_f = m_f/\rho_f$) so T_{IF} , v_* , C_{sat} and fluid properties vary with position and time. Hence the fouling rate and the fouling Biot number vary as $f(x, t')$.

3.3.3 Solution method

Fryer and Slater (1985) used the method of characteristics to convert the hyperbolic partial differential equations 3.38 and 3.39 into ordinary differential equations. The characteristic lines associated with the convectational enthalpy transport, with velocities v_c and

v_h , constrain the numerical integration to a distinct step size, which proves to be the largest satisfying the Courant-Friedrichs-Lewy criterion for the two stiff equations when using an explicit integration method (Press *et al.*, 1986). Fryer and Slater were interested in fast fouling, reaching an asymptote in about one hour. For slower fouling rates with a high spatial resolution, multistep methods such as those in Matlab[®] ‘ode15s’ are more efficient and are used here.

Equations 3.38 and 3.39 are integrated numerically over time. The spatial derivatives are approximated with a first order upwind scheme and finite Δx , giving for the hot stream

$$\frac{\partial}{\partial x} T_h(t', x) \approx \frac{T_h(t', x + \Delta x) - T_h(t', x)}{\Delta x} \quad (3.45)$$

and for the cold stream

$$\frac{\partial}{\partial x} T_c(t', x) \approx \frac{T_c(t', x + \Delta x) - T_c(t', x)}{\Delta x} . \quad (3.46)$$

This upwind scheme is preferred over central differencing schemes since advective enthalpy transfer dominates diffusive transfer and heat can only propagate in the direction of bulk flow. The continuous coordinates, t' and x , are discretized with a mesh of temporal, $n_{t'} = 1, 2 \dots N_{t'}$, and spatial, $n_x = 1, 2 \dots N_x$, nodes. N_x was set at 150, as larger values gave no appreciable increase in accuracy. The size of the time step is determined by ‘ode15s’.

Cleaning is assumed to remove all deposit. The initial temperatures of all nodes n_x at $n_{t'} = 0$ are set to the steady state profile for the clean exchanger, obtained by running an initial simulation without fouling, *i.e.* $dm_f/dt' = 0$. The temperatures converge rapidly to the clean distribution. This was verified by comparison with analytical results.

To define upwind derivatives at the inlet boundaries, $T_h(n_{t'}, N_x + 1)$ and $T_c(n_{t'}, 0)$ are set to zero. This is a computational measure as the unit operates with constant inlet temperatures. The boundary conditions

$$T_h(t', x) = T_{h,in} \quad x = L, \forall t' \quad (3.47a)$$

$$T_c(t', x) = T_{c,in} \quad x = 0, \forall t' \quad (3.47b)$$

are enforced by setting the numerical temporal derivatives at each inlet to zero, *i.e.*

$$\frac{\partial T_h(n_{t'}, N_x)}{\partial t'} = \frac{\partial T_c(n_{t'}, 0)}{\partial t'} = 0 . \quad (3.48)$$

3.3.4 Illustrative case study: evaluating crystallisation fouling performances of polymer coatings

Pääkkönen *et al.* (2015) studied scaling of CaCO_3 on a flat-plate AISI 316L stainless steel heat exchanger surface and measured initial mass deposition rates under transitional

and turbulent flow conditions. No induction period was observed and they reported that Equation 3.41 gave closest agreement with their data. The kinetic parameters, experimental conditions, and properties of the porous fouling layer are given in Table 3.5. The fouling model described above was verified against the results of Pääkkönen *et al.* (2015).

Table 3.5: Crystallisation fouling kinetic parameters, experimental conditions, and fouling layer properties (Pääkkönen *et al.*, 2015). $\pm 95\%$ confidence level.

Kinetic parameters		
k_d	Deposition rate factor	$1.62 \times 10^{20} \text{ m}^4 \text{ kg}^{-1} \text{ s}^{-2}$
E_a	Activation energy	$148\,000 \text{ J mol}^{-1}$
Operating conditions		
T_{IF}	Interface temperatures	59°C to 85°C
C_{IF}	CaCO_3 concentration	0.418 kg m^{-3}
D_h	Hydraulic diameter	0.03 m
v_c	Bulk velocities	0.18 m s^{-1} to 0.35 m s^{-1}
Re_c	Reynolds number	6000 to $12\,000$
Fouling layer properties		
ρ_f	Density	$1100 \pm 44 \text{ kg m}^{-3}$
k_f	Thermal conductivity	$0.97 \pm 0.10 \text{ W m}^{-1} \text{ K}^{-1}$

The value pricing of antifouling coatings is illustrated by comparing an uncoated SS and a polymer coated single-pass counter-current shell-and-tube HEX operating at constant flow rates and inlet temperatures. The coating introduces an additional thermal resistance to the overall heat transfer coefficient, which is evaluated using

$$U = (1/h_c + Bi_f/U_{cl} + \delta_{coat}/k_{coat} \log(r_h/r_c) + r_c/r_h h_h)^{-1}. \quad (3.49)$$

Baffles are not considered and the flow in the shell is assumed to be parallel to the tubes. The film heat transfer coefficients are estimated using the Gnielinski correlation with temperature dependent water properties and the appropriate hydraulic diameters (Bergman & Incropera, 2011),

$$Nu_m = \frac{(f_D/8)(Re - 1000)Pr}{1 + 12.7(f_D/8)^{1/2}(Pr^{2/3} - 1)} \quad 0.5 \lesssim Pr \lesssim 2000; \quad 3000 \lesssim Re \lesssim 5 \times 10^6, \quad (3.50)$$

where Pr is the Prandtl number and f_D is estimated with the Blasius correlation. As in the lumped model, the difference in U values means that the coated unit requires a

larger heat transfer area, calculated with Equation 3.37. For the uncoated unit, δ_{coat} is zero. The design and operating parameters of the two HEXs are summarised in Table 3.6. In practice, the several metres long HEX could be sectioned, *e.g.* into four manageable segments of around 2.5 m length.

Table 3.6: Design, operating and cost parameters of the coated and uncoated HEXs.

Design of the uncoated SS unit		
A	Heat transfer area	48.3 m ²
L	Length	10 m
–	Number of tubes	150
r_c	Inner tube radius	5.1 mm
r_h	Outer tube radius	6.4 mm
–	Tube pitch (hexagonal packing)	15.2 mm
–	Shell radius	103 mm
k_w	Tube thermal conductivity ³	16 W m ⁻¹ K ⁻¹
U_{cl}	Overall clean heat transfer coefficient	1199 W m ⁻² K ⁻¹
Q_{cl}	Clean heat duty	649 kW
Modified design of the coated unit		
k_{coat}	Coating thermal conductivity ³	0.1 W m ⁻¹ K ⁻¹
δ_{coat}	Coating thickness ³	10 μ m
A_{coat}	Heat transfer area	54.1 m ²
$U_{cl,coat}$	Overall clean heat transfer coefficient	1070 W m ⁻² K ⁻¹
Operation		
w_c, w_h	Cold and hot stream mass flow	4 kg s ⁻¹
$T_{h,in}$	Hot stream inlet temperature	90 °C
$T_{c,in}$	Cold stream inlet temperature	40 °C
C_c	CaCO ₃ concentration	0.418 kg m ⁻³
τ	Time taken for cleaning	3 d
v_c	Cold stream bulk velocity, uncoated	0.32 m s ⁻¹ to 3.15 m s ⁻¹
Re_c	Cold Reynolds number, uncoated	5070 to 23 000
Costs		
c_E	Cost per unit heat ³	5.7 US\$ GJ ⁻¹
C_{cl}	Cleaning cost per unit	2000 US\$
t_{lf}	Asset lifetime (depreciation)	5, 10, 15 year

³data taken from Gomes da Cruz *et al.* (2015)

Operating conditions were selected to be comparable to the conditions in the Pääkkönen *et al.* (2015) experiments. The fouling model Equation 3.41 is solved together with the enthalpy balances 3.38 and 3.39 in Matlab[®] on a desktop PC. As the fouling layer builds up, the increase in fluid velocities, caused by decreasing duct diameter, reduces the fouling rate significantly.

3.3.5 Results and Discussion

Figure 3.8 shows the temperature distribution in the uncoated exchanger at different times. The change in temperatures of both streams across the exchanger becomes smaller with time owing to fouling. There is little change in the cold stream temperature distribution near its inlet as there is less deposition here since the level of supersaturation, which drives crystallisation (Equation 3.41), is smaller. In the second half of the exchanger there is noticeable change over time as this is where fouling, driven by bulk temperature and saturation, is highest for the inverse solubility salt.

Fig. 3.9 shows the distribution of deposit in the uncoated exchanger at different times, expressed as the local fouling Biot number. Driven by bulk temperature and saturation, the Biot number at the hot end exceeds unity at extended time, indicating a significant change in U . The fouling layer formation kinetics are not trivial as a result of the dynamic interdependency between heat transfer and temperature sensitivities in the fouling model.

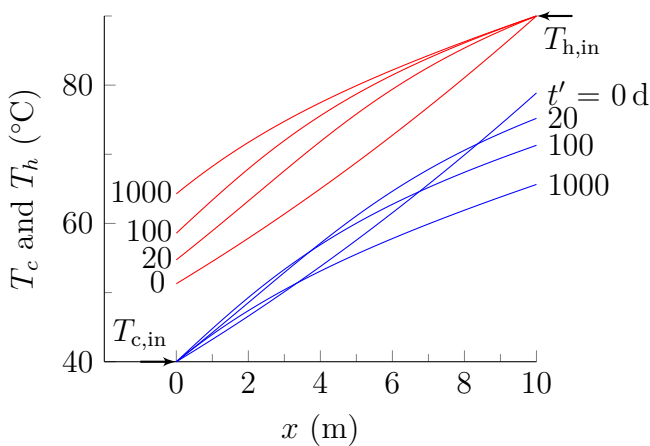


Figure 3.8: Hot stream (red lines) and cold stream (blue lines) bulk temperature distribution along the uncoated HEX at selected times, t' .

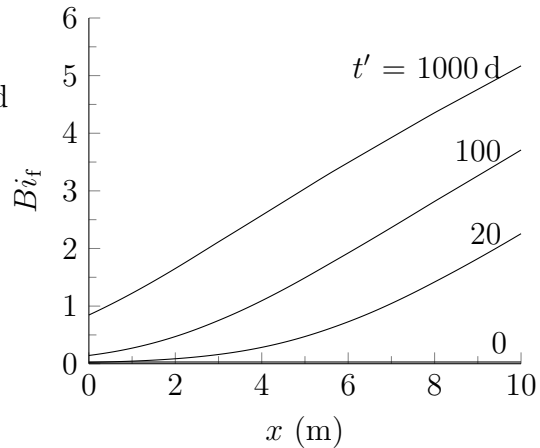


Figure 3.9: Fouling Biot number distribution in uncoated HEX at selected times, t' .

There is a noticeable transition from convex to slightly concave fouling distributions

over time, and autoretardation at the hot end. As the fouling layer grows, interface temperatures decrease. Duct narrowing causes the flow velocity to increase, resulting in a lower fouling rate.

Ishiyama *et al.* (2008) presented a technique to calculate the mean fouling rates in co- and counter-current HEXs assuming a linear change in temperature across the unit. They also assumed that the fouling layer thickness does not vary considerably over the tube length: fouling rates thus tended to increase monotonically across the unit. Figure 3.9 shows that their approach would not be applicable to this case. The fouling distribution is non-linear, resulting in an increasingly non-linear temperature distribution over time. The fouling distribution shows evidence of strong variations in local fouling rate, generated by different sensitivities to interface temperature in the Arrhenius rate constant and the solubility in Equation 3.41. After long periods of time, it has to be expected that the interface temperature, and hence the fouling layer thickness, becomes more and more uniform.

The effect of fouling on the overall fouling resistance for the uncoated unit is presented in Figure 3.10. The overall trend could be described as falling rate fouling and arises from two autoretardation mechanisms, namely decreasing interface temperatures and changes in sticking factor. This will be accompanied by an increase in cold stream pressure drop. Asymptotic fouling behaviour, such as reported by Zhao *et al.* (2002) for CaSO_4 fouling on a stainless steel surface, would require a suppression or removal term.

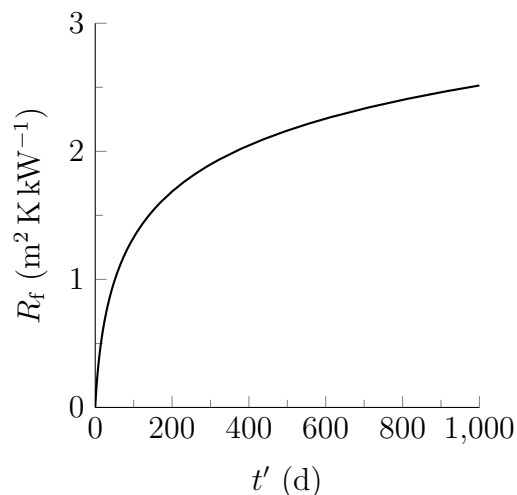


Figure 3.10: Evolution of the overall fouling resistance, R_f , of the uncoated unit over the processing time, t' .

The impact of fouling on the financial performance is plotted in Fig. 3.11. The optimal processing period, t_{opt} , is reached after 54 d, 144 d or 126 d of processing, depending on

whether cleaning scheduling is optimised for maximum average heat duty, time averaged operating cost or operating cost per unit heat transferred. The substantial differences in optimal processing periods indicate that cleaning is costly compared to the cost of thermal losses due to fouling.

At $t_{opt} = 144$ d, the overall fouling resistance is $1.5 \text{ m}^2 \text{ K kW}^{-1}$, which corresponds to a mean fouling layer thickness of $\delta_f \approx R_f k_f = 1.46$ mm. This is significant compared to the tube radius of 5.1 mm, such that approximating the fouling layer as a thin slab is not accurate. If deposits of this thickness were encountered regularly, the assumptions in deriving Eq. 3.49 would need to be revised.

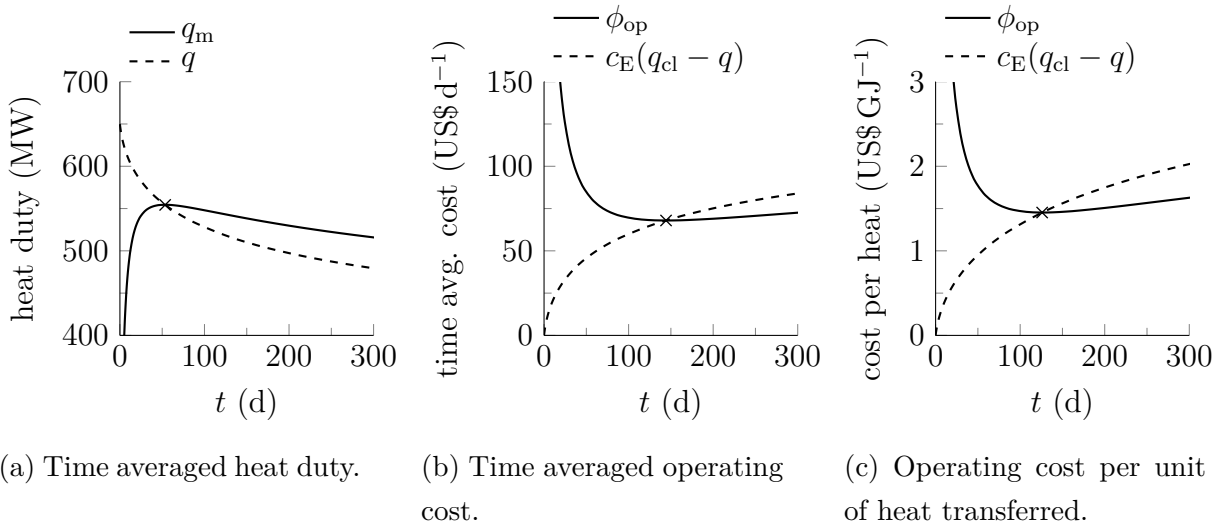


Figure 3.11: Effect of processing period length on (a) time averaged heat duty, (b) time averaged operating cost, and (c) operating cost per heat transferred for uncoated stainless steel HEXs in dynamic model case study. Crosses – optimal processing periods.

3.3.6 Effect of antifouling performance on coating value

Pääkkönen *et al.* (2015) only studied calcite deposition on SS, so the antifouling performance of a series of fictitious coatings is examined here in a sensitivity analysis. The parameters of the fouling model are varied to represent improved fouling characteristics:

- (i) Geddert *et al.* (2009) looked at fouling on modified surfaces at higher Reynolds numbers and reported that the deposition rate constant was smaller for surface modifications with antifouling properties. This is investigated by specifying the ratio of deposition rate constants, in the range 0.1 (good antifouling) $\leq k_{d,coat}/k_d \leq 1$ (no benefit).

- (ii) Mayer, Augustin, and Scholl (2012) found that antifouling surfaces exhibited lower adhesion forces between CaCO_3 crystals and surfaces, which is likely to facilitate cleaning. This would, primarily reduce the time taken for cleaning, τ , and is investigated for $0.1 \leq \tau_{\text{coat}}/\tau \leq 1$. An effect on cleaning cost is not studied here.

A coating providing fewer nucleation sites and with surface energy hindering heterogeneous nucleation is expected to promote longer induction periods at low flow velocities. However, reliable prediction of induction periods is difficult and is not considered here (see Gomes da Cruz *et al.* (2015), for examples). Since the crystallisation mechanism is unaffected by the coating after an initial crystal layer is formed, the activation energy, E_a , is unlikely to be affected.

The coated heat exchanger is presumed to be operated for the optimum processing period to minimise the time averaged operating costs, then cleaned. Figure 3.12 shows the effect of different levels of coating performance (deposition rate and cleaning time) on the dimensionless optimal operating cost, calculated by reference to the performance of the uncoated exchanger in Figure 3.11b. In general, a decrease in time required for cleaning has a limited effect on the operating cost as the operating periods are very long: this is evident from Equation 3.15b if τ is small compared to t_{opt} . A reduction in deposition rate constant gives an appreciable difference in operating cost. This provides guidance for the development of coatings, since innovations in other contexts often show a diminishing marginal benefit. In this case the induction period would have to be long in order to influence ϕ_{op} significantly.

Not shown in Figure 3.12 is the associated value of t_{opt} , which will be longer than 144 d. This also constitutes important guidance as the coating must maintain its integrity (*e.g.* not spall off) and performance over the extended period if it is to be considered for use in practice. Alternatively, these calculations can provide indications of the minimum life expectancy required of such coatings.

Capital costs are now considered. A coated exchanger could be considered to replace an existing unit, in a revamp or retrofit, or as an alternative to an uncoated unit for a new plant. The latter, the greenfield scenario, is considered here. The capital cost of the base unit, C_{base} , is calculated as in section 3.2.6. Other depreciation policies could be considered, depending on the accounting practice to be used. The total optimised annualised cost is then $\phi = \phi_{\text{base}} + \phi_{\text{op,opt}}$.

According to Hewitt and Pugh (2007), a 48.3 m^2 CS BEM type HEX (TEMA, 1999) cost approximately 150 £ m^{-2} in 1994. Conversion into US\$ and updating it with the chemical engineering plant index of 2017 yields an installed cost of $341 \text{ US\$ m}^{-2}$ for a

CS unit and roughly $682 \text{ US\$ m}^{-2}$ for a SS unit. Taking this cost as an estimate and assuming a 10 year asset lifetime, the amortised capital costs of the base units are $\phi_{\text{cap}} = 9.02 \text{ US\$ d}^{-1}$ for the uncoated SS unit and $\phi_{\text{cap,coat}} = 10.11 \text{ US\$ d}^{-1}$ for the slightly larger coated SS unit, before coating costs are added. Given that ϕ_{op} is $68 \text{ US\$ d}^{-1}$ for the uncoated unit, the contribution from capital expenditure is modest: the techno-economic analysis suggests that the heat transfer penalty due to the low thermal conductivity of the coating is negligible in comparison to the potential savings when processing streams prone to serious fouling. The maximum price for coating such an exchanger can be calculated from

$$c_{\text{coat,max,new}} = (\phi - \phi_{\text{coat}})t_{\text{lf}}/A_{\text{coat}} \quad . \quad (3.51)$$

Figure 3.13 shows a map of potential value prices calculated for the cases in Figure 3.12. Neither inflation nor the time value of money are considered here, but could be introduced to calculate the net present value.

The strong effect of asset lifetime, t_{lf} , is evident in the results in Figure 3.13. In practice, the asset lifetime is likely to be limited by the coating's durability. Assuming the coating is stable and retains its effectiveness, it creates maximum value if it prevents fouling completely. If this most promising result would apply to the current case, the coating value would be greater than $1200 \text{ US\$ m}^{-2}$ to $4000 \text{ US\$ m}^{-2}$, depending on t_{lf} . Provided the coating is stable and impermeable for the whole time in service, a FP coated carbon steel unit could be considered as described in section 3.2.6.

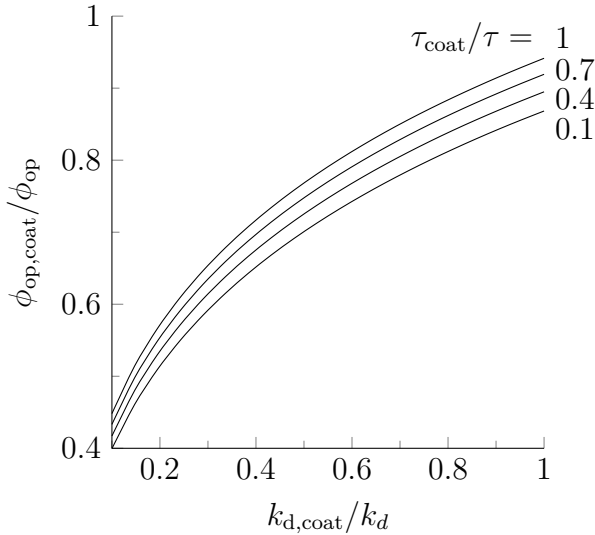


Figure 3.12: Effect of non-dimensional antifouling coating performance on the ratio of optimal operating cost to that of the uncoated exchanger.

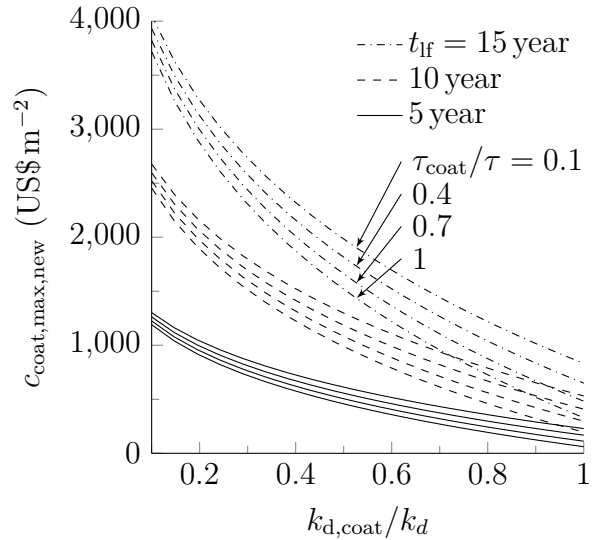


Figure 3.13: Value prices of coatings for different ratios of deposition rates, three asset lifetimes, and four dimensionless cleaning period lengths.

3.4 Summary

Two models were developed to assess the attractiveness of antifouling coatings. In the first modelling part, a lumped heat transfer model was used to assess the attractiveness of using coatings to mitigate fouling. Besides linear fouling, the case of asymptotic fouling has been investigated over a fouling and cleaning cycle and an approximate result has been identified, which yields solutions comparable to those obtained by numerical methods. The ‘value pricing’ concept was demonstrated for a case study on water scaling where fouling data were taken from a recent study on PFPE coatings. A sensitivity analysis was applied to a simple HEX model: this identified attractive regions for further investigation and scenarios where cleaning is not needed.

In the second modelling part, the enthalpy balances of a pure counter-current HEX were solved together with a fouling model to predict the heat duty and fouling dynamics in a simple HEX subject to crystallisation fouling. The HEX model was able to demonstrate non-linear fouling dynamics arising from different temperature and flow velocity dependencies in crystallisation fouling. A methodology for assessing the economic value of specific coatings was demonstrated for various combinations of antifouling effectiveness. In the case study considered, the low thermal conductivity of the polymer coating had negligible effect compared to the potential gain from fouling mitigation. A shorter cleaning period had a substantial, but limited effect on the operating cost compared to the thermal savings when reducing the deposition rate factor. This finding has direct impact on potential applications to be considered. HEXs processing foodstuffs like milk, tend to have shorter processing periods than HEXs exclusively subject to crystallisation fouling. Equations 3.5a-c suggest that the effect of cleaning time on operating cost is stronger if the processing period is shorter. This is a strong motivation to improve cleaning of foodstuffs with antifouling materials to reduce operating cost of HEXs.

There are several unknowns in the case studies which have been estimated or have been taken from literature. Data from characterisation of coating properties and fouling tests are gathered in the next chapters and these will improve the quality of the techno-economic assessment.

Chapter 4

Surface characterisation

4.1 Coating and substrate materials

Square 5×5 cm substrate plates were laser cut from 2mm thick 304 SS (material EN 1.4301 304, surface finish EN 10088-2 2R, supplier Mill Stainless Stockholders Ltd). SS was employed as a reference material typically used for plate heat exchangers in the food industry (Bylund, 2015). Chemours applied FP coatings on some of these plates with topcoats made from PFA, FEP and PTFE. The FPs were applied as dry powders (PFA-2, PFA-4) or as water-based suspensions (PFA-3, FEP-2, FEP-3, PTFE-2) which were sintered subsequently. In contrast, sample PTFE-1 is an epoxy resin with dispersed PTFE particles. Five of each coating sample were received. To widen the spectrum of materials studied towards a higher energy apolar surface, polypropylene (PP) film (West Design Products) was bonded to some SS plates with a two component epoxy glue (Araldite Standard).

The identification and determination of surface properties is important in attributing the results of fouling experiments to material characteristics. Geddert *et al.* (2009) highlighted important surface factors in the context of crystallisation fouling: surface energy, roughness, topography, and nucleation sites. The FPs studied do not have functional groups which may take part in chemical reactions with the foulant, but are of considerable thickness and add an additional heat transfer resistance.

4.2 Coating thickness, thermal resistance and surface topography

Relevant properties of the surfaces investigated are summarised in Table 4.1. The coating thickness, δ_{coat} , was measured at five points by micrometer, as the difference between the thickness of the coated plate and the plate after the coating had been scraped off. The coating heat transfer resistance, R_{coat} , was calculated analogous to Equation 3.1 as the the difference in reciprocal clean overall heat transfer coefficients, measured in the

microfluidic HEX, for coated and uncoated plates (apparatus discussed later). The mean thermal conductivity of the coating is given by $k_{\text{coat}} = \delta_{\text{coat}}/R_{\text{coat}}$.

The surface topography was scanned at five positions on each sample plate with a Zygo NewView 200 interferometer. The surface profile data were filtered with a 5×5 median filter and outliers (some points had erroneously large values) were interpolated with a triangulation-based linear approach. Typical topography plots for each surface are shown in Figure 4.1. The SS surface (Figure 4.1a) features fine striations associated with machining and polishing. On the other hand, PP (b) is very smooth on the small-scale but features a larger-scale waviness due to the imperfect distribution of epoxy glue underneath. The sintered particles from the dry powder manufacturing process are clearly visible on PFA-2 (c) and PFA-4 (e) and give the surfaces a grainy appearance, whereas the structures on PFA-3 (d) have a plate like appearance. The FEPs (f,g) have levelled out more during the sintering process and are smoother than the PFAs on the small-scale. The dispersed PTFE particles in PTFE-1 (h) stand out from the epoxy matrix and are apparent as red dots with a diameter of about $80 \mu\text{m}$. By far the roughest coating is PTFE-2 (i) with a peak-to-valley height of $\sim 16 \mu\text{m}$.

Table 4.1: Characteristics of the surfaces studied. Coating thickness, δ_{coat} , thermal resistance, R_{coat} , thermal conductivity, $k_{\text{coat}} = \delta_{\text{coat}}/R_{\text{coat}}$, and the arithmetic mean and root mean square roughness, S_a and S_q , respectively. \pm indicates standard deviation. Colours in the first column are labels to identify surfaces in other figures throughout this document.

Surface	δ_{coat} (μm)	R_{coat} ($\text{m}^2 \text{K kW}^{-1}$)	k_{coat} ($\text{W m}^{-1} \text{K}^{-1}$)	S_a (nm)	S_q (nm)
SS	–	–	–	40 ± 3	50 ± 4
PP	31.8 ± 7.3	0.300 ± 0.032	0.106 ± 0.027	154 ± 33	190 ± 43
PFA-2	102.0 ± 8.2	0.374 ± 0.045	0.273 ± 0.039	494 ± 47	617 ± 58
PFA-3	71.2 ± 3.5	0.268 ± 0.037	0.266 ± 0.039	556 ± 67	698 ± 79
PFA-4	44.6 ± 6.7	0.362 ± 0.033	0.123 ± 0.021	459 ± 79	574 ± 100
FEP-2	57.8 ± 3.3	0.396 ± 0.052	0.146 ± 0.021	381 ± 78	482 ± 92
FEP-3	54.4 ± 4.8	0.351 ± 0.024	0.155 ± 0.017	216 ± 35	269 ± 44
PTFE-1	41.8 ± 3.4	0.336 ± 0.048	0.124 ± 0.021	741 ± 73	956 ± 108
PTFE-2	34.6 ± 3.7	0.218 ± 0.036	0.159 ± 0.031	2286 ± 308	2814 ± 294

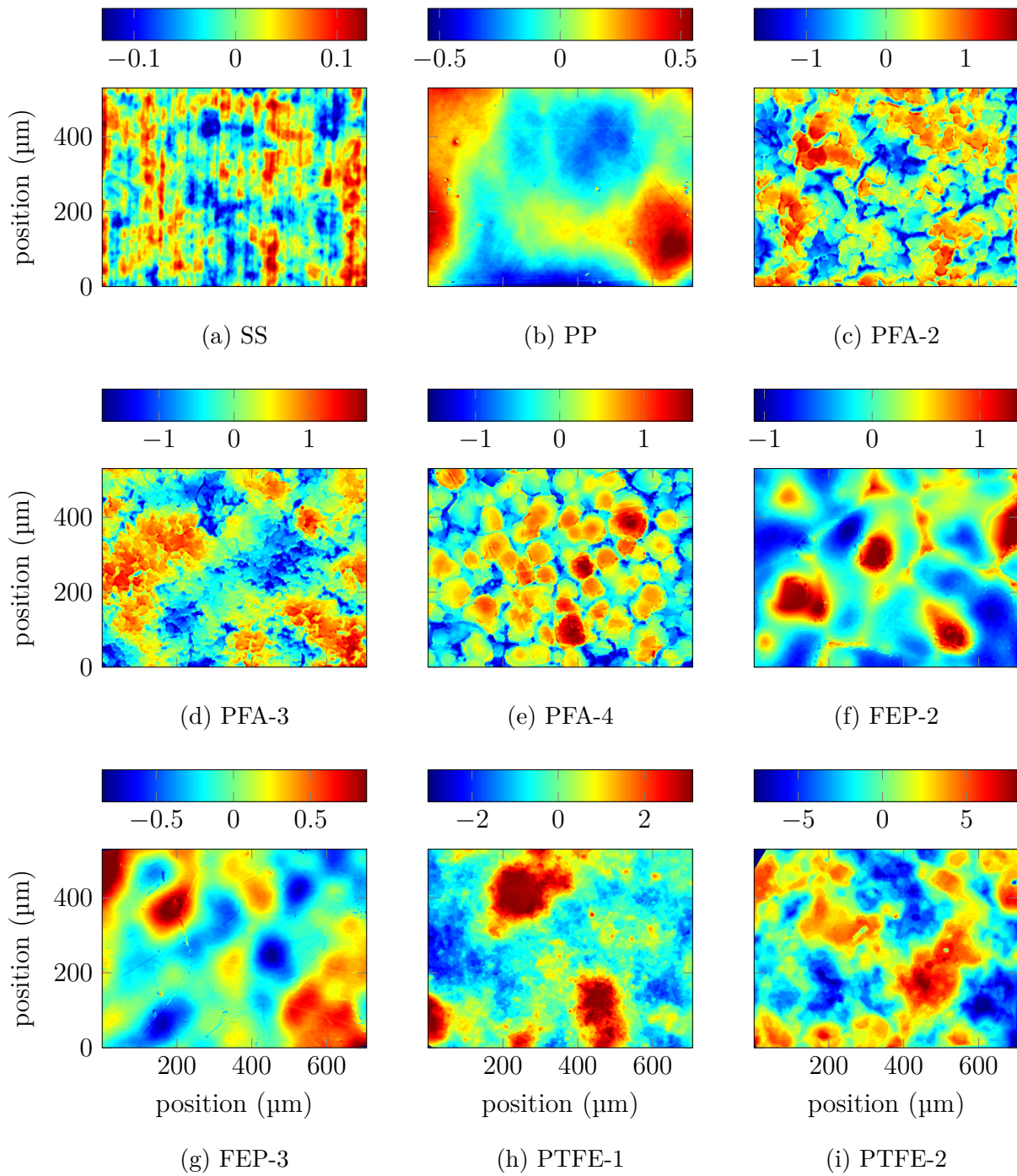
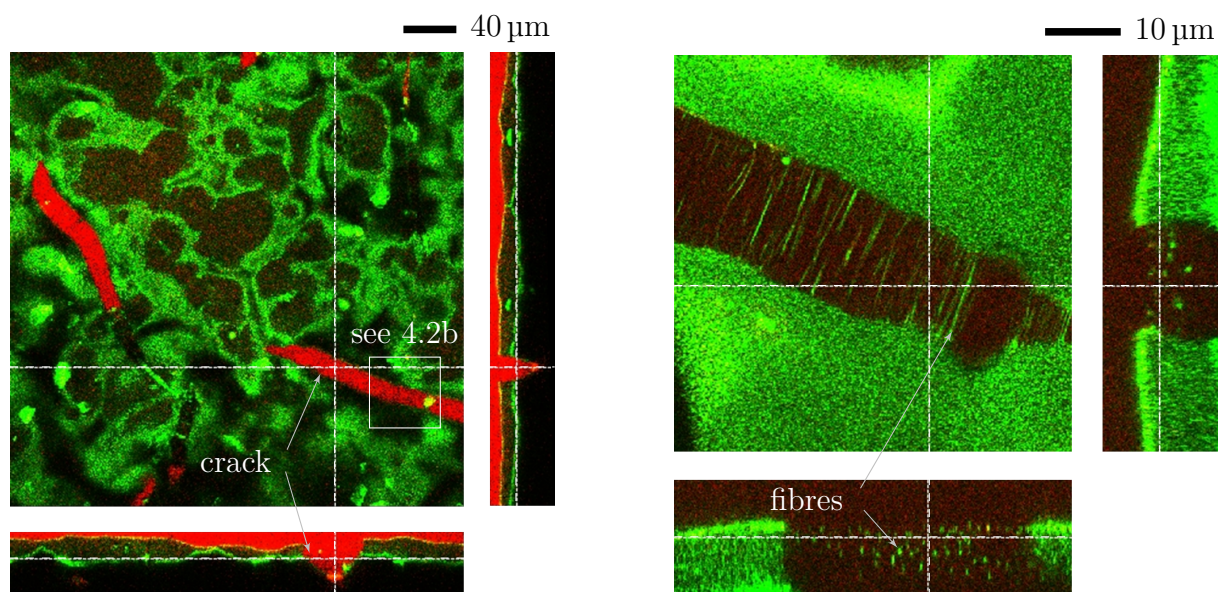


Figure 4.1: Filtered and interpolated surface topographies. Height scales are in micrometres and differ between figures.

The arithmetic mean roughness, S_a , and root mean square roughness, S_q , were calculated from these data and the results are summarised in Table 4.1. The areas used to calculate S_a and S_q were $530 \times 705 \mu\text{m}$ in size. Standard deviations were calculated on the basis of analysing five 2D-profiles separately. To identify surfaces in figures conveniently

throughout this document, a colour scheme is introduced in the first column of Table 4.1.

PTFE-2 was examined on a Leica SP5 CLSM with a $40\times$ oil immersion lens and $0.1\% \text{ g g}^{-1}$ oil red O in dodecane (both Sigma Aldrich) applied underneath a microscope cover slip. Dodecane has a low surface tension and ingressed into cracks generated during sintering of the coating. Excitation of oil red O with an argon laser at 514 nm highlighted fibrous structures in numerous cracks (see Figure 4.2). With these structures impeding cleanability, PTFE-2 was not considered for further tests.



(a) Overview

(b) Detail with visible fibres.

Figure 4.2: CLSM images of PTFE-2 surface infused with dodecane containing $0.1\% \text{ g g}^{-1}$ oil red O. Large images are top-views and narrow images are orthogonal sections. Red channel – oil red O; Green channel – reflection

4.3 Surface energy

The dispersive, electron donor, and electron acceptor surface energy components were determined by non-linear regression of Equation 2.9 using measured equilibrium contact angles with the test liquids listed in Table 4.2. Contact angle measurements were repeated 12 times using a goniometer (Dataphysics OCA-15).

Sets of three liquids were selected for each regression. For most surfaces, reverse osmosis water (H_2O), ethylene glycol ($\text{C}_2\text{H}_6\text{O}_2$), and dodecane ($\text{C}_{12}\text{H}_{26}$) were used. Ethylene gly-

col was preferred over formamide (CH_3NO) for contact angle regression analysis because its polarity differs more from water, dodecane, and diiodomethane. SS and PP feature high γ_{LW} values, so diiodomethane (CH_2I_2) was employed instead of dodecane to obtain reasonably large contact angles.

The surface energies of some important species involved in milk fouling were also characterised or reproduced from the literature: β -lactoglobulin (β -LG), milk fat globule (MFG), dicalcium phosphate dihydrate (DCPD), octacalcium phosphate (OCP) and hydroxyapatite (HAP). A thin film of denatured and polymerised β -LG (Sigma Aldrich, purity $\geq 90\%$, variant A and B) was generated by wetting a SS sample with a 1 g l^{-1} solution in reverse osmosis water and subsequent air drying for 20 min in an oven at 90°C . Contact angles of test liquids with the β -LG layer were determined by taking videos with a camera attached to the goniometer to capture the instant before the layer started to wick the sessile drops noticeably. Surface energy components of bovine MFGs and calcium phosphates were measured by Kiely and Olson (2003) and Wu and Nancollas (1998), respectively.

Table 4.2: Advancing contact angles, β , measured at 20 °C and surface energy components calculated with the van Oss *et al.* (1987) approach. Liquid parameters were taken from van Oss *et al.* (1992). Contact angles in grey were not used for surface energy determination. Angles reported to one decimal place. H₂O – water; CH₃NO – formamide; C₂H₆O₂ – ethylene glycol; C₁₂H₂₆ – dodecane; CH₂I₂ – diiodomethane; CW – complete wetting; ND – not determined; \pm standard deviation.

Liquid:	H ₂ O	CH ₃ NO	C ₂ H ₆ O ₂	C ₁₂ H ₂₆	CH ₂ I ₂			
γ^{LW} (mJ m ⁻²)	21.8	39.0	29.0	25.35	50.8			
γ^+ (mJ m ⁻²)	25.5	2.28	1.92	0	0			
γ^- (mJ m ⁻²)	25.5	39.6	47.0	0	0			
Surface	Contact angle (°)				Surface energy (mJ m ⁻²)			
	β				γ^{LW}	γ^+	γ^-	
SS	57.1 \pm 2.5	61.5 \pm 7.3	53.0 \pm 2.1	5.2 \pm 1.5	52.3 \pm 1.4	32.3 \pm 0.7	8.7 \pm 6.0 $\times 10^{-4}$	32.6 \pm 1.7
PP	103.5 \pm 1.1	87.5 \pm 3.6	75.6 \pm 1.9	CW	60.1 \pm 2.2	28.5 \pm 0.5	49 \pm 10 $\times 10^{-4}$	0.26 \pm 0.11
PFA-2	110.3 \pm 2.3	90.4 \pm 2.3	94.7 \pm 0.8	43.0 \pm 1.0	ND	16.1 \pm 1.2	2.3 \pm 5.4 $\times 10^{-4}$	0.53 \pm 0.33
PFA-3	108.2 \pm 2.5	92.8 \pm 4.4	91.8 \pm 1.8	44.6 \pm 1.5	ND	16.9 \pm 1.0	8.2 \pm 8.1 $\times 10^{-4}$	0.93 \pm 0.35
PFA-4	108.0 \pm 1.2	89.1 \pm 2.3	89.1 \pm 4.7	46.2 \pm 1.1	ND	18.0 \pm 0.9	4.6 \pm 5.6 $\times 10^{-4}$	1.0 \pm 0.3
FEP-2	108.4 \pm 1.4	92.9 \pm 5.0	92.6 \pm 1.6	41.6 \pm 4.2	ND	16.9 \pm 1.0	8.6 \pm 9.1 $\times 10^{-4}$	0.76 \pm 0.35
FEP-3	108.1 \pm 0.6	94.9 \pm 2.3	92.3 \pm 3.2	47.5 \pm 1.1	ND	16.3 \pm 0.8	8.5 \pm 7.2 $\times 10^{-4}$	1.1 \pm 0.3
PTFE-1	81.1 \pm 4.4	70.1 \pm 3.4	65.7 \pm 3.6	19.3 \pm 9.2	ND	23.8 \pm 1.5	0.18 \pm 0.16	11.5 \pm 1.7
PTFE-2	106.9 \pm 5.9	96.3 \pm 2.5	96.3 \pm 3.7	38.1 \pm 3.3	ND	16.9 \pm 2.2	$\approx 0 \pm 13 \times 10^{-4}$	1.4 \pm 1.0
β -LG	82.1 \pm 2.2	67.1 \pm 1.5	57.5 \pm 1.9	CW	44.0 \pm 1.8	36.1 \pm 0.9	6 \pm 50 $\times 10^{-4}$	6.1 \pm 0.8
MFG ¹						36.09	0.04	36.94
DCPD ²						26.4	1.6	31.7
OCP ²						21.6	2.2	19.7
HAP ²						36.2	0.9	16.0

¹ data from Kiely and Olson (2003); ² data from Wu and Nancollas (1998)

The surface energy of all materials involved is expected to decrease with increasing temperature. The surface tension of water reduces approximately with a rate of $-0.17 \text{ mJ m}^{-2} \text{ K}^{-1}$ (Vargaftik *et al.*, 1983), whereas the surface energy of low surface energy polymers reduces by around $-0.066 \text{ mJ m}^{-2} \text{ K}^{-1}$ (Shafrin & Zisman, 1972). At 90°C the surface energies of water and FPs are therefore reduced by about 18% and 24%, respectively. Measuring the surface energy at ambient temperature to explain phenomena taking place at elevated temperature is a common approximation in the field (Barish & Goddard, 2013; Boxler *et al.*, 2013c; Mauermann *et al.*, 2009; Rosmaninho & Melo, 2006).

With the exception of the calcium phosphates, all the solids in this study can be considered monopolar because their electron acceptor contribution to surface energy is smaller than 1 mJ m^{-2} (van Oss *et al.*, 1987). The dominant Lifshitz-van der Waals and electron donor contributions for the above materials are plotted in Figure 4.3. The oxide layer on SS and the MFG membrane are highest in surface energy and are most polar, followed by β -LG and PTFE-1 which also displays significant polarity, presumably due to the epoxy matrix (Bergslien, Fountain, & Giese, 2004). In contrast to the pure FPs, PP is apolar but has a high Lifshitz-van der Waals interaction parameter.

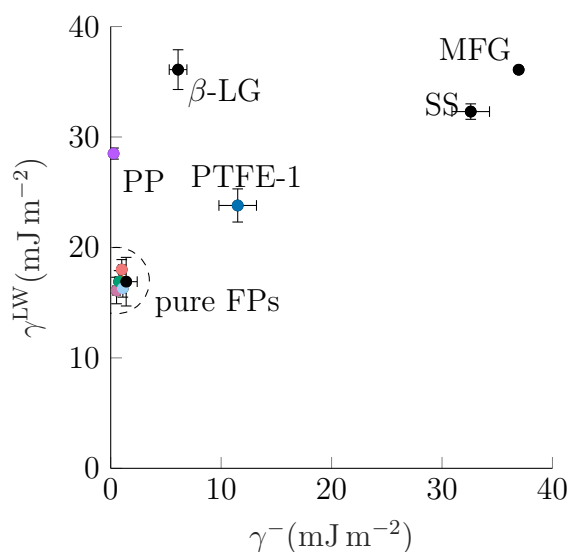


Figure 4.3: Apolar, γ^{LW} , and electron donor, γ^- , contributions to surface energy. Data (no uncertainty provided) for MFG reported by Kiely and Olson (2003). Error bars show standard deviation.

Chapter 5

Milk fouling studies

5.1 Introduction

This chapter reports the development and use of two laboratory HEX systems to investigate fouling from milk products on different surfaces. The motives of this work were to (i) measure the performance of FP coatings and SS to provide data for the techno-economic assessment of FP based antifouling coatings in dairy applications, and (ii) to study the effect of surface properties on the composition and structure of milk fouling deposits.

A microfluidic HEX apparatus with a rectangular flow channel with dimensions 2 mm wide and 0.65 mm high, operating in the laminar flow regime, was designed and used to probe the local composition of delicate raw milk fouling deposit *in-situ* with histology techniques employing CLSM. The purpose of this rig is to serve as a tool for testing various surfaces by using a limited amount of resources and allowing easy optical access. The evolution of pressure drop and final deposit mass were used as indicators of fouling performance because they were more sensitive to fouling than thermal data. In this case the unit processes two litres of ‘real’ raw milk in a once-through flow scheme, thereby addressing Mérian and Goddard (2012)’s criticism of antifouling testing using simple formulations which do not represent the complexity of real foodstuffs.

A larger bench-scale HEX rig based around a rectangular flow channel with dimensions 42 mm wide and 10 mm high, operating in the turbulent flow regime, was designed and built to approximate conditions at the hot end of a HTST pasteuriser or in the regenerative heating section of a UHT steriliser. Fouling resistance time series and final deposit mass were used as indicators of fouling performance in this unit. It was not feasible to run in once-through mode so 17 l of pressurised WP solution or raw milk were recirculated through the unit. This rig bridges the gap from laboratory- to industrial-scale.

All fouling experiments were performed under constant heat-flux conditions, *i.e.* electrically heated with fixed power rating. Assuming the fouling layer to be thin and not affecting the film heat transfer coefficient, this mode of operation has the advantage that the surface temperature is independent of the thermal resistance of the sample, coating and fouling layer. The microfluidic and bench scale HEXs were primarily designed and built by the author. The metal parts of the bench-scale HEX flow channel were ma-

chined to the authors specifications by Gautrey Engineering, Cottenham, UK and mains electrical wiring was executed by the CEB electronics technicians.

5.2 Materials

5.2.1 Raw milk

Raw milk was sourced from the University of Cambridge's Park Farm Holstein-Friesian herd and used on the same day. The milk was taken from a tank which received milk from more than 100 animals. The cows were fed a diet optimised for milk yield including grass, maize and grass silage, malt residue, potatoes, rumen protected fats, and other supplements. The pH of the raw milk as received at 6 °C was 6.70 ± 0.24 . Composition of a milk sample and typical raw milk compositional data taken from the literature are summarised in Table 5.1. The data lie within typical ranges reported in the literature, except for the casein and β -LG content (shown in grey). The data from protein specific enzyme-linked immunosorbent assay (ELISA) tests are not considered trustworthy as they contradict other experimental and literature data. Sample preparation for ELISA tests necessitated 500 to 78 000 fold dilution which may have introduced errors. Another source of error may have been aggregates concealing a fraction of the protein from the test.

Table 5.1: Composition of raw milk sample (Aug. 2017) and typical raw milk composition reported in the literature.

Constituent	Fraction (% g g ⁻¹)	Method of Analysis	Typical fraction (% g g ⁻¹)
Fat	3.8	NMR ¹	3.9 ² , 2.5 to 5.5 ³
Protein	3.1	Kjeldahl (N \times 6.25) ¹	3.4 ² , 2.3 to 4.4 ³
Casein	0.862 \pm 0.087	ELISA ^{1,4}	2.6 ² , 1.7 to 3.5 ³
β -LG	0.134 \pm 0.018	ELISA ^{1,5}	0.32 ^{2,3}
Ash	0.8	Ashing ^{1,6}	0.8 ² , 0.57 to 0.83 ³
Calcium	0.096	ICP-MS ⁷	
Calcium	0.104	ICP-OES ¹	0.124 ³

¹Determined by Premier Analytical Services, 76 Lincoln Rd, High Wycombe HP12 3QS, UK

²Data from Bansal and Chen (2006)

³Data from Walstra *et al.* (2005)

⁴Ridascreen FAST Casein ELISA kit (R4612), \pm standard deviation of three repetitions

⁵Romer AgraQuant β -LG ELISA kit (COKAL1048), \pm standard deviation of three repetitions

⁶Incineration in muffle furnace at 500 °C for 7 h

⁷Determined at the Department of Earth Sciences, Cambridge, UK

The calcium content was determined by inductively coupled plasma mass spectroscopy (ICP-MS) and ICP-OES which yielded similar results, both of which were comparable with literature values. For heat transfer calculations, the thermophysical data of raw milk were approximated as those of water (VDI, 2010) apart from the viscosity, which was taken from Fernández-Martín (1972b) for milk with 0.1 g g^{-1} total solids content (*e.g.* 0.75 mPa s at 60°C).

For experiments with the microfluidic HEX (Nov. 2016 to Mar. 2017) 2l of unmodified milk were degassed for 45 min at 20 kPa (absolute) in an ultrasonic bath at 56°C , *i.e.* just below its boiling point. After heating to 56°C , the pH dropped to 6.30 ± 0.06 , and increased slightly during degassing. CLSM micrographs of the milk presented in Appendix B indicate no visible effect of the procedure on the MFGs. In some cases, rapeseed oil or molten clarified butter was pumped through the microfluidic HEX to deposit a thin triglyceride (TG) film. The fat was added because it was suspected that apolar surfaces would interact differently with it than SS. Some composition data for the rapeseed oil and clarified butter are given in Table 5.2.

For experiments with the bench-scale HEX (Aug. 2017), 17l of unmodified milk were heated to 61°C under gentle stirring in the experimental rig's reservoir over 90 min. After heating the pH dropped to 6.59 ± 0.04 .

5.2.2 Whey protein solution

WP solution was used for the majority of fouling experiments with the bench-scale HEX. Hiprotal WP 35 concentrate (composition given in Table 5.3 and thermogravimetric analysis shown in Appendix A) was provided by FrieslandCampina, Amersfoort, NL, and dissolved in deionised water at 60°C to make 17l solution with a concentration of 18.2 g l^{-1} . This gives a whey protein fraction of 6.2 g l^{-1} which is typical for raw milk (Walstra *et al.*, 2005). The thermophysical properties of WP solution were approximated as those of water (VDI, 2010). For some experiments 900 ml WP solution from the 17l was replaced by single cream to give 10 g l^{-1} fat from cream and a total fat content of 10.46 g l^{-1} . This low concentration was chosen to keep the thermophysical properties relevant for flow behaviour and heat transfer close to the original properties of the WP solution. Some composition data for the single cream are given in Table 5.2.

Table 5.2: Composition of rapeseed oil (Sainsbury's SO organic rapeseed oil), clarified butter (East End pure butter ghee) and single cream (Sainbury's fresh single cream) according to packaging information.

Constituent	Rapeseed Oil	Clarified Butter	Single Cream
Fat	917 g l ⁻¹	998 g kg ⁻¹	190 g l ⁻¹
of which saturates	61 g l ⁻¹	670 g kg ⁻¹	120 g l ⁻¹
of which mono-unsaturates	544 g l ⁻¹		
of which polyunsaturates	269 g l ⁻¹		
Protein	<5 g l ⁻¹	<0.1 g kg ⁻¹	33 g l ⁻¹
Carbohydrate	<5 g l ⁻¹	<0.1 g kg ⁻¹	22 g l ⁻¹
of which sugars	<5 g l ⁻¹	<0.1 g kg ⁻¹	22 g l ⁻¹
Fibre	<5 g l ⁻¹	<0.1 g kg ⁻¹	<5 g l ⁻¹
Salt	<0.1 g l ⁻¹	<0.1 g kg ⁻¹	0.7 g l ⁻¹

Table 5.3: Composition of Hiprotal whey protein 35 and final 18.2 g l⁻¹ solution according to the supplied data sheet. Calcium fraction determined by ICP-MS at the Department of Earth Sciences, Cambridge, UK.

Constituent	Hiprotal WP 35	WP solution	Method of Analysis
Lactose	~51 % g g ⁻¹	~9.3 ‰ g g ⁻¹	not stated
Protein	34.1 % g g ⁻¹	6.2 ‰ g g ⁻¹	ISO 14891
Ash	6.5 % g g ⁻¹	1.2 ‰ g g ⁻¹	NEN 6810
Calcium	0.604 % g g ⁻¹	0.11 ‰ g g ⁻¹	ICP-MS
Free moisture	3.2 % g g ⁻¹	0.58 ‰ g g ⁻¹	ISO 5537
Organic milk salts	~2 % g g ⁻¹	~0.36 ‰ g g ⁻¹	not stated
Fat	2.2 % g g ⁻¹	0.40 ‰ g g ⁻¹	ISO 1736
Nitrate (NO ₃)	57 ppm	1.0 ppm	ISO 14673-2
Nitrite (NO ₂)	<0.1 ppm	<1.8 ppb	ISO 14673-2

5.3 Fouling layer analysis methods

5.3.1 Confocal laser scanning microscopy (CLSM)

Visualising protein and calcium phosphate

Confocal microscopy was used to study the distribution of calcium phosphate and protein within the fouling layers. Calcium green A1 (CG) and texas red sulfonyl chloride (TR-SC) (both Molecular Probes Inc.) show an increase in fluorescence on binding to calcium ions and amine groups, respectively. 50 μg of CG was dissolved in 50 μL dimethyl sulfoxide (purity 0.99 g g^{-1} , Alfa Aesar) under ultra-sonication and added to 10 ml deionised water. The final concentration of $\sim 4 \mu\text{M}$ is in the order of magnitude used by Thomas *et al.* (2000) to study calcium cell signalling. The solution was injected into the microfluidic HEX cell holding the fouling deposit and kept there for 25 min. Afterwards, 1 mg of TR-SC was dissolved in 10 ml deionised water just above the water freezing point to reduce the rate of dye hydrolysis (Lefevre *et al.*, 1996). The 160 μM TR-SC solution was injected into the cell shortly after mixing and again held therein for 25 min. The cell was then rinsed with deionised water and placed on a Leica TCS SP5 CLSM. The CG and TR-SC fluorophores were excited by an argon laser at 514 nm and a helium-neon laser at 633 nm, respectively. *In situ* images of deposits on FPs were taken with a 10 \times lens and the pinhole set to 53 μm . In some cases, deposits adhered strongly enough to be imaged *ex-situ* using a 40 \times oil immersion lens.

Visualising fat

Confocal microscopy was used to study the distribution of fat in milk and selected fouling deposits. Nile blue A shows an increase in fluorescence in apolar environments (Jose & Burgess, 2006). 20 mg l^{-1} of Nile blue A (Sigma-Aldrich) was dissolved in raw milk to study the effect of heating and ultrasonication on MFGs. The prepared milk was added between a cover slip and a microscope slide (two other cover slips acted as spacers) and was viewed with CLSM. Images were taken with a 40 \times oil immersion lens and a helium-neon laser exciting Nile blue A at 633 nm.

To take images of fat immobilised in fouling deposits, 20 mg l^{-1} of Nile blue A was dissolved in deionised water and added underneath a cover slip resting on the fouling layer. After about 20 min, the sample was placed on the CLSM and images were taken with a 10 \times lens and laser excitation at 633 nm.

5.3.2 Confocal thickness scanning (CTS)

Thickness scans of fouling deposits were conducted with a confocal chromatic thickness probe (Micro-Epsilon IFS2405-3) mounted above a motorised X-Y stage (Standa 8MTF-102LS05). The apparatus, developed within the research group, allows one to take raster scans of surfaces with a maximum size of 102×102 mm and a height range of 3 mm at sub micron-scale resolution. The fouling deposits on test plates from the bench-scale HEX were initially sputter coated with a 20 nm gold layer to generate a sharp optical interface for detection. In later cases applying graphite powder with a fine brush also sufficed. The test plates with deposit were scanned with a lateral resolution of 1 mm at $50 \times 50 = 2500$ points. A second scan of the cleaned test plates was used to subtract the contours of the substrate. This was instrumental when accounting for the uneven thickness of FP coatings. Many of the deposits generated on polymers could not be scanned because they detached on drying. The data were subsequently linearly interpolated and filtered with a 5×5 box linear filter using a Matlab[®] routine written by the author.

5.3.3 Inductively coupled plasma mass spectrometry (ICP-MS)

ICP-MS was used to determine the calcium mass fraction in raw milk, WP solution and fouling deposits generated from those solutions. All preparation work took place at ambient temperature and the material samples were left for acid digestion in a fume cupboard for one week. Before analysis with a Perkin Elmer Nexion 350D ICP-MS instrument all samples were further diluted 10-fold with 20 % g g^{-1} HNO_3 .

To determine the calcium fraction in raw milk, 46 g milk were placed in a glass beaker and heated on a hot plate to 80°C to yield 8.43 g gel by evaporation of water. 16.7 mg gel was loaded into a vial and acids were added for digestion (10.33 g 1 M HCL, 2.29 g 70 % g g^{-1} HNO_3). For analysis of Hiprotal WP 35, 85.5 mg powder was digested in acid (11.16 g 1 M HCL, 2.30 g 70 % g g^{-1} HNO_3).

Some fouling deposits from the bench-scale HEX were prepared as follows: the deposit (mass ranged from 4.8 to 16.3 mg) was separated from the substrate plates by washing with 1.81 to 11.38 g 1 M HCl in Petri dishes and removed with a plastic spatula. The liquids with suspended deposits were loaded into in vials and 0.37 to 2.3 g 70 % g g^{-1} HNO_3 was added for digestion. A control with 12.20 % g g^{-1} calcium prepared with CaCl_2 (anhydrous, Breckland Scientific Supplies) gave a measured fraction of 12.27 % g g^{-1} calcium, *i.e.* 0.57 % error.

5.4 The microfluidic heat exchanger apparatus

5.4.1 Design & construction

The fouling microfluidic apparatus is based around the microfluidic HEX cell shown in Figure 5.1. The cell has three main functions: (i) guiding the flow of the process fluid into the cell, past the test surface and out, (ii) heating the square test plate to the desired surface temperature and (iii) allowing microscope imaging. The cell is constructed as a composite sandwich with cross section depicted in Figure 5.1b. The channel body (labelled 1 on the Figure) is made of 3D printed polyamide PA2200 (3Dprintuk Ltd.) and holds a 180 μm thick borosilicate glass slip (2) on a stainless steel support shim. The

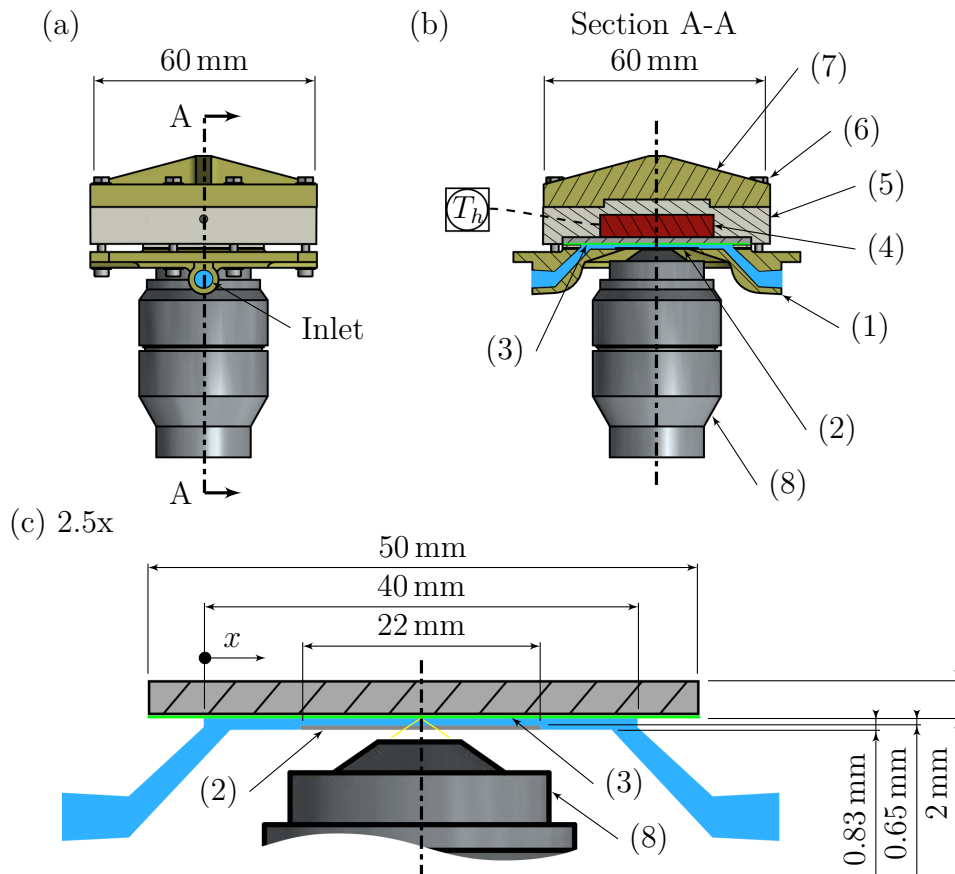


Figure 5.1: Microfluidic HEX assembly. Labels are explained in the text. (a) Side view, inlet facing front. (b) Cross section through plane AA showing channel, sample and heater. (c) Magnification of (b) showing sample and channel geometry. The width of the channel is 2 mm. Dash-dot lines indicate planes of symmetry.

walls of the channel are made of cast silicone rubber which also acts as a seal against the sample surface (3). The test plate is heated by a 12 V positive temperature coefficient heater (4) and the temperature of the heater, T_h , is measured by a thermistor (Epcos B57540G1103F000). The sample and heater are embedded in silicone rubber insulation (5). The cell is clamped with eight screws (6) via a compression plate (7) fabricated from acrylonitrile butadiene styrene on a MakerBot 2x 3D printer. The channel created between the glass slip and test surface is rectangular with dimensions $a \times b = 2 \times 0.65 \text{ mm}^2$ (5.1c). This was confirmed at the cell operating temperatures by confocal chromatic thickness measurement (Micro-Epsilon GmbH & Co. KG, IFS2405-3). The heat transfer area, A , is $a \times L = 80 \text{ mm}^2$. When being imaged the cell is located on the optical xyz-stage of an inverted CLSM, with the base plate machined to incorporate the lens (8). Figure 5.2 shows a photograph of the cell.

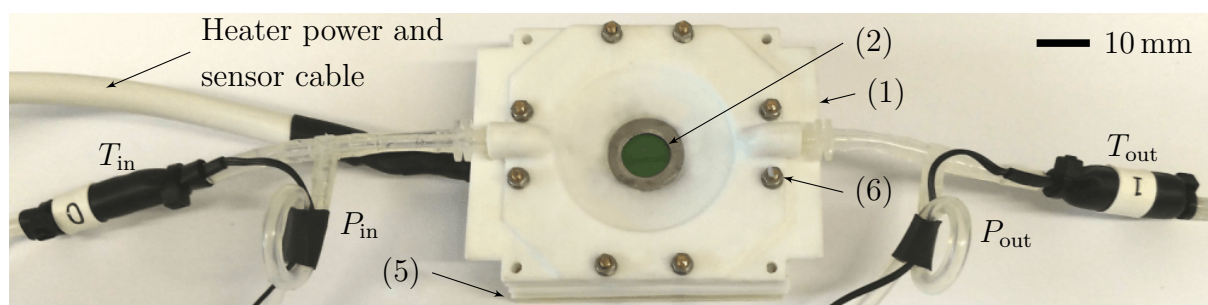


Figure 5.2: Photograph of the microfluidic HEX cell. Numbered labels are explained in the text and insulation on tubes is not shown.

Figure 5.3 shows how the HEX cell is integrated into the experimental system. Batches of deionised water, raw milk and 1 M sodium hydroxide are held at 56°C in separate containers in a heated water bath (9). The selected liquid is drawn successively by one of a series of proportional-integral controlled peristaltic pumps (10) at a flow rate of $12.10 \pm 0.67 \text{ g min}^{-1}$ (\pm standard deviation, otherwise indicated) and fed through a spiral copper tube in a second bath held at 63°C (11). β -LG aggregation starts at this temperature. The liquid is then pumped through the fouling cell (12). The typical flow rate gives an average flow velocity of $15.5 \pm 0.9 \text{ cm s}^{-1}$ in the duct and a Reynolds number of $Re = 213 \pm 12$ (see Section 5.4.2 for more details). The inlet and outlet temperatures, T_{in} and T_{out} , are measured with thermistors and the pressure drop across the cell, ΔP , is measured with a differential pressure sensor (NXP MPXV7002DP). The effluent is discharged into a waste bottle (13) resting on a load cell (14) and the mass flow rate, \dot{m} , is calculated from the change in bottle mass over time.

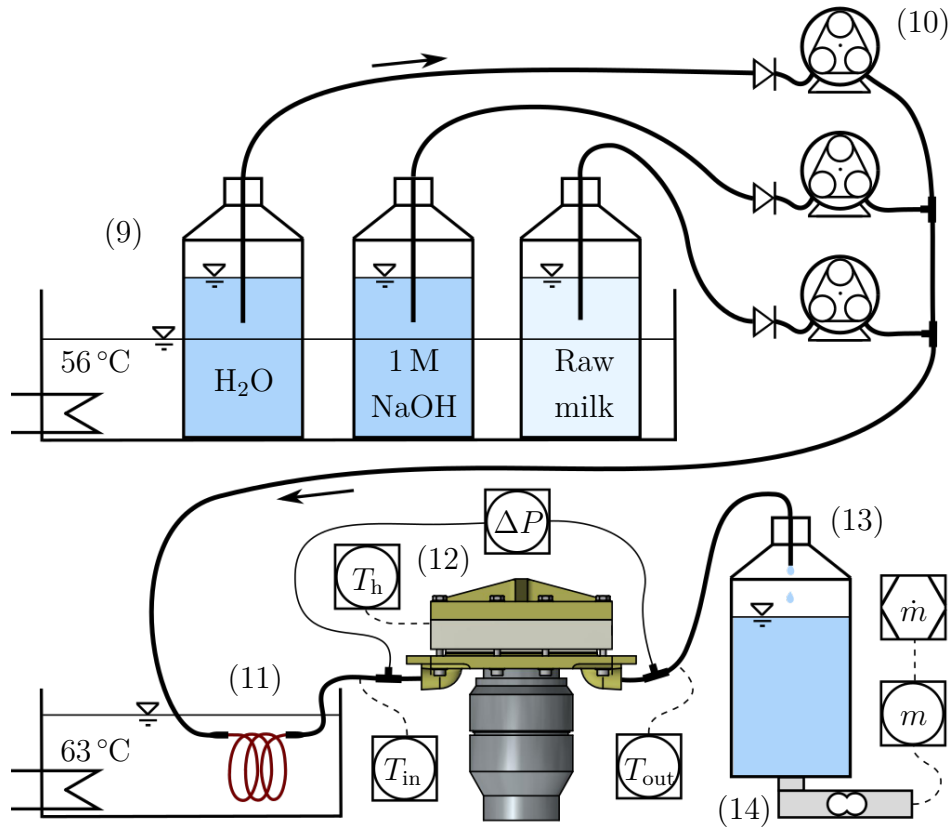


Figure 5.3: Microfluidic HEX process schematic. Labels explained in text.

All basic measurement, control and actuation functions were processed on an Arduino Mega 2560 microcontroller board programmed in C/C++. Higher level functions, such as set-point generation, data visualisation and storage, were programmed in a Python 2 module executed on a standard PC. The microcontroller and PC communicated bidirectionally via a USB connection and data were stored every five seconds.

5.4.2 Thermo-hydraulic characterisation

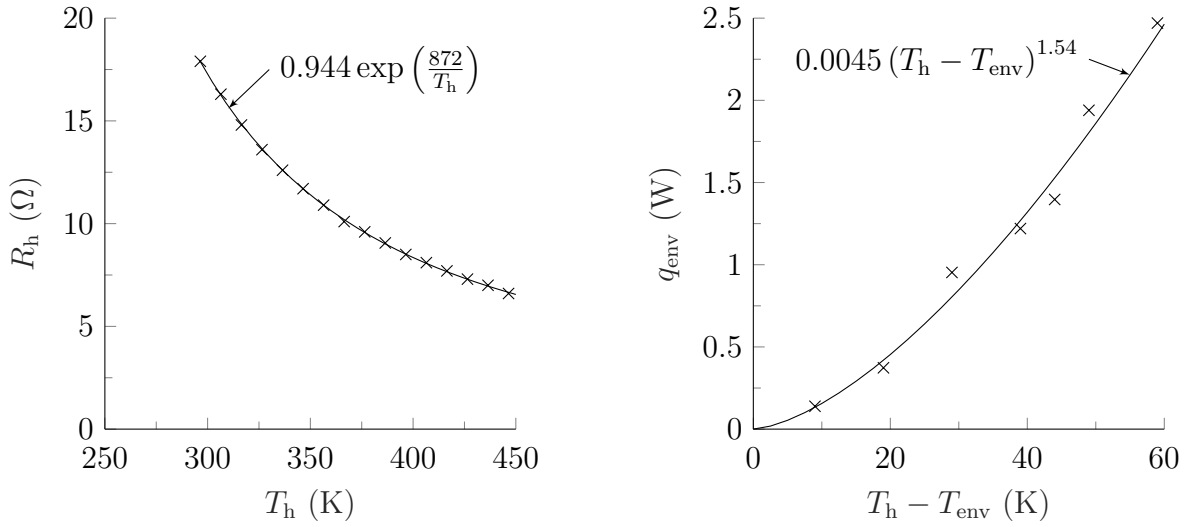
At steady state, the electrical power supplied to the heater, q_e , is transferred to the fluid, q , and the environment, q_{env} :

$$q_e = q + q_{env} \quad (5.1)$$

q_e is set by electrical pulse width modulation while taking the temperature dependent electrical heater resistance into account. It can be seen in Figure 5.4a that, within the practical temperature range, the heating element resistance, R_h , falls with increasing heater temperature, T_h . A decrease in resistance at temperatures below the Curie point

(here: ~ 503 K, from specification), where the resistance eventually increases sharply, is common for ceramic positive temperature coefficient resistors (Musat & Helerea, 2010).

The heat loss to the environment, q_{env} , was characterised as a function of temperature driving force in separate tests giving the results in Figure 5.4b. Here, the driving force is the difference between the heater temperature, T_{h} , and the temperature of the environment, T_{env} . The results are of the form $q_{\text{env}} \propto \Delta T^{1.54}$, which indicates natural convection limited heat transfer (Bergman & Incropera, 2011). The exponent is at the higher end of expected values, which may be a consequence of the increasing thermal conductivity of air with rising temperature.



(a) Electrical resistance.

(b) Effect of temp. driving force on steady state heat loss to the environment for drained flow channel, giving $q \approx 0$. $T_{\text{env}} = 21$ °C.

Figure 5.4: (a) electrical resistance and (b) heat loss in the microfluidic HEX. Crosses – measurements; lines – root mean square fitted correlations for $R_{\text{h}}(T_{\text{h}})$ and $q_{\text{env}}(T_{\text{h}}, T_{\text{env}})$.

The desired mean temperature of the wetted sample surface (see 3 in Figure 5.1), $T_{\text{s,m}}$, is set and the steady state power input, q_{e} , is calculated accordingly:

$$q_{\text{e}} = \left(T_{\text{s,m}} - \frac{T_{\text{out}} + T_{\text{in}}}{2} \right) Ah_{\text{m}} + q_{\text{env}}(T_{\text{h}}, T_{\text{env}}) . \quad (5.2)$$

where h_{m} denotes the mean film heat transfer coefficient. At an inlet temperature of 62 °C the viscosity of raw milk was approximately $\mu = 0.75$ mPa s. The Reynolds number in the centre of the test channel was $Re = 213 \pm 12$, so laminar flow was expected and confirmed visually by dye injection. The average Nusselt number was estimated from numerical steady state solutions for thermally developing laminar flow in rectangular channels heated from four sides reported by Wibulswas (1966) for the following conditions:

- (i) The channel is a simple rectangular duct. For simplicity, this is approximated by assuming a uniform channel height of 0.65 mm.
- (ii) The hydraulic boundary layer develops more quickly than the thermal boundary layer. The Prandtl number, Pr , at the inlet in this case is 4.8 and indicates faster momentum diffusion than thermal diffusion.
- (iii) The wall heat flux along, and temperatures perpendicular to, the main channel axis are uniform. This approximates the configuration in the fouling cell.

T_b increases linearly along the channel:

$$T_b(x) = (T_{\text{out}} - T_{\text{in}}) x/L + T_{\text{in}} . \quad (5.3)$$

Table 5.4 summarises the mean and local Nusselt numbers for a channel with aspect ratio 1/3. The mean Nusselt number of the channel is calculated as $Nu_m = \frac{1}{L} \int_0^L Nu \, dx$. The dimensionless coordinate, x^* , is defined as $x/D_h Pe$, where x is the axial distance along the channel (see Figure 5.1c), D_h is the hydraulic diameter, and $Pe = RePr$ is the Péclet number. The mean and local film heat transfer coefficient can be obtained from $h_m = Nu_m k/D_h$ and $h = Nu k/D_h$, respectively, where k is the thermal conductivity of the milk. Under the assumptions stated above, the local surface temperature, T_s , can be found from the overall enthalpy balance

$$T_s(x) = T_b(x) + \frac{q}{Ah(x)} = T_b(x) + \frac{\dot{m}c_p}{Ah(x)} (T_{\text{out}} - T_{\text{in}}) . \quad (5.4)$$

Here c_p is the (almost temperature insensitive) specific heat capacity and $T_b(x)$ is the bulk temperature, or mixing cup temperature to be precise, at location x . The overall heat transfer coefficient, U , is found from

$$U = \frac{\dot{m}c_p}{A} \frac{T_{\text{out}} - T_{\text{in}}}{T_h - \frac{1}{2}(T_{\text{out}} - T_{\text{in}})} . \quad (5.5)$$

Table 5.4: Average and local Nusselt numbers, Nu_m and Nu , for thermally developing laminar flow in rectangular channels with aspect ratio 1/3 heated from four sides for various dimensionless positions. Reproduced from Wibulswas (1966). For Nu_m , $x = L$.

x^{*-1}	0	20	40	80	120	160	200
Nu_m	4.77	6.06	7.09	8.48	9.52	10.31	10.97
Nu	4.77	5.00	5.39	6.21	6.92	7.50	8.02

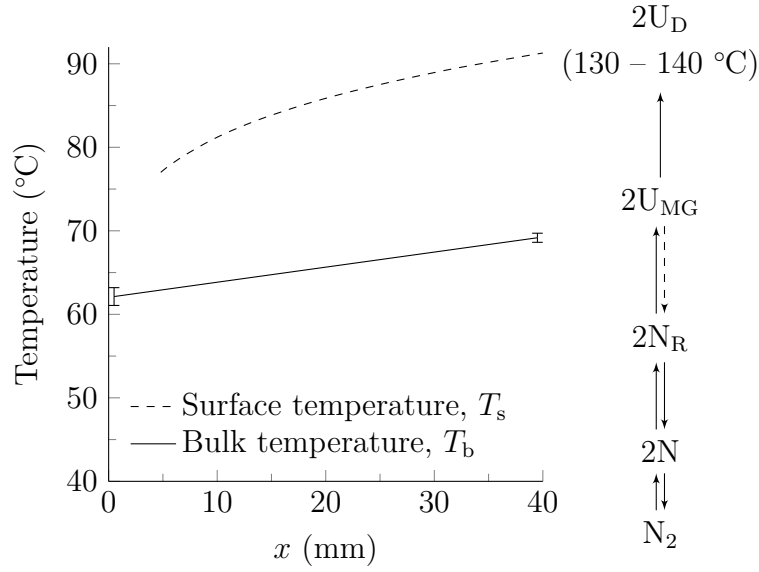


Figure 5.5: Estimated bulk and surface temperature distribution in the microfluidic fouling cell for standard operating conditions. Error bars indicate standard deviations. The schematic on the right illustrates the temperature dependency of BLG structural changes reported by Tolkach and Kulozik (2007), *cf.* Figure 2.2.

Figure 5.5 shows the initial calculated temperature distribution in the clean microfluidic HEX. The estimated temperature in the thermal boundary layer – taken as the average of the bulk and surface temperatures – favours β -LG being in the molten globule state.

Protein deposition, accompanied by an increase in ΔP , is expected to occur. The change in pressure drop can be related to the deposit thickness, δ_f , via the Hagen–Poiseuille equation (*e.g.* Suter & Skalak, 1993)

$$\Delta P = \frac{128}{\pi} L \mu \frac{\dot{m}}{\rho} \left(\frac{a + b - \delta_f}{2a(b - \delta_f)} \right)^4, \quad (5.6)$$

where a and b are the channel width and height, respectively. This assumes that the layer has uniform thickness and surface roughness does not change. The viscosity, μ , and density, ρ , are evaluated at the average bulk temperature: $\frac{1}{2}(T_{\text{out}} + T_{\text{in}})$. If $a \gg b \geq \delta_f$, Equation 5.6 can be written as

$$\Delta P \propto (b - \delta_f)^{-4}. \quad (5.7)$$

The pressure drop is significantly more sensitive to deposit build up than the mean heat transfer coefficient, which is proportional to the thickness of the deposit layer. ΔP in Equation 5.6 can be related to the pressure drop of the clean cell at the beginning of the

experiment, ΔP_{cl} , *viz.*

$$\frac{\Delta P}{\Delta P_{cl}} = \frac{\mu \dot{m}}{\mu_{cl} \dot{m}_{cl}} \left(\frac{(a + b - \delta_f) b}{(a + b)(b - \delta_f)} \right)^4 \quad (5.8)$$

By division, all constants and ρ (which is almost constant throughout the experiment) cancel. μ_{cl} is the viscosity and \dot{m}_{cl} is the flow rate at the beginning of the experiment. Given experimental data, this can be solved by iteration to give the thickness of the deposit.

5.4.3 Raw milk fouling studies on steel and fluoropolymers

Experimental protocol

Figure 5.6 shows an example of the evolution of the variables monitored during a micro HEX fouling test. Initially deaerated, deionised water was pumped through the cell until thermal steady state was reached for the desired mean surface temperature (marked t'_1 in Figure 5.6). In some cases, rapeseed oil or molten clarified butter was pumped through the cell before heating it up to deposit a thin TG film. The flow rate was 12 g min^{-1} for all experiments, which corresponds to a Reynolds number of 202 at the inlet. The liquid was then switched to de-aerated raw milk and the Figure shows a pronounced increase in ΔP and a modest increase in T_h as deposition occurred. At time t'_2 the fouling cell heater was turned off and cooled to 75°C with deionised water. The flow then stopped and the deposit was either studied with *in situ* CLSM or the cell was disassembled to remove the test plate and dry the deposit before weighing.

Following an experiment the test plate and channel body (see (1) in 5.1b) were cleaned by hand in six steps: (i) washed with a commercial dishwashing detergent at $\sim 55^\circ\text{C}$, (ii) rinsed with water at $\sim 55^\circ\text{C}$, (iii) washed with 1 M NaOH at $\sim 21^\circ\text{C}$, (iv) rinsed with water at $\sim 55^\circ\text{C}$, (v) washed with 0.5 M phosphoric acid at $\sim 21^\circ\text{C}$ and (vi) rinsed again. The rest of the system was cleaned by circulation of 1 M NaOH followed by deionised water, both at 62°C . Each test plate was re-used frequently and the clean performance monitored to determine whether irreversible changes occurred.

The associated thermal resistance, R_f , was calculated by inserting Equation 5.5 into 3.1 and setting $U_{cl} = U(t')$ shortly after $t' = t'_1$ when heat transfer stabilised. Over the course of this experiment the fouling resistance grew to about $R_f = 0.025 \text{ m}^2 \text{ K kW}^{-1}$. In most experiments, however, the change in thermal resistance was not significant over the time-scales studied.

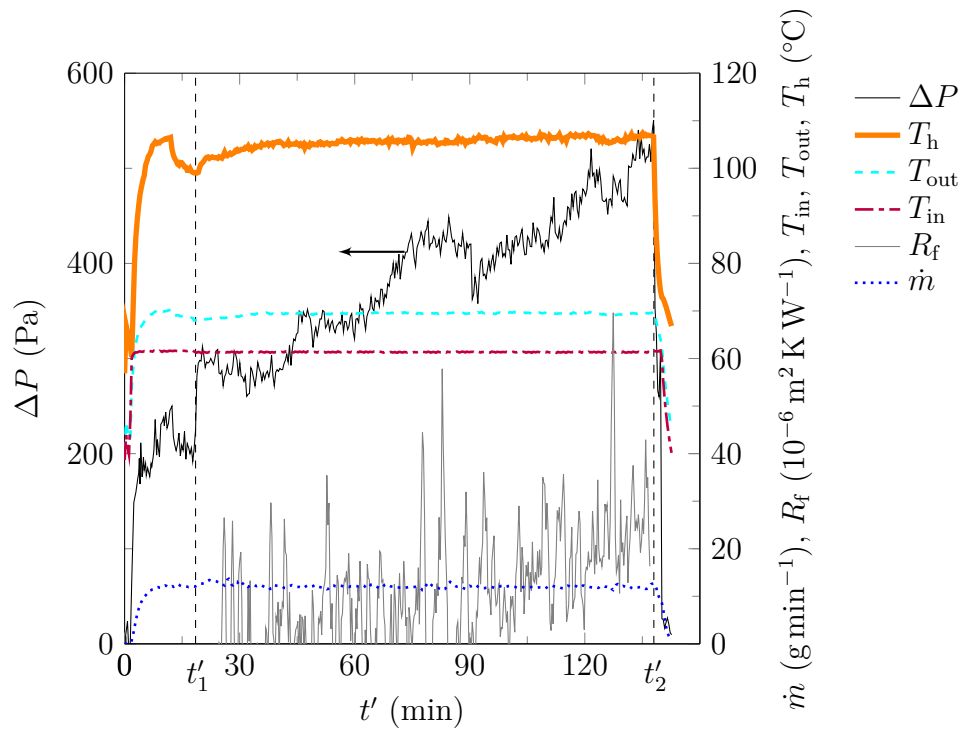


Figure 5.6: Example of microfluidic HEX monitoring record for a fouling test on stainless steel. ΔP – left axis; mass flow rate and temperatures – right axis. Vertical dashed line at t'_1 indicates when flow was changed from water to milk, t'_2 indicates end of experiment.

Evolution of pressure drop and deposit thickness

Figure 5.7a shows the pressure drop evolution over time for all surfaces studied without pre-wetting with TGs. PFA-2 showed fast accumulation of deposit and the experiments were stopped after 65 min. The pressure drop increased more slowly for PFA-3, but accelerated after 60 min and exceeded that of SS. FEP-2, however, performed better throughout. The performance of PTFE-1 is comparable to SS, nonetheless it shows a higher initial pressure drop. If the measured pressure drop of 400 Pa to 800 Pa is assumed to have occurred primarily in the thin HEX channel, the mean wall shear stress ranged from about 3 Pa to 6 Pa. The effect of depositing a thin TG film in the cell before the experiment can be seen in Figure 5.7b. Pre-wetting with rapeseed oil reduces the pressure drop of PFA-2 strongly throughout the experiment. Pre-wetting FEP-2 with clarified butter further improves the performance of the coating, albeit to a smaller extent.

The thicknesses of hypothetical uniform deposit layers which would give these increasing pressure drops were calculated according to Equation 5.8 and are shown in Figure 5.8.

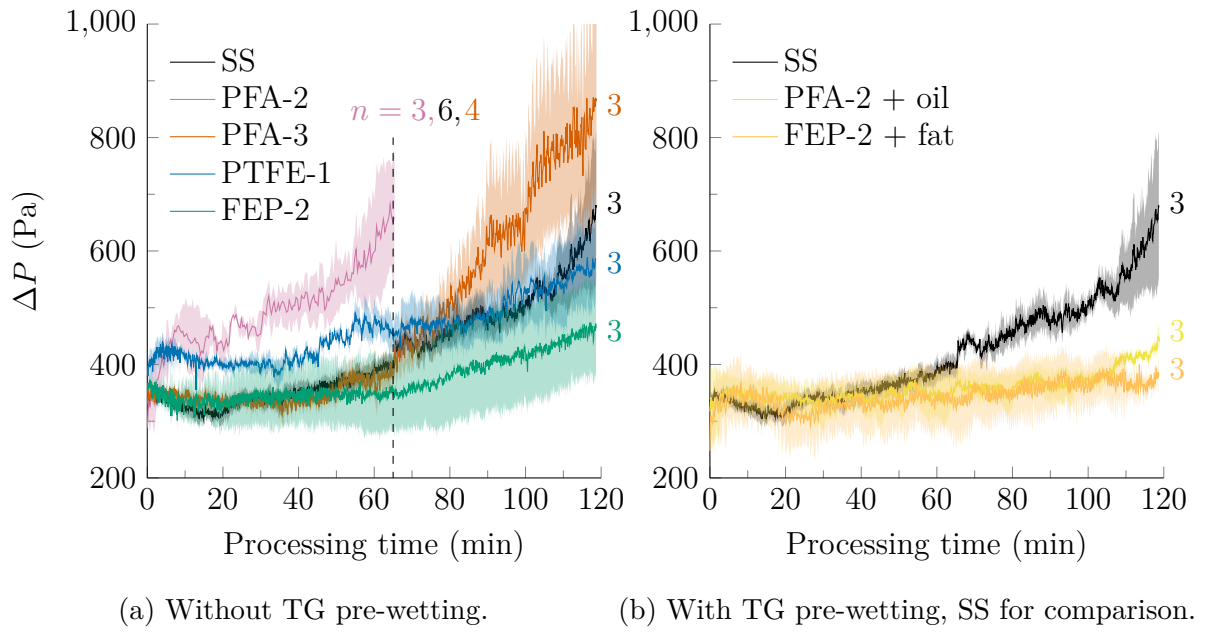


Figure 5.7: Pressure drop profiles for fouling tests with raw milk using the microfluidic HEX. n indicates the number of experiments performed. Some lasted 65 min, others 120 min. Figure 5.7b shows data for two experiments where rapeseed oil ('+oil') or clarified butter ('+fat') was pumped through the cell before bringing it to thermal steady state. Shaded bands indicate \pm standard error.

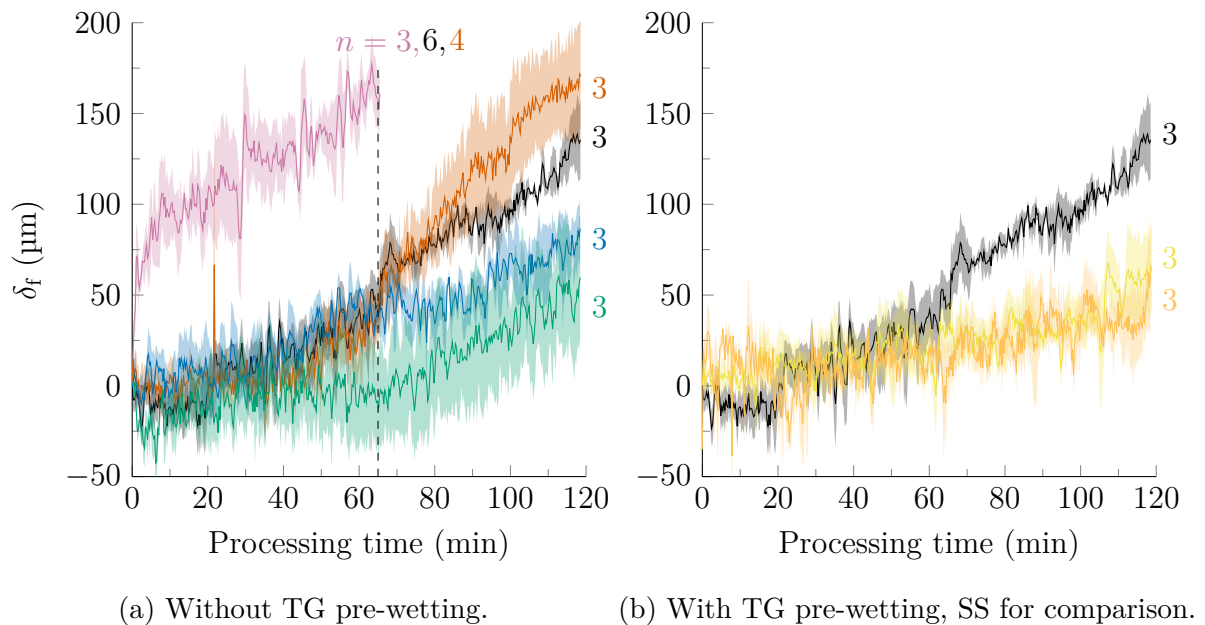


Figure 5.8: Estimated thickness evolution of uniform raw milk deposit layers in the microfluidic HEX calculated with Equation 5.8. n indicates the number of experiments performed and shaded bands indicate \pm standard error. Identifying line colours are the same as in Figure 5.7

These curves are noisier than the pressure drop data because the instantaneous changes in mass flow and changes in viscosity due to temperature fluctuations are taken into account. By including the mass flow, however, some variations seen in the pressure drop data do not manifest in the thickness curves. The initial slumps in pressure drop due to the stabilising mass flows evident in Figure 5.7 within the first 15 min are not seen in the thickness curves. Results for surfaces which were not pre-wetted with TGs are presented in Figure 5.8a. PFA-2 shows an initially rapid growth in fouling layer thickness followed by a steady linear increase.

The fouling layers on the polar surfaces SS and PTFE-1 grow with a noticeably linear trend. Growth on FEP-2 and PFA-3 remains stagnant or slow until 45 min and 65 min, respectively, but is then followed by steady growth. The final thickness on FEP-2 is $\sim 50 \mu\text{m}$ compared to $\sim 130 \mu\text{m}$ on SS. This corresponds to average fouling rates of $\sim 0.42 \mu\text{m min}^{-1}$ and $\sim 1.08 \mu\text{m min}^{-1}$ for FEP-2 and SS, respectively. TG pre-wetted surfaces show a slow linear growth in fouling layer thickness presented in Figure 5.7b.

The pressure drop and deposit thickness data for the polar surfaces SS and PTFE-1 were more reproducible than for the apolar surfaces. Although care was taken to remove all dissolved air from the milk prior testing, apolar surfaces were more prone to bubble nucleation which may be the reason for the larger variance seen in their tests.

Evolution of fouling resistance

The measured fouling resistances were calculated with Equation 5.5 and 3.1, setting $U_{cl} = U(t')$ shortly after heat transfer stabilised. Figure 5.9a presents the fouling resistance profile for SS. Although the data are noisy, a steady increase in fouling resistance until $R_f \approx 0.025 \text{ m}^2 \text{ K kW}^{-1}$ is evident. The data for the coated surfaces was much more noisy, an example of which is shown for FEP-2 in Figure 5.9b. Little measurable fouling over the first 65 min, which was evident in the ΔP data, can also be inferred from the thermal data (see arrows). The final fouling resistance for FEP-2 was comparable with the one obtained for SS. Dividing the fouling resistances by the processing time gives a fouling rate of $0.0125 \text{ m}^2 \text{ K kW}^{-1} \text{ h}^{-1}$. Corresponding data for the other surfaces are provided in Appendix C: these mirror the δ_f profiles.

Expressing the fouling resistances as fouling Biot numbers ($Bi_f = U_{cl}R_f$) gives $Bi_f = 2180 \cdot 0.025 \times 10^{-3} = 0.05$ for SS and $Bi_f = 1160 \cdot 0.025 \times 10^{-3} = 0.029$ for FEP-2. The smaller fouling Biot number for the tests with coated samples explains why the noise in Figure 5.9(b) is larger than in (a). Hartnett *et al.* (2001) showed that measurements of fouling resistance are impractical for $Bi_f < 0.1$, which is why fouling monitoring by pressure drop was preferred.

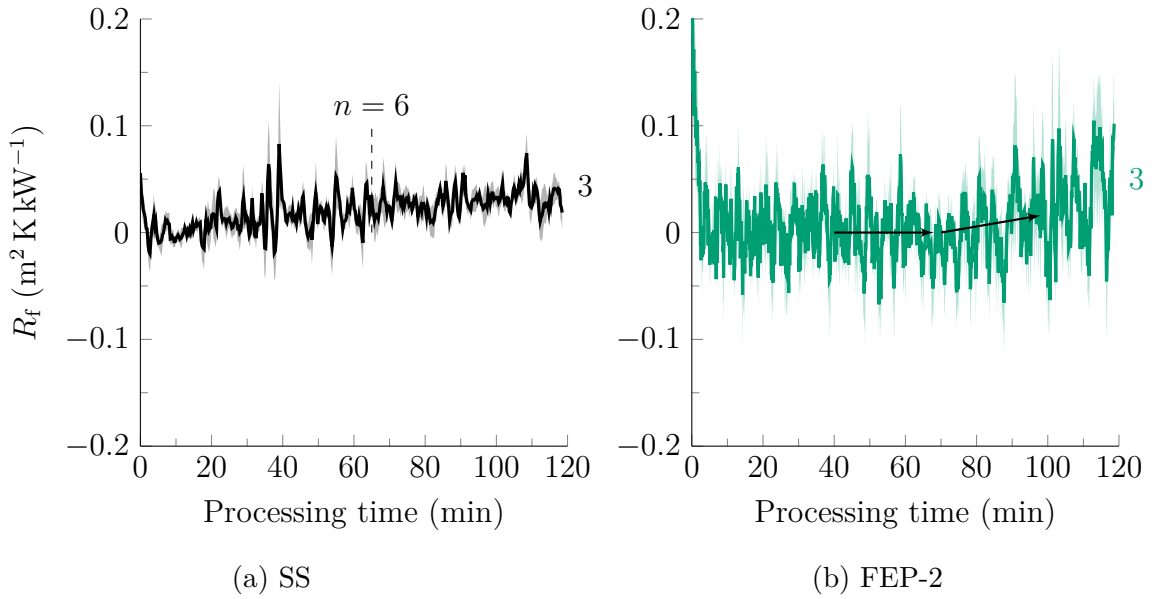


Figure 5.9: Fouling resistance profiles for raw milk fouling tests with microfluidic HEX on (a) SS and (b) FEP-2. Arrows in (b) mark a change in the fouling rate. n indicates the number of experiments performed and shaded bands indicate \pm standard error.

An estimate of the expected fouling resistance can be calculated from the deposit thicknesses *via* $R_f = \delta_f/k_f$. Hydrated whey protein gels have thermal conductivities of around $0.4 \text{ W m}^{-1} \text{ K}^{-1}$ (Tuladhar *et al.*, 2002b). Taking this as an estimate for the deposit thermal conductivity yields a final fouling resistance of $0.33 \text{ m}^2 \text{ K kW}^{-1}$ for SS and $0.13 \text{ m}^2 \text{ K kW}^{-1}$ for FEP-2. Dividing the expected fouling resistances by the processing time gives a fouling rate of $0.16 \text{ m}^2 \text{ K kW}^{-1} \text{ h}^{-1}$ for SS and $0.06 \text{ m}^2 \text{ K kW}^{-1} \text{ h}^{-1}$ for FEP-2. The fouling resistances estimated from pressure drop data are thus larger than those determined by thermal measurements. One reason for this might be the reduction in cross sectional flow area with progressing fouling, which increases flow velocities and enhances the heat transfer within the milk.

Deposit coverage

The mass of fouling deposit was determined after drying overnight and the data are presented as surface mass coverage in Figure 5.10. On a 90 % confidence level, there was significantly less deposit on the FEP-2, FEP-2+fat and PFA-2+oil plates compared to SS, which is consistent with the ΔP and δ_f results in Figures 5.7 and 5.8, respectively. Compared to plain PFA-2 after 65 min, oil pre-wetted PFA-2 accumulated roughly half the deposit in twice the time. The deposited mass on FEP-2 decreased slightly by pre-wetting with clarified fat. PFA-3 also accumulated less deposit, but gave a high pressure drop,

suggesting that the deposit was more voluminous. The PTFE-1 coating accumulated a similar amount to SS, which is consistent with the ΔP data in Figure 5.7a. Without pre-wetting, PFA-2 was not an effective coating as it accumulated a similar amount of deposit to the SS reference in half the time.

The steady growth in fouling layer thickness for SS justifies the calculation of an average mass deposition rate by dividing the deposit coverage by the processing time. The rate for SS was $5.1 \text{ mg m}^{-2} \text{ s}^{-1}$, which is larger than the rate obtained by Foster *et al.* (1989) (*c.f.* $1.1 \text{ mg m}^{-2} \text{ s}^{-1}$) from fouling experiments using raw milk at a surface temperature of around 100°C in a small stirred beaker with 200 ml volume and a bulk temperature of 60°C . Their small deposition rate may be related to the small liquid volume and hence the small total amount of fouling precursors present. Barish and Goddard (2013) studied raw milk fouling at more comparable flow conditions ($Re = 256$) in a model plate HEX at bulk temperatures from 65°C to 85°C and measured an average mass deposition rate of $4.0 \text{ mg m}^{-2} \text{ s}^{-1}$. They tested the performance of SS against a nickel coating with dispersed PTFE particles which gave an average mass deposition rate of $0.27 \text{ mg m}^{-2} \text{ s}^{-1}$. This compares favourably with the mass deposition rate of $3.5 \text{ mg m}^{-2} \text{ s}^{-1}$ achieved here with FEP-2.

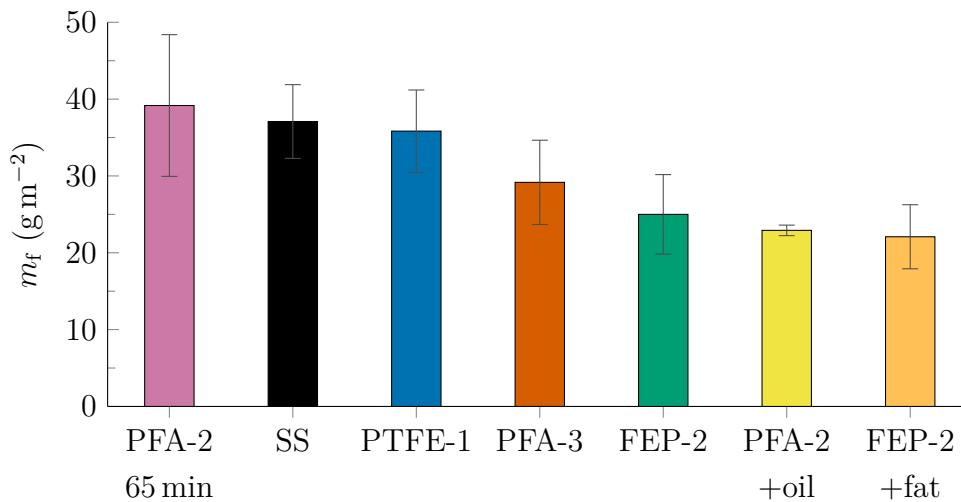


Figure 5.10: Deposit coverage (dry mass per unit area) from raw milk after a test duration of 120 min (except for PFA-2: 65 min, see Figure 5.7a). ‘+oil’ or ‘+fat’ indicate that rapeseed oil or clarified butter was pumped through the cell before bringing it to thermal steady state. Error bars show 90% confidence intervals based on three repetitions.

Deposit photographs

The photographs of deposits in Figure 5.11 show noticeable differences. On the polar surfaces (b,d), the layer is whitish and had a more brittle texture, indicating that it contained a larger amount of calcium phosphate (confirmed later by separate chemical analyses of deposits from the bench-scale HEX – see Table 5.5). The deposit was firmly attached to SS, whereas on PTFE-1 it partly flaked off. While the deposits on the apolar surfaces were easily cleaned, a strongly attached mineral layer remained on PTFE-1 and especially on SS after washing with 1 M NaOH solution (see Figure 5.11c). This layer was removed by washing with 0.5 M H_3PO_4 , which is consistent with it being calcium phosphate.

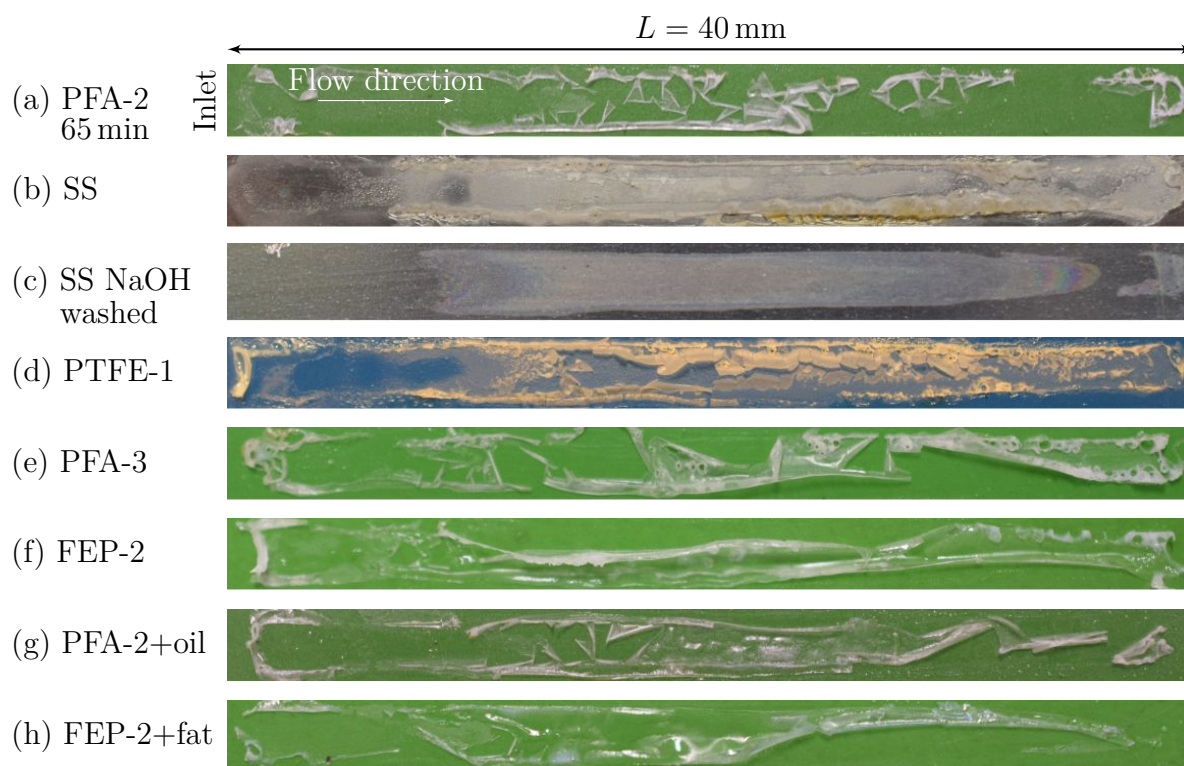


Figure 5.11: Representative pictures of dried raw milk deposits from microfluidic HEX after 120 min (or otherwise indicated) of processing on plain (a-f) and TG pre-coated (g,h) surfaces. Deposits on apolar surfaces detached after a few seconds of drying. Image (c) shows deposit on SS after washing with 1 M NaOH.

On the apolar surfaces (a,e-h) the deposit detached from the substrate after the first seconds of drying in ambient air. This suggests that (i) drying causes shrinkage and tension within the deposit; (ii) the cohesion of the dried deposit on apolar surfaces is stronger than its adhesion; and (iii) adhesion is facilitated by the presence of water.

Furthermore, the deposits formed on apolar surfaces were more transparent and softer to the touch, suggesting a higher protein content. On pre-wetted surfaces (g,h) some oily residue is visible, indicating that a fraction of TG remained at the surface until the end of the experiment. Otherwise, deposits formed on plain and pre-wetted FP surfaces appeared to be similar. No visible changes of the tested surfaces were observed.

Calcium and protein distribution in raw milk deposit

CLSM was used to study whether the surface affected the local composition of the deposit. Figure 5.12a-c shows an orthogonal CLSM section of the 120 min deposit on SS. The signals indicating the presence of (a) amines, (b) calcium ions and (c) both, are shown separately. Blue indicates the amine groups present in proteins and red the presence of Ca^{2+} ions. The deposit appears generally uniform in composition, with some patches of variation parallel (lateral) to the surface. In the asterisked regions there are relatively more amine groups than calcium ions, suggesting a higher protein content. This variation is unlikely to arise from the surface, as the surface chemistry would be expected to affect composition uniformly near the interface at the length-scales studied.

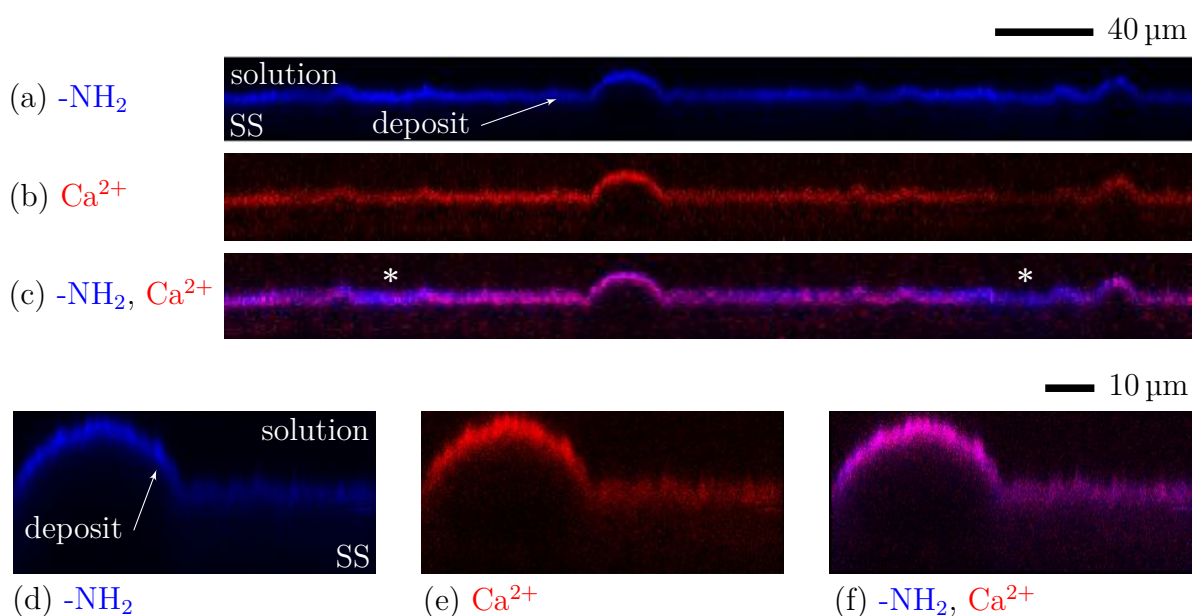
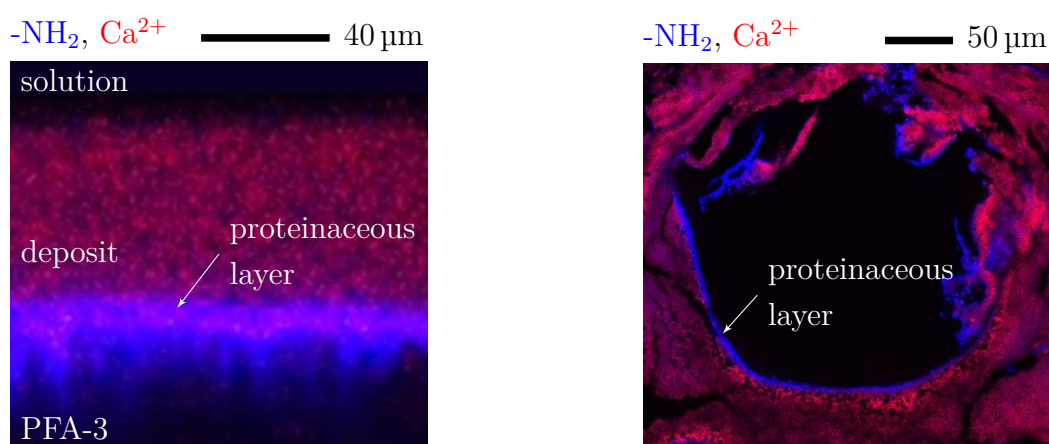


Figure 5.12: CLSM sections through a raw milk fouling layer on SS (see Figure 5.11b) taken (a-c) *in situ* with a 10× air lens and (d-f) *ex situ* with a 40× oil immersion lens. The amine and calcium data are shown individually in (a,b,d,e) and superimposed in (c,f). * highlight lateral variations in composition.

Higher resolution images, Figure 5.12d-f, were taken with a 40 \times oil immersion lens *ex situ*, and showed no spatial irregularities. At some points the fouling layer blistered. Given the instantaneous changes in the fouling layers on apolar surfaces when subject to drying (peeling off), these were studied with CLSM *in situ*, *i.e.* without disassembling the fouling cell.

Figure 5.13a shows an example of a deposit cross section on PFA-3. The deposit layer was considerably thicker than on SS and the apolar surface promoted the growth of a protein-dense layer extending up to 20 μm . The structure of the layer closely resembles those encountered around trapped air bubbles: an example of such a bubble on SS is shown in Figure 5.13b. In contrast to the previous images, this scan was taken parallel to the surface. The accumulation of protein at the interface is evident: the protein acts as a surfactant (Gunning *et al.*, 2004). An attempt was made to analyse the deposit composition with ICP-OES but the experiments yielded inconsistent data.



(a) Orthogonal CLSM section of a fouling layer on PFA-3 (Figure 5.11e). The substrate is at the base and the solution above. Image taken with 10 \times air lens *in situ*.

(b) CLSM image, scanned parallel to the surface, of deposit on SS (Figure 5.11b) showing the cross section of an air bubble. Image taken with 40 \times oil immersion lens *ex situ*.

Figure 5.13: CLSM images showing the composition of raw milk deposit generated with the microfluidic HEX on apolar surfaces.

Discussion

The pressure drop and deposit mass coverage data demonstrated that some FPs can mitigate raw milk fouling compared to stainless steel under these flow conditions. Their antifouling effectiveness is influenced by their topography, with the smoothest coating (FEP-2) performing best. Other authors have reported that low surface roughness has a

neutral to positive effect on milk fouling (Bansal & Chen, 2006; Kananeh *et al.*, 2010). Considering the size of proteins, calcium phosphate crystals, and their aggregates, the length-scale of surface roughness is important as interactions take place on the nanometre-scale (Rechendorff *et al.*, 2006). Zouaghi *et al.* (2018) conducted fouling experiments with WP solution and confirmed that protein and calcium containing species ingressed in crevices in – hydrophilic and hydrophobic – micro-patterned surfaces, leading to higher final deposit masses than on unstructured surfaces. Tests with PFA-2 and FEP-2 featured induction phases of 45 min and 65 min, respectively, with negligible increases in fouling layer thickness (Figure 5.8a). Depositing a thin TG film before processing reduces deposition markedly on the rough PFA-2 surface and to smaller extent on the smoother FEP-2 surface. Both rapeseed oil and milk fat were effective pre-coats. It is not clear from the data whether it is the smoothness of the TG layer leading to less deposition or the stabilisation of β -LG against heat denaturation by binding fatty acids. Considerable deposition occurred on all surfaces even though the bulk temperature was below 72°C, (*cf.* Visser & Jeurink, 1997) indicating aggregation and chemical reaction in the hot boundary layer drove fouling in this milk.

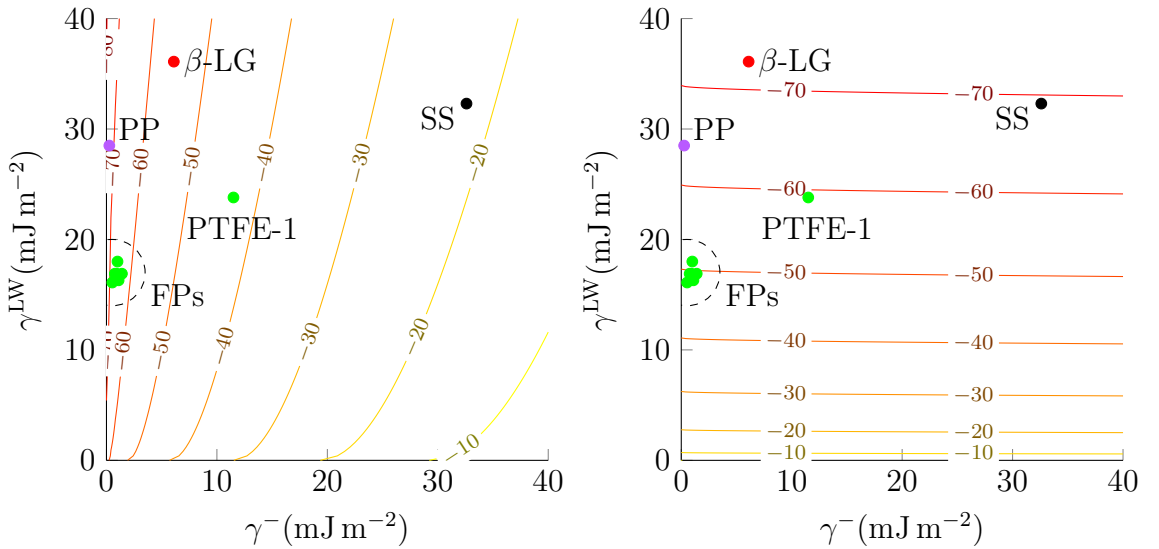
Adhesion of a mineral-rich sub-layer on SS, likely to be mainly calcium phosphate, was strong after 120 min of processing at a surface temperature of 85°C (see Figure 5.11c). Foster *et al.* (1989), working with SS at similar temperatures and for the same processing period, also reported a high calcium phosphate content at the deposit-substrate interface.

Apolar surfaces and air bubbles favoured protein deposition. Adsorption experiments by Luey, McGuire, and Sproull (1991) support these findings: they reported more β -LG adsorption on hydrophobic silicon than on hydrophilic silicon, although their study was performed at 15.6°C. Because of its low density, air can be considered as an apolar, low surface energy material in this context, in effect adsorbing similar proteinaceous matter as seen in Figure 5.13b.

The surface energies of the tested surface materials and denatured β -LG were determined by contact angle measurements (see Section 4.3). The materials were found to have $\gamma^+ \approx 0$, *i.e.* they are monopolar. The remaining contributions to surface energy from γ^{LW} and γ^- are plotted as dots in Figure 5.14a. According to Equation 2.4 the affinity of apolar surfaces to promote proteinaceous deposit can be explained by estimating the interfacial free energy of interaction, ΔG_{123}^{IF} , when denatured β -LG (subscript 1) adsorbs to a surface (2) in an aqueous environment (3). Contours of constant ΔG_{123}^{IF} plotted in Figure 5.14a indicate strong interaction of β -LG with other hydrophobic materials in water (*cf.* -65 mJ m^{-2} for FPs and -23 mJ m^{-2} for metals). The inter-particle interaction of denatured β -LG describes the tendency of β -LG to form aggregates and is therefore an

estimate of the cohesive strength of the fouling material. The free energy of inter-particle interaction is calculated to be $\Delta G_{113}^{\text{IF}} = -2\gamma_{13} = -56 \text{ mJ m}^{-2}$ (with subscripts 1: β -LG, 3: water, see also Figure 2.5b for visualisation), even though this is not accounting for chemical reactions within the fouling deposit, as discussed earlier in Section 2.2.1.

Dried deposits warped and detached from apolar surfaces, indicating stronger cohesion within the layer than adhesion to the surface. This view is supported by considering that removing water from the deposit (*i.e.* medium 3 becomes air) results in stronger interactions within the fouling deposit: $\Delta G_{113}^{\text{IF}} = -2\gamma_1 = -72 \text{ mJ m}^{-2}$ (with subscripts 1: β -LG, 3: air). Figure 5.14b demonstrates that the the adhesion to apolar surfaces remains largely unaffected by drying while the adhesion to PTFE-1 and SS increases markedly. On apolar surfaces the deposit cohesion becomes stronger than adhesion. On SS, drying decreases $\Delta G_{123}^{\text{IF}}$ of β -LG and the surface three-fold to -77 mJ m^{-2} , giving a reason for the strong adhesion of dry deposit to SS.



(a) $\Delta G_{123}^{\text{IF}}$ with 1: BLG 2: surface 3: water (b) $\Delta G_{123}^{\text{IF}}$ with 1: BLG 2: surface 3: air

Figure 5.14: Contours of interfacial free energy of interaction, $\Delta G_{123}^{\text{IF}}$ (mJ m^{-2}), of (subscript 1) denatured BLG and (2) monopolar surfaces, in (3) (a) water and (b) air. Monopolar surface electron donor, γ^{-} , and apolar, γ^{LW} , contributions to surface energy are displayed on the axes. The surface energy of denatured β -LG was determined by contact angle measurements on a hot air-dried film, see Table 4.2.

The change in interfacial free energy of interaction on drying indicates whether β -LG ‘sticks’ more or less when water is removed. This change in free energy is calculated as

$$\Delta G^{\text{drying}} = \Delta G_{12\text{air}}^{\text{IF}} - \Delta G_{12\text{water}}^{\text{IF}} \quad (5.9)$$

and can be plotted as the difference of the contours in Figure 5.14b and 5.14a. Figure 5.15 explains the surface energy characteristics needed to design a coating which features a ‘self-cleaning’ behaviour on drying. Materials in the lower-left corner have a release characteristic when an adhering β -LG layer dries. The interfacial free energy of interaction of β -LG with itself reduces by around 20 mJ m^{-2} on drying, *i.e.* physical interactions in protein aggregates become stronger. PP poses an interesting material as interactions with it do not change much on drying. This material, which was not studied with the microfluidic HEX, is included in studies with the bench-scale HEX in the next section.

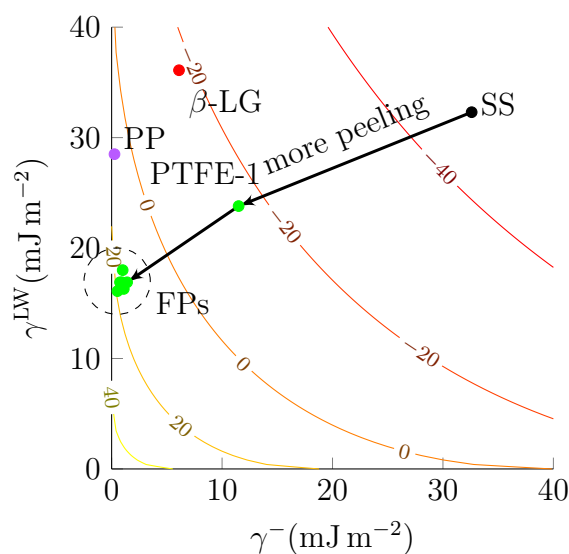


Figure 5.15: Contours of the change in interfacial free energy of interaction of denatured BLG and surfaces on drying, ΔG^{drying} . Monopolar surface electron donor, γ^- , and apolar, γ^{LW} , contributions to surface energy are displayed on the axes.

Simple crystal nucleation theories such as that by Rieke (1997) suggest minerals should also form on FPs. The interfacial free energies of three common forms of calcium phosphate, which are closely related to the interfacial free energies of heterogeneous nucleation, are depicted in Figure 5.16. The plots suggest that apolar surfaces are attractive for DCPD, OCP, and HAP to nucleate and to adhere. Nucleation and adhesion to SS is calculated to be much less attractive. This was not seen in the experimental observations and there might be several reasons for this:

- (i) Although calcium phosphate nucleation and/or calcium phosphate particle adhesion is promoted by apolar surfaces, fast adsorption of protein could be kinetically favoured. This view is supported by Visser and Jeurnink (1997) who argued that the first layer to be adsorbed is proteinaceous but can change composition over

time (Foster *et al.*, 1989; Foster & Green, 1990). Proteins adsorbed to hydrophobic materials expose their hydrophobic side chains (Miriani *et al.*, 2014), creating a hydrophobic interfacial region. For subsequent nucleation of calcium phosphate between adsorbed protein and FP, well hydrated calcium and phosphate ions have to leave parts of their solvation shell to diffuse through regions of hydrophobic matter – this is likely to make the process unfavourable.

- (ii) Wu, Zhuang, and Nancollas (1997) pointed out that arguments based on free energy of heterogeneous nucleation fail to explain why calcium phosphate does not nucleate on apolar polymers in biomineralisation. They concluded that electron donor and acceptor sites are a necessary condition for heterogeneous nucleation by providing a template for ordered lattice ion deposition. The current model does not consider local charge interactions of individual ions.
- (iii) Another reason for the absence of a mineral base-layer on FPs might be the geometric lattice mismatch between calcium phosphate and unordered polymer strands. Amjad (1998) noted that kinetics and energetics of calcium phosphate overgrowth depend strongly on the spacing and structure of the lattices involved as well as their relative orientations.
- (iv) The majority of calcium phosphate is bound in casein micelles, *i.e.* the interactions of casein micelles are be more important than assumed.

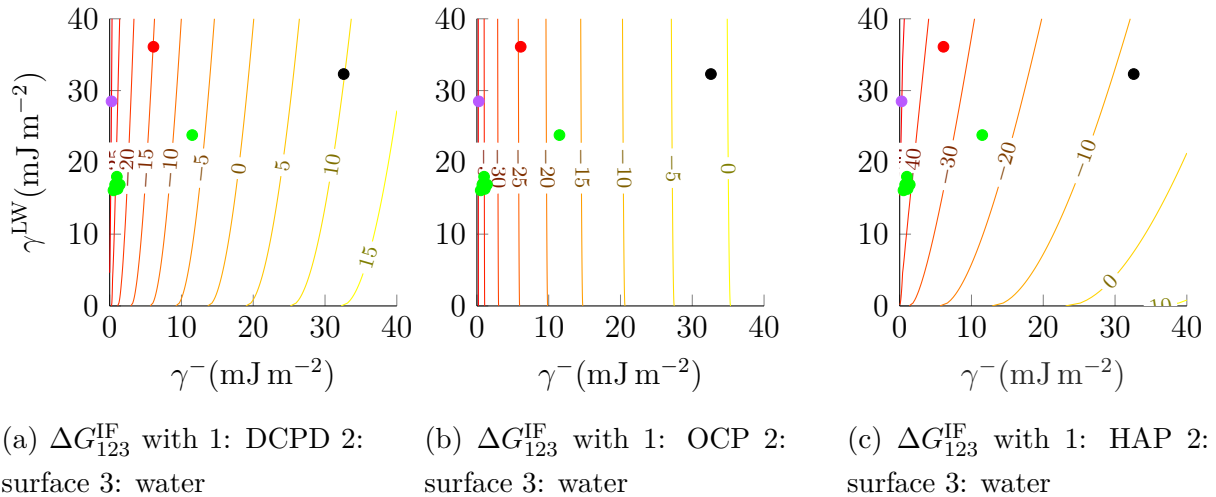


Figure 5.16: Contours of interfacial free energy of interaction, ΔG_{123}^{IF} (mJ m^{-2}), (subscript 1) of (a) DCPD (b) OCP (c) HAP and (2) monopolar surfaces in (3) water. Monopolar surface electron donor, γ^{-} , and apolar, γ^{LW} , contributions to surface energy are displayed on the axes. The surface energies of DCPD, OCP and HAP were taken from Wu and Nancollas (1998).

Expanding on hypothesis (i) one can calculate the free energy of interaction of a calcium phosphate (CP) layer developing between previously adsorbed β -LG and the surface:

$$\Delta G^{\text{CP integration}} = \Delta G_{\text{BLG,CP,water}}^{\text{IF}} + \Delta G_{\text{CP,surface,water}}^{\text{IF}} - \Delta G_{\text{BLG,surface,water}}^{\text{IF}} \quad (5.10)$$

This free energy is calculated for DCPD, OCP and HAP in Figure 5.17. DCPD is unlikely to form since $\Delta G^{\text{DCPD integration}}$ is positive for all surfaces in Figure 5.17a. The generation of an OCP layer is marginally attractive on SS in Figure 5.17b. It is, however, eventually expected for HAP to form, as the associated free energy reduction is largest for all surfaces (see Figure 5.17c). The reduction in free energy is about twice as high for SS than for apolar surfaces. Within this framework the integration of a mineral layer between β -LG and the SS surface could thus be explained – bearing in mind the simplifications and limitations of the approach.

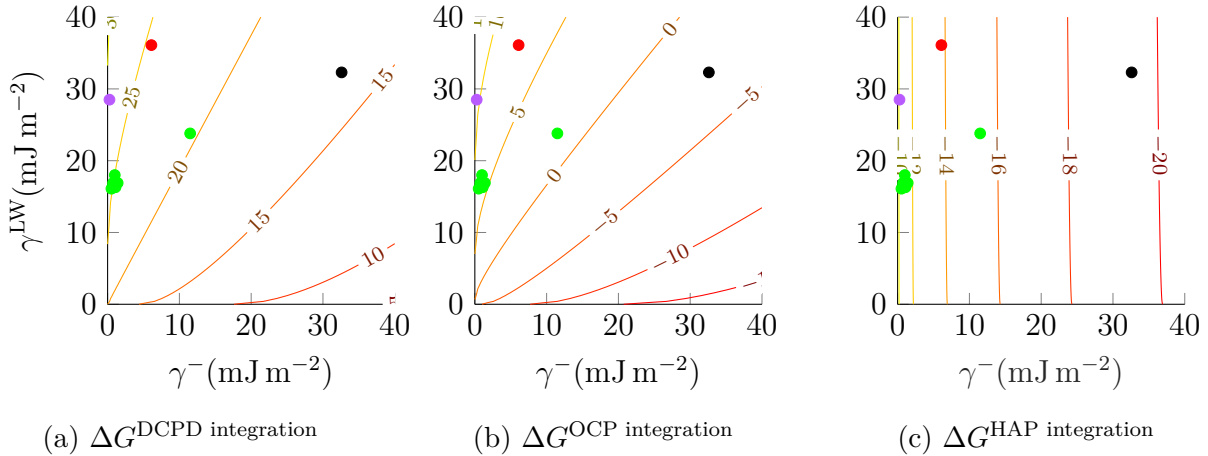


Figure 5.17: Contours of the change in interfacial free energy, $\Delta G^{\text{CP integration}}$ (mJ m^{-2}), of a layer of (a) DCPD (b) OCP and (c) HAP forming between adsorbed BLG and the surface. Monopolar surface electron donor, γ^- , and apolar, γ^{LW} , contributions to surface energy are displayed on the axes. The surface energies of DCPD, OCP and HAP were taken from Wu and Nancollas (1998).

Intermolecular forces of a material decay on the nanometre-scale (van Oss, 2003). Comparing this with the proteinaceous layer thicknesses of around $10 \mu\text{m}$ to $20 \mu\text{m}$ shown in Figure 5.13a,b suggests that the affinity for low polarity species is propagated as the fouling layer grows.

The appearance and properties of the fouling layers were affected by the nature of the surface. Those formed on polar surfaces were noticeably more white, indicating a high mineral content. Those formed on apolar surfaces were more transparent when wet,

loosely attached, and detached partially on drying in air. The latter features indicate properties which could be exploited in tailored cleaning solutions (*e.g.* combined alkaline-chelant rather than two-stage alkali-acid). Surfactants can successfully displace proteins from interfaces (Gunning *et al.*, 2004), which could further facilitate removal of protein rich deposit from apolar surfaces. These strategies add additional value to an antifouling coating by reducing cleaning times and simplifying cleaning solution chemistry. Surfaces of rough FPs, or ones which have become rough after a long time in service, could be ‘healed’ by wetting with TG before processing, *i.e.* during the HEX heat-up phase. A related option are liquid infused porous surfaces, where a structured surface wicks a lubricating liquid to give a slippery interface. The lubricating liquid is chosen to be immiscible with the process fluid. Liquid infused surfaces show potential to mitigate mineral fouling (Charpentier *et al.*, 2015).

The microfluidic HEX demonstrates that testing antifouling coatings does not necessarily require significant resources. The apparatus enables screening of coatings to identify candidates for plant-scale testing with small batches of raw milk and is suitable to use with microbially active species. The option to study delicate fouling deposits with *in-situ* microscopy sets it apart from many other fouling test rigs.

5.5 The bench-scale heat exchanger rig

5.5.1 Design & construction

The bench-scale fouling HEX rig is a compact mobile experimental station designed to investigate milk fouling on exchangeable sample plates under turbulent flow conditions. The rig recirculates liquid to limit the consumption of foulant solution. It is composed of three sub-systems: (i) the pressurised flow channel with the HEX test section, (ii) the heated tanks to supply the process fluids, and (iii) the electrical cabinet for control and data logging. Sub-systems (i) and (ii) are labelled in the process schematic in Figure 5.18.

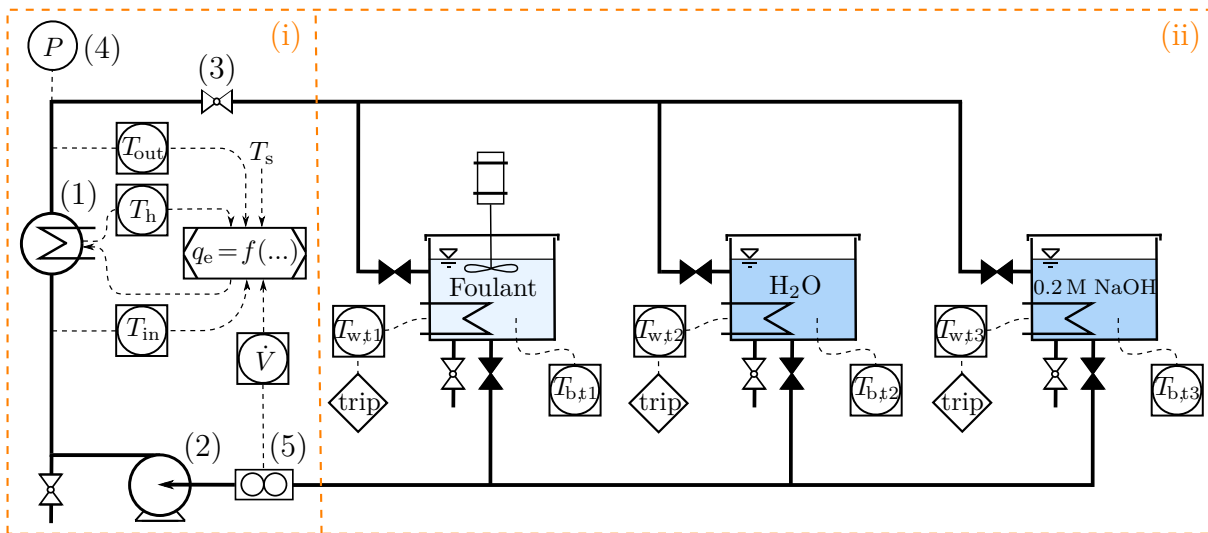


Figure 5.18: Bench-scale HEX process schematic with labelled sub-systems: (i) flow channel with HEX and (ii) heated tanks and pump. T – temperature, \dot{V} – flow rate. Numerical labels discussed in the text.

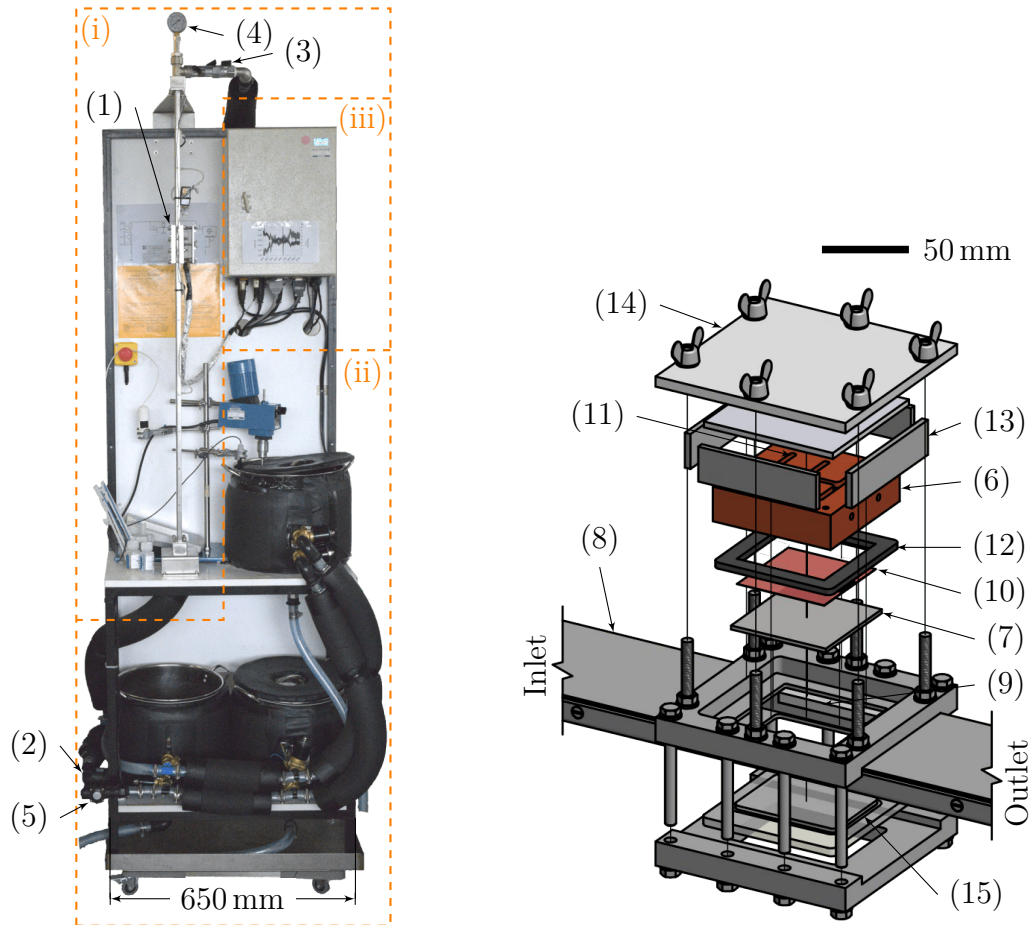
171 batches of fouling solution, water and 1 M sodium hydroxide (for cleaning) are held at 60 °C in separate tanks. The tank walls are heated by proportional-integral controlled silicone heater mats ($2 \times$ RS Pro Silicon Heater Mats with total $q_{e,max} = 800 \text{ W}$, $A = 0.12 \text{ m}^2$ per tank). The bulk temperature in the tanks is measured with thermistors embedded in thermowells. Thin film thermistors measure the temperature of the heated walls, $T_{w,t1...3}$, and are linked to high temperature trips to keep the wall temperatures below critical thresholds. In the water and sodium hydroxide tanks, wall temperatures are capped at 100 °C to prevent boiling. In the foulant tank, the wall temperature is

capped at 63 °C to prevent fouling and foulant inactivation. A stirrer (jiffy mixer blade, 67 mm diameter, ~500 rpm) keeps the temperature distribution within the foulant tank close to uniform. The three tanks are installed in parallel. One liquid at a time is pumped through the HEX section (labelled 1 in the Figure) by opening the associated solenoid inlet and outlet valves (normally closed) shown in black. The proportional-integral controlled centrifugal pump (2) and throttle valves (3) increase the absolute static pressure in the HEX section to retain dissolved air in solution at the temperatures experienced at the heat transfer surface. Pressure is measured with an analogue pressure gauge at the top of the flow channel (4). The volumetric flow rate is measured with a positive displacement sensor (5) and kept at $\dot{V} = 8.00 \pm 0.18 \text{ l min}^{-1}$ for all experiments. The HEX inlet, outlet and heater temperatures, T_{in} , T_{out} and T_{h} , are measured with thermistors. The electrical power requirement, q_e , to achieve a desired mean sample surface temperature, T_s , is calculated as a function of the fluid properties and instantaneous process measurements. This is discussed further in Section 5.5.3. After the liquid exits the throttle valves, it is fed back to its tank. For cleaning and maintenance purposes, four manual ball valves (three in the tank bases and one below the flow channel) allow complete drainage of the tanks and pipework.

Figure 5.19a is a photograph of the bench-scale HEX rig with sub-systems and key components labelled. The rig rests on a mobile base to enable relocation. The experimental station is based around the heated section of the channel, marked (1), which is illustrated by an exploded assembly drawing in Figure 5.19b. The process liquid enters the rectangular channel (width $a = 42 \text{ mm}$, height $b = 10 \text{ mm}$, length $L = 1.2 \text{ m}$) from the side labelled ‘Inlet’. Two cartridge heaters ($2 \times$ Acim Jouanin H8X40X200, total $q_{e,\text{max}} = 400 \text{ W}$) generate a heat flow from the copper block (labelled 6) through the sample plate (7), which sits flush with the channel walls (8). The bulk temperature gain across the heated section is ~5 mK under standard experimental conditions. Heating is thus confined to the thermal boundary layer, which minimises excessive heating of the recirculated foulant.

The sample rests on two channel inserts (9) made from PEEK and exposes a heat transfer surface of $A = 42 \times 50 \text{ mm}^2$ to the fluid. PEEK shows low creep at high temperatures and is thermally insulating. A thermally conductive pad (10) ensures good heat transfer between the copper block and the sample. Eight thermistors are inserted through boreholes (11) at different locations of the copper block to measure the temperatures at the interface to the thermally conductive pad. The heater temperature, T_{h} , is calculated as the arithmetic average of those readings. A silicone gasket (12) around the sample prevents leakage and reduces heat loss to the stainless steel channel walls. Heat loss is further reduced by silicone cladding (13) around the copper block. Six wing-nuts hold an aluminium compression plate (14) in place and allow quick assembly and removal of

heater and sample between experimental runs. On the other side of the channel, an acrylic window (15) allows the sample to be observed while processing transparent fluids.



(a) Photograph of bench-scale HEX rig.

(b) Exploded assembly drawing of the bench-scale HEX.

Figure 5.19: The bench-scale HEX assembly. Labels are explained in the text.

5.5.2 Control hard- & software

The control hard- and software are conceptually similar to ones designed for the microfluidic HEX system. A graphical process control user interface was programmed with TkInter (Python Software Foundation, 2016), shown in Appendix D. In the upper part of the interface, labelled (a), instantaneous measurement data are displayed and set-points can be selected in a process diagram. In the lower part of the interface, labelled (b), selected measurements are shown over time.

5.5.3 Thermo-hydraulic characterisation

As with the microfluidic HEX apparatus, experiments were performed under conditions of constant heat flux. The electrical resistance of the cartridge heaters was taken from the product data sheet. The required electrical heater power, q_e , to achieve a chosen mean surface temperature, $T_{s,m}$, of the HEX is calculated by taking heat loss to the environment, q_{env} , in Equation 5.2 into account. Separate tests at different heater temperatures were conducted where the flow channel was kept dry to simulate $q = 0$ and measure q_{env} . The results in Figure 5.20a are fitted with a power-law relationship for simple software implementation. In Figure 5.20b, the linear response of the power electronics and heater is demonstrated by measuring the heating rate, $dT_h/dt'|_{T_h \approx 100^\circ\text{C}}$, as a function of the set electrical heater power. $dT_h/dt'|_{T_h \approx 100^\circ\text{C}}$ was determined by measuring the change in heater temperature while heating for time intervals of 5 to 20 s. The reciprocal of the fitting coefficient in Figure 5.20b is the heat capacity of the heating unit. Assuming that most of the power is used to raise the temperature of the copper heater block, the specific heat capacity of copper is calculated to be $c_p = 377 \text{ J kg}^{-1} \text{ K}^{-1}$. This compares reasonably with the literature value of $384.6 \text{ J kg}^{-1} \text{ K}^{-1}$ (Atkins, 1986) and demonstrates that the heater power is determined and controlled correctly.

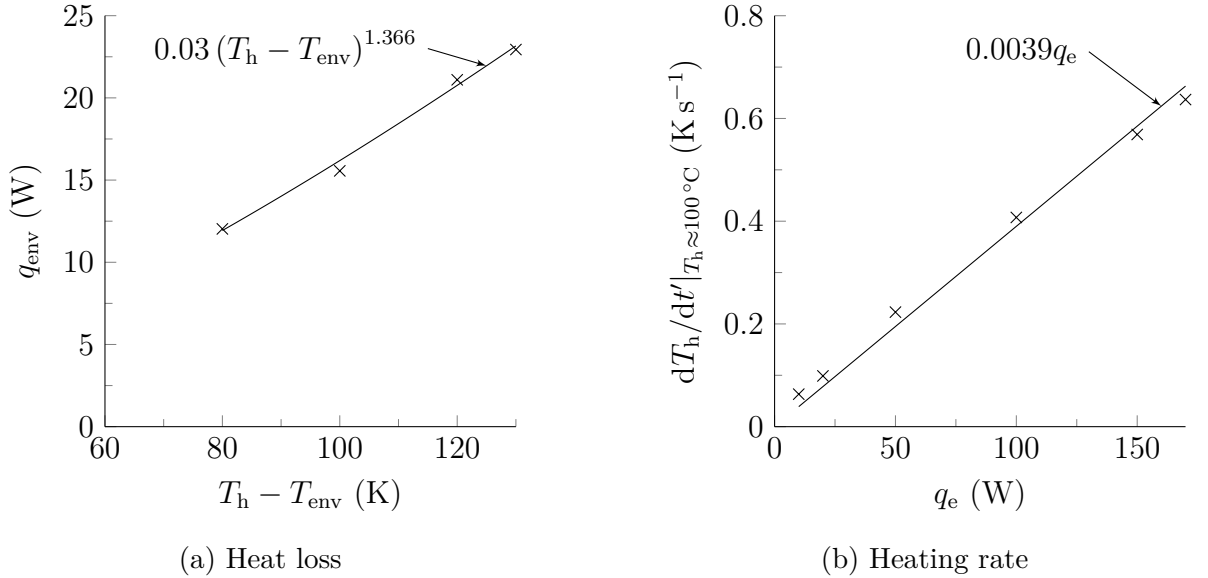


Figure 5.20: Bench-scale HEX heater characterisation: (a) steady state heat loss to the environment over temperature driving force at $T_{env} = 21^\circ\text{C}$ and (b) heating rate as a function of electrical heater power at $T_h \approx 100^\circ\text{C}$. The bench-scale HEX was drained in both cases, *i.e.* $q \approx 0$. Crosses – measurements; lines – root mean square fitted correlations.

To find the mean film heat transfer coefficient in Equation 5.2, it is rearranged to yield

$$h_m = \frac{q_e - q_{\text{env}}(T_h, T_{\text{env}})}{A \left(T_{s,m} - \frac{T_{\text{out}} + T_{\text{in}}}{2} \right)}. \quad (5.11)$$

Non-fouling experiments with water were carried out to find h_m for different flow rates. The mean surface temperature $T_{s,m}$ was estimated by employing a SS sample plate coated with water resistant thermochromic liquid crystals (coated by LCR Hallcrest with coating SLN40/R40C1W). Starting at 39.9°C, the black coating changes colour to red, green, blue, and back to black again. The onset temperature for colour change was verified by comparison against a second thermometer. During the experiments, the heater temperature, T_h , was increased until the middle third of the sample surface started to change colour. This situation was easy to identify, albeit somewhat arbitrary. An example of this is shown in Figure 5.21, where the indicated surface isotherm has a parabolic shape. The mean film heat transfer coefficients obtained are summarised in Figure 5.22. The flow in the channel was turbulent and the channel was hydrodynamically smooth at the tested flow rates. The Gnielinski correlation (see Equation 3.50) for hydrodynamically and thermally fully developed flow in circular pipes describes the data reasonably well. The Darcy friction factor in the Gnielinski correlation can be found with the Petukhov-correlation (Bergman & Incropera, 2011) which is valid for hydraulically smooth pipes, *viz.*

$$f_D = (0.790 \ln Re - 1.64)^{-2} \quad 3000 \lesssim Re \lesssim 5 \times 10^6. \quad (5.12)$$

In fouling experiments the Gnielinski and Petukhov correlations were used to estimate h_m in Equation 5.2 when calculating the required heat duty for the selected mean surface temperature.

Figure 5.23 shows data from further tests to determine the overall clean heat transfer coefficient, U_{cl} , using water at higher temperatures in an unpressurised HEX. There is a sharp increase in U_{cl} on increasing the heater temperature from 145°C to 150°C. This is likely to arise from the onset of nucleate boiling which increases heat transfer markedly. In milk fouling, boiling generally increases deposition (Burton, 1968; Jeurnink, 1995) and commercial pasteurisers avoid this regime by operating at elevated pressure (Bylund, 2015). To avoid phase changes of water and dissolved air, the bench-scale HEX was operated at 1.8 bar absolute pressure by closing the throttle valves at the flow channel outlet.



Figure 5.21: Thermochromic liquid crystal coated SS sample in bench-scale HEX observed through window. Onset of colour change in the middle third indicates a surface temperature of $\sim 40^\circ\text{C}$. White arrow indicates direction of flow and dashed curve illustrates a surface isotherm.

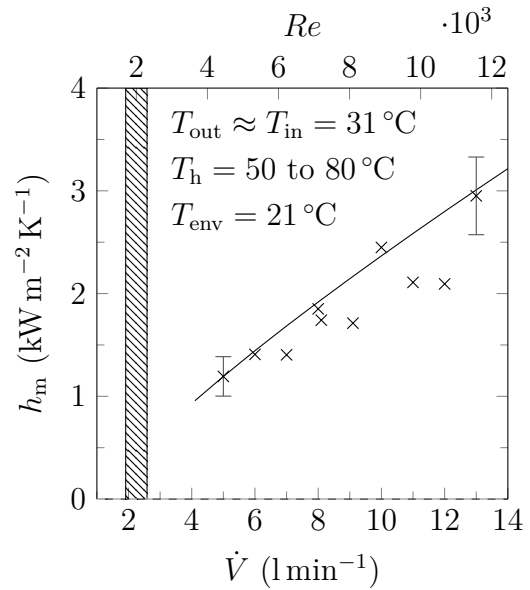


Figure 5.22: Bench-scale HEX mean film heat transfer coefficient, h_m , over volumetric flow rate, \dot{V} , and Reynolds number, Re . Crosses – measurements; Line – Gnielinski correlation (Equation 3.50). Error bars indicate estimated experimental standard deviation. Hatched area indicates the approximate transition zone from laminar to turbulent flow (Avila *et al.*, 2011).

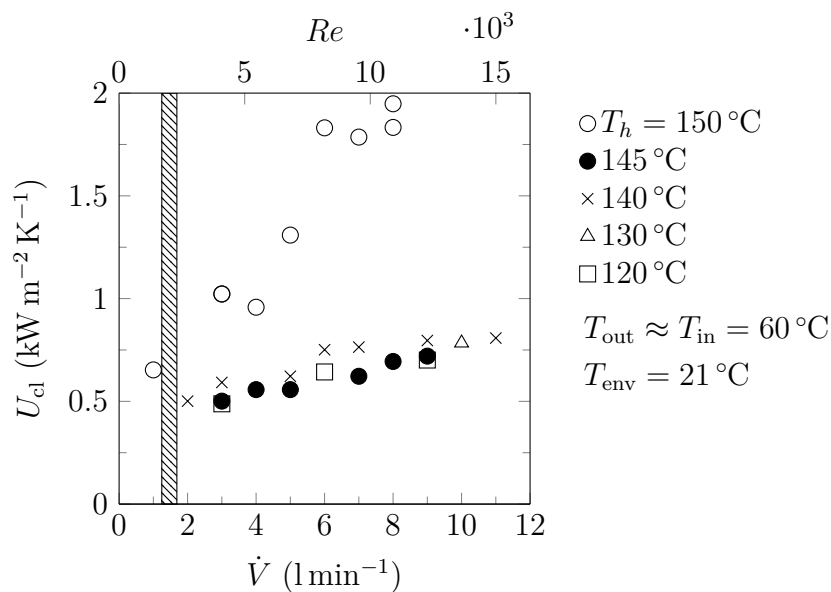


Figure 5.23: Overall heat transfer coefficient, U_{cl} , of unpressurised bench-scale HEX loaded with sample FEP-2 for different water flow rates, \dot{V} , and heater temperatures, T_h . Hatched area – transition zone from laminar to turbulent (Avila *et al.*, 2011).

5.5.4 Whey protein solution and raw milk fouling studies on steel and fluoropolymer surfaces

Experimental protocol

Before the experiment, piping and tanks were sanitised by circulating hot water at 75 °C. Figure 5.24 shows an example of the subsequent evolution of the monitored variables during a fouling test. Initially, deionised water was pumped through the HEX until thermal steady state was reached for the desired mean surface temperature (marked t'_1 in Figure 5.24).

The liquid was then switched to raw milk or, as in this case, WP solution and the figure shows a steady increase in T_h and drop in U as deposition occurred. A mean surface temperature $T_{s,m} = 89$ °C, a volumetric flow rate of $\dot{V} = 8$ l min⁻¹, and a bulk temperature of $T_{b,t1} = 61$ °C was used for all bench scale HEX experiments, except where noted otherwise. In some tests, 10 g l⁻¹ milk fat was added to the WP solution in the form of single cream before the experiment. The cream mixed in easily and made the solution more opaque.

During the processing period, the fouling resistance, R_f , was calculated according to Equation 3.1. Unlike with the microfluidic HEX, the increase in pressure drop was not statistically significant as the deposit thickness is small compared to the channel height. At time t'_2 the HEX heater was turned off and cooled to ~ 70 °C. The flow was then stopped and the HEX was drained and disassembled (see Figure 5.19b) to remove the test plate and dry the deposit before weighing.

Following an experiment the test plate was cleaned in six steps: (i) washed with a commercial dishwashing detergent, (ii) rinsed with water, (iii) washed with 1 M sodium hydroxide, (iv) rinsed with water, (v) washed with 0.5 M phosphoric acid and (vi) rinsed again. The HEX rig was cleaned with a SS dummy sample in place, with three steps: (i) circulation of 0.2 M sodium hydroxide at 50 °C for 15 min, (ii) neutralisation to pH 7 with phosphoric acid at ambient temperature and draining, (iii) circulation and draining of several 17 l deionised water batches at ambient temperature. Each test plate was re-used frequently and the clean performance monitored to determine whether irreversible changes occurred.

The pH of the foulant solution was monitored continuously with a Fisher Scientific Accumet AB15 meter. It was found that the thermal sanitation stage at the beginning of the experiment is necessary to kill thermophilic bacteria hosted by the experimental equipment which otherwise proliferate during the processing period. Figure 5.25 shows

the evolution of fouling resistance in the rig processing WP solution if the sanitation step was not conducted. The excretion of acids from bacteria reduces pH over time and accelerates fouling after 150 min to yield a thick deposit shown later in Figure 5.33a,iii (see studies on pH in milk fouling by Bansal & Chen, 2006; Foster *et al.*, 1989; Skudder, Brooker, Bonsey, & Alvarez-Guerrero, 1986). The pH in an idle tank (no processing, all valves shut, $T_{b,t1} = 61\text{ }^\circ\text{C}$) is constant for 230 min, indicating that the thermophiles reside primarily in the piping and flow channel.

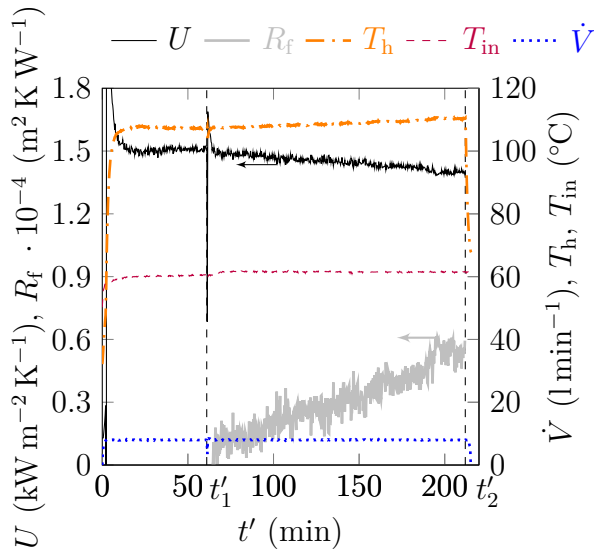


Figure 5.24: Example of bench-scale HEX monitoring record for a WP fouling test on SS. U and R_f – left axis; \dot{V} and temperatures – right axis. Vertical dashed line at t'_1 indicates when flow was changed from water to WP solution, t'_2 indicates end of experiment.

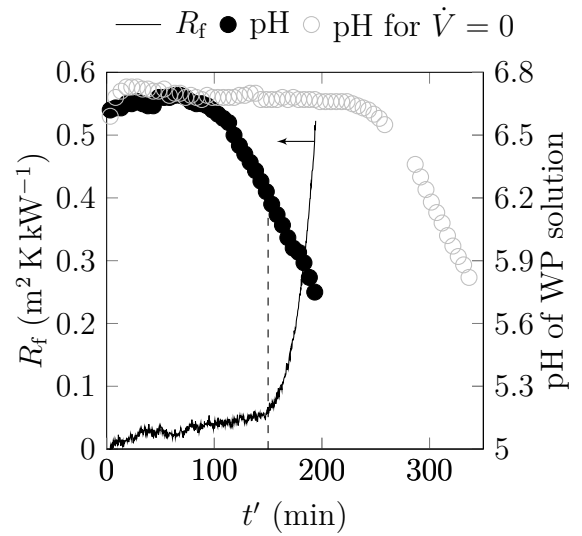


Figure 5.25: Evolution of fouling resistance, R_f , and pH (solid circles) for a bench-scale HEX fouling test with WP solution on SS. Hollow circles show pH evolution of WP solution in a stirred idle tank, *i.e.* $\dot{V} = 0$, at $T_{b,t1} = 61\text{ }^\circ\text{C}$. The dashed vertical line indicates the onset of rapid fouling.

Evolution of pH

Figure 5.26a shows that the pH of the WP solution remained constant at ~ 6.75 during processing. Adding cream did not change the pH of the WP solution significantly. The pH in raw milk (Figure 5.26b) was initially lower, at 6.6, and decreased gradually over time.

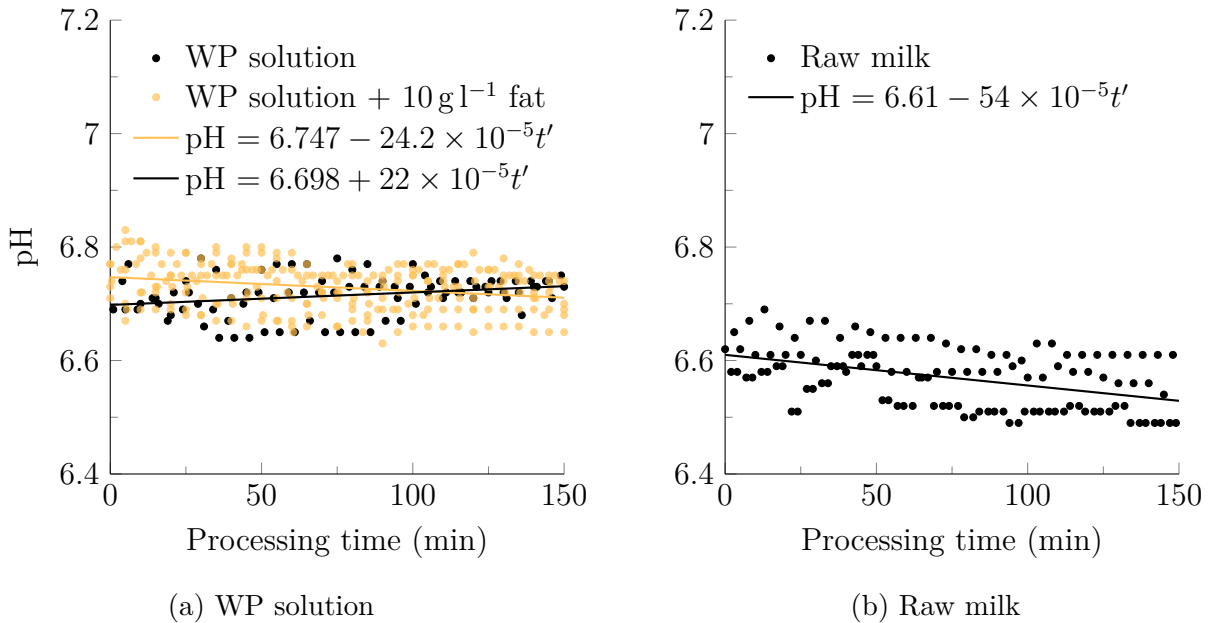


Figure 5.26: pH evolution of (a) WP solutions and (b) raw milk during bench-scale HEX fouling experiments. Straight lines are root mean square fitted to the data.

Evolution of fouling resistance

The evolution of fouling resistance while processing WP solution was measured for five different surfaces and results are shown in Figure 5.27. In Figure 5.27a, two groups of surfaces can be identified: (i) FEP-2 with a fouling rate of $\sim 0.04 \text{ m}^2 \text{ K kW}^{-1} \text{ h}^{-1}$, and (ii) SS, FEP-3, and PFA-4 with a fouling rate of $\sim 0.02 \text{ m}^2 \text{ K kW}^{-1} \text{ h}^{-1}$. These rates are intermediate between the fouling resistances estimated from pressure drop data (*c.f.* $0.16 \text{ m}^2 \text{ K kW}^{-1} \text{ h}^{-1}$ for SS and $0.06 \text{ m}^2 \text{ K kW}^{-1} \text{ h}^{-1}$ for FEP-2) and thermal data (*c.f.* $0.0125 \text{ m}^2 \text{ K kW}^{-1} \text{ h}^{-1}$ for SS and FEP-2) obtained from experiments using raw milk in the microfluidic HEX. Boxler *et al.* (2013c) reported a similar fouling rate of $0.019 \text{ m}^2 \text{ K kW}^{-1} \text{ h}^{-1}$ for a SS laboratory plate HEX heating 55 g l^{-1} WP isolate in a milk salt solution from 62°C to 85°C . Compared to WP concentrate, WP isolate contains a very small amount of lactose.

An induction period (see Section 3.2.1 for definition) was not observed for SS or the FPs. For PP, however, an induction period of 75 min is evident in Figure 5.27b. Large standard errors (shaded bands) indicate large variance between repeated measurements. The final fouling Biot numbers ranged from 0.04 for PFA-4 to 0.09 for SS and FEP-2. Further comparative analysis on the basis of fouling resistance is speculative and is thus not carried out here.

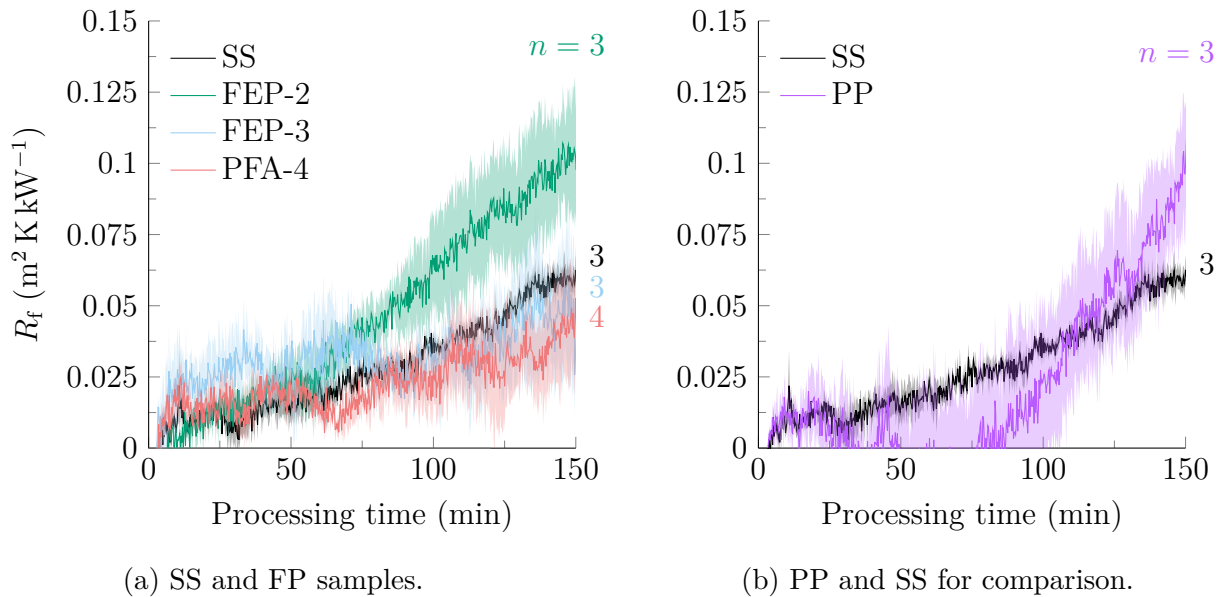


Figure 5.27: Fouling resistance profiles for fouling tests with bench-scale HEX using WP solution. n indicates the number of experiments performed. Shaded bands indicate \pm standard error.

Figure 5.28a shows that the fouling rates decreased for all three classes of surface when cream was added to the WP solution. Some tests with raw milk on SS and FEP-3 were carried out for comparison. Fouling with raw milk tended to be less than with WP solution. To generate more deposit, the mean surface temperature was set to $T_s = 92.5^\circ\text{C}$. Nevertheless, it is apparent from Figure 5.28b that this still gave small fouling resistances. Although the heat duty was corrected to give the set mean surface temperature at a higher process fluid viscosity, increased shear stress may have let to the low deposition rates.

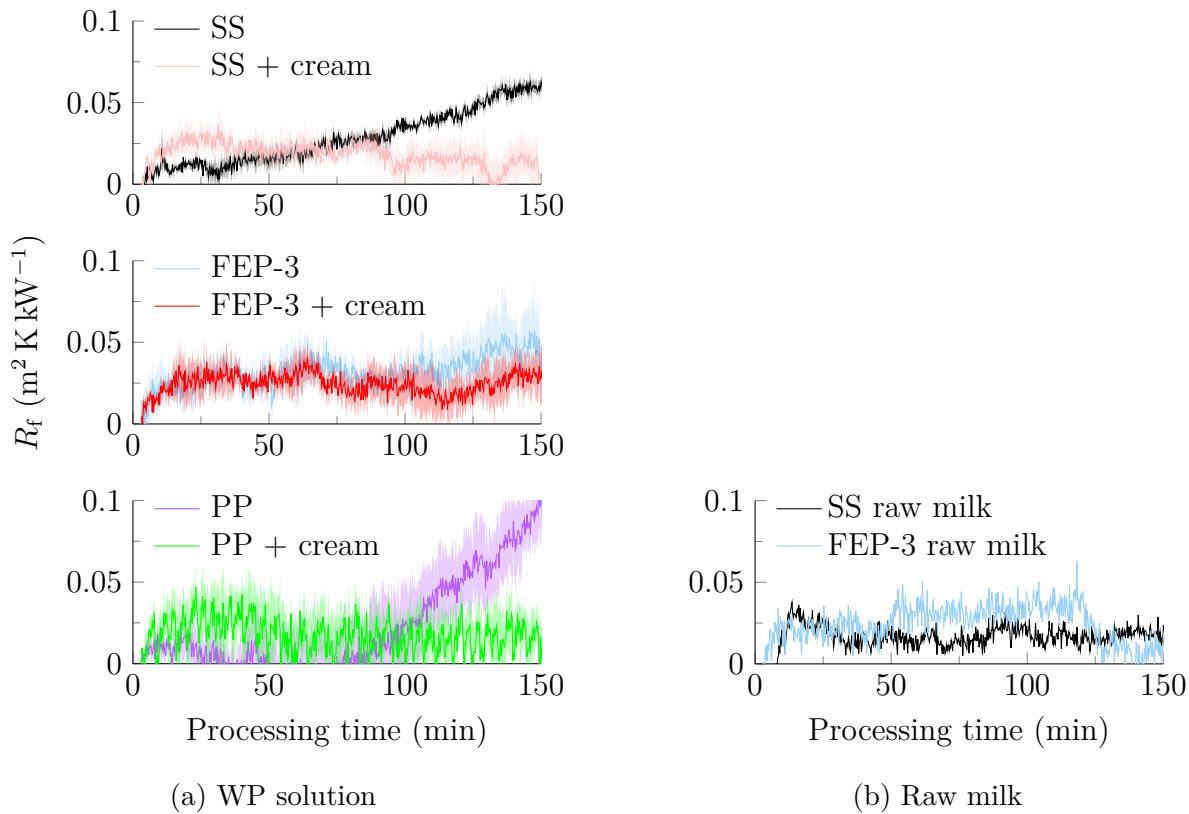


Figure 5.28: Fouling resistance profiles for fouling tests in bench-scale HEX with (a) WP solution with 10 g l^{-1} milk fat added at $T_s = 89^\circ\text{C}$ and (b) raw milk at $T_s = 92.5^\circ\text{C}$. In (a), upper reference data shows fouling resistance for WP solution with no added fat. Each experiment in (a) was repeated three times and single tests were performed with raw milk in (b). Shaded bands indicate \pm standard error.

Deposit coverage

The deposit coverages for these tests are presented in Figure 5.29. 90% confidence intervals, from repeated experiments, indicate a smaller variance than with fouling resistance. In plain WP experiments, all the coatings exhibited significantly better performance in mitigating mass deposition than SS, with FEP-3 and PFA-4 performing best. Deposit coverage was reduced by 50% when replacing SS with FEP-3.

The average mass deposition rate for SS of $1.5 \text{ mg m}^{-2} \text{ s}^{-1}$ was somewhat smaller than the rate reported by Belmar-Beiny *et al.* (1993) and much smaller than the mass deposition rate with the microfluidic HEX using raw milk (*c.f.* $5.1 \text{ mg m}^{-2} \text{ s}^{-1}$). Belmar-Beiny *et al.* processed a similar WP concentrate (35% g g^{-1} protein, 50% g g^{-1} lactose, 4.5% g g^{-1} fat and 6.5% g g^{-1} minerals) with a final protein concentration of $\sim 10 \text{ g l}^{-1}$ in solution (*cf.*

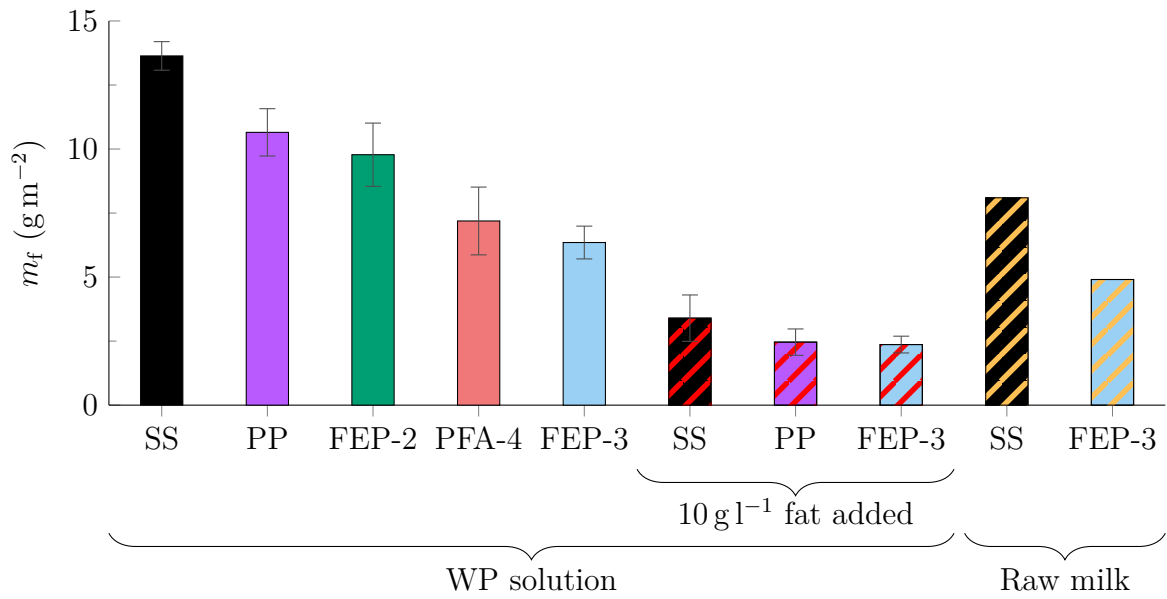


Figure 5.29: Deposit coverage (dry mass per area) for different surfaces tested in the bench-scale HEX for a duration of 150 min. Error bars show 90 % confidence intervals.

6.2 g l^{-1} here) in a tubular SS heat exchanger at surface temperatures of around 80°C and Reynolds numbers ranging from 2000 to 7000. At $Re = 7000$ their mass deposition rate on SS was $2.5 \text{ mg m}^{-2} \text{ s}^{-1}$ which gave a mass coverage of 9 g m^{-2} at the end of 1 h of operation. Important reasons for their higher deposition rate are the length of their heated section (*c.f.* 2.5 m and 0.05 m here), higher bulk temperatures as well as higher WP concentration.

Adding cream to the WP solution reduced the deposit coverage on all surfaces tested. Among the experiments with added cream, the differences in coverage were not statistically significant on a 90 % confidence basis, which is consistent with the fouling resistance data. Experiments with raw milk gave deposit coverages between those of the WP solution with and without added cream. The relative performance of FEP-3 and SS was comparable with that obtained for WP solution.

Comparison of the mass coverage with the fouling resistance data allows to deduce information about the structure and composition of the fouling deposits. Assuming the deposit to be a uniform slab, Equation 3.44 is used: $R_f = m_f / \rho_f k_f$. A large value of $\rho_f k_f$ generally indicates a dense deposit with high thermal conductivity. Note that all variables in Equation 3.44 correspond to properties of the wet layer. Here, m_f was measured after drying, so Equation 3.44 is used to identify differences in structure and composition rather than absolute values of $\rho_f k_f$. Figure 5.30 shows that deposit from WP solution on apolar surfaces is generally different in structure and/or composition than deposit generated on

SS. This applies both for smooth PP and rough PFA-4. The deposit on apolar surfaces shares a common $\rho_f k_f$ which is twice as high as the one for deposit generated on SS. This indicates that the latter deposit is significantly denser and/or more thermally conductive. The fouling resistances from the tests with added cream and from the tests with raw milk were too small to study this relationship.

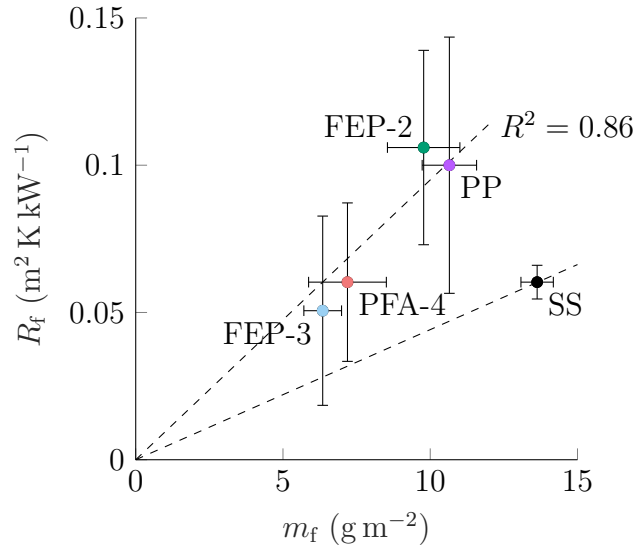


Figure 5.30: Relationship between final fouling resistance and whey protein dry deposit mass coverage for different surfaces tested with the bench-scale HEX. Dashed lines show root mean square fitted equation $R_f = m_f / \rho_f k_f$ to find values of $\rho_f k_f$ for polymer surfaces and SS. For polymer surfaces $\rho_f k_f = 105 \text{ kg}^2 \text{ m}^{-2} \text{ s}^{-3} \text{ K}^{-1}$ and for SS $\rho_f k_f = 226 \text{ kg}^2 \text{ m}^{-2} \text{ s}^{-3} \text{ K}^{-1}$. Error bars show 90% confidence intervals.

Calcium fractions in whey protein and raw milk deposits

The calcium contents of selected deposits were determined with ICP-MS and the results are reported in Table 5.5. The calcium fraction of the deposits from WP solution was low for all surfaces and matched approximately the fraction of 6 mg g^{-1} in the WP powder. Thermogravimetric data from deposits on SS and PP (Figure A.1c and d in Appendix A) indicated that they were devoid of lactose (*c.f.* WP concentrate data in Figure A.1b) and featured distinctive peaks of protein degradation also seen in data from pure β -LG (Figure A.1a). The degradation patterns of deposits generated on SS and PP were very similar up to 400°C : above this temperature the data was not reproducible. This indicates that the WP deposits had similar composition but differed in structure.

The calcium content of deposits from the raw milk was noticeably higher, by a factor of approximately 10. Taking there to be 0.1 g g^{-1} solids in raw milk, the calcium content

in the raw milk fouling deposits was about 10 times higher than in milk solids. The SS deposit contained 25% more calcium than FEP-3 deposit. The calcium fractions determined in this work lie within the range reported in the literature. Other researchers have measured a calcium fraction of around 5% g g^{-1} in deposits from raw milk generated at 100 °C on SS after 120 min of processing (Foster *et al.*, 1989). Visser and Jeurink (1997) determined 15.7% g g^{-1} calcium in deposit generated from skim milk at 69–85 °C bulk temperature. The amounts of deposit recovered from experiments with added cream were too small for compositional analysis.

Table 5.5: Calcium fraction of solution dry solids (reproduced from Table 5.1 and 5.3) and fouling deposits determined by ICP-MS. The raw milk dry solids calcium fraction is calculated by assuming 0.1 g g^{-1} dry solids.

Foulant	WP solution					raw milk	
Foulant solution solids (mg g^{-1})	6					~10	
Surface	SS	PP	FEP-2	PFA-4	FEP-3	SS	FEP-3
Deposit (mg g^{-1})	5.1	6.8	7.5	7.3	6.6	92.3	74.1

Calcium and protein distribution in whey protein deposit

The raw milk deposits from the microfluidic HEX featured more protein at the substrate-fouling interface on the apolar surfaces. The CLSM micrographs in Figure 5.31 demonstrate that the local protein and calcium fraction in WP deposits from the bench-scale HEX were not affected by the nature of the surface. However, the micrographs give further evidence for a less dense, spongy structure on PFA-4 (see asterisk in Figure 5.31b).

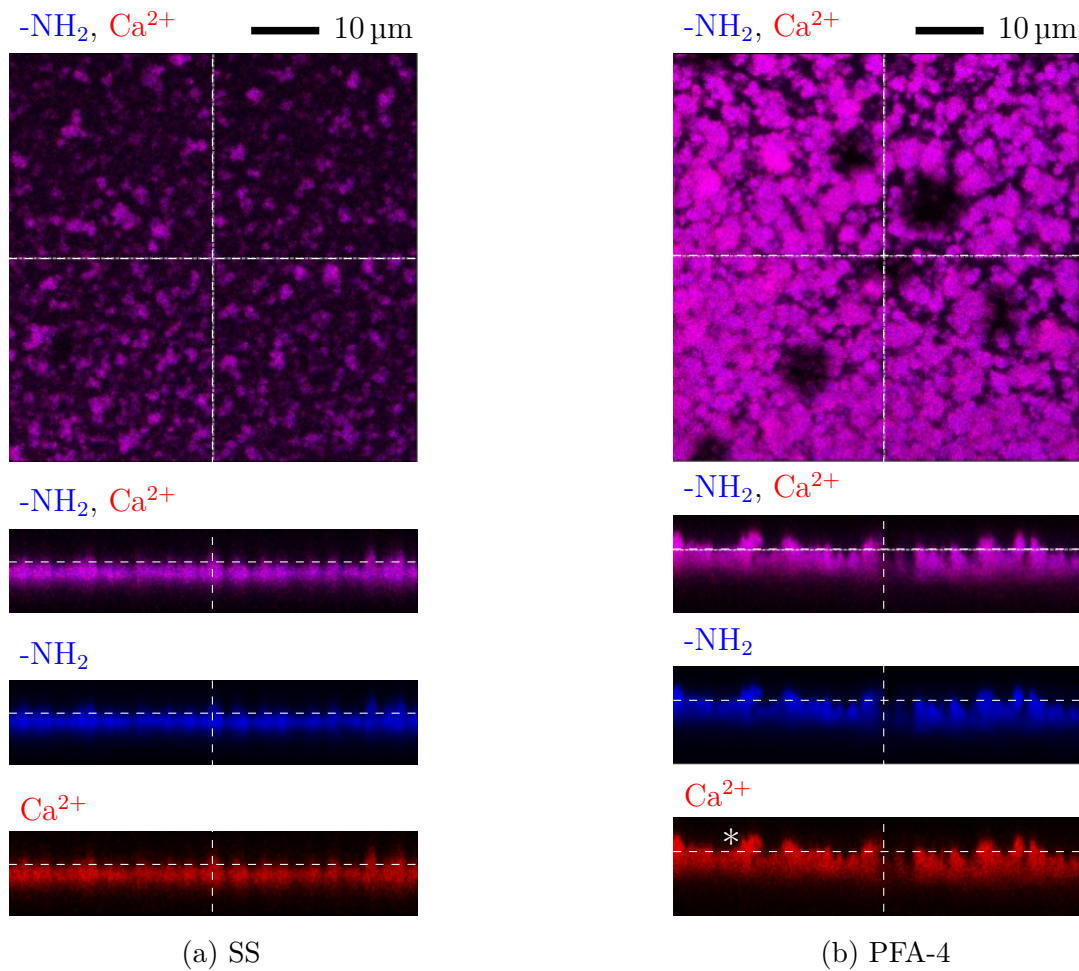


Figure 5.31: CLSM top views and orthogonal sections of whey protein fouling layers from the bench-scale HEX on (a) SS and (b) PFA-4. The channels for amine and calcium signals are labelled -NH_2 and Ca^{2+} , respectively. -NH_2 , Ca^{2+} designates superimposed channels. Images taken *ex situ* with $40\times$ oil immersion lens.

Fat in deposits from WP solution with added cream

The amount of fat incorporated into the deposits from WP solution with added cream varied strongly with the type of surface. On SS, only a few isolated fat droplets were found with CLSM as shown in Figure 5.32a. Fat in deposits on FEP-3 was arranged in clusters resembling the shapes of valleys in the surface topography (*c.f.* 5.32b and 4.1g).

This is further evidence that fat can conceal concave topography features of FP coatings as experiments with the microfluidic HEX suggested. On PP, the adsorption of numerous fat droplets of many sizes was evident (Figure 5.32c). The sizes of these droplets were comparable to the sizes of milk fat globules (see Appendix B). The fat on PP did not merge to form clusters to the same extent as observed on FEP-3.

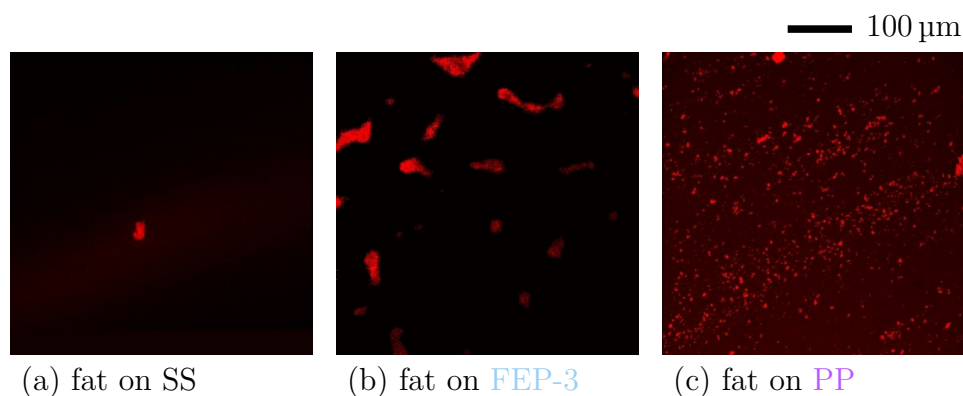


Figure 5.32: CLSM micrographs of fat at the deposit-sample interface from bench-scale HEX tests using WP solution with added cream on (a) SS, (b) FEP-3, and (c) PP. Red indicates fat stained with Nile blue A and images were taken with a $10\times$ lens with excitation at 633 nm.

Deposit photographs and thickness scans

Photographs of air-dried deposits sorted by surface type and foulant are arranged in Figure 5.33. The layers were thinner at the upstream and downstream edges of the samples and thickest at the sides of the channel.

On SS (photographs a,ii-v), the deposit was firmly attached and white-grey in colour. When there was no initial sanitation step and a pH drop occurred (see Figure 5.25), the deposit was thicker and featured a mud cracking pattern on the sub-millimetre scale (a,iii). In general, deposit from WP solution appeared to be homogeneous and was cleaned easily with 0.5 M NaOH. The deposit from raw milk (a,v) was rougher and did not develop into a homogeneous film. When cleaning it with 0.5 M NaOH, a thin mineral layer remained at the steel surface.

On PP, layers formed with the WP solution cracked and flaked off after the first seconds of drying at ambient conditions (b,iii), but the addition of cream resulted in thin deposits which remained attached and were oily to the touch (b,iv). Similar behaviour was found for FEP-3 (c,iv) if cream was added. WP deposits on FEP-2 (c,i) detached but also cracked in the centre of the sample surface, while they exclusively detached at the sides on FEP-3 (c,ii) and PFA-4 (c,iii). FEP-3 generated deposit with distinct features when processing raw milk (c,v): Deposits curled themselves up in numerous places, forming coils of up to 1 mm diameter and 3 mm to 15 mm length.

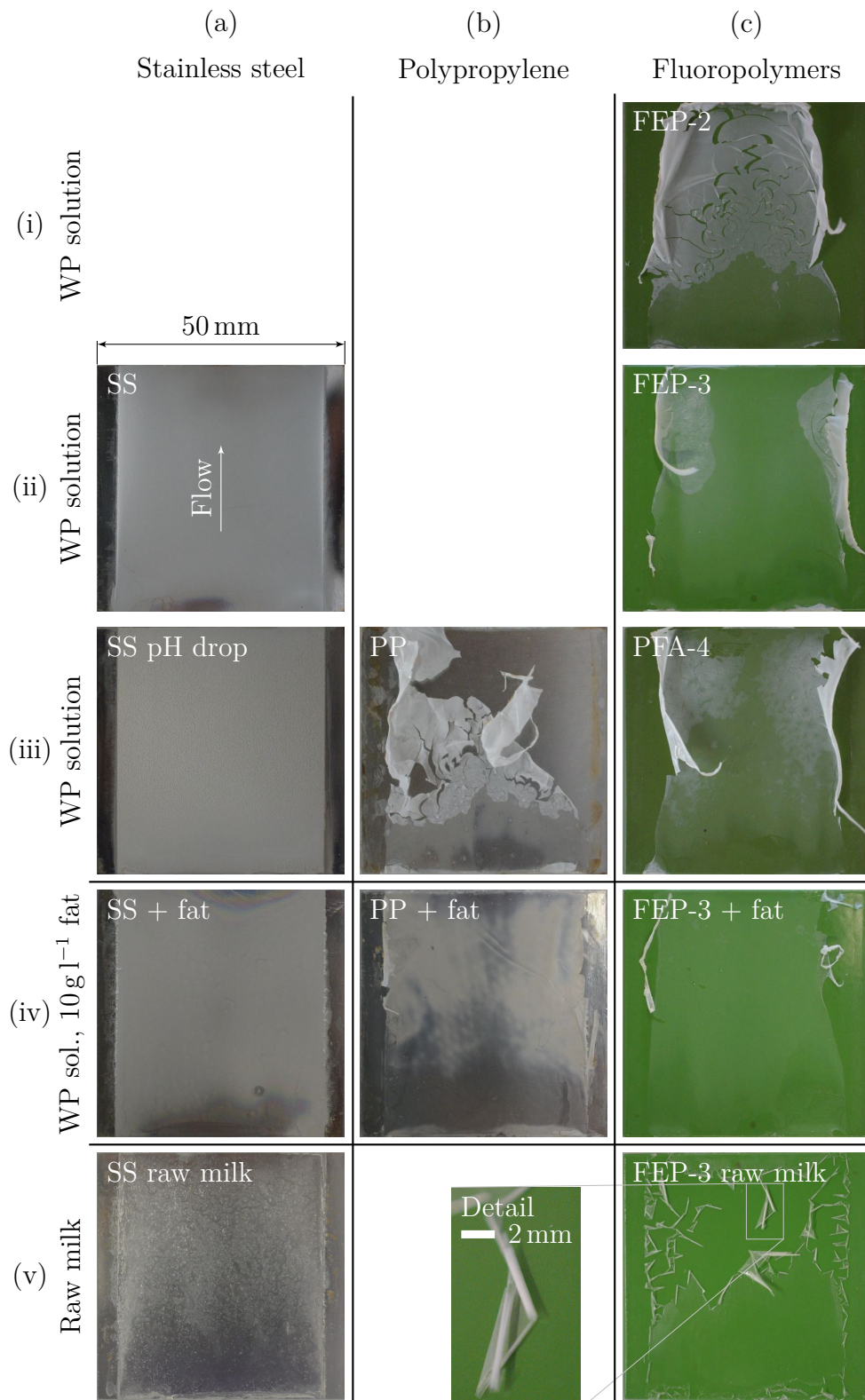


Figure 5.33: Representative photographs of dried deposits from bench-scale HEX after 150 min of processing WP solution at $\dot{V} = 81 \text{ min}^{-1}$, $T_{s,m} = 89^\circ\text{C}$, $T_{b,t1} = 61^\circ\text{C}$ on (a) SS, (b) PP, and (c) FPs. Tests in row (iv) had 10 g l^{-1} milk fat added and (a,iii) shows deposit on SS after 195 min of processing WP solution without the initial sanitation stage. $T_{s,m}$ was set to 92.5°C when processing raw milk.

Circular patterns from air bubble growth reported by some researchers (Barish & Goddard, 2013; Boxler *et al.*, 2013b; Lin & Chen, 2007) were not observed on any of the surfaces, indicating that pressurising the channel successfully suppressed air nucleation and boiling. No deposition was observed downstream of the heated stage and there were no changes of the surfaces visible to the naked eye after repeated use.

Some deposits from WP solution were scanned with the CTS tool (Section 5.3.2). Deposit thickness maps are presented in Figure 5.34. The thickness on SS ranged up to 60 μm but was limited to around 30 μm on other samples. On SS (a), thickness contours follow surface isotherms evident in the thermochromic liquid crystal heat transfer tests (Figure 5.21), confirming the fouling rate to be strongly temperature dependent. On FEP-3 (b), the fouling thickness appears to increase linearly with distance from the leading edge. In the white areas on this plot, the data were out of range due to the fouling layer lifting up at the sides.

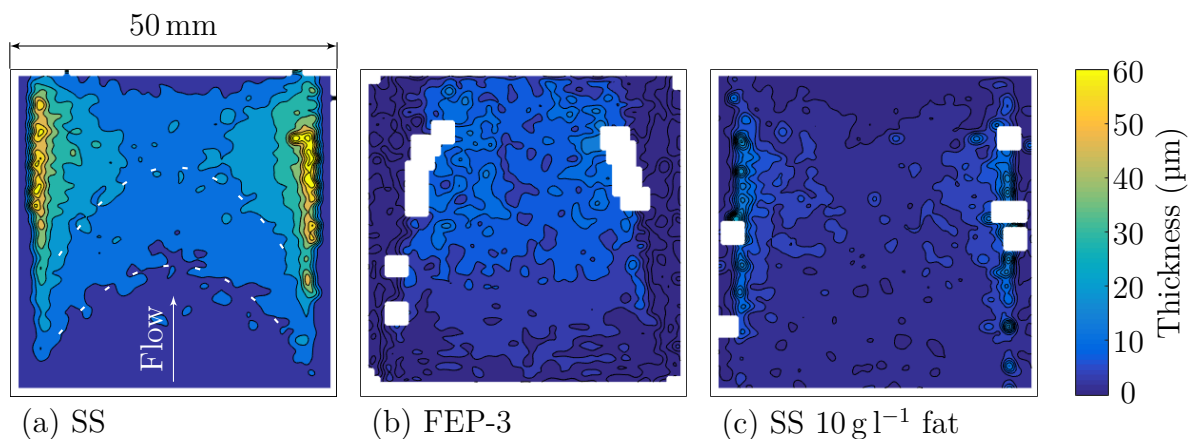


Figure 5.34: Dry thickness of deposit from WP solution generated in the bench-scale HEX on (a,c) SS and (b) FEP-3 determined by CTS. Dashed lines highlight contours. Figure (c) shows deposit thickness on SS from WP solution with 1% g g^{-1} milk fat added. Colour scale is uniform for all three plots. White areas indicate values out of range.

Adding cream to the WP solution (c) reduced the thickness of the deposit, in agreement with the fouling resistance and mass coverage data. All deposition patterns were axisymmetric along the channel's principal axis, indicating satisfactory thermal contact with the heater and symmetric flow fields.

The effect of flow rate on WP fouling

The behaviour of dried dairy deposits indicated that their adhesion to apolar surfaces is weaker than to SS. Thus, the effect of flow rate (and hence shear stress) in WP fouling was studied in the range from 5 l min^{-1} to 8 l min^{-1} for SS and for PFA-4 as a representative FP. All other variables were left unchanged and the surface temperature was maintained at $T_s = 89^\circ\text{C}$ by adjusting the required heat duty according to Equation 5.2. Higher flow rates than 8 l min^{-1} could not be achieved because that would have required the heater temperature to be raised above the maximum operating temperature of 160°C . Maintaining the assumption of a hydraulically smooth pipe, the Darcy friction factor, f_D , is estimated with the Petukhov correlation (see Equation 5.12) and inserted into the Darcy–Weisbach equation to estimate the mean surface shear stress (Bergman & Incropera, 2011)

$$\tau_m = \frac{1}{8} \rho f_D \left(\frac{\dot{V}}{ab} \right)^2. \quad (5.13)$$

The thermophysical properties of WP solution are approximated as those of water (VDI, 2010). The deposit coverage from fouling experiments at different flow rates is presented in Figure 5.35a. From 5 l min^{-1} to 7 l min^{-1} the deposit coverage on PFA-4 is slightly higher than for SS and increases for both surfaces with a similar trend. Above 7 l min^{-1} , the deposit coverage on PFA-4 reduces by 50 % compared to SS.

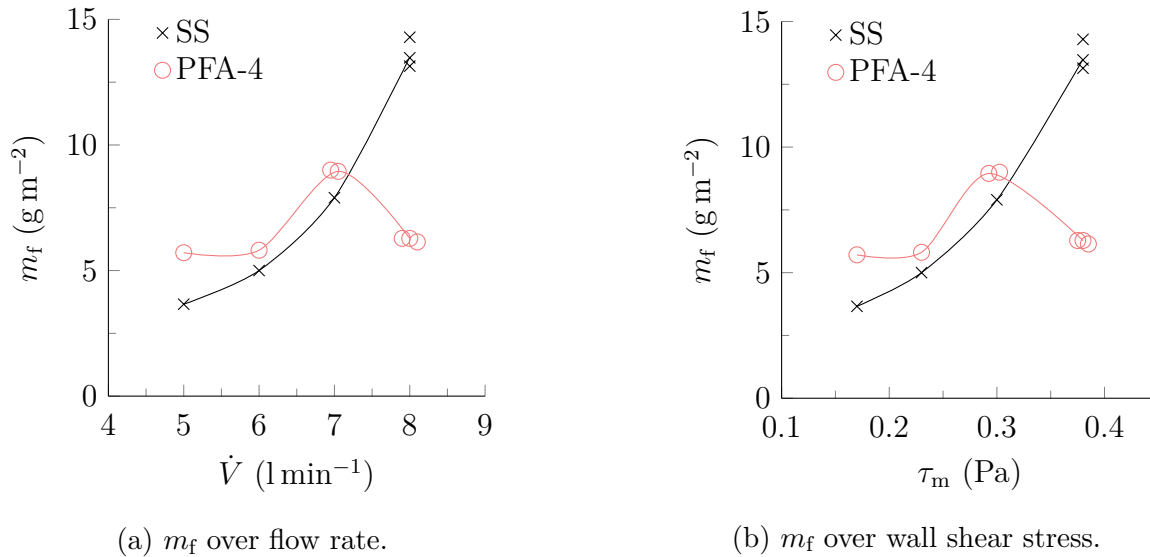


Figure 5.35: Deposit coverage (dry mass per area), m_f , from WP solution in the bench-scale HEX after a test duration of 150 min at $T_s = 89^\circ\text{C}$ for different (a) flow rates, \dot{V} , and (b) corresponding average wall shear stresses, τ_m . Some circles were offset horizontally for readability and lines are a guide to the eye.

Figure 5.35b presents the deposit coverage over the corresponding shear stresses determined using Equation 5.13. Even though the coverage on SS increases more gradually over shear stress than flow rate, the increase is still disproportionately large. The fouling resistance data for experiments at flow rates from 51 min^{-1} to 81 min^{-1} are shown in Figure 5.36. Note that for SS in (a) and PFA-4 in (b) the fouling resistances become negative, which indicates drifts in the overall heat transfer coefficient independent of fouling.

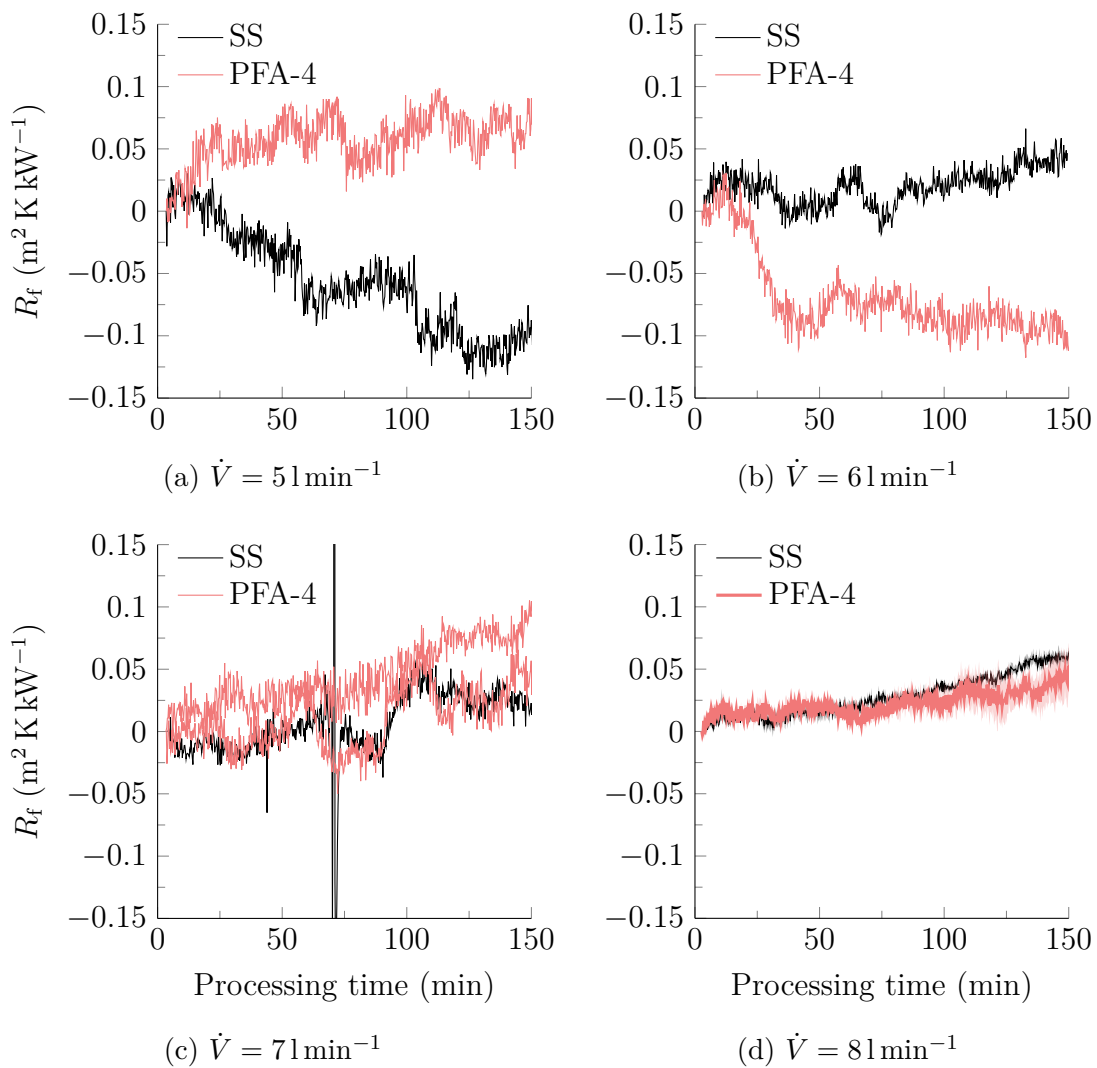


Figure 5.36: Fouling resistance profiles for fouling tests in bench-scale HEX with WP solution at $T_s = 89^\circ\text{C}$ for different flow rates. Experiments were performed once for graphs in (a-c) and repeated three times for (d). Graphs in (d) are reproduced from Figure 5.27a for completeness. Shaded bands in (d) indicate \pm standard error. Note: there seems to be a change in overall thermal conductivity independent of fouling, especially in (a-c).

Visual inspection (see Figure 5.37) reveals that the appearance of deposits varies slightly with flow rate. More white deposit on SS at the sides of the channel indicates higher mass coverage with increasing flow rate (*c.f.* (a) and (c)). The appearance of deposit on PFA-4 is similar for all flow rates tested. Due to higher flow velocities in the centre of the channel, heat transfer is more efficient in the middle of the sample, which can be seen in Figure 5.21, where the regions near the wall became hotter. If fouling occurs primarily at the sides of the sample, the overall heat transfer coefficient is not affected to the same extent as if there would be a uniform fouling layer. Hence, although deposit coverage on SS increased more than three-fold between 51 min^{-1} and 81 min^{-1} there was only a small effect on heat transfer.

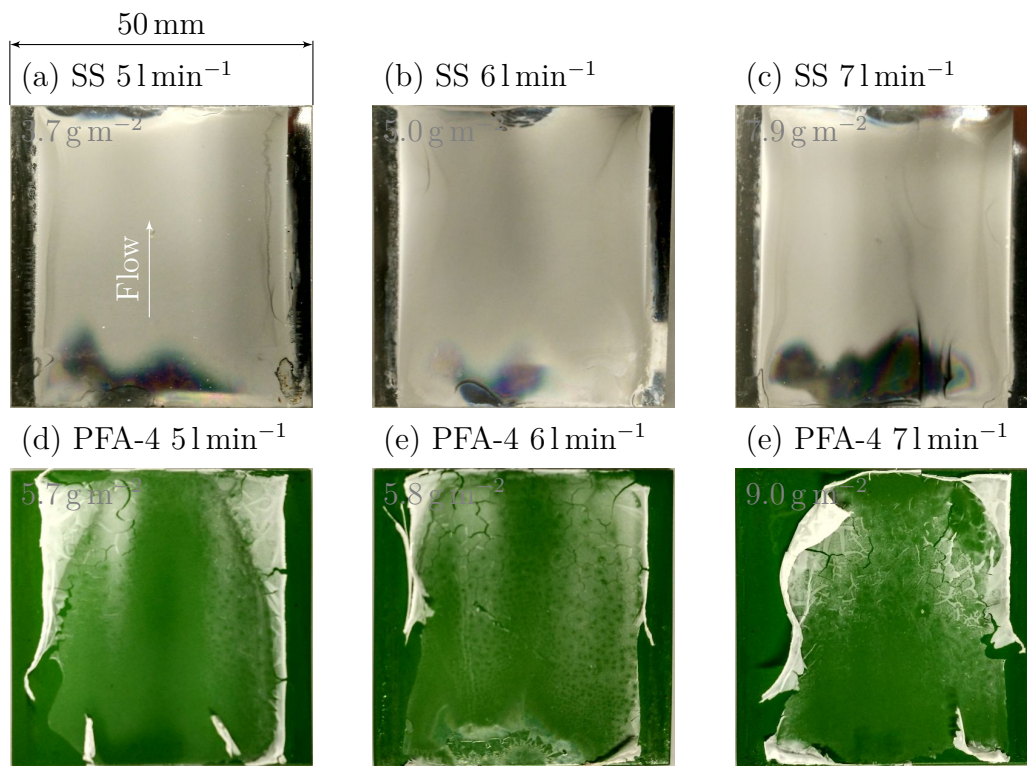


Figure 5.37: Representative pictures of dried deposits from bench-scale HEX after 150 min of processing WP solution at $\dot{V} = 51 \text{ min}^{-1}$ to 71 min^{-1} , $T_{s,m} = 89^\circ\text{C}$, $T_{b,t1} = 61^\circ\text{C}$ on SS (a-c) and and PFA-4 (d-e). Pictures of deposits at 81 min^{-1} are presented in Figure 5.33.

Discussion

By introducing the sanitation step at the beginning of the experiments, the pH of the WP solution remained constant and decreased slightly in raw milk. Severe thermal processing

of milk is known to reduce pH by shifts in the mineral balance, lipolysis and breakdown of lactose to organic acids (Adnan, 2009). Most importantly, dissolved calcium and phosphate become supersaturated at elevated temperature and associate with casein micelles. Walstra *et al.* (2005) noted that the molar ratio of Ca/P ≈ 1 of additionally formed calcium phosphate suggests the following simplified reaction



This reaction makes the milk become more acidic over time. The presence of about ten times more calcium in raw milk than in WP solution could explain why pH decreased measurably in milk. At the same time, less than 10% of the calcium in the solution would be expected to have crystallised after 150 min at a bulk temperature of 60 °C (see Figure 2.8 in Walstra *et al.*, 2005).

The fouling mass coverage from WP solution on PP was significantly higher than on FEP-3 and PFA-4. FPs as a group significantly outperformed SS, with the smoothest surface, FEP-3, accumulating 50% less mass. When adding cream, the deposit mass coverages reduced further but the differences in performances diminished. This surprising result suggests that milk fat plays a greater role in milk fouling at the conditions tested than inferred from experiments by previous workers (Foster *et al.*, 1989; Visser & Jeurnink, 1997). The recirculating flow scheme, shear stress in throttle valves, and relatively high bulk temperature may have led to the association of WP with milk fat (Lee & Sherbon, 2002). Bound fatty acids stabilise β -LG against denaturation (Considine *et al.*, 2007) – reducing the fouling potential of the solution for all surfaces. Processing raw milk gave 40% less mass coverage on FEP-3 than on SS, hence the relative performance with raw milk was comparable to using WP solution.

In contrast to the fouling mass coverage, no statistically significant reduction in fouling resistance relative to SS could be measured with any of the polymeric surfaces for either WP solution or raw milk. The variance in measured fouling resistance for repeated experiments does not allow detailed comparative analysis on this basis. It has been observed in Figure 5.36a,b that the overall heat transfer coefficient can change even at non-fouling conditions due to changes of the thermal conduction in the rest of the heated stack (sample – thermal interface pad – heater – thermistors). Water penetrating the interfaces between components during experiments was also observed a few times. This rendered precise measurement of fouling resistance challenging, although repeatability of the experimental conditions was excellent (see confidence intervals in Figure 5.29).

Some basic conclusions can be drawn from fouling resistance data, however: the induction period found for PP in Figure 5.27b may be caused due to enhanced film heat transfer

linked to growing structures on the smooth surface (see Section 3.2.1). In tests with the smooth SS surfaces this phenomenon was not observed, which indicates that the induction period on PP may indeed be caused by slow initial mass deposition. McGuire and Swartzel (1989) hypothesised that a surface material evoking minimal adhesion of substances from milk has a surface energy of around 30 mJ m^{-2} .

The amount of fat incorporated into the deposits from WP solution with added cream was found to depend strongly on the type of surface. Kiely and Olson (2003) estimated the surface energy components of MFGs shown in Table 4.2. The interfacial free energy of interaction, $\Delta G_{123}^{\text{IF}}$, can be calculated for MFGs in a similar manner to that for β -LG. Deeper insight is gained, however, by estimating the decay of ΔG_{123} of a MFG with diameter D over the separation distance from the heat transfer surface using Equation 2.6 and 2.7. Interaction potentials of a MFG in the vicinity of SS, FEP-3, and PP are plotted in Figure 5.38 in terms of multiples of the product of the Boltzmann constant ($k_{\text{B}} = 1.381 \times 10^{-23} \text{ J K}^{-1}$, Atkins, 1986) and temperature ($T = 362 \text{ K}$).

When the MFG approaches the SS surface in Figure 5.38a it experiences an attractive long range force due to Lifshitz-van der Waals interactions. At separations $l < 9 \text{ nm}$ hydrophilic repulsion by Lewis acid-base interactions dominates and results in a primary minimum of $-7.5 k_{\text{B}}T$ in the interaction potential at 9 nm . This minimum deepens with increasing MFG size. Based on this rationale, larger MFGs would be expected to accumulate close to the steel without making direct contact with the surface. This is consistent with CLSM images (*e.g.* Figure 5.32a) showing only a few isolated fat droplets on the steel surface after a fouling test using WP solution with added cream.

With FEP-3 (Figure 5.38b) the long-range forces are repulsive because $\gamma_1^{LW} > \gamma_3^{LW} > \gamma_2^{LW}$, with subscripts 1: MFG, 3: water, 2: FEP-3. At separations $l < 9 \text{ nm}$ hydrophobic attraction starts to dominate, however. Thus, MFGs adsorbing to FEP-3 face an energy barrier proportional to their diameter.

Attraction at all separations is found for PP, *i.e.* $\Delta G_{123}^{\text{LW}}(l)$ and $\Delta G_{123}^{\text{AB}}(l)$ are negative for all l (Figure 5.38c). This explains why numerous fat droplets of many sizes were found on PP (Figure 5.32c). Since the interfacial energy between fat and PP is negligible ($\gamma_{12} \ll 1 \text{ mJ m}^{-2}$), there is no driving force for MFGs to form clusters as seen on FEP-3. The mass coverage data in Figure 5.29 shows that PP's relative performance compared to FEP-3 is improved when cream was added to the WP solution. This demonstrates that PP could be attractive in applications where fat from the process stream can be exploited to form a weak link with the fouling deposit.

Compositional analysis revealed that much more calcium was present in the deposits generated from raw milk than from WP solution, both in absolute terms and relative to

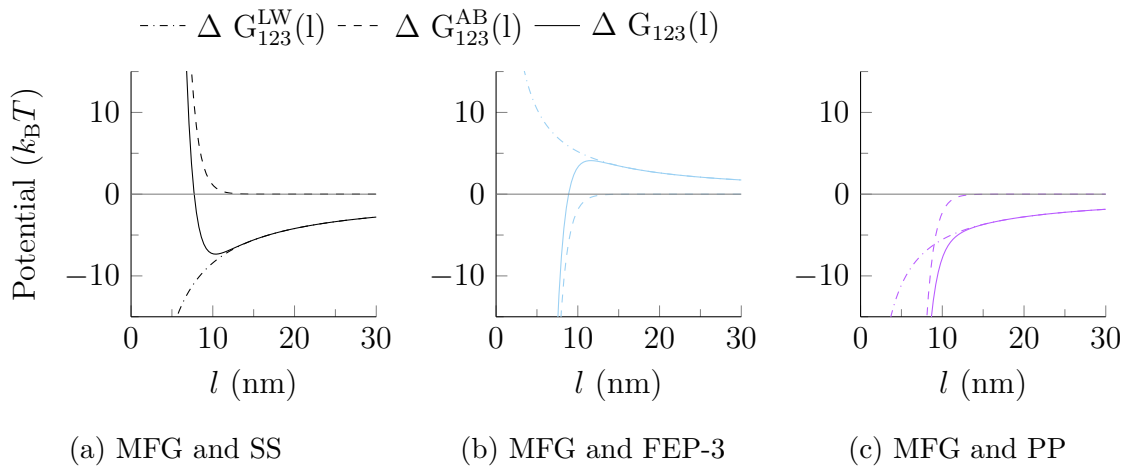


Figure 5.38: Interaction potentials over separation distance, l , of a MFG ($D = 2 \mu\text{m}$) and flat surfaces of (a) SS, (b) FEP-3, and (c) PP at $T = 362 \text{ K}$. LW – Lifshitz-van der Waals interactions; AB – Lewis acid-base interactions; IF – Total interfacial interactions.

the amount of calcium found in the dry solids fractions of the fouling solutions. While the WP concentrate is devoid of casein, in raw milk casein constitutes around $76 \% \text{ g g}^{-1}$ of all protein (Bansal & Chen, 2006). In raw milk, about two-thirds of calcium and half of the inorganic phosphate are bound to casein micelles (Gaucheron, 2005). Calcium phosphate can deposit indirectly as a constituent of casein micelles which interact with other proteins through disulphide bonds (Visser & Jeurnink, 1997). The surface chemistry also affected the calcium fraction of deposits from raw milk: deposits on SS contained 25% more calcium than on FEP-3. This is consistent with results from the microfluidic HEX where an affinity for protein was found for apolar surfaces. The calcium and protein composition of WP deposits was not affected by the nature of the surface, both overall and locally. Consequently, in the tested conditions WP fouling is dominated by protein deposition and calcium phosphates play a minor role.

Fouling resistance data, deposit coverages and CLSM micrographs suggest that WP deposits on polymeric surfaces were less dense and contained more water. The greater roughness of FP coatings compared to SS may have facilitated the attachment of spongy structures, but deposit on smooth PP was also significantly less dense. Effects of surface chemistry on deposit structure have been reported previously, *e.g.* Rosmaninho and Melo (2006) found crystals from simulated milk ultra-filtrate grown on PTFE to be thinner, but taller and more numerous than on SS.

Adhesion to SS was stronger than to apolar surfaces. Findings for SS are comparable with results of Liu *et al.* (2006) who measured the apparent adhesive and cohesive strength

of deposits generated from WP solution at around 90 °C. Similarly, they found adhesion to be significantly stronger than cohesion. Thick deposits on apolar surfaces tended to coil up on drying. Non-detaching layers from PP and FEP-3 were thin without exception (Figure 5.33b,iv and c,iv). This is a strong indication of competition between adhesive and cohesive forces. Thicker deposit gives rise to overall stronger cohesive forces, while adhesion is largely unaffected. Consequentially, there would be a threshold thickness for detachment on drying and – against intuition – thick dry deposits on apolar surfaces are easier to clean by mechanical means than thin ones. Deposits from raw milk were less homogeneous than from WP solution. On FEP-3, these inhomogeneities lead to weak points or localised stresses and made the layer coil up in numerous places (Figure 5.33c,v).

At flow rates from 5 l min⁻¹ to 7 l min⁻¹ the deposit coverages from WP solution on SS and PFA-4 were comparable and increased with flow rate. A steady rise in coverage on SS with increasing flow rate could indicate the importance of mass transfer in the fouling process. The trend changed for PFA-4 at 8 l min⁻¹ with deposit coverage reducing to half of the coverage on SS at the same flow rate. Britten *et al.* (1988) studied the effect of surface energy on fouling from raw milk with a range of polymer surfaces. They also found the deposit coverage from raw milk to be independent of surface chemistry at low wall shear stress. Their results indicated that apolar surfaces could give a lower activation energy for the desorption process and postulated that “this indicates that a material showing a surface energy sufficiently low, especially with respect to its polar contribution, could result in an activation barrier for desorption lower than the surface shear energy supplied by the flowing fluid.” The data suggests that such postulated regime applies to PFA-4 above a flow rate of 7 l min⁻¹ and a mean wall shear stress of 0.3 Pa at the conditions studied.

5.6 Summary

The results from the two experimental HEXs demonstrated that FPs can mitigate fouling from raw milk and WP solution. This reduction was generally more significant in mass coverage and less pronounced in terms of pressure drop and fouling resistance evolution over time. In tests with WP solution the deposits on apolar surfaces had lower thermal conductivity and/or density. The surface affected the structure of the deposit, even though the deposit was much thicker than the expected range of surface interactions. Apolar surfaces gave spongier deposits, although the deposit’s protein and mineral composition was unaffected by the nature of the surface.

Based on the results from the microfluidic HEX experiments, it can be concluded that,

at the interface, raw milk fouling deposit is richer in protein when generated at apolar surfaces than on SS. This difference in composition manifested also in lower calcium mass fractions of the bulk material generated with the bench-scale HEX.

The attraction of denatured protein towards apolar surfaces and the formation of a calcium phosphate layer on SS at later stages of fouling was explained with arguments based on the interfacial free energy of interaction of these materials in water. Explanation for the low adhesion and detachment of dry deposits on apolar surfaces followed the same arguments and underpinned their validity. It was shown that triglycerides present in the process fluid or in form of a pre-wetting film can reduce deposit attachment. PP was most effective in adsorbing fat from MFGs because its interaction potential with globules is negative at all distances.

At the conditions tested, a wall shear stress threshold of 0.3 Pa for low mass coverage was identified for PFA-4. The next chapter explores whether the experimentally determined fouling performance of FP coatings justifies their industrial application in regenerative sections of UHT sterilisers.

Chapter 6

Economic potential of FP antifouling coatings in UHT plate HEXs

6.1 Setting up the case

In this chapter the findings from the previous chapters are utilised to estimate the economic potential of FP coated plate HEXs in the UHT treatment of milk. Due to its simplicity, the lumped model from Section 3.2 is preferred over the numerical model for this application. There are a number of requirements towards the experimental fouling data and test conditions which are utilised in this analysis:

- (i) The fouling tests should be conducted with ‘real milk’ to account for the product which is processed in the dairy. As shown earlier, WP solution which is often used as milk simulant, can show very different behaviour.
- (ii) The HEX geometries used in fouling tests should be representative of industrial equipment. The bench-scale HEX only approximates a simple plate HEX.
- (iii) The test conditions should be comparable to industrial conditions: *e.g.* flow rate, flow regime, shear stress and temperature profiles.
- (iv) The test duration should be comparable with processing times of industrial equipment, *i.e.* in the order of a 8 h working shift or more.

Over the course of the project discussions were held with a dairy company about conducting trials with real milk on FP coated plates in their pilot plant, but these did not come to fruition. To adequately account for the requirements listed above, fouling data from Lalande *et al.* (1984) are utilised here. They studied UHT fouling of pre-pasteurised whole milk in a pilot scale SS plate HEX during regenerative heating (5–120 °C), water heating (120–138 °C), and cooling (138–5 °C). Each test consumed from 1700 to 5100 l of milk. They found proteinaceous type A fouling in the regenerative section (similar to what has been generated with the microfluidic and bench-scale HEX) and mineral-rich

type B fouling at the hot end of the water heated section. At intermediate temperatures from, 120 to 130 °C, there was little fouling. A schematic of a comparable process with a similar temperature profile is depicted in Figure 6.1. The temperatures in the schematic correspond to the clean system at steady state.

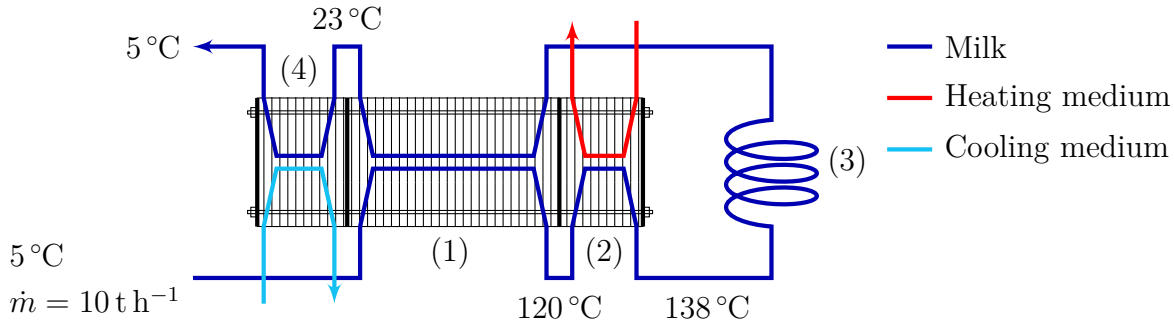


Figure 6.1: Simplified schematic of a plate HEX used for UHT treatment of pre-pasteurised milk based on Bylund (2015) and Lalande *et al.* (1984). The (1) regenerative, (2) heating, (3) holding and (4) cooling sections are indicated.

In this process 86% of the heat duty is provided by the regenerative heating section (labelled 1 in the schematic). To maintain throughput, a reduction in this section's heat duty (due to fouling) has to be compensated for by increasing the utility water temperature or flow rate in the subsequent heating section (2): this is common practice in dairy operation (Bylund, 2015). There is a marginal cost associated with supplying heat at a higher temperature. In the worst case one runs into a constraint because the duty may not be able to be supplied at the desired rate and the desired temperature. This was analysed by Ishiyama, Paterson, and Wilson (2009) who looked at thermal and pressure drop limitations in refinery pre-heat trains. Furthermore, fouling in the regenerative section increases the cooling load in section (4). Hence, for the steriliser there are two major thermal costs: (i) the cost of increasing the temperature or flow rate of the hot utility water, and (ii) the increase in cooling utility because the regenerator does not remove sufficient heat due to fouling.

Lalande *et al.* (1984) reported average fouling mass coverages in the regenerator after different operating periods. Assuming a deposit thermal conductivity of $0.5 \text{ W m}^{-1} \text{ K}^{-1}$ and a density of 1030 kg m^{-3} (Georgiadis & Macchietto, 2000) the fouling resistance at the end of these tests can be estimated with Equation 3.44. Figure 6.2a shows the $R_f - t'$ profile estimated from the Lalande *et al.* (1984) data fitted to the asymptotic fouling model (Equation 3.3). Considering that the channels in a plate heat exchanger are very narrow, the maximum fouling layer thickness is constrained to be smaller than half the channel width. Here, a maximum thickness of 1 mm was set, which gives an asymptotic

fouling resistance of $R_f^\infty = 2 \text{ m}^2 \text{ K kW}^{-1}$. Comparing the obtained asymptotic fouling profile (black line) with the linear fouling model (dashed line) from the techno-economic study on milk fouling by Gomes da Cruz *et al.* (2015) using data taken from Barish and Goddard (2013), it is clear that their estimation gave very similar results for processing periods up to a day long. Both profiles feature induction periods of a few hours.

To illustrate the breadth of data reported in the literature, Figure 6.2b shows data from experiments with skim milk reported by Fryer (1986) using a heated SS tube with an internal diameter of 4.6 mm. The experiment, conducted with a wall temperature of 102°C and a Reynolds number of 4350, resulted in rapid and severe fouling. Assuming a typical clean heat transfer coefficient for a plate HEX of $U_{cl} = 5 \text{ kW m}^{-2} \text{ K}^{-1}$ (Bylund, 2015) a HEX subject to these fouling kinetics would suffer a reduction in performance of 50% within the first three minutes ($Bi_f = R_f U_{cl} = 0.2 \text{ m}^2 \text{ K kW}^{-1} 5 \text{ kW m}^{-2} \text{ K}^{-1} = 1$). Application of these kinetics to simulate an industrial process is not considered realistic.

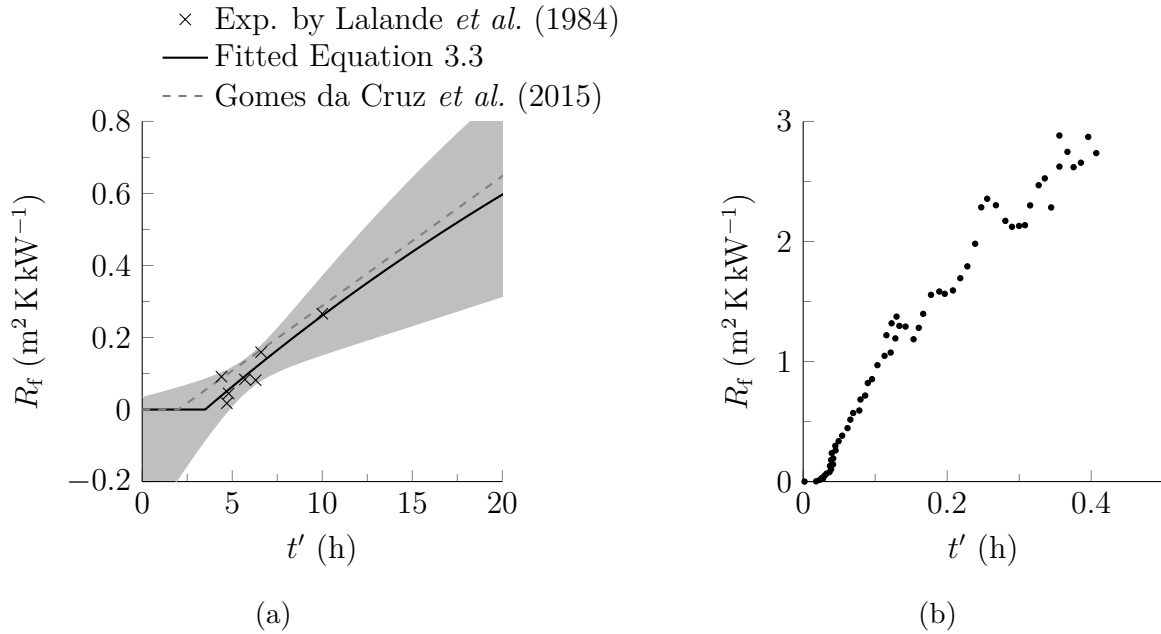


Figure 6.2: Fouling resistance evolution of SS HEX in UHT case study. In (a), crosses show fouling resistances calculated from deposited masses in a regenerative heating section reported by Lalande *et al.* (1984) with a fit to Equation 3.3 shown as black line (Parameters: $t_{ind} = 3.5 \text{ h}$, $t_f = 46.6 \text{ h}$, $R_f^\infty = 2 \text{ m}^2 \text{ K kW}^{-1}$). The grey area shows simultaneous 95% confidence bounds of the fit with $R^2 = 0.85$. The dashed line shows the fouling resistance from techno-economic study by Gomes da Cruz *et al.* (2015). Plot (b) shows fouling data reported by Fryer (1986) using skim milk. Note the different axes in (a) and (b).

Experiments with FP coatings in the bench-scale HEX have shown that fouling from raw

milk could be reduced by 39 % on the basis of mass. Experiments with WP concentrate gave a reduction by 53 % in mass and around 30 % in final fouling resistance. FP coated samples in the raw milk fouling experiments with the microfluidic HEX reduced deposition by up to 36 %. It is not possible to infer the reduction of fouling in the considered regenerator of Figure 6.1 confidently. One can, however, make an educated guess by taking the average of the above reductions, giving $39.5 \pm 9.8 \%$. With this, the asymptotic fouling resistance of the FP coated regenerative section is reduced to $R_{f,coat}^\infty = (1 - 39.5 \pm 9.8 \%)R_f^\infty = 1.21 \pm 0.12 \text{ m}^2 \text{ K kW}^{-1}$. The fouling timescale is not changed.

Other case study parameters of the uncoated and coated unit are summarised in Table 6.1. The coated HEX is much larger than the uncoated unit because of the thermal resistance of the coating. Simply using a larger SS HEX may be financially attractive since more load is taken from the heating and cooling section. This is, however, not considered here as this is a universal option which is applicable to any HEX, also a coated one.

Table 6.1: UHT steriliser case study parameters.

Design		
A	Regenerative section area, uncoated ¹	14.0 m ²
A_{coat}	Regenerative section area, coated ²	38.6 m ²
Coating and thermal properties		
R_{coat}	Coating thermal resistance ³	0.351 m ² K kW ⁻¹
c_p	Milk heat capacity ⁴	3950 J kg ⁻¹ K ⁻¹
U_{cl}	Clean overall heat transfer coefficient, uncoated ⁵	5000 W m ⁻² K ⁻¹
Q_{cl}	Clean heat duty	1.26 MW
Fouling performance		
t_{ind}	Induction period, uncoated and coated	3.5 h
R_f^∞	Asymptotic fouling resistance, uncoated	2.00 m ² K kW ⁻¹
$R_{f,coat}^\infty$	Asymptotic fouling resistance, coated	1.21 m ² K kW ⁻¹
t_f	Fouling timescale, uncoated and coated	46.6 h
τ	Cleaning period, uncoated and coated ⁵	78 min

Table continues on the next page

¹set by the author

²calculated using Equation 3.37

³see FEP-3 in Table 4.1

⁴data taken from Fernández-Martín (1972a) for milk with 4 % fat and 6 % other solids

⁵data taken from Bylund (2015)

Operation		
\dot{m}_c, \dot{m}_h	Cold and hot stream mass flow	10 t h ⁻¹
$T_{c,in}$	Cold stream inlet temperature	5 °C
$T_{h,in}$	Hot stream inlet temperature	138 °C
Costs		
c_E	Cost per unit heat not transferred	25.5 US\$ GJ ⁻¹
C_{cl}	Cleaning cost ⁶	150 US\$
t_{lf}	Asset lifetime (depreciation)	2 year

Since fouling increases the cooling and heating load to the same extent, the cost per unit heat not transferred due to fouling is calculated as the sum of the two. The average non-household cost of natural gas including all taxes and levies was 0.035 €/kWh (12.0 US\$ GJ⁻¹) in the EU during the first half of 2017 (Eurostat, 2017b). The price for electricity during the same period was 0.14 €/kWh (47.2 US\$ GJ⁻¹) (Eurostat, 2017a). Refrigerators typically remove around 3.5 units of heat per unit of electricity consumed (Alsaad & Hammad, 1998), so the total cost per unit heat not transferred due to fouling is taken as $c_E = 12.0 \text{ US\$ GJ}^{-1} + 47.2 \text{ US\$ GJ}^{-1} / 3.5 = 25.5 \text{ US\$ GJ}^{-1}$. The asset lifetime (here, the lifetime of the coating) is set to two years, which is much shorter than the lifetime of the SS base unit and reflects the vulnerability of the polymer layers to degradation.

6.2 Results and discussion

Figure 6.3 shows the objective functions (Equations 3.5a,b,c) for the uncoated and coated unit over the processing period. The coated unit (red lines and marks) transfers more heat and has lower operating costs than the uncoated unit (black lines and marks). To illustrate the effect of the increased heat transfer area resulting from the thermal resistance of the coating, the orange lines indicate the hypothetical case of a HEX with the coating possessing no thermal resistance. This shows that around half of the improvement in the objective functions stems from the increase in heat transfer area (which incurs a higher capital cost).

The approximate optimal processing periods for the uncoated unit (shown as black dots in Figure 6.3) deviate markedly from the exact solutions because $a_4 = 1.74 \ll 2.8$. Hygienic

⁶data taken from Gomes da Cruz *et al.* (2015)

considerations, however, may constrain the maximum possible processing period. Tetra Pak (2007) tested consumption milk pasteuriser run times of around 20 h and found no risk to food safety and quality. Here, the effect of a hygienic constraint on the economics of the coated unit will be modest if it is allowed to be operated for more than 20 h.

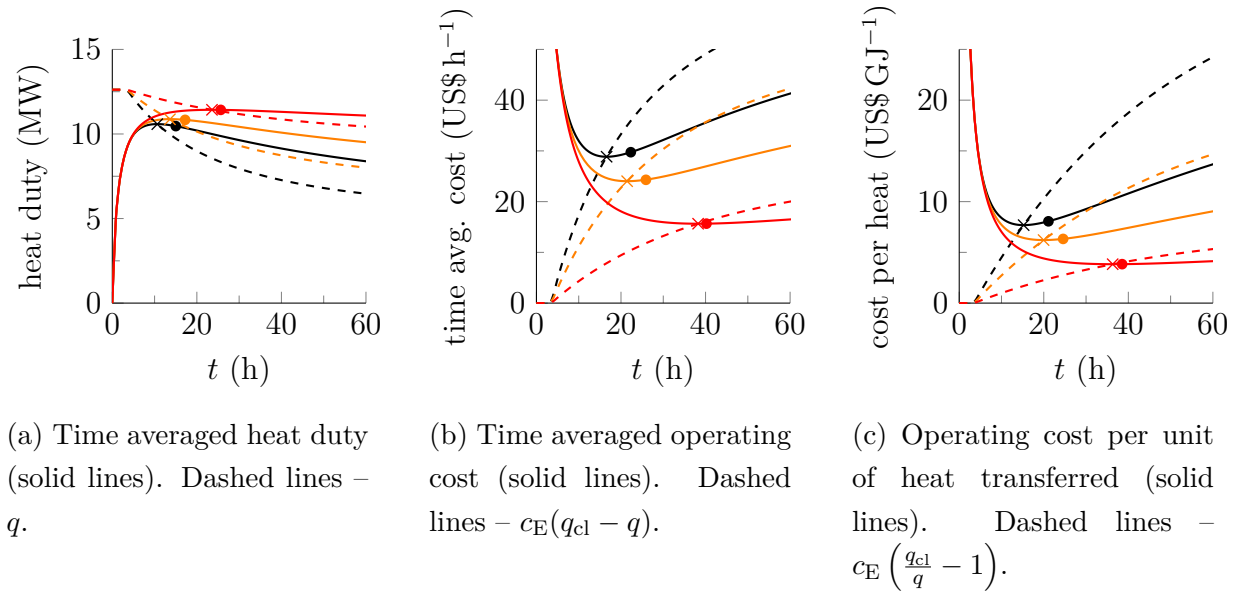


Figure 6.3: Effect of processing period length on (a) time averaged heat duty, (b) time averaged operating cost, and (c) operating cost per heat transferred for uncoated (black) and coated (orange, red) stainless steel HEXs in UHT case study. Orange lines and marks show the case of a HEX with the coating possessing no thermal resistance. Crosses – optimal processing periods; solid dots – approximate optimal processing periods.

The optimised schedules and performance indices for the uncoated and coated HEX are summarised in Table 6.2. The coating (coated HEX A) extends the optimal processing periods by a factor of 1.58 to 2.97, depending on the objective function which is used for scheduling. When scheduling for maximum q_m , 8% more heat is transferred by the coated HEX, while costs are halved when optimising for ϕ_{op} or ϕ_Q . The column ‘coated HEX B’ summarises the results for the hypothetical unit with a coating having no thermal resistance. This case shows the cost reduction resulting from the superior fouling performance rather than an increase in heat transfer area. The improved fouling characteristics introduce cost reductions by 16 to 19% when optimising for ϕ_{op} or ϕ_Q , respectively.

The capital costs of the base units, C_{base} , are now considered. According to Hewitt and Pugh (2007), a SS plate HEX with a heat transfer area of around 100 m^2 cost approximately 100 £ m^{-2} in 1995. Conversion into US\$ and updating it with the chemical

Table 6.2: Comparison of optimal performance indices in UHT case study (parameters in Table 6.1). t_{opt} and $t_{\text{opt,approx}}$ are calculated with Equation 3.4a-c using the exact and approximate heat duty, respectively.

	Uncoated HEX	Coated HEX A	Coated HEX B	Units
Design				
R_{coat}	–	0.351	0	$\text{m}^2 \text{K kW}^{-1}$
U_{cl}	5000	1815	5000	$\text{W m}^{-2} \text{K}^{-1}$
a_4	1.74	4.36	2.22	1
Optimised schedule for maximum q_{m}				
$t_{\text{opt}} + \tau$	10.6 + 1.3	23.6 + 1.3	13.6 + 1.3	h
$t_{\text{opt,approx}} + \tau$	15.0 + 1.3	25.6 + 1.3	17.2 + 1.3	h
$t_{\text{opt,coat}}/t_{\text{opt}}$	–	1.58	1.28	1
$q_{\text{m,opt}}$	10.6	11.4	10.9	MW
$q_{\text{m,coat,opt}}/q_{\text{m,opt}}$	–	1.08	1.03	1
Optimised schedule for minimum ϕ_{op}				
$t_{\text{opt}} + \tau$	16.6 + 1.3	38.2 + 1.3	21.5 + 1.3	h
$t_{\text{opt,approx}} + \tau$	22.3 + 1.3	40.2 + 1.3	25.9 + 1.3	h
$t_{\text{opt,coat}}/t_{\text{opt}}$	–	2.30	1.30	1
$\phi_{\text{op,opt}}$	28.9	15.6	24.1	US\$ h^{-1}
$\phi_{\text{op,coat,opt}}/\phi_{\text{op,opt}}$	–	0.54	0.84	1
Optimised schedule for minimum ϕ_{Q}				
$t_{\text{opt}} + \tau$	15.2 + 1.3	36.3 + 1.3	20.0 + 1.3	h
$t_{\text{opt,approx}} + \tau$	21.1 + 1.3	38.5 + 1.3	24.6 + 1.3	h
$t_{\text{opt,coat}}/t_{\text{opt}}$	–	2.97	1.32	1
$\phi_{\text{Q,opt}}$	7.7	3.8	6.2	US\$ GW^{-1}
$\phi_{\text{Q,coat,opt}}/\phi_{\text{Q,opt}}$	–	0.49	0.81	1

engineering plant index to 2017 yields an installed cost of 228 US\$ m^{-2} . For the following steps it is assumed that cleaning scheduling is done to minimise ϕ_{op} . Table 6.3 summarises the capital costs and maximum coating costs of the three options. The capital costs are negligible compared to the operating cost incurred by fouling. This is partly because of the high heat transfer coefficient (performance per area) of plate HEXs and because of the substantial costs of heating and cooling involved. The column ‘coated HEX B’

attempts to calculate the value of the coating by using the reduction in operating cost attributable to the coating and considering the larger heat transfer area which needs to be installed. The maximum coating cost of 1950 US\$ m⁻² needs to be shared between the coating manufacturer and operator.

Table 6.3: Capital costs and maximum coating costs per area of the HEXs considered in the UHT case study with parameters given in Table 6.1.

	Uncoated HEX	Coated HEX A	Coated HEX B	Unit
R_{coat}	–	0.351	0	m ² K kW ⁻¹
Capital cost of the base unit				
C_{base}	3197	8808	8808	US\$
Time averaged cost				
$\phi_{\text{base}} = C_{\text{base}}/t_{\text{lf}}$	0.18	0.50	0.50	US\$ h ⁻¹
$\phi_{\text{opt}} = \phi_{\text{op,opt}} + \phi_{\text{base}}$	29.1	16.1	24.6	US\$ h ⁻¹
$\phi_{\text{opt,coat}}/\phi_{\text{opt}}$	–	0.55	0.85	1
Max. coat. cost per area: new, greenfield unit				
$c_{\text{coat,max,new}} =$ $(\phi_{\text{opt}} - \phi_{\text{opt,coat}})t_{\text{lf}}/A_{\text{coat}}$	–	5896	2041	US\$ m ⁻²
Max. coat. cost per area: revamped unit				
$c_{\text{coat,max,rev}} =$ $(\phi_{\text{op,opt}} - \phi_{\text{opt,coat}})t_{\text{lf}}/A_{\text{coat}}$	–	5805	1956	US\$ m ⁻²

Müller-Steinhagen and Zhao (1997) stated the low thermal conductivity of polymers such as PTFE was one of the main disadvantages of polymer based antifouling coatings in HEXs. This did not hold true for the case study coatings in Chapter 3 because the coatings were thin and the clean heat transfer coefficients of the uncoated units were relatively small. Here, the thermal resistance of the coated unit required a substantial increase in heat transfer area for identical heat duty. This highlights the importance of developing coatings with lower thermal resistance.

Further tests could establish whether the lower adhesion and the nature of the fouling deposit on the FP enhances cleaning. This could either reduce the cleaning cost through lower detergent consumption and disposal or by shortening the time required to remove the deposits from the heat transfer surface. Figure 6.4 is a map of coating values for different degrees of improvement. The value of such coatings ranges from 1956 (the current case ‘Coated HEX B’) to a maximum possible value of around 12 500 US\$ m⁻²

for a coating which enables instant cleaning at no cost. A first order Taylor expansion about the parameters used for the case ‘coated HEX B’ illustrates the incremental return of improved coating performance (subscript ‘new’) on the economic value:

$$c_{\text{coat,max,rev}} = \left(11546 - 4200 \frac{R_{f,\text{new}}^\infty}{R_{f,\text{coat}}^\infty} - 3000 \frac{C_{\text{cl,new}}}{C_{\text{cl}}} - 2390 \frac{\tau_{\text{new}}}{\tau} \right) \text{US\$ m}^{-2}. \quad (6.1)$$

The magnitudes of the coefficients in the individual terms indicate the financial returns of improvements of the respective performance characteristics relative to the base case. Developments either to mitigate fouling or promote cleaning of UHT plants are justified by substantial financial benefits. The pay-off of further developments is greatest for a reduction in asymptotic fouling resistance, followed by reduced cleaning costs and cleaning time. The effort associated with improvements of these characteristics is, however, unclear at this point but may become clearer at later stages of coating development and assessment.

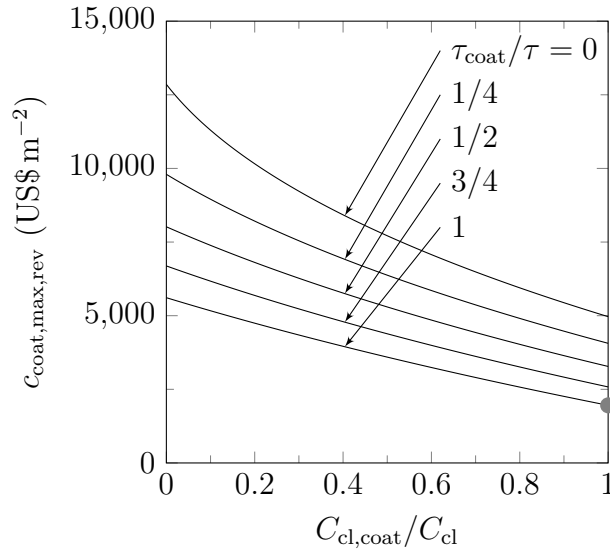


Figure 6.4: Effect of cleaning enhancement on value prices of coatings for different ratios of cleaning costs, $C_{\text{cl,coat}}/C_{\text{cl}}$ and five dimensionless cleaning period lengths, τ_{coat}/τ . The grey solid circle marks the case study unit ‘coated HEX B’.

6.3 Summary

The value of a FP antifouling coating in a UHT plate HEX was quantified by combining the lumped techno-economic model developed in Chapter 3 with experimental data taken from Lalande *et al.* (1984) and coating performance data from Chapter 5. The coating

reduces the heating and cooling load by reducing fouling in the regenerative section. Furthermore, longer operating periods reduce downtime and cleaning costs. The value of the coating was considered by assuming a coating thermal resistance of zero, hence suppressing effects of a varying heat transfer area. Due to the coating, the operating cost reduced by 16% which gave the coating a value price of around 2000 US\$ m⁻². A Taylor expansion about the parameters used for the coated case revealed that there is scope for considerable incremental return on improved coating fouling and cleaning performance.

Chapter 7

Conclusions and future work

This chapter summarises the key-findings of this dissertation and identifies work for further investigation. Conclusions from experimental and techno-economic work are considered separately and an outlook is given in the final section.

7.1 Conclusions

7.1.1 Experimental studies

Two experimental apparatuses were designed and constructed to study fouling of milk and WP solution at temperatures prevalent at the hot end of a pasteuriser or in the regenerative heating section of a UHT steriliser.

The microfluidic HEX apparatus was designed to operate in the laminar flow regime and to have the capability to probe the local composition of delicate fouling deposit *in-situ* with histology techniques employing CLSM. The mean wall-shear stress in tests ranged from 3 to 6 Pa. Fouling monitoring by measuring pressure drop across the microfluidic cell was more precise than by using thermal data.

A larger bench-scale HEX operated in the turbulent flow regime was more representative of conditions in an industrial plate HEX, albeit with smaller average wall shear stresses of 0.17 to 0.39 Pa. Fouling resistance time series were used as indicators of fouling performance but measurements of final deposit masses were more reproducible. The rig bridged the gap from laboratory- to industrial-scale.

Results from the two experimental HEXs demonstrated that FP coatings can mitigate fouling from raw milk and WP solution. The surface properties affected the structure and composition of the deposit. At the interface to apolar surfaces, raw milk fouling layers were high in protein whereas a strongly attached mineral-rich layer was present at the interface to SS. The larger fraction of minerals in deposit generated on SS was confirmed with ICP-MS, which measured a higher calcium content of raw milk deposit on SS than on FEP-3. In tests with WP solution the deposits on apolar surfaces were more spongy

and had a lower thermal conductivity and/or density than on SS. The calcium fraction was similar, however.

In general, the surface affected the structure and composition of the deposit, even though the deposit was much thicker than the range of surface interactions. The attraction of denatured protein towards apolar surfaces and the formation of a calcium phosphate layer on SS at later stages of fouling was explained with arguments based on the interfacial free energy of interaction of these materials in water. Explanation for the low adhesion and detachment of dry deposits on apolar surfaces followed the same arguments. It was shown that triglycerides present in the process fluid or in form of a pre-wetting film can reduce deposit attachment. PP was most effective in adsorbing fat from MFGs because its interaction potential with globules is negative at all distances.

At the conditions tested in the bench-scale HEX, a wall shear stress threshold of 0.3 Pa for low mass coverage was identified for PFA-4. Above this threshold, deposition was lower on PFA-4 but kept increasing on SS.

7.1.2 Techno-economics of antifouling coatings

A spatially resolved numerical model and a lumped model were developed to assess the financial attractiveness of antifouling coatings. The two approaches were introduced with case studies based on data reported in the literature. Underlying of these techno-economic assessments is the cleaning-scheduling problem which attracted widespread interest by previous researchers.

Utilising the *NTU*-effectiveness method with linear and asymptotic fouling models provided valuable insights, such as identifying scenarios where cleaning of HEXs is not attractive. Explicit solutions were identified for cases of equal heat capacity flow rate, which apply to various applications of preheaters and economisers where the stream on one side of the exchanger passes the other side at a later time. It was shown that cleaning-scheduling based purely on thermal arguments always gives operating periods shorter than scheduling based on financial considerations including the cost of cleaning. The methodology is, in general, not only applicable to HEX cleaning-scheduling and value pricing of coatings but also for techno-economic analysis of any kind of antifouling and cleaning technique. The development of this model is therefore one of the major achievements within this thesis.

In the second modelling part the enthalpy balances of a counter-current HEX were solved together with a fouling model to predict the fouling dynamics of a simple HEX subject

to crystallisation fouling. Although the numerical model provided physical insight into fouling kinetics and would – in principle – allow predictions of fouling behaviour in other flow fields and geometries, it requires a substantial amount of experimental data for parameter estimation.

The data from coating characterisation and fouling tests with the microfluidic and bench-scale HEX were utilised in a final case study on the economics of a generic FP antifouling coating applied in the regenerative heating section of a UHT steriliser. To compensate for the thermal resistance of the coating with a performance similar to those tested in the experimental sections, the heat transfer area of the coated unit had to be increased substantially. As a result of the reduction in fouling and the increase in heat transfer area, the application of the coating extended the optimal processing period and lowered the operating cost. The value of the coating inferred from the reduction in fouling was estimated to be around 2000 US\$ m⁻². Further guidance on the marginal benefit of coating improvements was given.

7.2 Future work

7.2.1 Experimental studies

After finalising the experimental work with the bench-scale HEX in Cambridge the unit was shipped to Chemours, Belgium for further studies. The local staff were trained in operation and maintenance of the HEX apparatus. In the future, researchers and research students will conduct experiments on fouling and cleaning of FP coated surfaces. An interesting question is whether the compositional differences between deposits on FP surfaces and SS allow different cleaning methodologies. The high protein content of deposits at the interface to apolar surfaces may allow complete removal by an alkaline cleaning solution. A less intense acid-stage to dissolve mineral-rich deposit may suffice or may be omitted entirely.

Fouling experiments with the bench-scale HEX at different flow rates (Figure 5.35) indicated that deposition is suppressed or removal is enhanced on PFA-4 at flow rates above 71 min⁻¹, whereas the fouling mass on SS grew steadily within the range of flow rates tested. This suggests that there are two relevant mechanisms in series, the first (*e.g.* mass transport) giving increased deposition with flow rate irrespective of the surface properties and the second being a surface specific deposition limiting factor. This limiting factor may be a surface specific sticking probability. Jeurnink *et al.* (1996) studied

deposition of heated whey proteins on chromium oxide surfaces and developed a fouling model with subsequent stages: (i) activation of molecules, (ii) transport to the surface, and (iii) attachment characterised by a sticking probability. They found a sticking probability of much less than one for chromium oxide. There is reason to suspect that the sticking probability on other surfaces is different and varies with shear stress or residence time.

Histology techniques and ICP-MS indicated that apolar heat transfer surfaces promoted the formation of proteinaceous interfacial layers, whereas SS promoted the formation of a calcium phosphate-rich layer. Further studies analysing the local composition at the interface could *e.g.* elucidate which form of calcium phosphate is generated. Following arguments based on interfacial free energy, a layer of hydroxyapatite would be expected (see Figure 5.17).

Performing fouling tests does certainly involve a lot of working hours and manual work, especially if different surfaces are to be tested. Experiments with the microfluidic HEX demonstrated that the results are useful and comparable to results from larger scale units like the bench-scale HEX. It became clear that fouling tests could in principle be automated in a similar set-up. Repetitive cycles of fouling and cleaning could be done autonomously by pumping solutions with peristaltic pumps through a microfluidic HEX. Pressurising the unit would render degassing procedures before the experiment unnecessary. For extended operation time, biologically active species like raw milk could be cold-stored in a fridge and be heated just prior injection into the fouling cell (*c.f.* the pre-heater (11) in Figure 5.3).

7.2.2 Techno-economics of antifouling coatings

The developed techno-economic models remain effective tools to supplement experimental fouling and cleaning studies. The operational and financial benefit arising from any identified performance improvement can be easily computed.

To enable predictions of fouling in HEXs with different design and operating conditions, a mechanistic fouling model (similar to the one described in Section 3.3) could be parametrised for a specific foulant on SS and FP coatings. This will require a set of fouling experiments *e.g.* at different flow rates, temperatures, and foulant concentrations. At last, this will help to demonstrate and optimise the application of FP coatings in other cases of interest. Ideally, careful analysis of the experiments could provide further insight into fouling mechanisms on different surfaces, *e.g.* information about sticking probabilities.

7.2.3 Millimanipulation

An improved millimanipulation tool, described in Appendix E, was designed and manufactured during this project. The tool was not applied to milk fouling deposits because they were thinner than anticipated. It was, however, successfully applied to measure the adhesive and cohesive strength of baked sponge cake batter on various surfaces (see Appendix E). In the context of future milk fouling cleaning studies, this technique is suitable to quantify the release characteristics of antifouling coatings – given a sufficient deposit thickness.

In conjunction with models predicting adhesive and cohesive behaviour, fouling layer properties and interface interactions can be further analysed. By abruptly stopping the scraping process, stress relaxation may be measured *in situ*. The rheological properties of soft solid layers could be deduced by comparing experimental observations (stripping speed, force, deformation) with structural or fluid dynamic simulations of the scraping process. Combining this information with compositional data would give a better understanding of the complex interactions in fouling layers.

Appendix A

Thermogravimetric analysis

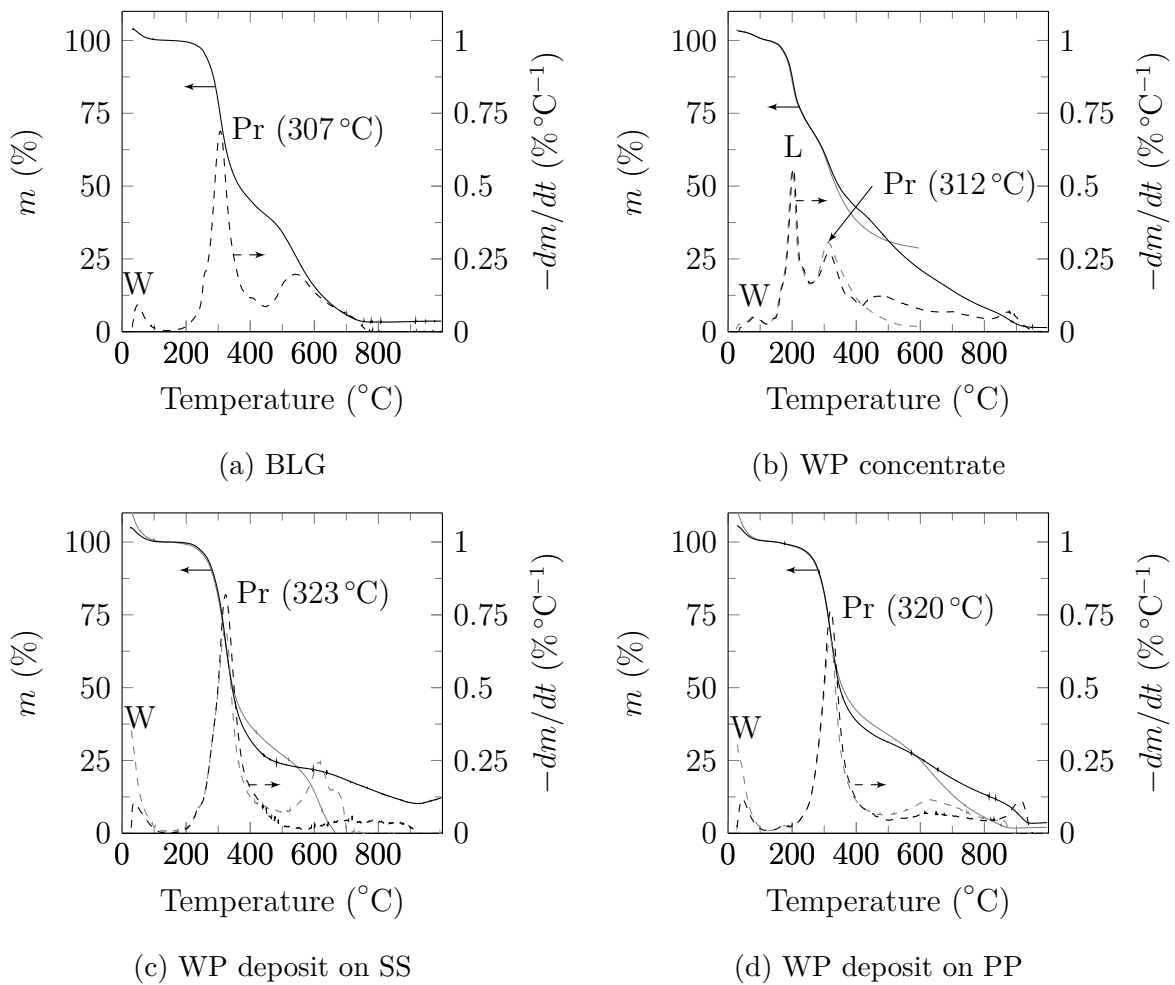
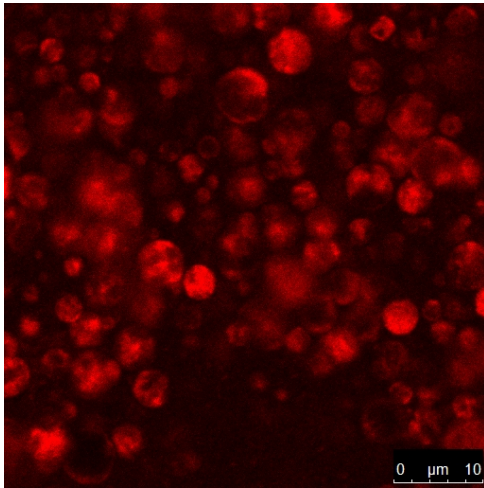


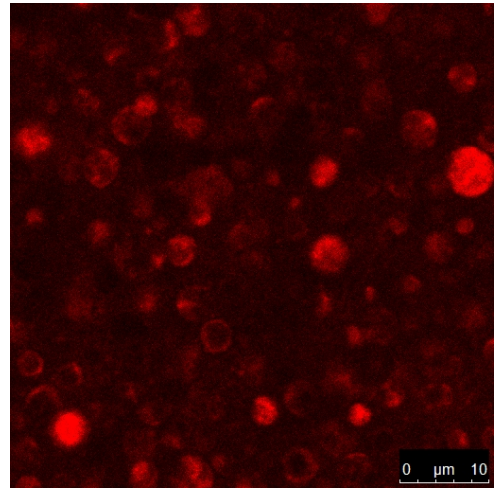
Figure A.1: Thermogravimetric analysis (TA instruments Q500) results of (a) β -LG, (b) Hiprotal WP 35 concentrate and bench-scale HEX deposits from WP solution on (c) SS, and (d) PP. Samples were heated with a rate of 10 K min^{-1} in a nitrogen atmosphere (purge rate 60 ml min^{-1}). Note that the data is only reproducible up to 400°C in (b) and (c). The following peaks are marked: W – water evaporation; L – lactose decomposition (Listiohadi *et al.*, 2009); Pr – protein decomposition.

Appendix B

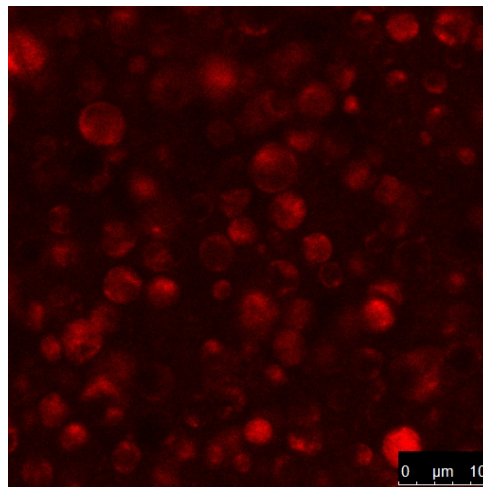
Raw milk CLSM micrographs



(a) Raw milk as received at 6 °C



(b) Raw milk heated to 56 °C



(c) Raw milk heated to 56 °C and ultrasonicated for 45 min at 20 kPa absolute pressure

Figure B.1: CLSM images of raw milk as received (a) and treated (b,c). Milk fat globules were stained with Nile blue A and images were taken with a Leica TCS SP5 (40x oil immersion lens) with a helium-neon laser excitation at 633 nm.

Appendix C

Microfluidic HEX fouling resistance evolution

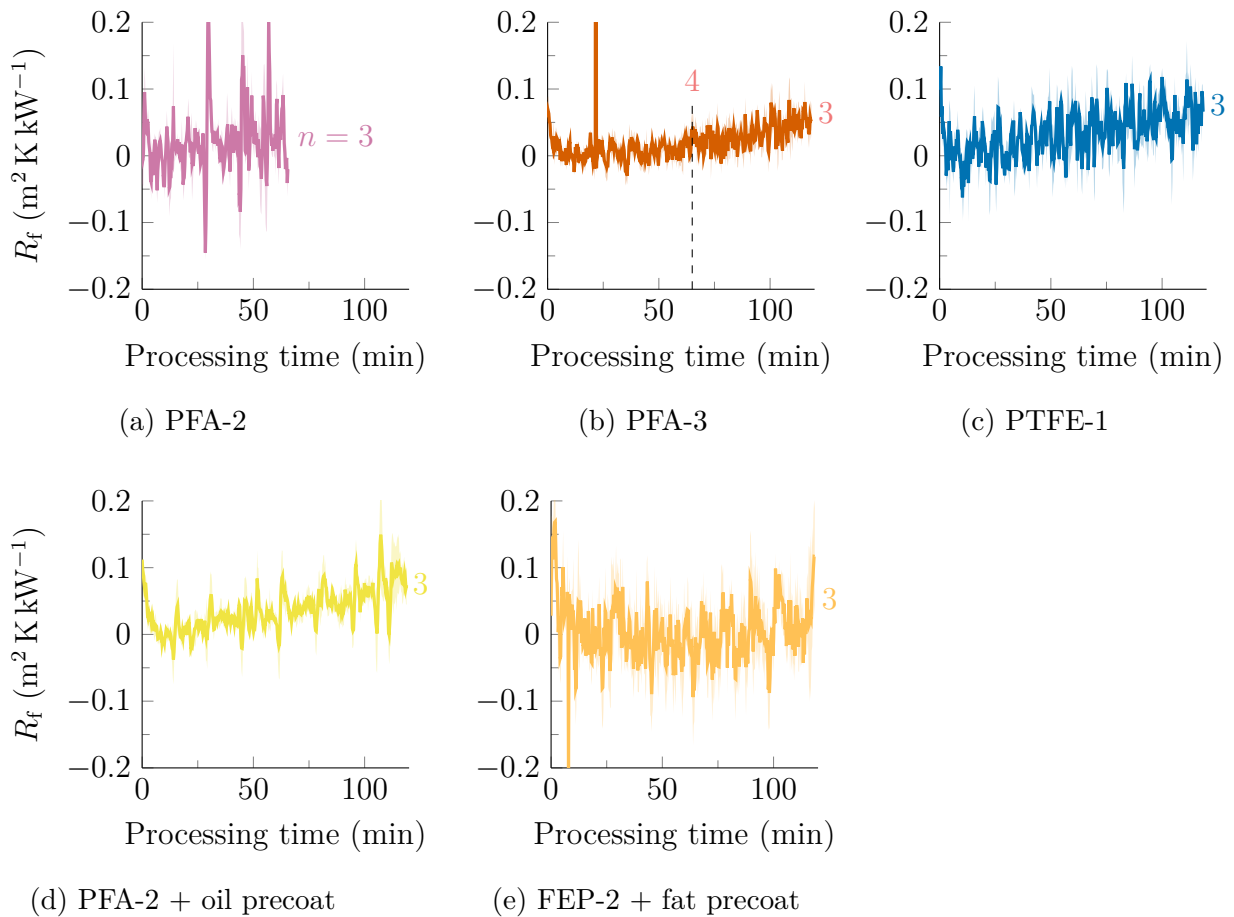


Figure C.1: Fouling resistance profiles for raw milk fouling tests with microfluidic HEX on (a) PFA-2, (b) PFA-3, (c) PTFE-1, (d) PFA-2 oil precoated and (e) FEP-2 fat precoated. n indicates number of experiments and shaded bands indicate \pm std. err.

Appendix D

Bench-scale HEX rig graphical user interface

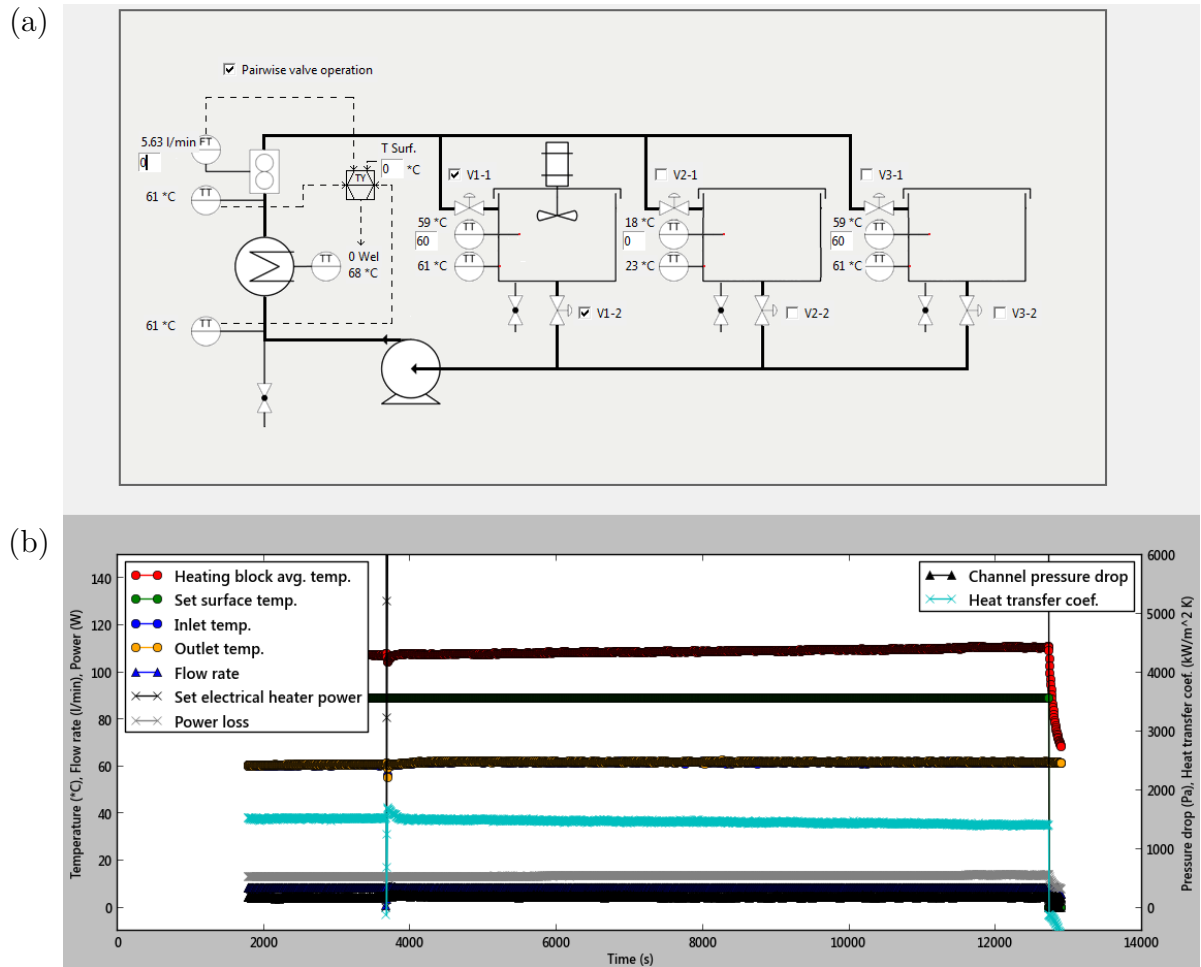


Figure D.1: Graphical user interface of the bench-scale HEX rig. (a) process diagram with instantaneous measurement data and set-point input boxes. (b) selected measurement data shown over time after a fouling experiment on SS.

Appendix E

Appended publication on Millimanipulation

The adhesive and cohesive strengths of fouling deposits are of particular interest when designing cleaning routines as they determine the mechanism and rates at which the deposit is removed. Soft solid fouling layers are highly non-uniform since they experience a wide range of conditions during their build-up. Unlike other soft solid materials, such as petroleum jelly, the rheological properties of fouling layers cannot be studied in common rheometers because removing them induces damage. Furthermore, standard rheometers are not able to measure layer properties as a function of position. Consequently, fouling layer adhesion and rheological properties have to be studied *in situ*, on the heat transfer surface. Experimental techniques for doing this can be categorised as methods employing controlled strain and controlled shear stress conditions (Ali *et al.*, 2015).

Hydrodynamic approaches employ controlled (or estimated) shear stress conditions. Ali *et al.* (2015) gave an overview of hydrodynamic methods such as the parallel plate flow cell, impinging jet, radial flow cell, rotating disk and fluid dynamic gauging. They noted that none of these techniques provides a direct measure of the forces within a deposit or the strength of attachment. An alternative method was presented by Mayer *et al.* (2012) who measured the forces to remove individual CaCO_3 crystals with a bending-beam arrangement in an electron microscope stage.

Controlled strain methods have also been employed. Zhang *et al.* (1991) studied the deformation of cells with a ‘micromanipulation’ technique, which squeezes a single cell between the ends of two optical fibres. Liu *et al.* (2002) modified this set-up to investigate the adhesive and cohesive behaviour of different fouling layers.

Inspired by the work of Liu *et al.*, Ali *et al.* (2015) developed a technique called ‘millimanipulation’, where a vertical stainless steel probe ploughs through a deposit layer at a defined speed. Stripping the layer at different positions is possible. This allows non-uniform material properties to be quantified. Their tool was designed to work with layer thicknesses in the order of millimetres, whereas that of Zhang *et al.* was intended for features with characteristic lengths less than 100 μm .

Within this project, a next generation millimanipulation tool was manufactured to the author’s specifications. It was designed to overcome the problems faced with the set-up described by Ali *et al.* (2015), namely

- i) friction at the probe mounting, which led to hysteresis effects due to self-locking.
- ii) the range of measurable forces was fixed.
- iii) limited space around the sample hindered observation and positioning of additional equipment.
- iv) a force component due to wall shear stress beneath the probe impeded measurement data interpretation.

The fouling layers generated within this project turned out to have thicknesses in the order of micrometres – too thin for effective study with the millimanipulation device. The tool was, however, used to investigate the effect of surface coatings on the detachment of baked sponge cake batter, which contained approximately 1/3 bubbles by volume in a ‘continuous’ phase of emulsified oil in a flour/syrup suspension. Detachment in the dry state was studied for aluminium, 304 SS and seven different fluoropolymer coatings. The surfaces differed in surface energy and roughness. The shear force required to detach baked cake, the work done, and the mass of residue remaining on the surface were measured. The ability of oil to displace water from a surface was shown to be a key factor determining adhesion of these materials. A publication describing the millimanipulation tool and its application is appended below.

Bibliographical data:

Magens, O. M., Liu, Y., Hofmans, J. F. A., Nelissen, J. A., & Ian Wilson, D. I. (2017). Adhesion and cleaning of foods with complex structure: Effect of oil content and fluoropolymer coating characteristics on the detachment of cake from baking surfaces. *Journal of Food Engineering*, 197, 48–59.



Adhesion and cleaning of foods with complex structure: Effect of oil content and fluoropolymer coating characteristics on the detachment of cake from baking surfaces



Ole M. Magens^a, Yingda Liu^a, Jurgen F.A. Hofmans^b, Joke A. Nelissen^b, D. Ian Wilson^{a,*}

^a Department of Chemical Engineering and Biotechnology, University of Cambridge, New Museums Site, Pembroke Street, Cambridge, CB2 3RA, UK

^b Chemours Belgium, A. Spinoystraat 6A, 2800, Mechelen, Belgium

ARTICLE INFO

Article history:

Received 9 August 2016

Received in revised form

22 September 2016

Accepted 3 November 2016

Available online 4 November 2016

Keywords:

Adhesion

Cake

Cleaning

Cohesion

Fouling

Surface energy

ABSTRACT

The effect of surface coating on the detachment of a complex microstructured food material, was investigated using an improved version of the millimanipulation device described by Ali et al. (2015 *Food & Bioproducts Processing*, Vol. 93, 256–268). The test material was baked sponge cake batter, which contains approximately 27 vol% bubbles in a 'continuous' phase of emulsified oil in a flour/syrup suspension. Detachment in the dry state was studied for aluminium, 304 stainless steel and seven different fluoropolymer coatings. The surfaces differed in surface energy and roughness. The shear force required to detach baked cake, the work done, and the mass of residue remaining on the surface were measured. Virtually all samples detached by cohesive or mixed failure, where adhesion to the surface was stronger than or comparable with cohesive interactions within the cake. The shear force was almost independent of surface composition, energy and roughness, but strongly related to the oil content of the cake. The mass of residue was found to be linearly dependent on the calculated work of adhesion of oil to the surface in an aqueous environment. The quantitative findings are consistent with confocal microscopy images of uncooked batter contacting polar and non-polar surfaces which show very different oil spreading behaviour at the batter-substrate interface. The ability of oil to replace water from a surface is shown to be a key factor determining adhesion of these materials.

© 2016 Elsevier Ltd. All rights reserved.

1. Introduction

The adhesive properties of soft solids on surfaces are critical for many industrial and household applications. Whilst adhesion is desired in many applications, such as coating operations, in others the adhesion of unwanted species and their accumulation to form fouling deposits is an ongoing problem. In the food sector the presence of such layers can reduce process efficiency and productivity. Their ability to harbour micro-organisms can compromise hygienic operation, while cross-contamination (particularly in multi-product plant) can affect product quality or compromise batch integrity. Processes handling materials prone to adhere – which can be the product itself, as in heat exchanger fouling – are therefore subject to regular cleaning, monitoring and inspection.

Adhesion can often be managed by controlling the surface

morphology and composition (Detry et al., 2010). Coatings and surface modifications can mitigate the initiation and build-up of deposits and/or promote the release of soil under certain conditions, facilitating cleaning (Mérian and Goddard, 2012). In the cleaning map of Fryer and Asteriadou (2009), the promotion of soil release from the substrate provides an alternative to the use of chemical and/or thermal energy which would otherwise be needed to remove complex soils with strong cohesive interactions. Promoting soil release (termed adhesive failure by Fryer and Asteriadou) would in effect move the soil to a less complex region on their map.

Successful coatings can accrue long-term process cost savings (Gomes da Cruz et al., 2014) as well as improving safety and hygiene.

1.1. Surface energy and work of adhesion

The scientific principles underpinning adhesion and cohesive interactions are well established. In an aqueous environment the

* Corresponding author.

E-mail address: diw11@cam.ac.uk (D. Ian Wilson).

forces between a substrate and an adhering layer are determined by contributions from electrostatic, Van der Waals, and solvation forces (Israelachvili, 2010). Since many soiling layers are many microns thick (they are visible to the naked eye) cohesive interactions also determine how the layer responds to an imposed force.

The surface topology and roughness play a role, by (i) determining the area available for interaction; (ii) controlling the interaction such as by the lotus leaf effect, where small, regular features modify the effective contact angle; and (iii) affecting the nature of the soiling layer, via the potential to promote nucleation (e.g. for crystallisation, see Junghahn, 1964; or condensation, see Zamuruyev et al., 2014), and mechanical interlocking.

The surface tension of a liquid or the surface energy of a solid is classically treated as the sum of dispersion and polar forces, i.e. $\gamma = \gamma^d + \gamma^p$. Interfacial tensions obey the geometric mean 'combination rules' described by Fowkes (1963). For cases where both dispersive and polar interactions operate across the interface between medium 1 and 2 the interfacial tension is given by (Owens and Wendt, 1969).

$$\gamma_{12} = \gamma_1 + \gamma_2 - 2\left(\sqrt{\gamma_1^d \gamma_2^d} + \sqrt{\gamma_1^p \gamma_2^p}\right) \quad (1)$$

Here, γ_i is the surface tension between substance i and vacuum: the subscript for vacuum is omitted for convenience, as in many texts. Moreover, $\gamma_{i,\text{air}} \approx \gamma_i$. The thermodynamic work of adhesion in an immersed system is estimated from the difference in total interfacial energy when adhering species 1 wets a substrate 2 in medium 3. As outlined by Clint and Wicks (2001), for an oil (1) to adhere to a solid substrate (2) when immersed in water (3), the work of adhesion, W_{123} is given by

$$W_{123} = \gamma_{23} + \gamma_{13} - \gamma_{12} \quad (2)$$

where γ_{23} , γ_{13} and γ_{12} are the interfacial tensions between substrate/water, oil/surrounding medium and oil/substrate, respectively. By combining Equations (1) and (2) it can be shown that

$$W_{123} = 2\left(\gamma_3 + \sqrt{\gamma_1^d \gamma_2^d} + \sqrt{\gamma_1^p \gamma_2^p} - \sqrt{\gamma_2^d \gamma_3^d} - \sqrt{\gamma_2^p \gamma_3^p} - \sqrt{\gamma_1^d \gamma_3^d} - \sqrt{\gamma_1^p \gamma_3^p}\right) \quad (3)$$

Considering the relatively weak intermolecular interactions within and with a gas, for oil to attach to the same substrate when surrounded by air, W_{123} collapses to

$$W_{12} = 2\left(\sqrt{\gamma_1^d \gamma_2^d} + \sqrt{\gamma_1^p \gamma_2^p}\right) \quad (4)$$

The oil will exhibit a contact angle, β , which is related to the interfacial energies by the Young-Laplace equation. Equation (2) then gives

$$W_{123} = \gamma_{13}(1 + \cos \beta) \quad (5)$$

The above relationships can be applied readily when the surface is uniform and there is one adhering species.

Food materials pose particular challenges when designing and predicting the performance of 'non-stick' coatings as a result of their multicomponent nature and heterogeneous microstructure. An aqueous solution may contain species which adsorb preferentially to different surfaces. Many foods feature emulsions with two liquid phases differing considerably in terms of hydrophobicity. This multiphase nature extends further with baked goods such as

cake which may contain bubbles as well as solid components. This aspect, of variable microstructure and composition within a food material, is often neglected when considering adhesion to process surfaces. *A priori* prediction of adhesion of food materials is often, therefore, very approximate. Adhesion and removal behaviour of food and related structure products therefore have to be studied *in situ*, on the surface where they experience processing, under conditions which reflect those encountered during processing.

1.2. Measurement methods and experimental studies

Experimental techniques have been developed to study the adhesion or removal behaviour of complex soils on process surfaces. These can be categorised as applying a controlled or measured strain, or controlled stress, to the soil layer (Ali et al., 2015). Hydrodynamic approaches employ controlled (or estimated) shear stress conditions and monitor the response. Examples include the parallel plate flow cell and fluid dynamic gauging. These approaches provide useful information for design and operation when fluid flow is used to remove soils, e.g. in cleaning-in-place operations.

Controlled strain devices have been developed for studies at different length scales. Plynometers, which reproduce the rubbing action and frictional force imposed by hand cleaning, are used at the product length scale (Zorita et al., 2010). Nano/microscale measurements are now possible: Mayer et al. (2012) measured the force required to dislodge individual CaCO_3 crystals with a bending-beam arrangement mounted in a scanning electron microscope chamber.

Capturing the contributions from different components of a composite, microstructured soil requires investigation at intermediate length scales. Zhang and co-workers (e.g. Akhtar et al. (2010)) modified the micromanipulation technique originally developed to study deformation of cells (Zhang et al., 1991) to investigate the adhesive and cohesive behaviour of fouling layers. In this version of micromanipulation a stainless steel probe is dragged through the deposit at a set height relative to the substrate at a defined speed. This allows the forces to be measured and their variation with height to be quantified. Ali et al. (2015) developed a variant of this method which they called 'millimanipulation' to study viscoplastic layers at larger length scales. Ashokkumar and Adler-Nissen (2011) reported a similar scraping device to investigate the adhesion of foodstuffs (pancake, turkey meat, carrots and sweet potato) fried on different surfaces.

In the current work, three failure modes were observed which we label as adhesive, mixed, or cohesive (see Fig. 1). The influence of adhesion and cohesion on removal behaviour were discussed by Hoseney and Smewing (1999): sticky substances are associated with high adhesive forces and low cohesive forces. Adhesive failure occurs if the adhesive forces at the interface are weaker than the cohesive forces within the deposited material: the cake separates cleanly from the substrate, leaving little or no residual material. Conversely, in cohesive failure, breakage occurs at a shear plane within the cake, leaving a residual layer across the circular area of contact. Mixed failure arises when both occur, which is associated with the substrate surface and/or test material being heterogeneous. Non-stick coatings should promote adhesive failure, for ease of cleaning or for removal by forces exerted during processing.

Ashokkumar and Adler-Nissen (2011); Ashokkumar et al. (2010) evaluated the cleanability of different surfaces soiled by frying carrot, sweet potato, turkey meat and pancake at temperatures between 160 and 240 °C with and without applying oil prior to frying. Their cleaning procedure involved water rinsing, soaking in cleaning solutions and scrubbing with different sponges. They

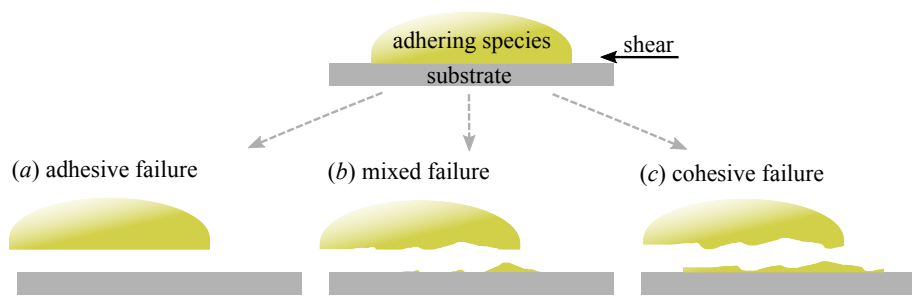


Fig. 1. Schematic of the failure modes encountered in experiments.

reported significant effects of surface roughness on removal forces and amount of residue, which they related to bubble nucleation behaviour. Smoother surfaces gave poorer removal performance. The pancakes studied in their frying experiments featured porous structures generated by high heat fluxes which promote boiling and rapid moisture loss on the heated surface.

Cake is an aerated food product and is likewise generated by baking a three-phase material, the batter. The heat fluxes in baking are generally smaller and more uniform than in frying. During baking the air bubbles present are expanded by the change in temperature, evaporation and release of carbon dioxide from the degradation of baking soda. The 'continuous phase' is a multiphase dispersion, comprising an emulsion of oil droplets in a suspension of flour particles in a sucrose solution. During baking, the starch in the flour gelatinises and sets at higher temperatures to capture the structure (see Chesterton et al., 2013). Whilst the characteristic sizes of surface active molecules and proteins are of order nanometres, flour particles, oil droplets and air bubbles have diameters of tens to several hundred micrometres. The material is therefore heterogeneous at different length scales and was chosen as a representative material to test the performance of non-stick coatings for the food industry.

Coated baking trays are often used to minimise adhesion on baking lines. A new version of the millimanipulation device reported by Ali et al. (2015) is employed here which allows a wider range of forces to be studied. The removal characteristics of sponge cake prepared from a standard commercial cake mix were studied for seven different fluoropolymer (FP) coated stainless steel plates, as well as uncoated stainless steel and aluminium surfaces. The influence of surface topography as well as work of adhesion, evaluated using Equation (3), were investigated. The effects of cake formulation and baking time were also studied and the findings are

compared with the results reported for frying by Ashokkumar and Adler-Nissen (2011); Ashokkumar et al. (2010, 2012).

2. Materials and methods

2.1. Surfaces tested

Table 1 is a summary of the surfaces investigated. The majority of substrate plates were 304 stainless steel with dimensions either (i) square, 5×5 cm, thickness 2 mm (EN 1.4301 304, EN 10088-2 2R) or (ii) circular, 5 cm diameter, 1 mm thick (EN 1.4301 304, EN 10088-2 2B). Chemours supplied five different coated square and two coated circular substrates. Uncoated circular stainless steel and square aluminium alloy substrates were included as references, representing metals commonly used in bakery equipment. Surfaces were cleaned in dishwashing solution followed by rinsing with copious amounts of tap water.

2.1.1. Surface energies

The dispersive and polar surface energy components of the test surfaces were determined according to the Owens and Wendt (1969) model with water, formamide, ethylene glycol and dodecane. Twelve contact angle measurements were taken for each liquid on each coating and the results are summarised in Table 2. PTFE-1 (used), SS and AL were strongly hydrophilic with surface energies more than twice the others. As expected, alongside with the other fully fluorinated coatings, the liquid based PTFE coating (PTFE-2) had a low total surface energy. Its dispersive and polar surface energy components are close to the values of $\gamma^d = 17$ mJ/m² and $\gamma^p = 0.6$ mJ/m² reported for PTFE by Clint and Wicks (2001). The non-zero polar component may arise from end-groups in the polymerisation reaction. The contact angle data were also analysed

Table 1

Summary of surfaces studied. S_a and S_q are, respectively, the arithmetic mean and root mean square roughness of the substrates. \pm indicates standard deviation.

Name	Symbol	Shape	Thickness (mm)	Surface	S_a (nm)	S_q (nm)
SS	▲	circular	1	stainless steel; EN 1.4301 304, EN 10088-2 2B	65 ± 9.6	90 ± 17
AL	△	square	1	aluminium alloy	351 ± 31	425 ± 37
PFA-1	■	circular	1	liquid based perfluoroalkoxy alkane (PFA)	1447 ± 205	1760 ± 240
PFA-2	■	square	2	powder based PFA	490 ± 47	610 ± 58
PFA-3	■	square	2	liquid based PFA	560 ± 67	700 ± 80
FEP-1	+	circular	1	liquid based fluorinated ethylene propylene (FEP)	380 ± 54	470 ± 65
FEP-2	×	square	2	liquid based FEP	380 ± 78	480 ± 92
PTFE-1	◇	square	2	epoxy resin with dispersed polytetra-fluoroethylene (PTFE) particles	740 ± 73	960 ± 110
PTFE-2	◆	square	2	liquid based PTFE	2290 ± 310	2810 ± 290

Table 2

Equilibrium contact angle, β , measured at 20 °C, and surface energy components calculated from the Owens and Wendt (1969) approach. \pm indicates 95% confidence interval of the mean. Liquid parameters taken from (van Oss et al., 1992). β_{ows} is the contact angle for rapeseed oil ($\gamma^d = 33.8 \text{ mJ/m}^2$, $\gamma^p \approx 0 \text{ mJ/m}^2$; Esteban et al. (2012)) in water ($\gamma^d = 21.8 \text{ mJ/m}^2$, $\gamma^p = 51.0 \text{ mJ/m}^2$) on the surface calculated from Equation (5). Angles reported to one decimal place.

Liquid	Water	Formamide	Ethylene glycol	Dodecane	Surface energy (mJ/m ²)		β_{ows}
γ^d (mJ/m ²)	21.8	39.0	29.0	25.4	γ^d	γ^p	(°)
γ^p (mJ/m ²)	51.0	19.0	19.0	0.0			
Surface	β (°)				γ^d	γ^p	(°)
SS	64.3 ± 1.9	61.5 ± 2.0	51.8 ± 2.9	4.0 ± 0.9	18.4 ± 5.2	21.0 ± 5.9	98.8
AL	57.6 ± 8.8	67.6 ± 8.2	41.2 ± 2.6	5.1 ± 1.4	18.8 ± 6.6	20.8 ± 7.4	108.0
PFA-1	105.4 ± 5.3	93.4 ± 3.3	90.7 ± 2.6	37.9 ± 1.3	17.2 ± 3.6	0.7 ± 0.8	45.1
PFA-2	110.3 ± 1.8	90.4 ± 1.8	94.7 ± 0.7	43.0 ± 0.8	17.6 ± 2.0	0.2 ± 0.2	36.4
PFA-3	108.2 ± 2.0	92.8 ± 3.5	91.8 ± 1.5	44.6 ± 1.2	16.7 ± 2.1	0.5 ± 0.4	42.5
FEP-1	98.0 ± 3.1	93.5 ± 1.3	91.0 ± 1.5	37.6 ± 1.8	15.2 ± 3.9	2.1 ± 1.6	58.6
FEP-2	108.4 ± 1.1	92.9 ± 4.0	92.6 ± 1.3	41.6 ± 3.3	17.2 ± 2.2	0.4 ± 0.3	40.4
PTFE-1	81.1 ± 3.5	70.1 ± 2.8	65.7 ± 2.9	19.3 ± 7.3	20.8 ± 3.2	7.2 ± 2.0	77.9
PTFE-1 used	63.0 ± 4.9	63.7 ± 3.7	61.4 ± 4.0	15.4 ± 3.9	18.0 ± 5.5	17.3 ± 5.7	101.7
PTFE-2	106.9 ± 4.7	96.3 ± 2.0	96.3 ± 3.0	38.1 ± 2.6	16.2 ± 3.8	0.5 ± 0.7	42.6
borosilicate glass slip	11.3 ± 1.13	9.7 ± 0.69	8.4 ± 0.16	0 ± 0 ^a	20.5 ± 4.7	45.6 ± 7.5	154.2
PVCA slip	103.8 ± 0.37	83.9 ± 0.96	79.5 ± 3.0	25.2 ± 1.1	22.3 ± 1.2	0.5 ± 0.2	41.5

^a Contact angle too small to identify, set to zero.

in terms of the van Oss et al. (1988) theory, which characterises the surface energy in terms of electron donor and acceptor sites. This indicated that electron donor components were dominant for all the surfaces tested (data not presented) and hence this theory was not used in the calculations as the system studied features no strong Lewis acid–acid or base–base repulsions.

After baking, indelible marks were evident on the PTFE-1 plates (see Supplementary Material 1), which remained after repeated cleaning in detergent solution. Contact angle measurements on the stained areas revealed that polar interactions had increased two-fold, while dispersive interactions decreased. This change is consistent with degradation of the epoxy resin during baking: this material is known to degrade at 180 °C.

2.1.2. Topology and roughness

The surface topology was scanned at five positions on each surface with a Zygo NewView 200 interferometer. The surface profile data were filtered with a 5 × 5 median filter and missing data were interpolated with a triangulation-based linear approach. Typical topology plots for each surface are shown in Fig. 2. Both metal surfaces feature striations associated with machining and polishing. The arithmetic mean and root mean square roughness was calculated according to ISO 25178 are summarised in Table 1. Standard deviations were calculated on the basis of analysing the five profiles separately.

2.2. Cake material

A commercial cake mix (Betty Crocker™ Classic Vanilla Cake Mix) was used to generate cake test layers. Spray dried hen egg (internationalegg.co.uk) was used rather than fresh eggs to improve reproducibility. It was reconstituted with deionised water using a 12:37 mass ratio of egg powder to water. The typical ingredients of the cake mix and the spray dried egg as sold are given in Table 3. The total lipid content was varied between 6.11 wt% and 20.20 wt% by adding vegetable oil (100% rapeseed oil, Sainsbury's supermarket) while maintaining the masses of all other ingredients constant (see Table 4). The total constituent fractions of the cake batters were calculated by assuming that the fibre and salt fractions in the spray dried egg and the vegetable oil were negligible, as well as there being no water in the cake mix, egg powder and vegetable oil. The ingredients were combined in a large bowl with a spatula,

then whisked using a planetary mixer (Kenwood™ Chef KMC010) for 3 min at Setting 1 (67 rpm) until a smooth consistency was achieved. The air volume fraction of the batter, ϕ_{air} , calculated with Equation (6), was around 27 vol%.

$$\phi_{\text{air}} = 1 - \frac{\rho}{\rho_s} \quad (6)$$

Here ρ_s is the density of the deaerated suspension, obtained by centrifuging 50 ml samples at 1200 g for 15 min.

2.3. Confocal laser scanning microscopy

To visualise how the lipids in the batter interact with test surfaces, an oil soluble dye (9 wt% oil loading dough + oil Red O, Sigma Aldrich, dye content $\geq 75\%$) was mixed with rapeseed oil and filtered with a 0.45 μm pore size syringe filter (Sartorius Stedim Minisart®) before adding it to the batter mix. The dyed batter was then applied using a 20 ml BD™ syringe to (polar) borosilicate and (non-polar) polyvinyl chloride acetate (PVCA) cover slips. Confocal laser scanning microscopy was conducted on a Leica TCS SP5 microscope with an argon laser exciting the fluorophore at 514 nm, a 40 × oil immersion lens (HCX PL APO 40 × 1.25–0.75 oil) and the pinhole set at 60.6 μm .

2.4. Millimanipulation device

The millimanipulation tool shown in Fig. 3 offered superior and more flexible performance than the device reported by Ali et al. (2015). The sample is moved (the probe (1) is effectively static) and the force is measured by the transducer (2; 0–10 N or 0–20 N HBM S2M). The force measured by the transducer is amplified by a ratio set by the position of the transducer on the tower (3). The axis (4) can move at a steady speed, up to 20 mm/s, or move then rest with a full step resolution of 5 μm . These tests featured a sharp bottom edge on the probe, reducing the resistance from any material underneath the probe. The sample may be tested immersed in a temperature controlled bath (5), in ambient air on a plain sample holder (6).

Fig. 4 (a) illustrates the millimanipulation action. A vertical blade is brought into contact with the layer (here, a small cake) and moved through the layer at a set speed, v . The voids in the structure render it compressible and the deformation induced by the blade

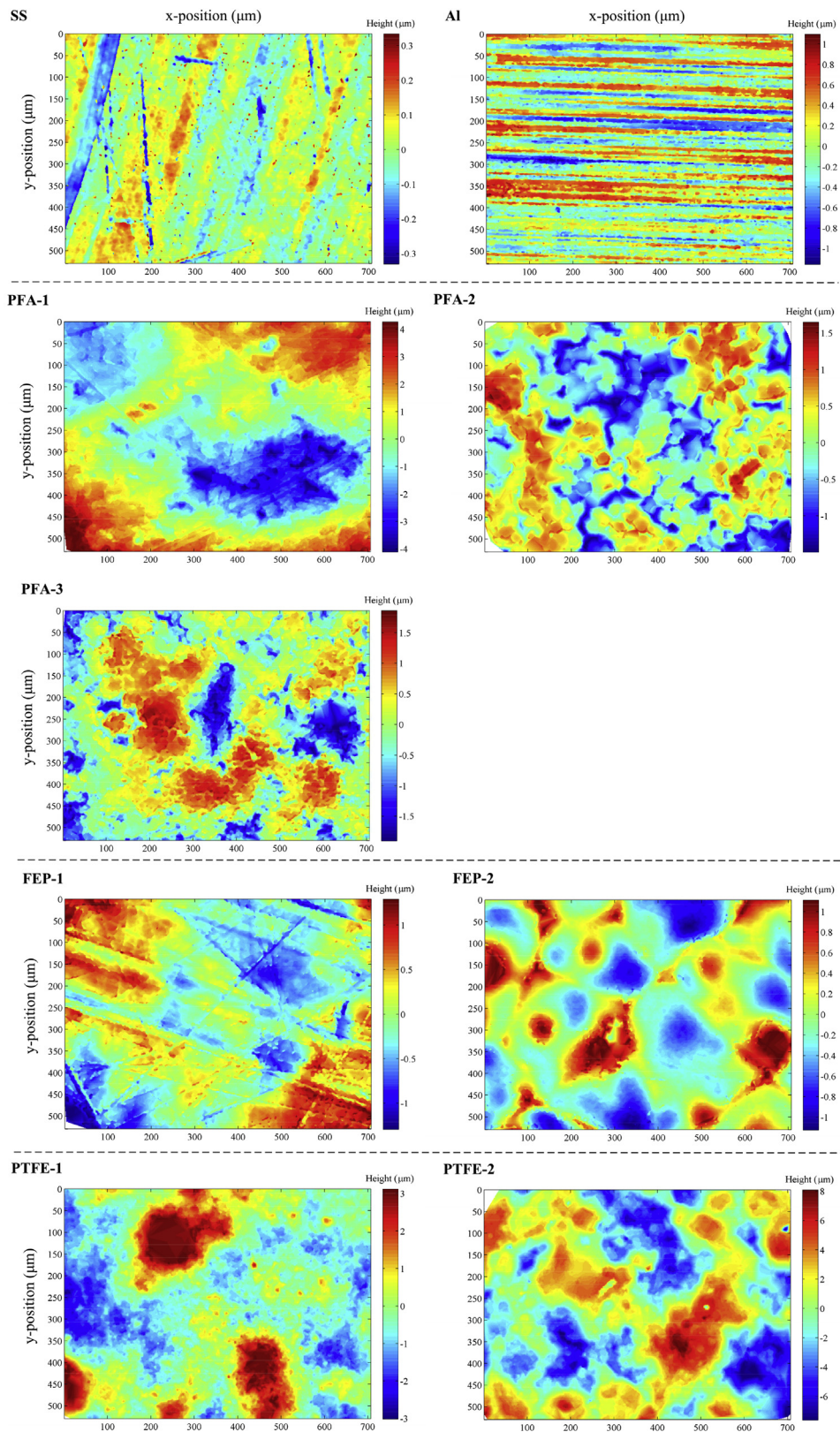


Fig. 2. Filtered and interpolated substrate surface topologies. Height scale differs between substrates.

motion (a combination of compliance and yield) detaches the cake in a complex fashion, often lifting it off at varying positions. This was overcome by baking cake samples in the holding ring device

shown in Fig. 4 (b and c). The test cake here is small compared to many baked products, starting as a short cylinder of batter with diameter, D , of 50 mm and height 10 mm. The wall of the holder is

Table 3
Ingredients and constituents of cake mix and spray dried egg, taken from packaging.

Betty Crocker™ Classic Vanilla Cake Mix	
Ingredients: sugar, wheat flour, palm fat, raising agents: monocalcium phosphate, sodium bicarbonate, modified corn starch, salt, Emulsifiers: propane- 1, 2-dial esters of fatty acids, mono-diglycerides of fatty acids, Flavouring, Stabiliser: Xanthan gum	
Constituent	Fraction (wt%)
Fat	7.8 (of which 4.1 are saturates)
Carbohydrates	79.3 (of which 47.1 are sugars)
Fibre	1.4
Protein	5.1
Salt	1.6
Spray dried hen egg	
Ingredients: Pasteurised and spray dried hen eggs	
Constituent	Fraction (wt%)
Fat	42
Carbohydrates	5
Protein	46

Table 4
Ingredients and total constituent fractions of the cake batter recipes used. **Bold** text indicates preparation according to the recipe on the packaging.

Ingredient							
Cake mix (g)	135.00						
Egg powder (g)	13.96						
Deionised water (g)	118.94						
Vegetable oil (g)	0.00	5.47	11.16	17.10	23.30	29.77	60.47
Mass fraction in batter (all in wt%)							
Lipids	6.11	8.00	9.87	11.75	13.63	15.51	20.20
Carbohydrates	40.22	39.42	38.61	37.81	37.00	36.20	32.81
Fibre	0.71	0.69	0.68	0.66	0.65	0.64	0.57
Protein	4.96	4.87	4.77	4.67	4.57	4.47	4.05
Salt	0.81	0.79	0.77	0.76	0.74	0.73	0.66
Water	44.40	43.51	42.62	41.73	40.85	39.96	36.22

constructed from PTFE and a grid of 316 stainless steel 1 mm diameter rods in the lower section ensures that the strain is transmitted evenly through the base layer of the cake. The cake then detaches across the substrate/cake interface when the ring is moved laterally by the millimanipulation blade. As shown in Fig. 4 (b), a pin on the blade ensures that the shear force is applied at the base of the ring. The contribution from the area under the PTFE ring to the force measured, F , is negligible. The process is videoed with a

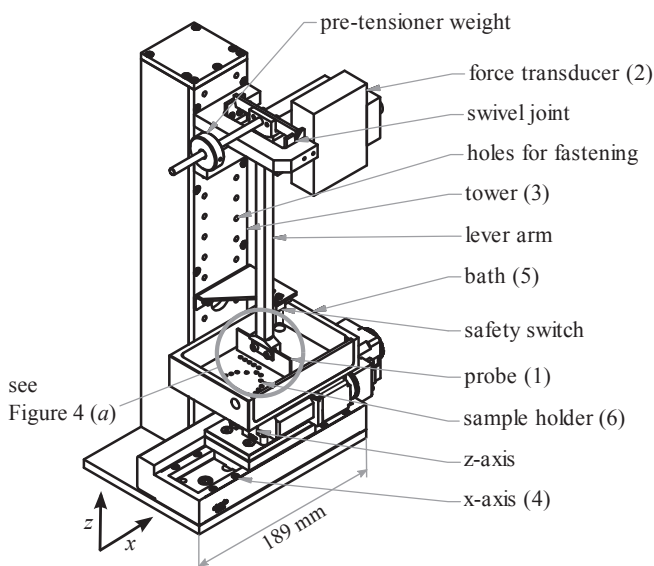


Fig. 3. Schematic of the millimanipulation device. Components not shown: axis controllers and force transducer amplifier.

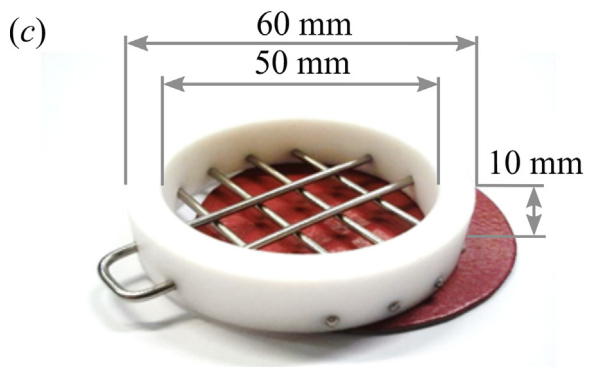
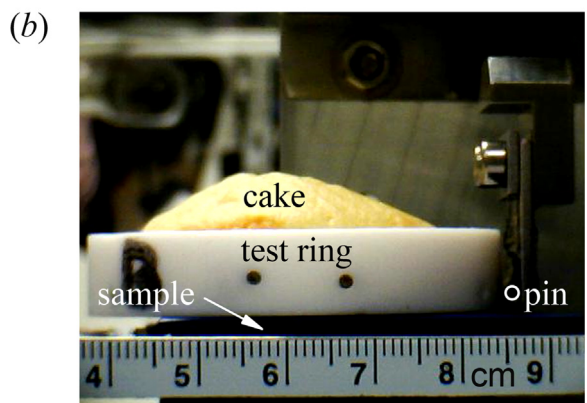
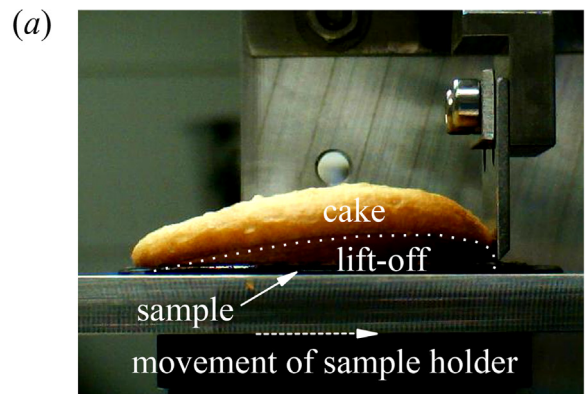


Fig. 4. Millimanipulation of baked cake (a) without and (b) with support ring. Dotted line in (a) shows the cake lifting up, which is prevented in (b) by the support ring detailed in (c) ensuring a defined fracture plane.

digital microscope and the amount and distribution of any residual layer remaining on the substrate recorded by imaging and weighing.

For experimental preparation the substrate plate and its test ring were each weighed before the latter was clamped onto the plate using three 51 mm fold-back clips. The compression provided by the clips prevented the ingress of batter beneath the ring which could result in an annulus of sticky material. 11.00 ± 0.05 g of cake batter was filled into the chamber thus formed using a 20 ml BD™ syringe. Care was taken to fill the gaps between the rods so that the cake batter covered the coated plate completely. The ‘mini-cakes’ were baked in a pre-heated Carbolite® oven at 180 °C for 8 min, then left to cool for 30 min in a temperature-controlled room at 22 ± 1 °C. The clamps were then removed and the combined mass of the plate, test ring and cake was measured. The mass of the cooled cake weighed 9.37 g on average, representing a 15% mass loss on baking. Following millimanipulation testing the plate and any residual material was weighed and photographed.

Fig. 5 (a) shows a typical force profile during a steady shear test. The signal is filtered with a finite impulse response band-stop filter

to remove 50 Hz noise. After contact with the probe, setting $x = 0$, the force increases linearly with displacement up to about 4 N, after which the increase is non-linear, reaching a peak and falling sharply as the majority of the connections within the cake and/or between the cake and the surface rupture. This suggests that the material contains elastic elements with a distribution of limiting strains. Detailed interpretation of these results in terms of micro-structural models was not attempted. Subsequently, the force decreases sharply and approaches a steady value associated with friction as the sheared material moves over the fracture plane. The low friction coefficient of PTFE and the light-weight ring (the average mass of the rings was 20.2 g) reduced the frictional contribution from the ring to less than 0.05 N during manipulation testing (measured without cake present).

The peak force F_{\max} is extracted from each force profile as indicated on the Figure and converted to the maximum shear stress, τ_{\max} , by dividing by the cake contact area. The breakage work per area (see Equation (7)), W_b , is determined by calculating the work done (per unit area) from $x = 0$ to X , where X is the intercept on the x -axis of the projection of the tangent passing through the point of inflection, I, marked in Fig. 5 (a):

$$W_b = \frac{1}{A} \int_0^X F dx \quad (7)$$

Fig. 5 (b) shows the force profile obtained by a second mode of testing, labelled *relaxation testing*. The probe was moved 1 mm and then held in place for 20 s, labelled interval I, before being moved a further 1 mm, followed by 20 s delay (interval II), and then a further 1 mm (and interval III). The force decays with a quasi-exponential trend in interval I, indicating a visco-elastic response of the material. The peak force after interval I is similar to the initial value, but the decay response is very different: this feature, and the small force peak after interval II, indicates that rupture at the shear plane is complete. Further consideration of such data and analysis are not presented here: this mode of operation affords new insights into the material behaviour.

3. Results and discussion

3.1. Removal behaviour

The majority of tests, on all surfaces and for all oil contents, featured cohesive or mixed failure (see Fig. 1), leaving measurable amounts of residual material on the coated surface. This indicated that the strength of the adhesive interactions of the cake material with the surfaces was comparable or stronger than the cohesive interactions within the cake. The peak shear stress, τ_{\max} , and breakage work, W_b , should then both be influenced strongly by the forces required to disrupt the cake structure, and be less sensitive to the presence of a coating. The reverse would apply if the tests exhibited mostly adhesive failure. τ_{\max} and W_b showed a strong, positive correlation for all surfaces which confirms this hypothesis (see Supplementary Material 2). Cake with a high rapeseed oil content left lumps, a few mm in diameter, on the stainless steel surface. This indicates that the cohesive strength of the cake was weak compared to the material's adhesion to the steel. Peak shear stress is used as the indicator of forces in subsequent plots.

The effect of scraping speed, v , was investigated to see if this would promote a transition in breakage mechanism. Tests conducted with scraping speeds in the range 0.1–8 mm/s for the reference formulation on two fluoropolymer coated surfaces exhibited a logarithmic increase in τ_{\max} with v and no systematic difference in failure mode (data not reported).

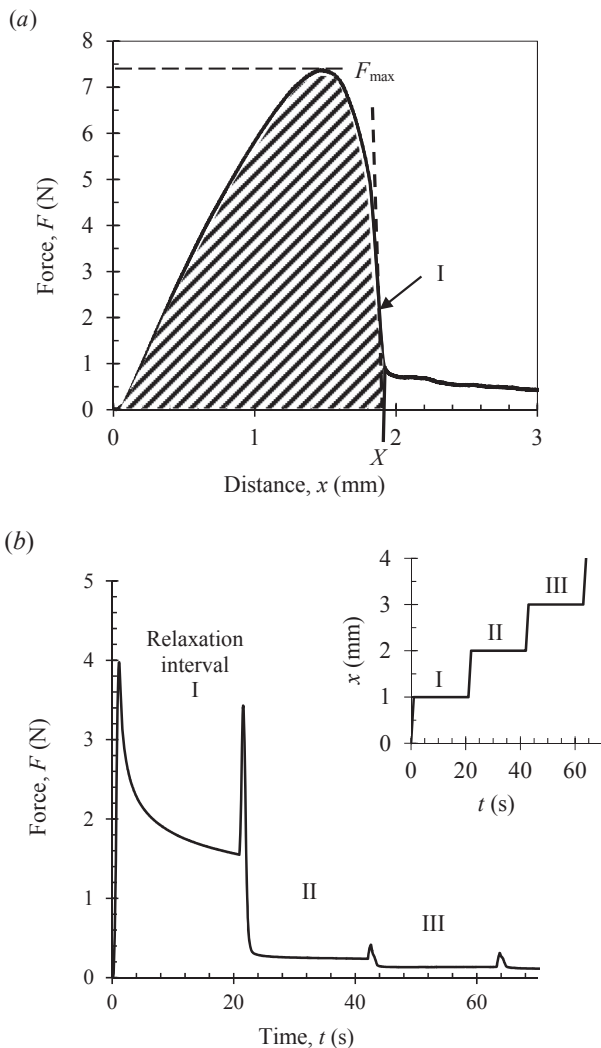


Fig. 5. Typical millimanipulation force profiles for shearing of baked cake (PFA-2, 6.11 wt% total lipids). (a) standard test at $v = 1$ mm/s: I marks the point of inflection and X shows the limit of integration to obtain the breakage work with Equation (7). (b) Relaxation test: Inset shows probe motion history, 1 mm/s, 1 mm scrape interval, 20 s stop period.

3.2. Effect of cake formulation

Fig. 6 and Table 5 indicate that the addition of oil reduces the cohesive strength of the cake.

Fig. 6 (b) shows that, with the exception of uncoated stainless steel, the peak shear stress decreases with increasing oil content up to about 8 wt% and is effectively constant thereafter. The similarity in trend for the remaining coatings and aluminium indicate that the contribution from surface properties is small by comparison, which is consistent with the hypothesis that τ_{max} is determined by the cohesive strength of the cake material.

The τ_{max} values for the PTFE-2 coating are twice as large as the other fluoropolymer coatings and decrease steadily with increasing oil content, unlike the other fluoropolymer coatings. This was the roughest surface tested, with S_a and S_q values of 2.3 μm and 2.8 μm , respectively, and maximum peak to valley distances of about 14 μm . The latter distance is large enough to harbour smaller flour particles. The large τ_{max} values are not, however, accompanied by high m_{res} values, indicating that the large difference in surface roughness has caused a difference in the mechanical properties of the surface layer.

A simple explanation for the difference in τ_{max} behaviour for the two metals is not available. The measured surface energy components are similar. The uncoated stainless steel is significantly smoother than the aluminium (Table 1) but this cannot be readily linked to the presence of a maximum in the cohesive forces. The thermal diffusivity of the aluminium is approximately 20 \times that of the stainless steel so the aluminium surface would be expected to reach the oven temperature more quickly. Temperature-driven hardening at the surface would then be expected to be manifested by greater adhesive or cohesive strength on the aluminium plates. This is not evident, and the similarity of the aluminium results to most of the coated surfaces indicates that heat transfer through the metal plate is not a significant factor. The additional thermal resistance imparted by coating is therefore not important. Similarly, the thickness of the plate had little effect.

Fig. 6 (a) shows that the lipid content has a relatively small effect on the amount of residue with the exception of the uncoated stainless steel. The m_{res} values for all PFA coatings and FEP-2 are

effectively constant, while FEP-1 shows a minimum around 12 wt% oil. Coating PTFE-1 gives m_{res} values similar to aluminium, both exhibiting a decrease in m_{res} with increasing cake oil content. The uncoated stainless steel results are again anomalous, giving values similar to the aluminium until 14 wt% and then a wide range of values at the highest oil loading. The anomalous datum of steel (20 wt% lipids), marked L, gave high m_{res} and low τ_{max} values compared to the other steel tests (see also Table 5). This suggests a lower cohesive strength than adhesive strength, and is thought to arise from the oil preferring not to wet the surface but remaining in the bulk material.

The effect of surface energy on oil behaviour in the batter is demonstrated by the series of confocal microscopy images in Fig. 7, obtained with the 8 wt% oil content formulation on transparent surfaces. No baking was done. In (a), the microscope cover slip is made of strongly polar borosilicate glass whereas in (b) it is made from non-polar PVCA. Some oil droplets are evident suspended in the bulk of the dough whereas others are adhering to the substrates. The oil does not wet the polar borosilicate glass readily, instead forming discrete droplets with sizes up to 20 μm . The contact angle measured from the image is around 130°. The work of adhesion is low, estimated as 5.2 mJ/m^2 for an ideal system of rapeseed oil on borosilicate glass when immersed in water. The contact angle calculated from Equation (5) was 154.2° (see Table 2 for calculated oil-surface-water contact angles), which is comparable with the observed value. The difference is attributed to surface active components and the batter's resistance to deformation.

In contrast, the work of adhesion of the oil on PVCA in water was calculated to be 91.5 mJ/m^2 . The affinity for the oil to stay at the non-polar polymer is demonstrated by Fig. 7 (b), where the oil wets the PVCA surface readily and spreads across the surface. The contact angle is around 25°, which compares favourably with the value of 41.5° calculated for oil on PVCA in water. Quantitative analysis of the fluorescence intensity data (see Supplementary Material 3) showed the oil content to be greatest at the interface, whereas on the borosilicate glass the maximum oil content was located approximately 5 μm from the interface, which is consistent with the oleophobicity of the surface in an aqueous environment.

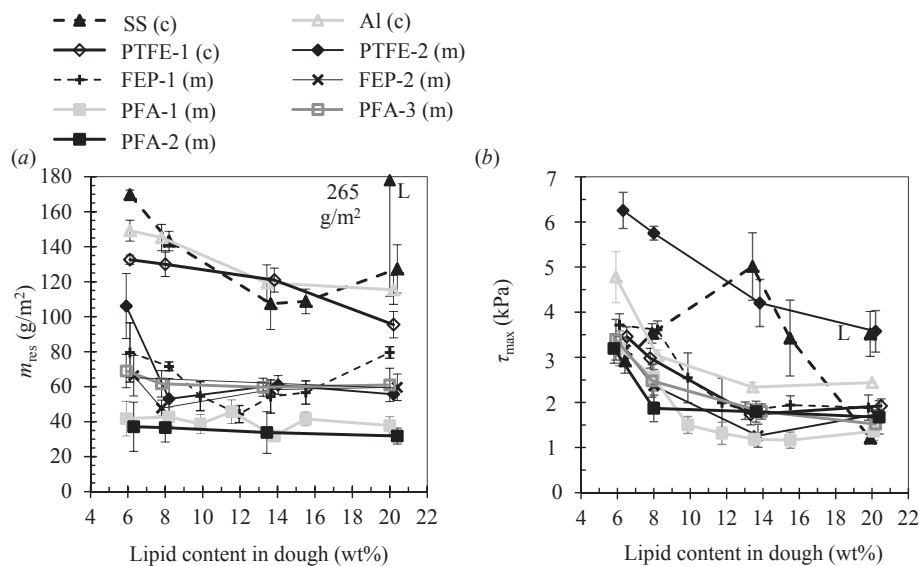
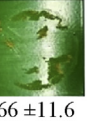
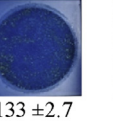
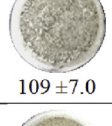
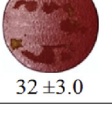
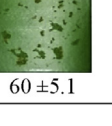
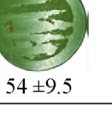
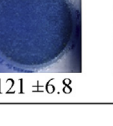
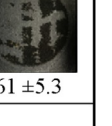


Fig. 6. Effect of lipid content on (a) residue coverage, and (b) and peak shear force, for nine surfaces. Some markers are offset in lipid content for clarity and connecting lines are reading aids. Datum labelled L indicates anomalous data where lumps of cake were left on SS plates. Legend labels (c) and (m) indicates cohesive and mixed failure, respectively. Error bars show ± 1 standard error.

Table 5
Photos of typical residue left on the substrates after Millimanipulation for four different total lipid fractions. Anomalous case where lumps of cake were left on SS plates at 20.2 wt% lipid is shown. Numbers are average residue masses in g/m^2 and \pm indicate standard errors.

		Substrate (residue masses in g/m^2)								
		SS	AL	PFA-1	PFA-2	PFA-3	FEP-1	FEP-2	PTFE-1	PTFE-2
Lipid fraction (wt%)	6.11	 169 \pm 2.7	 149 \pm 5.9	 42 \pm 9.9	 37 \pm 14.0	 69 \pm 9.6	 80 \pm 16.9	 66 \pm 11.6	 133 \pm 2.7	 106 \pm 18.6
	8	 143 \pm 5.6	NA 145 \pm 7.5	 43 \pm 5.2	NA 37 \pm 8.2	NA 62 \pm 7.5	 72 \pm 2.5	NA 48 \pm 4.6	NA 130 \pm 7.0	NA 53 \pm 11.6
	13.63	 109 \pm 7.0	 119 \pm 10.3	 32 \pm 3.0	 34 \pm 11.9	 60 \pm 5.1	 54 \pm 9.5	 58 \pm 2.7	 121 \pm 6.8	 61 \pm 5.3
	20.2	 127 \pm 13.8  265 (lumps)	 115 \pm 8.3	 38 \pm 5.0	 32 \pm 4.6	 61 \pm 9.6	 80 \pm 3.2	 60 \pm 7.6	 96 \pm 7.6	 56 \pm 0

3.3. Effect of surface roughness

Surface roughness and surface energy have been reported to influence the performance of surface coatings. The influence of individual factors on m_{res} and low τ_{max} were quantified, for each oil content, and the Pearson correlation coefficients of the samples are presented in Table 6. Multi-variate techniques were not attempted as the results are unlikely to offer deterministic insight. The peak shear stress data do not show a systematic dependency on any of the parameters tested, with the largest coefficient being 0.69. This

is consistent with τ_{max} being determined by forces involved in cohesive failure, which is expected to be determined chiefly by batter formulation rather than surface characteristics. Plots for peak shear stress over roughness for four batter formulations are provided in Supplementary Material 4.

The correlation coefficients for m_{res} for all oil contents studied show a very weak, negative correlation with S_a and S_q , indicating that there is little direct influence of surface roughness on the amount of residual layer. Similar findings were reported for bacterial adhesion on stainless steels by Detry et al. (2010). An estimate

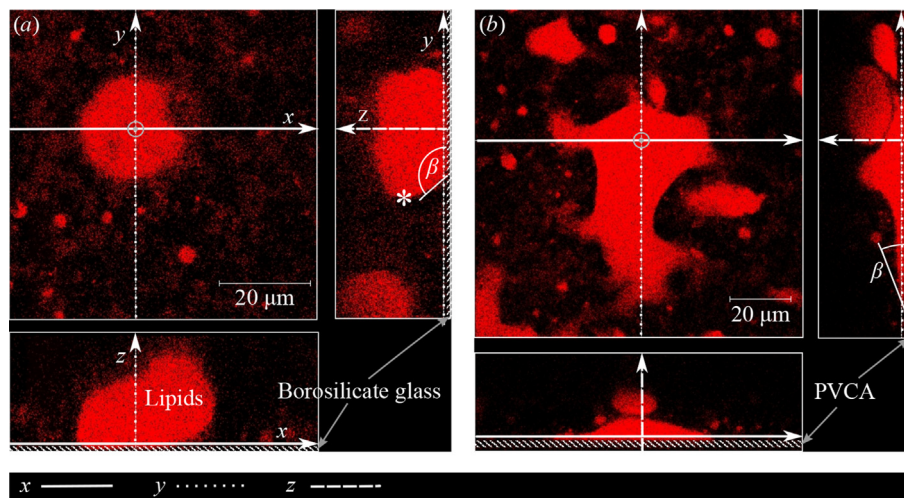


Fig. 7. Orthogonal section images obtained by CSLM of cake dough with 8 wt% total lipids on (a) borosilicate glass and (b) PVCA cover slips. Red indicates lipids labelled with Oil Red O. (For interpretation of the references to colour in this figure legend, the reader is referred to the web version of this article.)

Table 6

Sample Pearson correlation coefficients between surface properties and residual mass and maximum shear stress for different total lipid contents. Coefficients in **bold** indicate highest correlation for a specific lipid content.

Lipid content	m_{res} (g/m ²)				τ_{max} (Pa)			
	6.11	8	13.63	20.2	6.11	8	13.63	20.2
γ	0.87	0.97	0.93	0.88	-0.038	0.0023	0.36	-0.072
γ^d	0.62	0.67	0.60	0.60	-0.33	-0.20	0.48	-0.38
γ^p	0.87	0.97	0.95	0.88	0.014	0.036	0.32	-0.017
W_{123}	-0.89	-0.99	-0.95	-0.91	0.0041	-0.072	-0.33	0.037
S_a	-0.22	-0.43	-0.33	-0.49	0.69	0.63	0.15	0.67
S_q	-0.21	-0.42	-0.33	-0.48	0.68	0.63	0.14	0.67
Substrate thickness	-0.31	-0.41	-0.17	-0.46	0.12	-0.044	-0.17	0.27

of roughness-related coverage can be obtained by assuming that the support ring slides across the top of the highest asperities. The residual mass can then be estimated from the peak-to-valley dimension. This will be an overestimate. Taking the largest peak-to-valley value, 14 μm with PTFE-2, and batter density of approximately 950 kg/m³, gives a coverage of 13 g/m². This is smaller than all those measured, and indicates that m_{res} is not determined by filling the surface features. The values measured on most of the coated plates, or 40–70 g/m², correspond to a layer thickness of 40–70 μm , which is similar to the sizes of the structural components in the cake, *i.e.* the oil droplets (5–20 μm) and flour particles.

3.4. Work of adhesion

Table 6 reports a strong positive correlation between the residual mass and all three components of surface energy, particularly for γ^p , for which correlation coefficients ranged from 0.87 to 0.97. This result is consistent with the postulation of m_{res} being linked to oil wetting behaviour outlined above. A stronger, negative, correlation is evident when the surface energy components are combined in the theoretical work of wetting, W_{123} . Fig. 8(a) illustrates that a high work of adhesion of the oil phase, and thus its tendency to wet the surface, deters cake retention.

An explanation for this behaviour is that the surface coating determines whether the oil spreads readily across the surface or is present as discrete ‘islands’, resulting in different fractions of surface area in direct contact with the aqueous matrix. The cluster of smaller m_{res} values in Fig. 8(a) belong to surfaces with $\gamma_{12} < \gamma_{23}$, giving from Equations (2) and (5) an oil contact angle in water less

than 90°, indicating that the oil will prefer to spread on the substrate. The baking time is too short for the oil to react to give a cohesive material (8 min at 180 °C is not sufficient time to cause polymerisation of the oil: Ali et al. (2015) baked their lard layers for several hours), whereas the starch and proteins in the matrix undergo various transformations in this time. The oil thus tends to shear rather than rupture during testing, requiring a smaller shear force. Regions with high matrix contact will register higher peak force. It should be noted that the W_{123} values are calculated for simple oil-matrix-substrate interactions and do not account for the volume fraction of oil in the batter, which will determine the availability of oil to coat the surface.

The results obtained for the 6.11 wt% lipid formulation, with no additional rapeseed oil, are presented in Fig. 8 (b). This shows a similar trend but there is more scatter. In this case the lipids are palm fat and lipids present in the egg powder, a fraction of which are solid at room temperature. They are less mobile in terms of wetting and also provide stronger resistance to shear when tested at room temperature.

3.5. Discussion

Fluorocarbon-based coatings are often considered for ‘non-stick’ applications and many studies have demonstrated their effectiveness for food operations, including frying (Ashokkumar and Adler-Nissen, 2011), thermal processing of milk (Gomes da Cruz et al., 2014) and handling caramel (Goode et al., 2013). Goode et al. used atomic force microscopy to measure the adhesion forces between stainless steel or fluoro-coated glass (FCG) surfaces and (i)

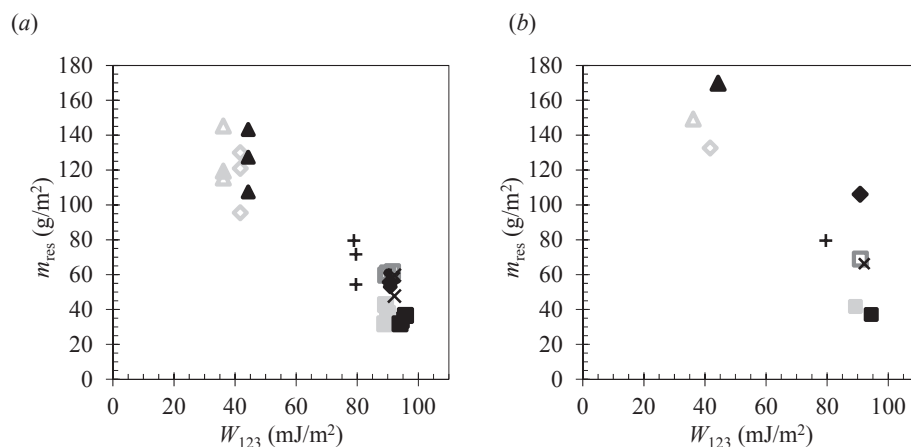


Fig. 8. Effect of work of adhesion on residual mass of cake remaining on surface after testing, for (a) cakes containing additional rapeseed oil, total lipid fraction 8, 13.63 or 20.02 wt %, and (b) cakes with no added oil, containing higher melting point lipids from the cake mix (palm fat) and egg powder amounting to 6.11 wt% lipids. W_{123} was calculated using Equation (3) with solid surface energy components from Table 2, oil parameters ($\gamma^d = 33.8$ mJ/m², $\gamma^p = 0$ mJ/m²) and water parameters ($\gamma^d = 21.8$ mJ/m², $\gamma^p = 51.0$ mJ/m²). Symbols given in Table 1.

wey protein concentrate, (ii) sweetened condensed milk, and (iii) caramel, over the temperature range 30–90 °C. The protein concentrate did not adhere strongly to FCG at temperatures up to 70 °C but adhered strongly at 90 °C, which is attributed to denaturation of the protein and a change in its surface characteristics. Caramel (containing 11 wt% fat) adhered strongly to FCG initially and this diminished with contact times longer than 1 s. The adhesion of caramel at short contact times depended on temperature whereas it was independent of temperature at longer times, suggesting that the material involved in adhesion changed over the first second of contact. On the basis of the results presented above we postulate that this behaviour is related to the time for lipids to diffuse to and adsorb at the interface, replacing the polar aqueous phase.

It is interesting to compare these findings with the results for pancake frying reported by Ashokkumar et al. (2010). Their pancake formulations differed noticeably from the cake mixes studied here (egg white 13.3%, egg yolk 8%, milk 40%, 33.3% wheat flour, 5.3% sugar: water content 59.3%, all w.b.). The contact angle data from Ashokkumar et al. (2012) were used to estimate W_{123} for adhesion of the frying oil to the different surfaces, assuming an initially aqueous environment. In cases where no oil was added prior to frying the cleaning rating (a visual characterisation) was independent of W_{123} . When oil was added, the deposit was harder to clean from polar metallic surfaces (with lower W_{123} values), which is consistent with Fig. 8. However, the relationship between cleaning rating and W_{123} is much less pronounced. The simple work of adhesion model assumes a liquid water phase competing with the oil in wetting. During frying, bubble formation and water evaporation is likely to remove the water phase from the surface soon after contact, giving rise to the insensitivity to W_{123} .

The cake materials investigated here demonstrate that ‘non-stick’ behaviour is not universal and is determined by the surface and the soil properties. It would be a challenge to identify a surface which would resist attachment of this material as it contains three components with very different wetting characteristics: oil, a sugar/starch aqueous phase, and bubbles likely to have surface active proteins at the liquid/vapour interface. Moreover, the material is processed in such a way (semi-quiescent baking) that allows adhering components to migrate to the surface.

Finally, it must be noted that cleaning with a liquid involves a new series of interactions and is likely to promote detachment of the residues, particularly if surfactants or shear forces are present. This highlights the difference between attachment and cleaning.

4. Conclusions

Millimanipulation was used to evaluate the performance of stainless steel plates coated with seven different fluorocarbon coatings, alongside stainless steel and aluminium surfaces as reference. The surface energies and topographies of the surfaces were measured and the former was used to calculate the ideal energy of wetting associated with oil attaching to the surface when immersed in water.

The removal tests were conducted in the dry state. There was little influence of scraping speed and surface roughness, but a strong sensitivity to cake oil content. This result, alongside the observation of residual material on all surfaces, confirmed that the cake was a sticky material wherein adhesion to the surface was stronger than cohesive interactions within the cake matrix. The removal forces were mostly sensitive only to oil content, whereas the amount of residue was found to be directly related to the oil's work of adhesion to the surfaces assuming the cake matrix to resemble an aqueous environment.

The ability of oil to replace water from a surface seems to be a

key mechanism for a ‘non-stick’ surface in baking applications involving water and oil containing doughs or oil pre-wetted moulds. In frying, where the foodstuff is placed on a hot surface, the situation is different. High temperatures evaporate water too quickly to allow the oil to be driven to the surface by hydrophobic repulsion.

Acknowledgements

A Jardine Postgraduate Scholarship for YL from the Jardine Foundation and a PhD studentship for OMM from Du Pont/Che-mours and is gratefully acknowledged. The millimanipulation device was constructed to OMM's specifications by Gautrey Engineering, Cottenham, UK.

Appendix A. Supplementary data

Supplementary data related to this article can be found at <http://dx.doi.org/10.1016/j.jfoodeng.2016.11.004>.

Nomenclature

Roman

A	cake contact area m^2
D	diameter of test cake m
F	force N
m_{res}	residual mass per area g/m^2
S_a	roughness according to ISO 25178, arithmetic mean m
S_q	roughness according to ISO 25178, root mean square m
W	adhesion/breakage work per area J/m^2
v	millimanipulation velocity m/s
x	scraping distance m
X	upper integration limit in calculation of breakage work per area m

Greek

β, β_{ows}	contact angle, value for oil in water on surface °
γ	surface energy, surface tension mJ/m^2
ρ, ρ_s	density of the cake batter, centrifuged cake batter (suspension) kg/m^3
τ, τ_{max}	shear stress, peak value kPa
ϕ_{air}	air volume fraction

Subscripts

1	adsorbing species
2	surface
3	surrounding medium
b	breakage
i	integer

Superscripts

d	dispersive
p	polar

References

- Akhtar, N., Bowen, J., Asteriadou, K., Robbins, P.T., Zhang, Z., Fryer, P.J., 2010. Matching the nano- to the meso-scale: measuring deposit-surface interactions with atomic force microscopy and micromanipulation. *Food Bioprod. Process* 88, 341–348. <http://dx.doi.org/10.1016/j.fbp.2010.08.006>.
- Ali, A., De'Ath, D., Gibson, D., Parkin, J., Alam, Z., Ward, G., Wilson, D.I., 2015. Development of a “millimanipulation” device to study the removal of soft solid fouling layers from solid substrates and its application to cooked lard deposits. *Food Bioprod. Process* 93, 256–268. <http://dx.doi.org/10.1016/j.fbp.2014.09.001>.
- Ashokkumar, S., Adler-Nissen, J., 2011. Evaluating non-stick properties of different surface materials for contact frying. *J. Food Eng.* 105, 537–544. <http://>

- dx.doi.org/10.1016/j.jfoodeng.2011.03.018.
- Ashokkumar, S., Adler-Nissen, J., Møller, P., 2012. Factors affecting the wettability of different surface materials with vegetable oil at high temperatures and its relation to cleanability. *Appl. Surf. Sci.* 263, 86–94.
- Ashokkumar, S., Thomsen, B.R., Raagaard, Hinke, J., Møller, P., Adler-Nissen, J., 2010. Cleanability evaluation of different surfaces by fouling from contact frying of foods. In: *Fouling and Cleaning in Food Processing*. Department of Chemical Engineering, University of Cambridge, pp. 24–33.
- Chesterton, A.K.S., De Abreu, D.A.P., Moggridge, G.D., Sadd, P.A., Wilson, D.I., 2013. Evolution of cake batter bubble structure and rheology during planetary mixing. *Food Bioprod. Process* 91, 192–206. <http://dx.doi.org/10.1016/j.fbp.2012.09.005>.
- Clint, J.H., Wicks, A.C., 2001. Adhesion under water: surface energy considerations. *Int. J. Adhes. Adhes.* 21, 267–273. [http://dx.doi.org/10.1016/S0143-7496\(00\)00029-4](http://dx.doi.org/10.1016/S0143-7496(00)00029-4).
- Detry, J.G., Sindic, M., Deroanne, C., 2010. Hygiene and cleanability: a focus on surfaces. *Crit. Rev. Food Sci. Nutr.* 50, 583–604. <http://dx.doi.org/10.1080/10408390802565913>.
- Esteban, B., Riba, J.-R., Baquero, G., Puig, R., Rius, A., 2012. Characterization of the surface tension of vegetable oils to be used as fuel in diesel engines. *Fuel* 102, 231–238. <http://dx.doi.org/10.1016/j.fuel.2012.07.042>.
- Fowkes, F.M., 1963. Additivity of Intermolecular Forces at Interfaces. I. Determination of the contribution to surface and interfacial tensions of dispersion forces in various liquids. *J. Phys. Chem.* 67, 2538–2541. <http://dx.doi.org/10.1021/j100806a008>.
- Fryer, P.J., Asteriadou, K., 2009. A prototype cleaning map: a classification of industrial cleaning processes. *Trends Food Sci. Tech.* 20, 255–262. <http://dx.doi.org/10.1016/j.tifs.2009.03.005>.
- Gomes da Cruz, L., Ishiyama, E.M., Boxler, C., Augustin, W., Scholl, S., Wilson, D.I., 2014. Value pricing of surface coatings for mitigating heat exchanger fouling. *Food Bioprod. Process* 93, 343–363. <http://dx.doi.org/10.1016/j.fbp.2014.05.003>.
- Goode, K.R.R., Bowen, J., Akhtar, N., Robbins, P.T.T., Fryer, P.J.J., 2013. The effect of temperature on adhesion forces between surfaces and model foods containing whey protein and sugar. *J. Food Eng.* 118, 371–379. <http://dx.doi.org/10.1016/j.jfoodeng.2013.03.016>.
- Hoseney, R.C., Smewing, J.O., 1999. Instrumental measurement of stickiness of doughs and other foods. *J. Texture Stud.* 30, 123–136. <http://dx.doi.org/10.1111/j.1745-4603.1999.tb00206.x>.
- Israelachvili, J.N., 2010. *Intermolecular and surface forces* third edition. Intermol. Surf. Forces. <http://dx.doi.org/10.1016/B978-0-12-375182-9.10025-9>.
- Junghahn, L., 1964. Methoden zum Herabsetzen oder Verhindern der Krustenbildung. *Chem. Ing. Tech. - CIT* 36, 60–67. <http://dx.doi.org/10.1002/cite.330360110>.
- Mayer, M., Augustin, W., Scholl, S., 2012. Adhesion of single crystals on modified surfaces in crystallization fouling. *J. Cryst. Growth* 361, 152–158. <http://dx.doi.org/10.1016/j.jcrysgro.2012.09.032>.
- Mérian, T., Goddard, J.M., 2012. Advances in nonfouling materials: perspectives for the food industry. *J. Agric. Food Chem.* 60, 2943–2957. <http://dx.doi.org/10.1021/jf204741p>.
- Owens, D.K., Wendt, R.C., 1969. Estimation of the surface free energy of polymers. *J. Appl. Polym. Sci.* 13, 1741–1747. <http://dx.doi.org/10.1592/phco.30.10.1004>.
- van Oss, C.J., Chaudhury, M.K., Good, R.J., 1988. Interfacial Lifshitz-van der Waals and polar interactions in macroscopic systems. *Chem. Rev.* 88, 927–941. <http://dx.doi.org/10.1021/cr00088a006>.
- van Oss, C.J., Giese, R.F.F., Li, Z., Murphy, K., Norris, J., Chaudhury, M.K.K., Good, R.J., 1992. Determination of contact angles and pore sizes of porous media by column and thin layer wicking. *J. Adhes. Sci. Technol.* 6, 413–428. <http://dx.doi.org/10.1163/156856192X00755>.
- Zamuruyev, K.O., Bardaweel, H.K., Carron, C.J., Kenyon, N.J., Brand, O., Delplanque, J.P., Davis, C.E., 2014. Continuous droplet removal upon dropwise condensation of humid air on a hydrophobic micropatterned surface. *Langmuir* 30, 10133–10142. <http://dx.doi.org/10.1021/la5004462>.
- Zhang, Z., Ferenczi, M.A., Lush, A.C., Thomas, C.R., 1991. A novel micromanipulation technique for measuring the bursting strength of single mammalian cells. *Appl. Microbiol. Biotechnol.* 36, 208–210. <http://dx.doi.org/10.1007/BF00164421>.
- Zorita, S., Niquet, C., Bonhoure, J., Robert, N., Tessier, F.J., 2010. Optimisation of a model food mixture using response surface methodology to evaluate the anti-adhesive properties of cooking materials. *Int. J. Food Sci. Technol.* 45, 2494–2501. <http://dx.doi.org/10.1111/j.1365-2621.2010.02459.x>.

References

- Adnan, T. (2009). *Milk Processing and Quality Management*. Chichester, UK: Wiley-Blackwell.
- Albert, F., Augustin, W., & Scholl, S. (2011). Roughness and constriction effects on heat transfer in crystallization fouling. *Chem. Eng. Sci.*, *66*(3), 499–509.
- Ali, A., De'Ath, D., Gibson, D., Parkin, J., Alam, Z., Ward, G., & Wilson, D. I. (2015). Development of a 'millimanipulation' device to study the removal of soft solid fouling layers from solid substrates and its application to cooked lard deposits. *Food Bioprod. Process.*, *93*, 256–268.
- Alsaad, M. A., & Hammad, M. A. (1998). The application of propane/butane mixture for domestic refrigerators. *Appl. Therm. Eng.*, *18*(9-10), 911–918.
- Amjad, Z. (1998). *Calcium Phosphates in Biological and Industrial Systems*. NY, US: Springer Science and Business Media.
- Atkins, P. W. (1986). *Physical Chemistry*. Oxford, UK: Oxford University Press.
- Auty, M. A. E., Twomey, M., Guinee, T. P., & Mulvihill, D. M. (2001). Development and application of confocal scanning laser microscopy methods for studying the distribution of fat and protein in selected dairy products. *J. Dairy Res.*, *68*(3), 417–427.
- Avila, K., Moxey, D., de Lozar, A., Avila, M., Barkley, D., & Hof, B. (2011). The onset of turbulence in pipe flow. *Science*, *333*(6039), 192–196.
- Baier, R. E. (2006). Surface behaviour of biomaterials: The theta surface for biocompatibility. *J. Mater. Sci. Mater. Med.*, *17*(11), 1057–1062.
- Balasubramanian, S., & Puri, V. M. (2008). Fouling mitigation during product processing using a modified plate heat exchanger surface. *Transactions of the ASABE*, *51*(2), 629–639.
- Balasubramanian, S., & Puri, V. M. (2009). Reduction of milk fouling in a plate heat exchanger system using food-grade surface coating. *Transactions of the ASABE*, *52*(5), 1603–1610.

-
- Bansal, B., & Chen, X. D. (2006). A critical review of milk fouling in heat exchangers. *Compr. Rev. Food Sci. Food Saf.*, 5(2), 27–33.
- Bansal, B., Chen, X. D., & Müller-Steinhagen, H. (2008). Analysis of ‘classical’ deposition rate law for crystallisation fouling. *Chem. Eng. Process. Process Intensif.*, 47(8), 1201–1210.
- Barish, J. A., & Goddard, J. M. (2013). Anti-fouling surface modified stainless steel for food processing. *Food Bioprod. Process.*, 91(4), 352–361.
- Barish, J. A., & Goddard, J. M. (2014). Stability of nonfouling stainless steel heat exchanger plates against commercial cleaning agents. *J. Food Eng.*, 124, 143–151.
- Barthlott, W., & Ehler, N. (1977). *Raster-Elektronenmikroskopie der Epidermis-Oberflächen von Spermatophyten*. Stuttgart, DE: Akademie der Wiss. u.d. Literatur.
- Belmar-Beiny, M. T., Gotham, S. M., Paterson, W. R., Fryer, P. J., & Pritchard, A. M. (1993). The effect of Reynolds number and fluid temperature in whey protein fouling. *J. Food Eng.*, 19(2), 119–139.
- Bergman, T. L., & Incropera, F. P. (2011). *Fundamentals of Heat and Mass Transfer*. NYC, US: Wiley.
- Bergslien, E., Fountain, J., & Giese, R. (2004). Characterization of the surface properties of epoxy-type models used for multiphase flow studies in fractured media and creation of a new model. *Water Resour. Res.*, 40(5), W05112.
- Besevic, P., Clarke, S. M., Kawaley, G., & Wilson, D. I. (2017). A novel fouling cell to study influence of solution on crystallisation fouling. In *Heat Exch. Fouling Clean. Conf.* (pp. 49–57). Aranjuez, Spain.
- Beuf, M., Rizzo, G., Leuliet, J. C., Müller-Steinhagen, H., Yiantsios, S., Karabelas, A., & Benezech, T. (2004). Fouling and cleaning of modified stainless steel plate heat exchangers processing milk products. In *Heat Exch. Fouling Clean. Conf.* (pp. 99–107). Santa Fe, NM, US.
- Bohnet, M. (1985). Fouling von Wärmeübertragungsflächen. *Chem. Ing. Tech.*, 57(1), 24–36.
- Bott, T. R. (1995). *Fouling of Heat Exchangers*. Amsterdam, Netherlands: Elsevier.

- Bott, T. R. (1997). Aspects of crystallization fouling. *Exp. Therm. Fluid Sci.*, *14*(4), 356–360.
- Bott, T. R. (2001). Potential physical methods for the control of biofouling in water systems. *Chem. Eng. Res. Des.*, *79*(4), 484–490.
- Boxler, C., Augustin, W., & Scholl, S. (2013a). Cleaning of whey protein and milk salts soiled on DLC coated surfaces at high-temperature. *J. Food Eng.*, *114*(1), 29–38.
- Boxler, C., Augustin, W., & Scholl, S. (2013b). Fouling of milk components on DLC coated surfaces at pasteurization and UHT temperatures. *Food Bioprod. Process.*, *91*(4), 336–347.
- Boxler, C., Augustin, W., & Scholl, S. (2013c). Influence of surface modification on the composition of a calcium phosphate-rich whey protein deposit in a plate heat exchanger. *Dairy Sci. Technol.*, *94*(1), 17–31.
- Britten, M., Green, M. L., Boulet, M., & Paquin, P. (1988). Deposit formation on heated surfaces: effect of interface energetics. *J. Dairy Res.*, *55*(04), 551.
- Burton, H. (1968). Section G. Deposits from whole milk in heat treatment plant — a review and discussion. *J. Dairy Res.*, *35*(2), 317–330.
- Bylund, G. (2015). *Dairy Processing Handbook*. Lund, Sweden: Tetra Pak.
- Casado, E. (1990). Model optimizes exchanger cleaning. *Hydrocarb. Process.*, *69*, 71–76.
- Cevallos, J. G., Bergles, A. E., Bar-Cohen, A., Rodgers, P., & Gupta, S. K. (2012). Polymer heat exchangers — history, opportunities, and challenges. *Heat Transf. Eng.*, *33*(13), 1075–1093.
- Charpentier, T. V. J., Neville, A., Baudin, S., Smith, M. J., Euvrard, M., Bell, A., Wang, C., & Barker, R. (2015). Liquid infused porous surfaces for mineral fouling mitigation. *J. Colloid Interface Sci.*, *444*, 81–86.
- Chenoweth, J. M. (1988). Liquid fouling monitoring equipment. In L. Melo, T. R. Bott, & C. Bernardo (Eds.), *Fouling Science and Technology. NATO ASI Series (Series E: Applied Sciences)* (Vol. 145, pp. 49–65). Dordrecht, NL: Springer.
- Coletti, F., Ishiyama, E. M., Paterson, W. R., Wilson, D. I., & Macchietto, S. (2010). Impact of deposit aging and surface roughness on thermal fouling: Distributed model. *AIChE J.*, *56*(12), 3257–3273.

-
- Considine, T., Patel, H. A., Singh, H., & Creamer, L. K. (2007). Influence of binding conjugated linoleic acid and myristic acid on the heat- and high-pressure-induced unfolding and aggregation of β -lactoglobulin B. *Food Chem.*, *102*(4), 1270–1280.
- dos Santos, J. d. S. T., Fernandes, A. C., & Giuliatti, M. (2004). Study of the paraffin deposit formation using the cold finger methodology for Brazilian crude oils. *J. Pet. Sci. Eng.*, *45*(1-2), 47–60.
- Dupeyrat, M., Labbé, J.-P., Michel, F., Billoudet, F., & Daufin, G. (1987). Mouillabilité et interactions solide-liquide dans l'encrassement de divers matériaux par du lactosérum et du lait. *Lait*, *67*(4), 465–486.
- Dupré, M. A. (1869). *Théorie Mécanique de la Chaleur*. Paris, FR: Gauthier-Villars.
- Dürr, S., & Thomason, J. C. (2010). *Biofouling*. Oxford, UK: Wiley-Blackwell.
- Eaton, P. E. (1983). *Fouling test apparatus*. (US Patent 4,383,438)
- Epstein, N. (1983). Thinking about heat transfer fouling: A 5 x 5 matrix. *Heat Transf. Eng.*, *4*(1), 43–56.
- Epstein, N. (1994). A model of the initial chemical reaction fouling rate for flow within a heated tube, and its verification. In *Proc. 10th int. heat trans. conf.* (Vol. 10, p. 225-229). Brighton, UK.
- Euler, L. (1783). De serie Lambertina Plurimisque eius insignibus proprietatibus. *Acta Acad. Scient. Petropol.* *2*, 29–51.
- Eurostat. (2017a). *Electricity prices for non-household consumers - bi-annual data (from 2007 onwards)*. http://ec.europa.eu/eurostat/product?code=nrg_pc_205&language=en&mode=view. (Accessed: 23.03.2018)
- Eurostat. (2017b). *Gas prices for non-household consumers - bi-annual data (from 2007 onwards)*. http://ec.europa.eu/eurostat/product?code=nrg_pc_203&language=en&mode=view. (Accessed: 23.03.2018)
- Fernández-Martín, F. (1972a). Influence of temperature and composition on some physical properties of milk and milk concentrates. I. Heat capacity. *J. Dairy Res.*, *39*(01), 65–73.
- Fernández-Martín, F. (1972b). Influence of temperature and composition on some physical properties of milk and milk concentrates. II. Viscosity. *J. Dairy Res.*, *39*(1), 75–82.

- Fickak, A., Hatfield, E., & Chen, X. D. (2012). Influence of run time and aging on fouling and cleaning of whey protein deposits on heat exchanger surface. *J. Food Res.*, *1*(1), 212–224.
- Förster, M., & Bohnet, M. (2000). Modification of molecular interactions at the interface crystal/heat transfer surface to minimize heat exchanger fouling. *Int. J. Therm. Sci.*, *39*(7), 697–708.
- Foster, C. L., Britten, M., & Green, M. L. (1989). A model heat-exchange apparatus for the investigation of fouling of stainless steel surfaces by milk I. Deposit formation at 100 °C. *J. Dairy Res.*, *56*(2), 201–209.
- Foster, C. L., & Green, M. L. (1990). A model heat exchange apparatus for the investigation of fouling of stainless steel surfaces by milk II. Deposition of fouling material at 140 °C, its adhesion and depth profiling. *J. Dairy Res.*, *57*(3), 339–348.
- Fowkes, F. M. (1962). Determination of interfacial tensions, contact angles, and dispersion forces in surfaces by assuming additivity of intermolecular interactions in surfaces. *J. Phys. Chem.*, *66*(2), 382–382.
- Fowkes, F. M. (1963). Additivity of intermolecular forces at interfaces. I. Determination of the contribution to surface and interfacial tensions of dispersion forces in various liquids. *J. Phys. Chem.*, *67*(12), 2538–2541.
- Fryer, P. J. (1986). *Modelling heat exchanger fouling*. Unpublished PhD dissertation, University of Cambridge.
- Fryer, P. J., & Slater, N. K. H. (1985). A direct simulation procedure for chemical reaction fouling in heat exchangers. *Chem. Eng. J.*, *31*(2), 97–107.
- Garrett-Price, B. A. (1985). *Fouling of Heat Exchangers. Characteristics, Costs, Prevention, Control and Removal*. Park Ridge, New Jersey: Noyes Publications.
- Gaucheron, F. (2005). The minerals of milk. *Reprod. Nutr. Dev.*, *45*(4), 473–483.
- Geddert, T., Bialuch, I., Augustin, W., & Scholl, S. (2009). Extending the induction period of crystallization fouling through surface coating. *Heat Transf. Eng.*, *30*(10–11), 868–875.
- Geometrical Product Specifications (GPS). Surface Texture: Areal* (Standard). (2016). Geneva, CH: International Organization for Standardization.

-
- Georgiadis, M. C., & Macchietto, S. (2000). Dynamic modelling and simulation of plate heat exchangers under milk fouling. *Chem. Eng. Sci.*, *55*(9), 1605–1619.
- Glastrup, J. (1996). Degradation of polyethylene glycol. A study of the reaction mechanism in a model molecule: Tetraethylene glycol. *Polym. Degrad. Stab.*, *52*(3), 217–222.
- Gomes da Cruz, L., Ishiyama, E. M., Boxler, C., Augustin, W., Scholl, S., & Wilson, D. I. (2015). Value pricing of surface coatings for mitigating heat exchanger fouling. *Food Bioprod. Process.*, *93*, 343–363.
- Gordon, K. P., Hankinson, D. J., & Carver, C. E. (1968). Deposition of milk solids on heated surfaces. *J. Dairy Sci.*, *51*(4), 520–526.
- Gunning, P. A., Mackie, A. R., Gunning, A. P., Wilde, P. J., Woodward, N. C., & Morris, V. J. (2004). The effect of surfactant type on protein displacement from the air–water interface. *Food Hydrocoll.*, *18*(3), 509–515.
- Hagsten, C., Altskär, A., Gustafsson, S., Lorén, N., Ham, L., Innings, F., Paulsson, M., & Nylander, T. (2016). Composition and structure of high temperature dairy fouling. *Food Struct.*, *7*(2), 13–20.
- Hartnett, J. P., Irvine, T. F., Cho, Y. I., & Greene, G. A. (2001). *Advances in Heat Transfer* (No. Bd. 35). San Diego, CA, US: Elsevier Science.
- Hays, G. F. (1989). Fouling allowances are self-fulfilling prophecies. In *National heat transfer conf.* (pp. 325–330). Philadelphia, PA, US.
- Helalizadeh, A., Müller-Steinhagen, H., & Jamialahmadi, M. (2000). Mixed salt crystallisation fouling. *Chem. Eng. Process. Process Intensif.*, *39*(1), 29–43.
- Hewitt, G. F., & Pugh, S. J. (2007). Approximate design and costing methods for heat exchangers. *Heat Transf. Eng.*, *28*(2), 76–86.
- Holsinger, V. H., Rajkowski, K. T., & Stabel, J. R. (1997). Milk pasteurisation and safety: a brief history and update. *Rev. Sci. Tech. l'OIE*, *16*(2), 441–451.
- Howell, D., & Behrends, B. (2006). A review of surface roughness in antifouling coatings illustrating the importance of cutoff length. *Biofouling*, *22*(6), 401–410.
- Huang, K., & Goddard, J. M. (2015). Influence of fluid milk product composition on fouling and cleaning of Ni–PTFE modified stainless steel heat exchanger surfaces. *J. Food Eng.*, *158*, 22–29.

- Ishiyama, E. M., Paterson, W. R., & Wilson, D. I. (2008). Thermo-hydraulic channelling in parallel heat exchangers subject to fouling. *Chem. Eng. Sci.*, *63*(13), 3400–3410.
- Ishiyama, E. M., Paterson, W. R., & Wilson, D. I. (2009). The effect of fouling on heat transfer, pressure drop, and throughput in refinery preheat trains: Optimization of cleaning schedules. *Heat Transf. Eng.*, *30*(10-11), 805–814.
- Ishiyama, E. M., Paterson, W. R., & Wilson, D. I. (2014). Aging is important: Closing the fouling–cleaning loop. *Heat Transf. Eng.*, *35*(3), 311–326.
- Israelachvili, J. N. (2011). *Intermolecular and Surface Forces* (Vol. 3). Waltham, MA, US: Elsevier.
- Jain, A., & Bhosle, N. B. (2009). Biochemical composition of the marine conditioning film: implications for bacterial adhesion. *Biofouling*, *25*(1), 13–19.
- Javidi, M., Javadpour, S., Bahrololoom, M. E., & Ma, J. (2008). Electrophoretic deposition of natural hydroxyapatite on medical grade 316L stainless steel. *Mater. Sci. Eng. C*, *28*(8), 1509–1515.
- Jeurnink, T., Verheul, M., Stuart, M. C., & De Kruif, C. G. (1996). Deposition of heated whey proteins on a chromium oxide surface. *Colloids Surf. B Biointerfaces*, *6*(4-5), 291–307.
- Jeurnink, T. J. M. (1995). Fouling of heat exchangers by fresh and reconstituted milk and the influence of air bubbles. *Milchwissenschaft*, *50*(4), 189–193.
- Jose, J., & Burgess, K. (2006). Benzophenoxazine-based fluorescent dyes for labeling biomolecules. *Tetrahedron*, *62*(48), 11021–11037.
- Junghahn, L. (1964). Methoden zum Herabsetzen oder Verhindern der Krustenbildung. *Chemie Ing. Tech.*, *36*(1), 60–67.
- Kananeh, A. B., Scharnbeck, E., Kück, U. D., & Rübiger, N. (2010). Reduction of milk fouling inside gasketed plate heat exchanger using nano-coatings. *Food Bioprod. Process.*, *88*(4), 349–356.
- Karlsson, C. A.-C., Wahlgren, M. C., & Trägårdh, A. C. (1996). β -Lactoglobulin fouling and its removal upon rinsing and by SDS as influenced by surface characteristics, temperature and adsorption time. *J. Food Eng.*, *30*(1-2), 43–60.
- Kern, D. Q., & Seaton, R. E. (1959). A theoretical analysis of thermal surface fouling. *British Chem. Eng.*, 258–262.

-
- Kiely, L. J., & Olson, N. F. (2003). Short communication: Estimate of non electrostatic interaction free energy parameters for milk fat globules. *J. Dairy Sci.*, *86*(10), 3110–3112.
- Kim, H. J., Decker, E. A., & McClements, D. J. (2002). Role of postadsorption conformation changes of β -lactoglobulin on its ability to stabilize oil droplets against flocculation during heating at neutral pH. *Langmuir*, *18*(20), 7577–7583.
- Lalande, M., Tissier, J.-P., & Corrieu, G. (1984). Fouling of a plate heat exchanger used in ultra-high-temperature sterilization of milk. *J. Dairy Res.*, *51*(4), 557–568.
- Lee, S. J., & Sherbon, J. W. (2002). Chemical changes in bovine milk fat globule membrane caused by heat treatment and homogenization of whole milk. *J. Dairy Res.*, *69*(4), 555–567.
- Lefevre, C., Kang, H. C., Haugland, R. P. R. P., Malekzadeh, N., Arttamangkul, S., & Haugland, R. P. R. P. (1996). Texas Red-X and rhodamine Red-X, new derivatives of sulforhodamine 101 and lissamine rhodamine B with improved labeling and fluorescence properties. *Bioconjug. Chem.*, *7*(4), 482–489.
- Lin, S. X. Q., & Chen, X. D. (2007). A laboratory investigation of milk fouling under the influence of ultrasound. *Food Bioprod. Process.*, *85*(1), 57–62.
- Listiohadi, Y., Hourigan, J. A., Sleigh, R. W., & Steele, R. J. (2009). Thermal analysis of amorphous lactose and α -lactose monohydrate. *Dairy Sci. Technol.*, *89*(1), 43–67.
- Liu, W., Christian, G., Zhang, Z., & Fryer, P. (2002). Development and use of a micromanipulation technique for measuring the force required to disrupt and remove fouling deposits. *Food Bioprod. Process.*, *80*(4), 286–291.
- Liu, W., Christian, G. K., Zhang, Z., & Fryer, P. J. (2006). Direct measurement of the force required to disrupt and remove fouling deposits of whey protein concentrate. *Int. Dairy J.*, *16*(2), 164–172.
- Luey, J.-K., McGuire, J., & Sproull, R. D. (1991). The effect of pH and NaCl concentration on adsorption of β -lactoglobulin at hydrophilic and hydrophobic silicon surfaces. *J. Colloid Interface Sci.*, *143*(2), 489–500.
- Ma, R. S. T., & Epstein, N. (1981). Optimum cycles for falling rate processes. *Can. J. Chem. Eng.*, *59*(5), 631–633.
- Macchietto, S., Hewitt, G. F., Coletti, F., Crittenden, B. D., Dugwell, D. R., Galindo,

- A., Jackson, G., Kandiyoti, R., Kazarian, S. G., Luckham, P. F., Matar, O. K., Millan-Agorio, M., Müller, E. A., Paterson, W., Pugh, S. J., Richardson, S. M., & Wilson, D. I. (2011). Fouling in crude oil preheat trains: A systematic solution to an old problem. *Heat Transfer Eng.*, *32*(3-4), 197-215.
- Magens, O. M., Hofmans, J., Pabon, M., & Wilson, D. I. (2015). Value pricing of antifouling coatings in heat exchangers. In *Heat Exch. Fouling Clean. Conf.* (pp. 350–357). Enfield, Ireland.
- Mauermann, M., Eschenhagen, U., Bley, T., & Majschak, J.-P. (2009). Surface modifications – Application potential for the reduction of cleaning costs in the food processing industry. *Trends Food Sci. Technol.*, *20*(SUPPL. 1), S9–S15.
- Mayer, M., Augustin, W., & Scholl, S. (2012). Adhesion of single crystals on modified surfaces in crystallization fouling. *J. Cryst. Growth*, *361*(1), 152–158.
- McGuire, J., & Swartzel, K. R. (1989). The influence of solid surface energetics on macromolecular adsorption from milk. *J. Food Process. Preserv.*, *13*(2), 145–160.
- McKeen, L. W. (2007). *Fluorinated Coatings and Finishes Handbook*. Norwich, NY, US: William Andrew Publishing.
- Mérian, T., & Goddard, J. M. (2012). Advances in nonfouling materials: Perspectives for the food industry. *J. Agric. Food Chem.*, *60*(12), 2943–2957.
- Miriani, M., Eberini, I., Iametti, S., Ferranti, P., Sensi, C., & Bonomi, F. (2014). Unfolding of beta-lactoglobulin on the surface of polystyrene nanoparticles: Experimental and computational approaches. *Proteins Struct. Funct. Bioinforma.*, *82*(7), 1272–1282.
- Morison, K. R., & Tie, S.-H. (2002). The development and investigation of a model milk mineral fouling solution. *Food Bioprod. Process.*, *80*(4), 326–331.
- Müller-Steinhagen, H., & Zhao, Q. (1997). Investigation of low fouling surface alloys made by ion implantation technology. *Chem. Eng. Sci.*, *52*(19), 3321–3332.
- Mullin, J. W. (2001). *Crystallisation* (Vol. 4). Oxford, UK: Butterworth-Heinemann.
- Musat, R., & Helerea, E. (2010). Characteristics of the PTC heater used in automotive HVAC systems. In *Ifip adv. inf. commun. technol.* (Vol. 314, pp. 461–468).
- Mwaba, M. G., Golriz, M. R., & Gu, J. (2006). A semi-empirical correlation for crystallization fouling on heat exchange surfaces. *Appl. Therm. Eng.*, *26*(4), 440–447.

-
- Nigo, R. Y., Chew, Y. M. J., Houghton, N. E., Paterson, W. R., & Wilson, D. I. (2009). Experimental studies of freezing fouling of model food fat solutions using a novel spinning disc apparatus. *Energ. Fuel*, *23*(12), 6131–6145.
- Oldani, V., Bianchi, C. L., Biella, S., Pirola, C., & Cattaneo, G. (2013). Use of perfluoropolyether coatings to prevent fouling on heat exchanger metal surfaces. In *Heat Exch. Fouling Clean. Conf.* (pp. 316–323). Budapest, Hungary.
- Oliveira, R. (1997). Understanding adhesion: A means for preventing fouling. *Exp. Therm. Fluid Sci.*, *14*(4), 316–322.
- Owens, D. K., & Wendt, R. C. (1969). Estimation of the surface free energy of polymers. *J. Appl. Polym. Sci.*, *13*(8), 1741–1747.
- Pääkkönen, T. M., Riihimäki, M., Simonson, C. J., Muurinen, E., & Keiski, R. L. (2015). Modeling CaCO₃ crystallization fouling on a heat exchanger surface – Definition of fouling layer properties and model parameters. *Int. J. Heat Mass Tran.*, *83*, 84–98.
- Patel, J. S., Bansal, B., Jones, M. I., & Hyland, M. (2013). Fouling behaviour of milk and whey protein isolate solution on doped diamond-like carbon modified surfaces. *J. Food Eng.*, *116*(2), 413–421.
- Pogiatzis, T. A., Vassiliadis, V. S., Mergulho, F. J., & Wilson, D. I. (2015). Choosing when to clean and how to clean biofilms in heat exchangers. *Heat Transf. Eng.*, *36*(7-8), 676–684.
- Premathilaka, S. S., Hyland, M. M., Chen, X. D., Watkins, L. R., & Bansal, B. (2007). Interaction of whey protein with modified stainless steel surfaces. In *Heat Exch. Fouling Clean. Conf.* (pp. 150–161). Tomar, Portugal.
- Press, W. H., Teukolsky, S. A., Flannery, B. P., & Vetterling, W. T. (1986). *Numerical Recipes: The Art of Scientific Computing*. Cambridge, UK: Cambridge University Press.
- Pritchard, A. (1988). The economics of fouling. In L. F. Melo, T. R. Bott, & C. A. Bernardo (Eds.), *Fouling science and technology* (Vol. 145, p. 31-45). Springer Netherlands.
- Python Software Foundation. (2016). *TkInter - Python Wiki*. <https://wiki.python.org/moin/TkInter>. (Accessed: 05.11.2017)
- Rechendorff, K., Hovgaard, M. B., Foss, M., Zhdanov, V. P., & Besenbacher, F. (2006).

- Enhancement of protein adsorption induced by surface roughness. *Langmuir*, 22(26), 10885–10888.
- Rieke, P. C. (1997). Application of Van Oss-Chaudhury-Good theory of wettability to interpretation of interfacial free energies of heterogeneous nucleation. *J. Cryst. Growth*, 182(3-4), 472–484.
- Rosmaninho, R., & Melo, L. F. (2006). Calcium phosphate deposition from simulated milk ultrafiltrate on different stainless steel-based surfaces. *Int. Dairy J.*, 16(1), 81–87.
- Rosmaninho, R., & Melo, L. F. (2007). Effect of proteins on calcium phosphate deposition in turbulent flow as a function of surface properties. *Exp. Therm. Fluid Sci.*, 32(2), 375–386.
- Rosmaninho, R., & Melo, L. F. (2008). Protein-calcium phosphate interactions in fouling of modified stainless-steel surfaces by simulated milk. *Int. Dairy J.*, 18(1), 72–80.
- Rungraeng, N., Cho, Y.-C., Yoon, S. H., & Jun, S. (2012). Carbon nanotube-polytetrafluoroethylene nanocomposite coating for milk fouling reduction in plate heat exchanger. *J. Food Eng.*, 111(2), 218–224.
- Sadeghinezhad, E., Kazi, S. N., Badarudin, A., Zubair, M. N. M., Dehkordi, B. L., & Oon, C. S. (2013). A review of milk fouling on heat exchanger surfaces. *Rev. Chem. Eng.*, 29(3), 169–188.
- Santos, O., Nylander, T., Schillén, K., Paulsson, M., & Trägårdh, C. (2006). Effect of surface and bulk solution properties on the adsorption of whey protein onto steel surfaces at high temperature. *J. Food Eng.*, 73(2), 174–189.
- Shafrin, E. G., & Zisman, W. A. (1972). Effect of temperature on wetting of high- and low-energy solid surfaces. *J. Phys. Chem.*, 76(22), 3259–3267.
- Simons, J.-W. F. A., Kusters, H. A., Visschers, R. W., & de Jongh, H. H. J. (2002). Role of calcium as trigger in thermal β -lactoglobulin aggregation. *Arch. Biochem. Biophys.*, 406(2), 143–152.
- Siperko, L. M., & Thomas, R. R. (1989). Chemical and physical modification of fluoropolymer surfaces for adhesion enhancement: a review. *Journal of Adhesion Science and Technology*, 3(1), 157-173.
- Skudder, P. J., Brooker, B. E., Bonsey, A. D., & Alvarez-Guerrero, N. R. (1986). Effect

of pH on the formation of deposit from milk on heated surfaces during ultra high temperature processing. *J. Dairy Res.*, 53(1), 75.

- Steinhagen, R., Müller-Steinhagen, H., & Maani, K. (1993). Problems and costs due to heat exchanger fouling in New Zealand industries. *Heat Transfer Eng.*, 14(1), 19-30.
- Sutera, S. P., & Skalak, R. (1993). The history of poiseuille law. *Annu. Rev. Fluid Mech.*, 25(1), 1-19.
- TEMA. (1999). *Standards of the Tubular Exchanger Manufacturers Association* (Vol. 8). Tarrytown, NY, US.
- Tetra Pak. (2007). *Consumption milk pasteurizers can be run much longer than 8 hours* (Tech. Rep.). Lund, Sweden: Tetra Laval S. A.
- Thomas, D., Tovey, S. C., Collins, T. J., Bootman, M. D., Berridge, M. J., & Lipp, P. (2000). A comparison of fluorescent Ca²⁺ indicator properties and their use in measuring elementary and global Ca²⁺ signals. *Cell Calcium*, 28(4), 213-223.
- Thomas, P. A. F., Stoks, W. A. J., & Buegman, A. (2001). *Abrasion resistant coatings*. (US Patent 6,291,054)
- Tolkach, A., & Kulozik, U. (2007). Reaction kinetic pathway of reversible and irreversible thermal denaturation of β -lactoglobulin. *Lait*, 87, 301-315.
- Tuladhar, T. R., Paterson, W. R., & Wilson, D. I. (2002a). Investigation of alkaline cleaning-in-place of whey protein deposits using dynamic gauging. *Food Bioprod. Process. Trans. Inst. Chem. Eng. Part C*, 80(3), 199-214.
- Tuladhar, T. R., Paterson, W. R., & Wilson, D. I. (2002b). Thermal conductivity of whey protein films undergoing swelling. *Food Bioprod. Process.*, 80(4), 332-339.
- Valluri, S. R., Jeffrey, D. J., & Corless, R. M. (2000). Some applications of the Lambert W function to physics. *Can. J. Phys.*, 78(9), 823-831.
- van Oss, C. J. (2003). Long-range and short-range mechanisms of hydrophobic attraction and hydrophilic repulsion in specific and aspecific interactions. *J. Mol. Recognit.*, 16(4), 177-190.
- van Oss, C. J., Good, R. J., & Chaudhury, M. K. (1987). Determination of the hydrophobia interaction energy—Application to separation processes. *Sep. Sci. Technol.*, 22(1), 1-24.

- van Oss, C. J., Chaudhury, M. K., & Good, R. J. (1987). Monopolar surfaces. *Adv. Colloid Interface Sci.*, *28*, 35–64.
- van Oss, C. J., Giese, R. F. F., Li, Z., Murphy, K., Norris, J., Chaudhury, M. K., & Good, R. (1992). Determination of contact angles and pore sizes of porous media by column and thin layer wicking. *J. Adhes. Sci. Technol.*, *6*(4), 413–428.
- van Oss, C. J., & Good, R. J. (1992). Prediction of the solubility of polar polymers by means of interfacial tension combining rules. *Langmuir*, *8*(12), 2877–2879.
- Vargaftik, N. B., Volkov, B. N., & Voljak, L. D. (1983). International tables of the surface tension of water. *J. Phys. Chem. Ref. Data*, *12*(3), 817–820.
- VDI. (2010). *VDI Heat Atlas*. Berlin, DE: Springer.
- Visser, J. (1988). Adhesion and removal of particles I. In L. Melo, T. R. Bott, & C. Bernardo (Eds.), *Fouling Science and Technology. NATO ASI Series (Series E: Applied Sciences)* (Vol. 145, p. 87-104). Dordrecht, NL: Springer.
- Visser, J., & Jeurnink, T. J. M. (1997). Fouling of heat exchangers in the dairy industry. *Exp. Therm. Fluid Sci.*, *14*(4), 407–424.
- Walstra, P., Wouters, J. T. M., & Geurts, T. J. (2005). *Dairy Science and Technology* (Vol. 2). Boca Raton, FL, US: Taylor & Francis.
- Wibulswas, P. (1966). *Laminar-flow heat-transfer in non-circular ducts*. Phd dissertation, University College London.
- Wilson, D. I. (2005). Challenges in cleaning: Recent developments and future prospects. *Heat Transf. Eng.*, *26*(1), 51–59.
- Wu, W., & Nancollas, G. H. (1998). The dissolution and growth of sparingly soluble inorganic salts: a kinetics and surface energy approach. *Pure Appl. Chem.*, *70*(10), 1867–1872.
- Wu, W., Zhuang, H., & Nancollas, G. H. (1997). Heterogeneous nucleation of calcium phosphates on solid surfaces in aqueous solution. *J. Biomed. Mater. Res.*, *35*(1), 93–9.
- Xu, Z. M., Yang, S. R., Guo, S. Q., Zhao, H., Qi, B., & Zhang, Z. B. (2005). Costs due to utility boiler fouling in China. *Heat Transfer Asian Res.*, *34*(2), 53–63.
- Yang, Q., Wilson, D. I., Chang, S., & Shi, L. (2015). A new approach for mitigating

-
- biofouling by promoting online cleaning using a sacrificial paraffin coating. *Heat Transf. Eng.*, *36*(7-8), 695-705.
- Yoon, J., & Lund, D. B. (1994). Comparison of two operating methods of a plate heat exchanger under constant heat flux condition and their effect on the temperature profile during milk fouling. *J. Food Process. Eng.*, *17*(3), 243–262.
- Young, T. (1805). An Essay on the Cohesion of Fluids. *Philos. Trans. R. Soc. London*, *95*, 65–87.
- Zamuruyev, K. O., Bardaweel, H. K., Carron, C. J., Kenyon, N. J., Brand, O., Delplanque, J. P., & Davis, C. E. (2014). Continuous droplet removal upon dropwise condensation of humid air on a hydrophobic micropatterned surface. *Langmuir*, *30*(33), 10133–10142.
- Zare, D., McGrath, K. M., & Allison, J. R. (2015). Deciphering β -lactoglobulin interactions at an oil–water interface: A molecular dynamics study. *Biomacromolecules*, *16*(6), 1855–1861.
- Zhang, Z., Ferenczi, M. A., Lush, A. C., & Thomas, C. R. (1991). A novel micromanipulation technique for measuring the bursting strength of single mammalian cells. *Appl. Microbiol. Biotechnol.*, *36*(2), 208–210.
- Zhao, Q., Liu, Y., Müller-Steinhagen, H., & Liu, G. (2002). Graded Ni–P–PTFE coatings and their potential applications. *Surf. Coatings Technol.*, *155*(2-3), 279–284.
- Zhao, Q., Liu, Y., Wang, C., Wang, S., & Müller-Steinhagen, H. (2005). Effect of surface free energy on the adhesion of biofouling and crystalline fouling. *Chem. Eng. Sci.*, *60*(17), 4858–4865.
- Ziels, N. W., & Schmidt, W. H. (1945). Catalytic effect of metals and light on fats and oils. *Oil Soap*, *22*(12), 327–330.
- Zouaghi, S., Six, T., Nuns, N., Simon, P., Bellayer, S., Moradi, S., Hatzikiriakos, S. G., André, C., Delaplace, G., & Jimenez, M. (2018). Influence of stainless steel surface properties on whey protein fouling under industrial processing conditions. *J. Food Eng.*, *228*, 38–49.